

On the design of rockfall protection galleries

Report

Author(s):

Schellenberg, Kristian

Publication date:

2009

Permanent link:

<https://doi.org/10.3929/ethz-a-005816027>

Rights / license:

[In Copyright - Non-Commercial Use Permitted](#)

Originally published in:

IBK Bericht 315

ON THE DESIGN OF ROCKFALL PROTECTION GALLERIES

Kristian Schellenberg

Institute of Structural Engineering

Swiss Federal Institute of Technology Zurich

January 2009

Preface

Rockfall is one of the important natural hazards in Switzerland; not in terms of damage caused or people killed, but in terms of frequency and potential threat. By the decreasing cultivation of alpine forests and the retreat of permafrost due to global warming, rockfall events will increase in both, frequency and extent in near future. Since society does not accept natural hazards as inevitable incidents anymore, owners of transportation networks will be forced to increase their respective mitigation activities.

Inspired by three rockfalls on protective structures in 2003, Kristian Schellenberg started his research by establishing an inventory of all endangered structures of the Swiss road and railway networks. He identified shortcomings in the Swiss design guidelines for rockfall structures and updated the experience of our institute with respect to dynamic testing that had got – apart from earthquake engineering – less priority for more than twenty years. His experiments culminated in large-scale falling-weight tests at the site of the Federal Institute for Forest, Snow and Landscape Research (WSL), his most important research partner. A fellowship of the Japanese Society for Promotion of Science allowed for a three month stay at the Muroran Institute of Technology, Japan in autumn 2007 to compare test results and modeling techniques.

The excellent cooperation with WSL was also the starting point of the idea to organize an Interdisciplinary Workshop on Rockfall Protection as a follow-up to the Joint Japan-Swiss Scientific Seminar hosted in 1999 by the Swiss Federal Institute of Technology in Lausanne (EPFL) in 1999. Finally, WSL, EPFL and ETH Zurich jointly accounted for the workshop, which took place at Morschach, well above the lake of Lucerne, on June 23-25, 2008. Researchers, practitioners and officials from the domains of geology, geography, structural, geotechnical, risk and forestry engineering as well as land-use planning exchanged their views and experiences on the different aspects of rockfall protection. The workshop coincided with the completion of Kristian Schellenberg's present thesis and crowned his work.

Zurich, January 2009

Prof. Thomas Vogel

Summary

Galleries are common measures to protect roads and railways from rockfall. Rockfall is one of the most relevant natural hazards in the mountainous regions of Switzerland. The recent Swiss design concept is based on the application of a static equivalent force. This approach is simple in use for the engineers in practice, however, the dynamic behavior of the structure is not satisfactorily taken into consideration.

The aim of this research is to provide a better understanding of the dynamic response of rockfall protection galleries. This will improve the prediction accuracy of their impact load capacity. An analytical model based on a system of multiple degrees of freedom and different simplifications is shown. The model enables predicting shear failure as well as bending failure due to impact.

In order to verify and calibrate the model, various tests from small to large-scale were performed. The small-scale tests were used to evaluate the adequate test setup for laboratory research. Although the falling weight test setup is the most complex one, it proved to be the most appropriate. In mid-scale tests different cushion layers were evaluated and in particular the performance of the measurement equipment. Large-scale tests in a scale 1:2 provided the required data to calibrate the analytical model as well as future numerical models. Three series of slabs with different thicknesses with and without shear reinforcement were subjected to increasing impact loads until failure. In the last series punching tests were performed with different boundary conditions and a smaller loading area.

Zusammenfassung

Galerien sind eine verbreitete Massnahme, um Strassen und Bahnlinien vor Steinschlag zu schützen. Steinschlag ist eine relevante Gefährdung in den Bergregionen der Schweiz. Das Bemessungskonzept gemäss der aktuellen Richtlinie in der Schweiz berücksichtigt die Belastung aus einem Steinschlagereignis mittels einer statisch äquivalenten Ersatzkraft, die eine einfache Anwendung in der Praxis erlaubt. Es stellt sich die Frage, in wie fern das dynamische Verhalten der Struktur in Rechnung getragen ist.

Das Ziel dieser Arbeit ist, zu einem besseren Verständnis über das Tragverhalten von Steinschlaggalerien beizutragen und eine präzisere Vorhersage der Tragfähigkeit der Galerie bei Stossbelastung zu ermöglichen. Ein Modell bestehend aus einem Mehrmassenschwinger wird vorgeschlagen. Das Modell ermöglicht, sowohl ein Durchstanzen wie auch ein Biegeversagen vorherzusagen.

Um das Modell zu kalibrieren bzw. zu verifizieren, wurden Versuche in verschiedenen Massstäben durchgeführt. In klein-massstäblichen Versuchen wurde zunächst nach dem geeigneten Versuchsaufbau gesucht, um Steinschlaggalerien im Labor untersuchen zu können. Der Fallversuch stellte sich als der best geeignete Versuchsaufbau heraus, obwohl dieser der Komplizierteste ist. Bei Versuchen im mittleren Massstab wurden verschiedene Eindeckungsmaterialien getestet und insbesondere die Messinfrastruktur erprobt. Grossversuche im Massstab 1:2 lieferten schliesslich die Messwerte, um das Modell und künftige FE-Simulationen zu kalibrieren. Platten von unterschiedlicher Stärken sowie mit und ohne Schubbewehrung wurden jeweils mit steigender Fallhöhe bis zum Bruch belastet. In einer vierten Versuchsreihe wurden Fallversuche durchgeführt, bei welchen die Platten infolge unterschiedlicher Auflagerbedingungen und einer reduzierten Lastfläche auf Durchstanzen versagten.

Table of contents

Preface	iii
Summary	v
Zusammenfassung	vi
1. Introduction	1
1.1. Existing structures	1
1.2. Motivation	4
1.3. Aims and scope	5
2. State of the art	7
2.1. Cushion layer	8
2.2. Dynamic material properties	9
2.3. Local structural behavior	12
2.4. Global structural behavior	12
2.5. Experimental studies	13
2.6. Analytical modeling	14
2.7. Numerical modeling	15
2.8. Guidelines and recommendations	16
3. Experimental research	21
3.1. Small-scale tests	21
3.2. Medium-scale tests	27
3.3. Large-scale tests	34
3.4. Punching tests	42
4. Analytical model	45
4.1. Assignment of the three masses	47
4.2. Spring properties	50
4.3. Damping elements	60
4.4. Numerical integration	61
4.5. Calculation and verification methods	62
5. Calibration of the model	63
5.1. Global response	63
5.2. Punching behavior	72
5.3. Sensitivity of the single parameters	76
6. Results	79
6.1. Comparison with guideline	79
6.2. Evaluation of ultimate load capacity	81
6.3. Case study	82

7. Conclusions	89
8. Outlook.....	91
Notation	93
Acknowledgements.....	95
References	97
Appendices	105
A. Structures considered in the survey.....	106
B. Test results of large-scale tests.....	115
C. Numerical solving of the SMDF	128
D. Input and output of SMDF for large-scale test.....	133
E. Input and output of SMDF for the punching tests.....	155
F. Parameter sensitivity of SMDF	166

1. Introduction

In mountainous countries like Switzerland, rockfall is one of the most important natural hazards today. The associated risks due to rockfall are usually reduced by means of structures such as galleries protecting roads and railways.

In the past, impact energies up to 3000 kJ could only be absorbed by galleries, often called rock sheds. Today other protection measures such as flexible barriers in the loose zones or in the rockfall trajectories are also competitive solutions. Nevertheless, there are many cases where protective galleries are still the appropriate solution. The important advantage of galleries compared to flexible barriers for example, are their resistance to normal events (lower magnitude than the design level, e.g. return period of 10 years) without damage to the structure itself and with no disturbance and distraction of road or railway users by fine particles getting through the mesh openings. Flexible barriers dissipate the energy imposed by a rockfall exclusively by plastic deformation. Consequently, the remaining protection after the first rockfall event is smaller. Moreover, due to the sag of the barrier under the pressure of the impacting rocks, the barriers have to be placed at a certain distance from the object to be protected.

The relatively high erection costs (estimated between 15'000 and 20'000 Euro per meter length) justify the use of galleries only when at least one of the following most significant situations occurs: (1) the threatened zone is short, well defined and (2) the rate of occurrence of medium magnitude events is high and total protection is therefore needed [Jacquemoud, 1999]. The risk that is reduced by the protective gallery obviously depends on the importance of the road or railway. By-passing endangered zones with tunnels is an expensive alternative which is nevertheless going to be used more frequently for very important lifelines.

1.1. Existing structures

In Switzerland, there are more than 350 protective galleries, including avalanche galleries and tunnel entrances that could be endangered by falling rocks and therefore provide a certain degree of protection to the users. Most of them (220) are located on cantonal or local roads. About 80 are part of the national road net and 50 of the railway network. The majority of these structures were built between 1960 and 1990 and about 80% of them are covered by a so called cushion layer. In case of a rockfall event, the cushion layer distributes the contact stresses, reduces the decelerations in the impacting body and increases the impact duration. Locally available granular soil or gravel is mostly used as cushion layer material.

A database containing the galleries in Switzerland where rockfall can be expected has been created with special emphasis on the different types and typical dimensions. The considered structures are listed in Appendix A. Not only national roads are considered, but also cantonal and local roads where 220 of the 347 galleries are located. 17 galleries of the Swiss Federal Railways (SBB) and 32 of the private owned railways are also recorded.

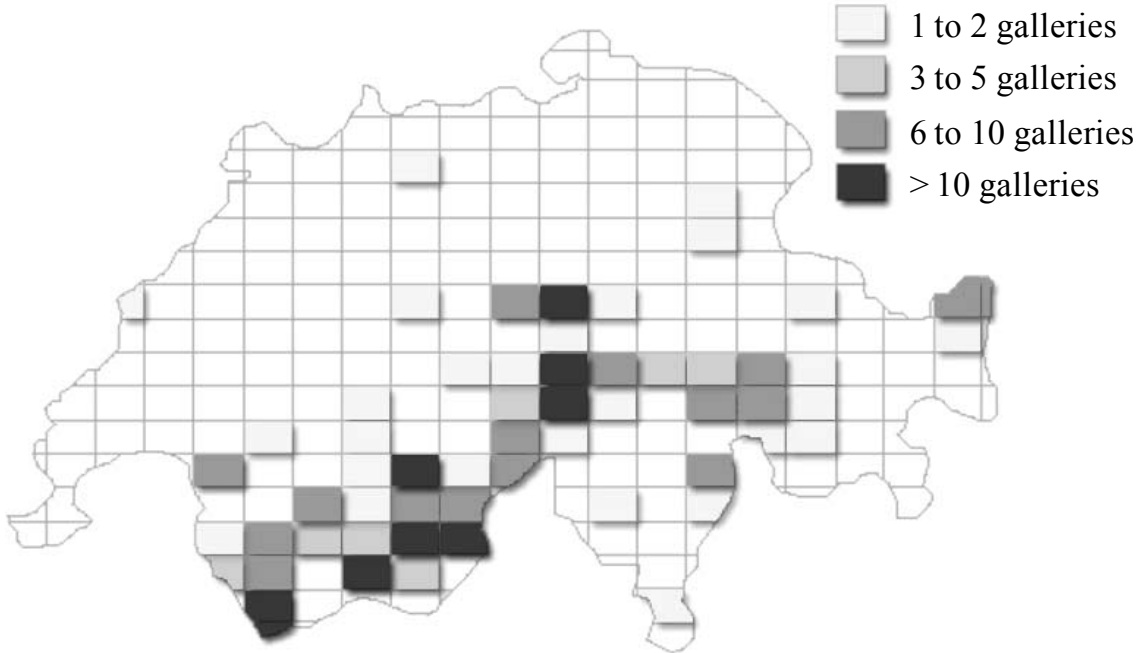


Figure 1-1: Geographical distribution of the protection galleries in Switzerland

Galleries are not only built to protect against possible rockfall events. However, many of these galleries can still be struck and damaged by the impact of a falling or rolling rock, even if they have not been designed exclusively for this purpose. The remaining galleries where due to the topography rockfall impact is not a concern have not been included in the database. It was necessary to rely on the experience of local engineers who are well familiar with the surroundings. In most cases the excluded galleries are avalanche protection galleries located on flat slopes without loose rocks on the terrain surface. Endangered tunnel entrances are also added to the database in all cases where the owner indicated a risk of rockfall. Another difficulty is to distinguish between a tunnel portal and a short gallery adjacent to a tunnel. Thus also the tunnel portals are considered.

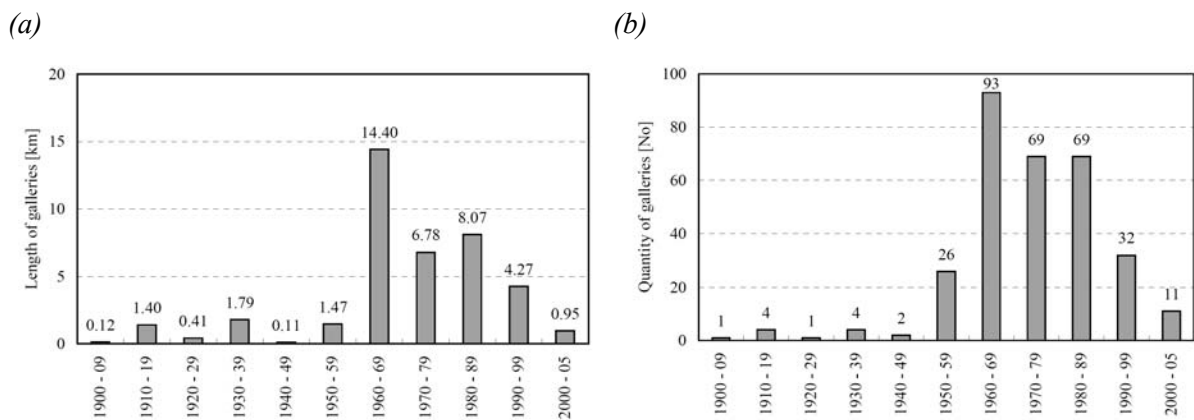


Figure 1-2: Age of the galleries classified according to a) length and b) quantity

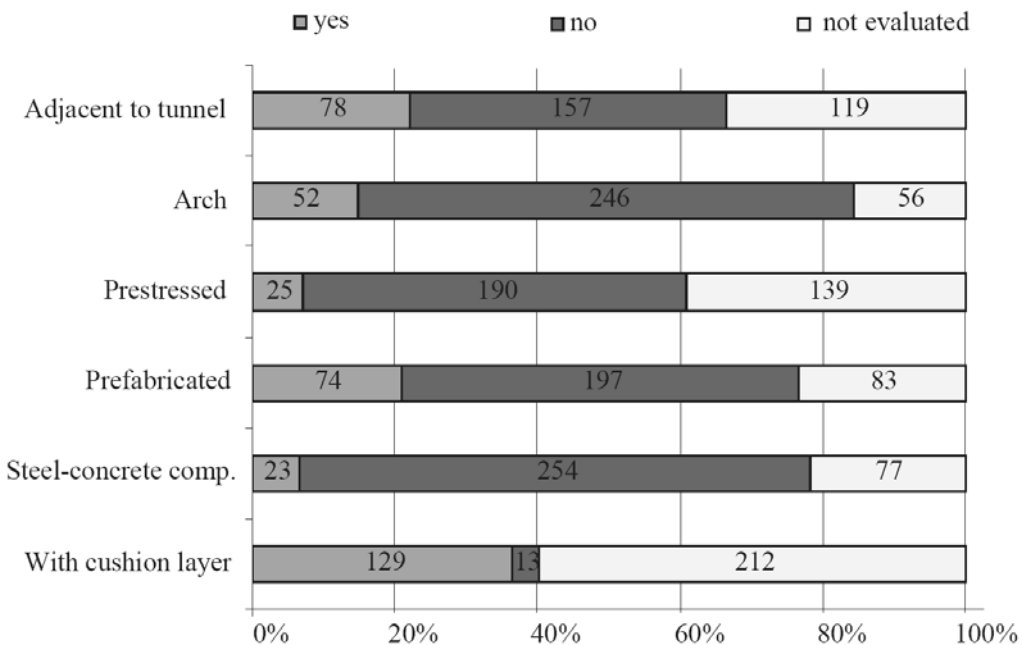


Figure 1-3: Evaluation of the gallery stock

Only 10 out of the 26 Swiss cantons have rockfall galleries. These are concentrated in the alpine regions. With 181 and 59 objects, respectively, the Cantons Wallis and Grisons have the majority of these structures.

A total number of 347 objects are filed in the database and evaluated as far as possible by the accessible documentation (Figure 1-3):

- 94% of the classified galleries are covered with a cushion layer,
- 49% of the galleries are adjacent to a tunnel,
- 28% are built with precast elements,
- 17% are arched structures,
- 12% have pre-stressed components and
- 7% are composite steel and concrete structures.

At least 119 (34%) of the considered 347 galleries correspond to the common type: flat slab, cast in place reinforced concrete, neither pre-stressed nor post-tensioned.

One third out of the almost 42 km total gallery length was built in the 1960s during the extension of the national road network. This corresponds to a total number of 93 galleries. In the 1970s and 1980s 35% of the galleries were built corresponding to a total number of 138 objects.

1.2. Motivation

Several recent incidents have shown that in the mountainous regions of Switzerland rockfall is one of the most significant natural hazards. In 2003 three galleries were hit by rocks within a very short period of time and the gallery roofs failed (Ripplistal, Chüebalm and Axenstrasse). Fortunately, people were not injured in any of these incidents. In May 2006 a rockfall killed two people on the national highway A2 in Gurtellen Canton Uri.

Chüebalmtunnel, January 4th, 2003: Approximately 150 m³ of rock debris fell from 70 meters and punched through the gallery (Figure 1-4a). Some blocks weighed up to 5 tons (3400 kJ). The failure occurred where the tunnel profile changes due to a change in the tunneling method from underground excavation to cut-and-cover. The affected area of the arched structure was not reinforced. The road had to be closed completely for one month and partially closed for some additional weeks.

Axenstrasse, February 11th, 2003: The highway is protected against snow avalanches by a cantilevering roof constructed with corrugated steel sheets and a 20 cm reinforced concrete topping. On top of this slab there is a soil cushion layer of thickness 10 cm [ASTRA, 2003]. Several blocks with sizes of 3 to 5 m³ fell from 50 to 70 meters (3600 to 8500 kJ) and destroyed the slab of the gallery (Figure 1-4b). The structure was originally designed for an impact of a 200 kg block falling from an altitude of 100 m (195 kJ).

Galerie Ripplistal, April 29th, 2003: Ripplistal is a snow avalanche gallery on the national highway N2 in Canton Uri. On top of the concrete slab there is a 50 cm thick sand layer. However, the structure was not designed for rock impacts [Chikatamarla, 2006]. A single 20 m³ block fell down the slope from approximately 900 meters in several steps, hit the gallery with an estimated energy of 25'000 kJ and punched through one span of the gallery (Figure 1-4c).



Figure 1-4: (a) Chüebalmtunnel [Chikatamarla, 2006], (b) Axenstrasse [Chikatamarla, 2006] and (c) Ripplistal [ASTRA, 2003]

These events are of great importance, since the acceptance of fatalities and excessive material damage to public infrastructure in our society is decreasing. Because of the global warming and subsequent reduction of permafrost zones and more extreme rainfall in the alpine regions, rockfalls are expected to become even more frequent events in areas that are already endangered today. In addition, new rockfall areas will develop in places that were previously considered to be safe (e.g. **Vitznau, 19th November 2003**). Taking account the high mobility requirements also in alpine regions, engineers need to improve the protection against rockfall hazards.

The impact load capacity of existing galleries is of great interest in order to decide on the necessity of renovation or strengthening. The first Swiss design guideline for rockfall galleries was published in 1998 [ASTRA, 1998]. The guideline is based on impact tests carried out in

1996 [Montani et al., 1996] that focused on the influence of the cushion layer. Older galleries were mostly designed with oversimplifications. In recent years the impact of falling rocks has been studied mainly from the geotechnical point of view. The damping properties of cushion layers and in particular the resulting stress distribution at impact were studied. Further research was performed on the dissipation capacity of different cushion materials [Chikatamarla, 2006].

For structural engineers in practice it is essential to have a simple model at their disposal that describes the complex processes during impact. Researchers, however, strive to model the phenomena as realistically as possible. A knowledge and awareness of the inaccuracies due to oversimplification are of vital importance in the revision of codes and guidelines.

1.3. Aims and scope

The load bearing capacity of the concrete slab and the influence of the dynamic effects is investigated in the present project. It is the aim to develop an efficient and simple but still adequate design method for new galleries which at the same time allows for a reasonable evaluation of existing ones.

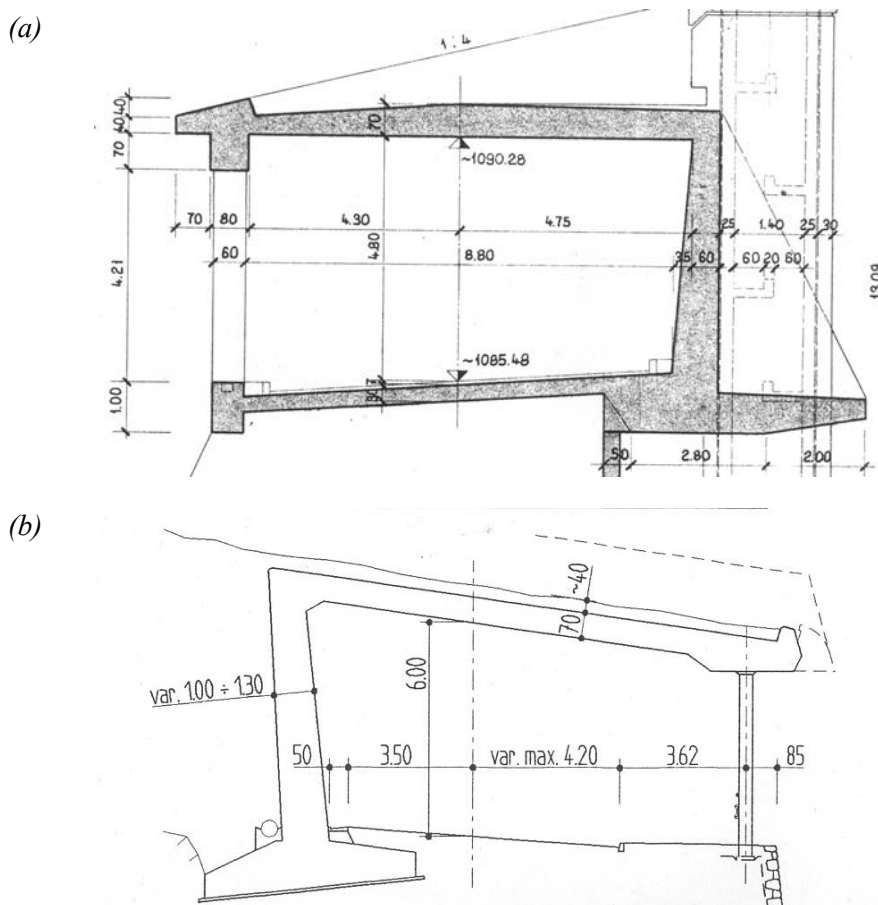


Figure 1-5: Typical rockfall galleries in Switzerland (a) Galeria Val Funtana, 1971, (b) Avalanche gallery Buggital from 1982

1. Introduction

As shown above, most existing galleries in Switzerland consist of reinforced concrete slabs that are covered with a cushion layer. Typically, protection galleries have a span of 9 m (over road or railway) with a slab thickness of approximately 0.70 m. The mountain side of the galleries is supported at the retaining wall; the valley side is supported on columns (Figure 1-5). Typical column spacing is 7 meters.

The magnitude of a rockfall impact is difficult to predict since the processes that take place during the event are governed by large uncertainties. Research in these specific fields is ongoing and progressing.

By suitably investing public resources local authorities can mitigate the risk of casualties or damage. Defining the design load for the specific rockfall galleries includes all aspects of the determination of occurrence and magnitude of the rockfall as well as event probabilities and is beyond the scope of the present research project.

Engineers need a simple and efficient design procedure so they can perform the design of a rockfall gallery with reasonable effort and within a reasonable period of time. Therefore, the focus is on how to design a protection gallery for a given loading scenario, or to quantify the impact that an existing gallery is able to withstand. In the future, only a combination of advances in research within all the involved fields describing the rockfall event will lead firstly to a mitigation of the effects of rockfall events and secondly to a substantial increase of the safety of roads and railroads by means of adequately designed protection structures.

2. State of the art

Different fields of research are involved in the design of protective galleries covered by a cushion layer against the impact due to rockfall. In this research, impact velocities and energies are taken from the results of trajectory analyses or accepted as a given design level and are not further discussed. Provided that rockfall occur and that a gallery should protect the users of a road or a railway line, the following aspects have to be addressed:

- Energy dissipation and damping effect of cushion materials (see Chap. 2.1)
- Non-linear and strain rate-dependent material behavior (see Chap. 2.2)
- Local behavior close to the impact location (see Chap. 2.3)
- Global dynamic structural behavior (see Chap. 2.4)

In these four points, various aspects of geotechnical, structural and material engineering have to be considered and all the processes involved have an important dynamic component.

From a scientific point of view, the dynamic behavior of structures and the corresponding resistance have always been a subject of interest due to the potential military application, e.g. the development of protective shelters and the development of the corresponding weapons to overcome that resistance. For reasons of confidentiality, many research results have not been published or can only be found circuitously [Newmark, 1962], [TM 5-1300, 1990], [Drake et al., 1989]. Today, the focus of research has shifted to protective structures that have to withstand impacts either due to civil activities (e.g. explosions, airplane crashes or ship collisions) or those of natural origin and research results therefore are exchanged more freely. The design procedure for rockfall galleries is basically the same as for most other impact problems. The main variables are defined by the different range of impact velocities. Consequently, the influences of dynamic material properties and inertial forces play a less prominent role.

In this chapter, relevant results derived from corresponding research fields are briefly reported and related to the problem of impacts due to rockfall.

In general, impact problems are mainly classified by the impact velocity (low or high velocity) and by the way the kinetic energy is dissipated (soft or hard impact). Depending on the impact velocity and stress rates, a rough classification is proposed for example in [Zukas et al., 1982]. The range up to an impact velocity of 500 m/s is governed by the low velocity regime, which covers most applications of structural dynamics including impact due to rockfall. Typical loading times for low velocity impacts are in the range of milliseconds and the local behavior of such structures interacts with the general deformation stage [Schlütter, 1987]. Commonly, the low-velocity regime is divided into two sub-regimes: up to 50 m/s materials remain basically in the elastic stage and yielding may only occur locally. For impact velocities above 50 m/s, materials are expected to behave plastically.

The second important classification concerns soft and hard impacts. By the common definition, for soft impacts the impacting body dissipates most of the kinetic energy while for hard impacts most of the energy is dissipated in the impacted structure. According to this

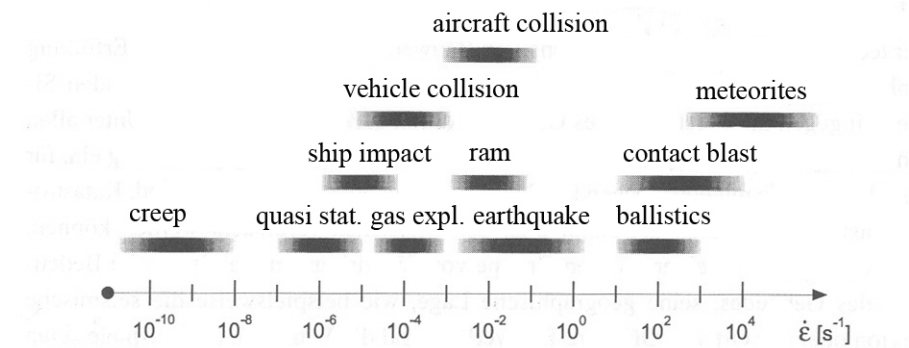


Figure 2-1: Typical strain rates for different impacts [Schmidt-Hurtienne, 2001]

definition, rockfall should be considered a hard impact, because the protective structure has to dissipate the impact energy by means of deformations. However, the cushion layer provides a large part of the required deformation in such a way that the impact on the concrete structure can be considered a soft one. About 80% of all galleries in Switzerland are equipped with a covering cushion layer. For soft impacts the influence of the structural deformation on the impact procedure is assumed to be small. In reality, of course, all impacts behave somewhere between a soft and a hard impact. The question as to how far the galleries meet this requirement for soft impact and to what extent the impact force-time history is influenced by the structural deformations requires further consideration.

Figure 2-1 shows typical orders of magnitude of strain rates for different loadings [Schmidt-Hurtienne, 2001]. Rockfall results in strain rates from $10^{-5} s^{-1}$ to $10^{-2} s^{-1}$. According to [Toutlemonde et al., 1995], soft impacts lead to strain rates of about $10^{-4} s^{-1}$ and hard impacts to $10^{-1} s^{-1}$, respectively.

On the methodical level, the following issues are also addressed in this chapter:

- Experimental research with different scales (see Chap. 2.5)
- Analytical modeling (see Chap. 2.6)
- Numerical modeling (see Chap. 2.7)

Finally, design guidelines as well as recommendation to quantify the impact forces of rockfall are presented in Chap. 2.8.

2.1. Cushion layer

In order to understand the influence of the covering layer, falling weight tests were carried out at EPF Lausanne until 1996 [Montani et al., 1996]. They focused on the penetration depth of the rock into the cushion layer and the generated reaction forces at the supports. The impact velocity, the thickness of the cushion layer and the soil's Young's modulus were varied in this evaluation. These research activities continued concentrating on rockfall trajectories [Labiouse et al., 1999] and on the influence of slope properties on them [Heidenreich, 2004].

Since 2001, the Institute for Geotechnical Engineering (IGT) of ETH Zurich has carried out centrifuge model tests and numerical analysis focusing on damping effects of cushion materials exposed to rockfall. Good agreement between the two methods was shown [Chikatamarla et al., 2004b]. Consequently, the distributions of contact stresses between soil layer and concrete slab in both time and location (Figure 2-2) can be numerically modeled.

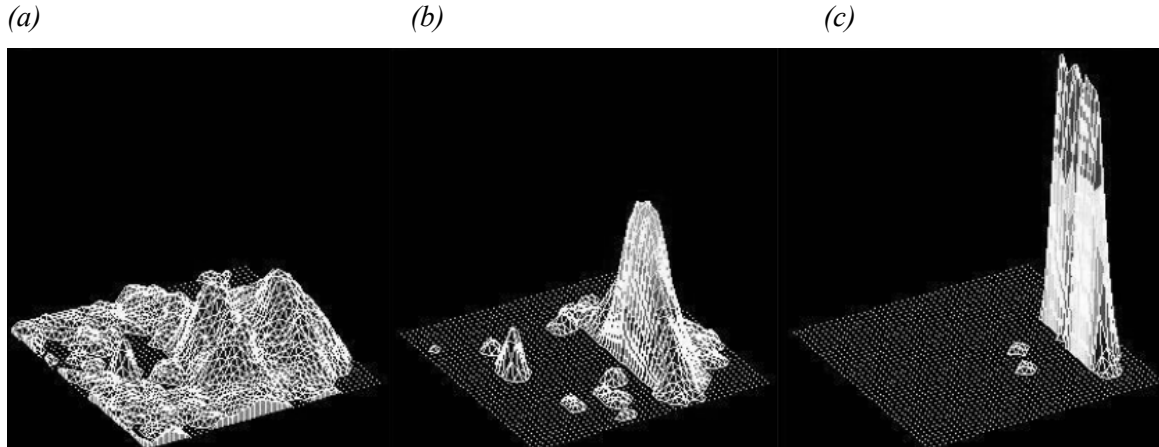


Figure 2-2: Contact stress distributions for (a) sand layer equal to rock diameter, (b) sand layer equal to half of rock diameter and (c) without sand layer [Chikatamarla et al., 2004b]

They merely depend on impact velocity, rock weight, thickness and properties of the cushion layer.

Theoretically, these contact stresses can be applied as acting on the structural parts of the galleries, but this approach is only suitable if the deformations of the galleries are assumed not to influence the load characteristics.

2.2. Dynamic material properties

The determination of dynamic strength values for short loading periods is a vital issue of dynamic material research. For both concrete and reinforcing steel the relevant results were mainly found in the 1980s.

Stiffness and strength properties of materials increase with strain rate and can reach a multiple of the static values. The ultimate strains increase as well, especially with brittle materials.

The failure of concrete subject to uniaxial compression or tension is caused by the development and growth of micro-cracks. The same dynamic mechanisms can be assumed for both types of loadings although for compression the crack's direction differs from that one of loading [Schmidt-Hurtienne, 2001].

According to [Bischoff et al., 1995] and [Tang et al., 1992], the ultimate strain increases with the strain rate and for dynamic loading the ascending branch of the stress-strain curve proceeds affine to the static one.

Already in the 1980s test results from the University of Karlsruhe showed that the modulus of elasticity is hardly affected by the strain rate [Schlüter, 1987]. Schmidt-Hurtienne states that the initial elasticity should be almost unchanged provided that the strain rate effect is caused by a delayed formation of micro-cracks. The delayed deterioration processes by dynamic loading was shown by acoustic emission measurements on specimens that had been statically and dynamically preloaded [Bischoff et al., 1991].

In [Eibl et al., 1989], it is demonstrated that the growth of a macro-crack due to an impact can be stopped if one succeeds in suddenly reducing the stress level to values below the static strength. Curbach and Eibl also showed that the dynamic crack propagation velocity amounting $v_{cr} = 200$ to 500 m/s lies well below that one of Raleigh waves. Also [Reinhardt,

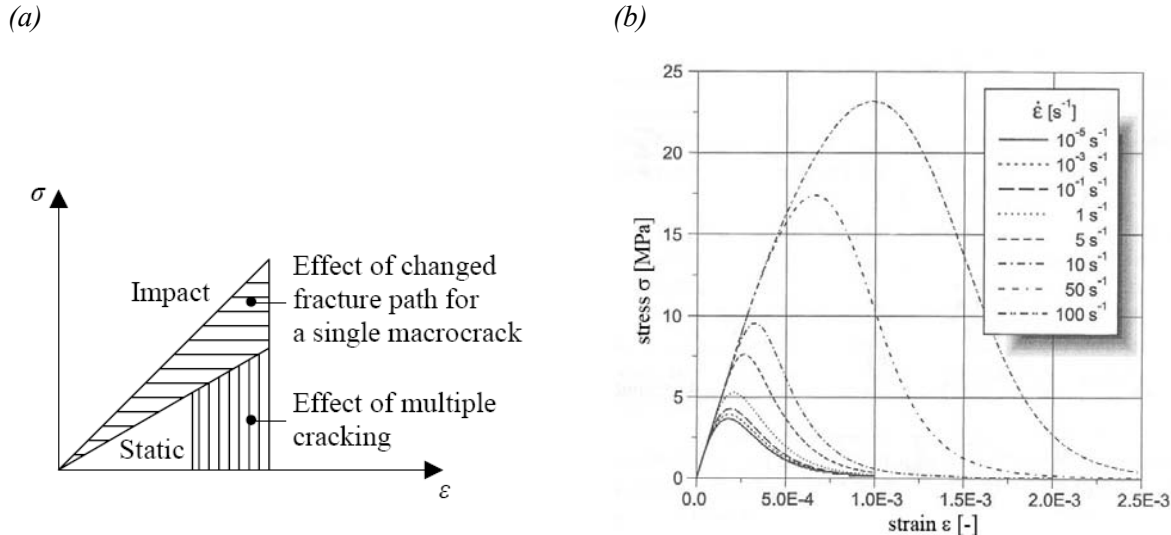


Figure 2-3: (a) Effects of fracture mechanics on stress-strain diagrams [Zielinski et al., 1982], taken from [Leppänen, 2002] and (b) Stress-strain-relationship for constant strain rates in tension: general exponential relaxation model [Schmidt-Hurtienne, 2001]

1982] describes the limitation of the crack propagation velocity to inertial effects within the microstructure of concrete.

[Zielinski et al., 1982] examined the stress-strain behavior of concrete in tension due to impact and found a larger ultimate strain. Stress-strain diagrams indicated greater energy absorption during tensile fracture due to impact than during static tensile fracture. They explain this phenomenon by simultaneous extensive overall cracking of the specimen and the development of single cracks forced to develop along shorter paths through zones of higher resistance (Figure 2-3a).

By compression, the dynamic strength increase exhibits more scatter compared to the tensile strength. According to Schmidt-Hurtienne, only for strain rates above 10^{-1} s^{-1} does the compressive strength increase reach a considerable level. The ratio of strain rate effects in tension and in compression is equal to that of ultimate strains.

[Kupfer et al., 1973] examined the behavior of concrete subjected to three-dimensional short time loading, resulting in an increase in strength of up to 16% and 27% for $\sigma_1 = \sigma_2$ and for a ratio of principal stresses $\sigma_1/\sigma_2 = 2.0$, respectively.

According to Schmidt-Hurtienne, however, progress in the field of dynamic material behavior has been modest. The measurement of multidimensional waves in concrete specimens reaches the limits of measuring techniques. That is why tests concentrate on axial dynamic wave experiments [Zielinski, 1982], [Weerheim, 1992] or [Buzaud et al., 1999]. In [Zukas et al., 1982] it is stated that by increasing the load intensity and exceeding the yield criterion the material behaves plastically instead of elastically. With compressive stresses exceeding the uniaxial strength by several times, the material behavior is governed by resistance to volumetric compression. Waves with such high pressure have a higher propagation velocity and form a shock wave.

For the dynamic loading of reinforcing steel, an increase of tensile strength, yield point and ultimate strain can be observed. For strain rates of about 10 s^{-1} , the increase amounts to 10 to 20% compared with static values. Tests are reported by [Berner, 1981], [Ammann, 1983] and [Brandes, 1985]. Berner's tests showed a larger scatter probably because of the use of

different steel products than due to the expected influence of strain rate (Figure 2-4a). The increased requirements concerning ductility and strain hardening in recent years may have had a favorable influence on the dynamic properties.

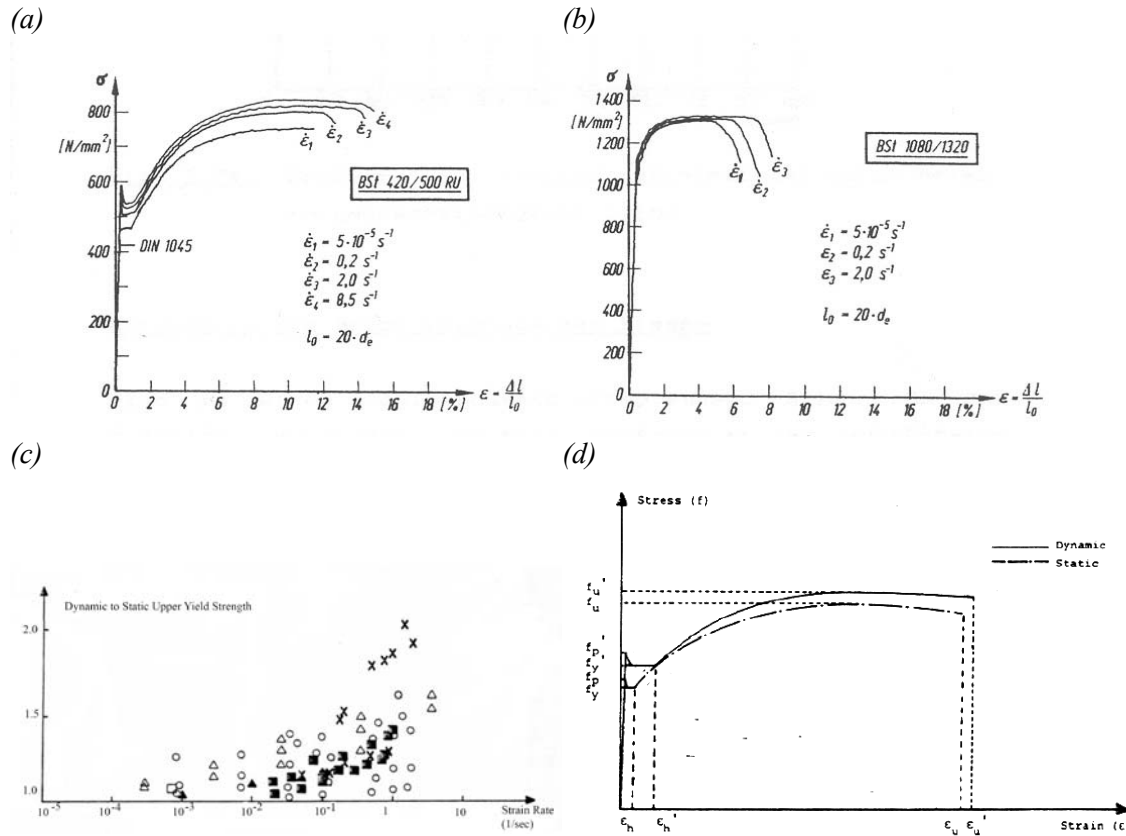


Figure 2-4 (a) and (b) Influence of the strain rate on the stress-strain behavior of two different reinforcing steels [Berner, 1981], (c) Increase of the yield point for different strain rates [Soroushian et al., 1986] and (d) Qualitative change of the stress-strain curve of reinforcing steel subject to dynamic loading [Lee et al., 2001]

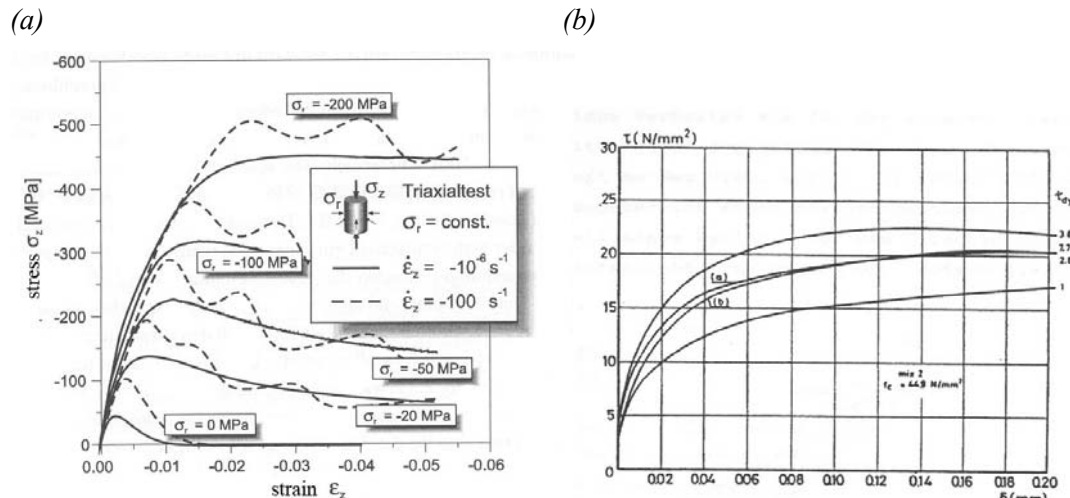


Figure 2-5: (a) Comparison of static and dynamic compressive cylinder strength with constant radial stress [Schmidt-Hurtienne, 2001], (b) Increase of bond strength with increasing strain rates from [Reinhardt et al., 1980]

Further dynamic tests shown in Figure 2-4b) are reported by [Soroushian et al., 1986]. Figure 2-4c) shows a qualitative comparison of static and dynamic stress-strain relationships based on [Lee et al., 2001] given in [Berthet-Rambaud, 2004].

Bond resistance depends on the relative displacement between steel and concrete, on the lateral pressure and on the level of steel stresses [Kobarg, 1986]. Close to yielding, the bond resistance decreases considerably. Bond tests with high strain rates were performed by [Hjorth, 1976] and [Reinhardt et al., 1980]. For ribbed reinforcement bars, a marked increase in strength was found (Figure 2-5b)).

2.3. Local structural behavior

Even for static loading, punching resistance is still a research issue [Muttoni, 2008]. Dynamically, concrete slabs often fail locally in shear by punching. The angle of the punching cone varies between about 25 and 70°. In contrast to beams, slabs always fail first at the location of impact. In the stage of maximum deflection of the first mode, however, the supports can fail in shear as well [Schlüter, 1987].

Further local damage, besides punching can be induced by aspects of wave propagation. One of the most damaging effects is scabbing. A strong compression wave is converted into a tension wave at the surface opposite to the impact exceeding the tensile strength. Spalling designates the loosening of pieces of concrete at the location and surface of the impact. [Rossmanith et al., 2005] considered spalling and scabbing as an interaction of stress waves with the microstructure of the material and presented both ongoing experiments and numerical simulations. According to [Ali, 2002], the U.S. Army Waterways Experiment Station executed 374 tests in 1988 that led to empirical formulas for the design of structural concrete elements published in the non-classified report *Spall Damage of Concrete Structures*. [Süper, 1982] analyzed numerically thick concrete slabs subject to impacts. It concentrates on reflections in an early stage, i.e. the first back and forth of the wave front, when stresses reach a maximum.

In [Schwieger, 1973] the maximum impact forces and the maximum strains of a cantilever beam subject to lateral impact are investigated. It is shown that the local behavior is independent of the boundary conditions as long as the wave reflected at the beam ends has not reached the impacting point again.

2.4. Global structural behavior

For static loading, maximum stresses and strains occur together with maximum loading. For impact loading, this is no longer true: Maximum shear occurs close to the location of the largest impact independent of deflection, span and structural support conditions, and inertial forces in the vicinity of the impact reduce the effective shear forces. Extreme values of bending moments, however, depend on support conditions and span, but occur only some time after the impact. Numerous analytical and numerical models, at least for beams, are available [Norris et al., 1959], [Johnson, 1972], [Ammann, 1983], [Block, 1983].

A comprehensive introduction and overview of impact on concrete structures is given in [CEB, 1988], the state of the art up to 1987 is well reported in [Schlüter, 1987].

To examine the transient dynamic properties of slabs during an impact in the lower velocity range, the structural intensity approach is applied in [Liu et al., 2004]. The instantaneous intensity component is a time-dependent vectorial quantity equal to the change of energy

density in a given infinitesimal volume. From this evaluation, it is stated that to forecast the structural behavior local and global behavior have to be considered independently. Load history, contact area and stress distribution at the interface of impacting and impacted body have to be known.

2.5. Experimental studies

In Germany, tests with hard impacts on reinforced concrete slabs have been carried out since 1977. The tests served to determine the forces between impacting body and concrete, examining the punching resistance due to dynamic loading as well as the efficiency of stirrups. For this purposes, reinforced concrete slabs measuring 2.3 x 2.3 m were impacted by a falling weight of 1000 kg [Süper, 1982].

To explore large events in the laboratory, tests in a geotechnical centrifuge have been executed, reaching accelerations of up to 60 times gravity [Chikatamarla et al., 2004b]. By making use of the scaling laws, a rock of weight approx. 25 tons can be modeled by a weight of 120 g. Heights of fall up to 13 m have been investigated (130 mm at 100 g). An aluminum plate of 170 x 170 mm represents the gallery that is covered with a damping cushion layer. A pressure sensitive layer (Tekscan pressure pad) is placed in between, measuring the distribution of the impact in space and time. Bearing forces, strains along the diagonals on the soffit and the acceleration in the centre of the slab were also measured (Figure 2-6a).

By interpreting results of down-scaled tests, scale effects may have to be considered. The work of Bažant is summarized in [Bažant, 2004] and [Barr et al., 1982] treats hard impacts on reinforced concrete.

Slabs of a meter square consisting of various types of fiber-reinforced concrete were impacted with increasing height of fall until failure. For each impact deflections and fracture pattern were recorded [Gholipour, 2004].

Researchers in Japan examined the shear resistance of 27 test beams without shear reinforcement subjected to the impact of free falling weights of 300 kg (Figure 2-6b) [Kishi et al., 2002b]. The spans of the beams were 1000, 1500 and 2000 mm, respectively, the impact velocities reached from 1 to 5 m/s. Empirical formulas for the required static shear resistance are given.

Full-scale tests were also executed to confirm the ultimate impact-resistant capacity of pre-stressed concrete rock sheds constructed over highways (Figure 2-7b) [Kishi et al., 2002a]. Two different types, an inverted L-frame and a fully rigid frame, were tested by dropping steel weights of 3 and 5 tons with increasing height of fall. The roof was covered by a 90 cm thick sand cushion. Further Japanese tests are reported in [Masuya et al., 1999] and [Masuya, 2005].

In France, impact tests with a 1/3 scale model of a rockfall gallery was performed [Mougin et al., 2005]. A slab measuring 4.8 m x 12 m in plan of 0.28 m thickness was impacted by a block weighing 450 kg with heights of fall of 15 and 30 m (Figure 2-7a), simulating common and exceptional impact loading, respectively. For the final destructive test, a block of 810 kg was released at 37 m height. The emphasis was on punching failure. The setup was equipped with strain gages attached to different layers of reinforcement, displacement transducers and accelerometers at the soffit and load cells at the bearings of the slab and a further accelerometer at the impactor. The impact was also recorded by a high-speed camera (1000 fps). The experimentally measured impact duration and force were compared with analytical methods and code requirements.

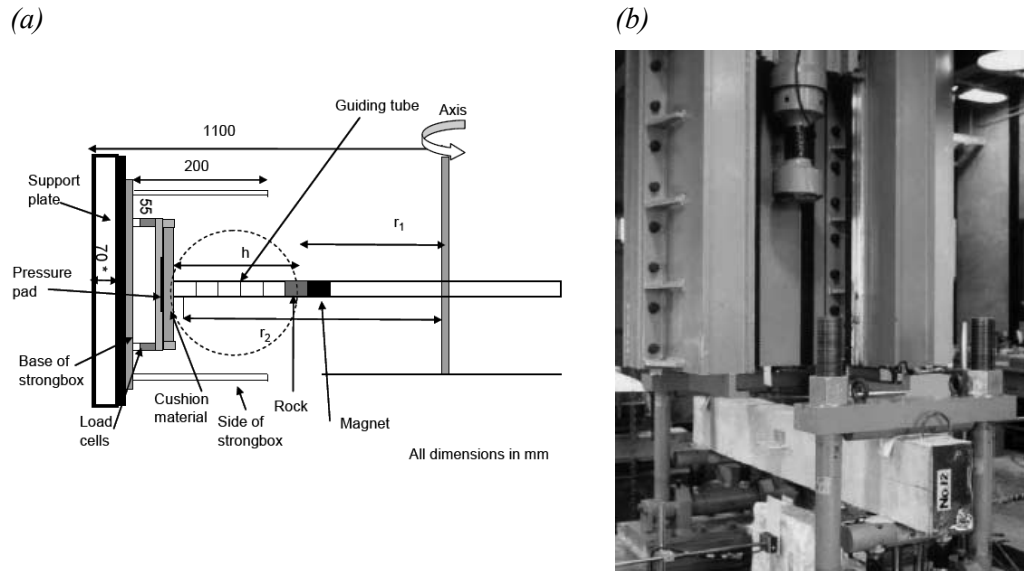


Figure 2-6 (a) Sketch of centrifuge test set-up [Chikatamarla et al. 2004b] (b) Laboratory experimental set-up for impact loading of reinforced concrete beams [Kishi et al., 2002b]

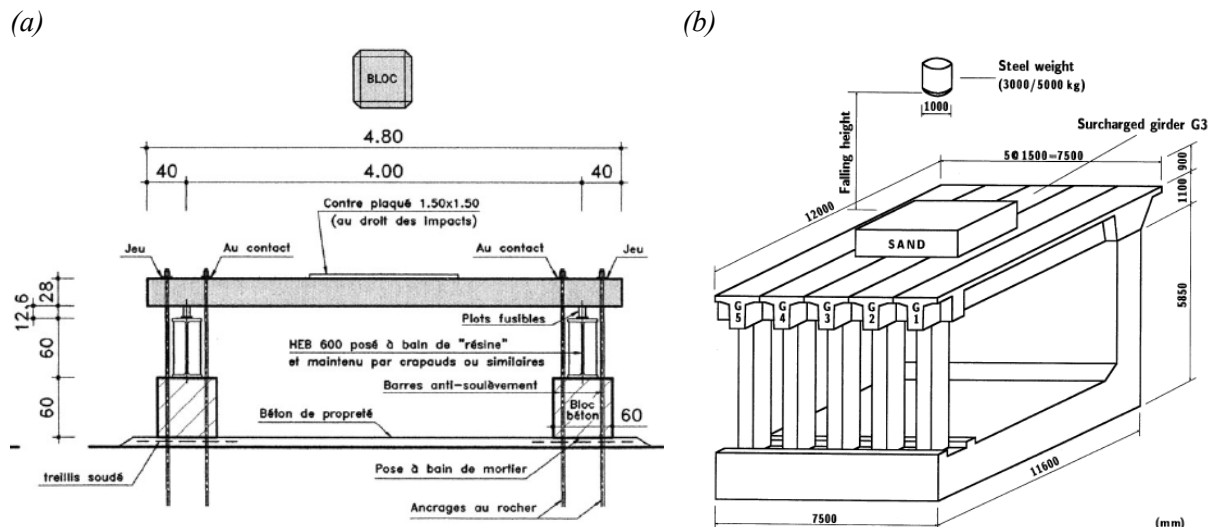


Figure 2-7 (a) Cross-section of falling weight tests [Berthet-Rambaud, 2004], (b) Full-scale experimental setup for pre-cast rockfall gallerie [Kishi et al., 2002a]

2.6. Analytical modeling

Some aspects concerning the analytical modeling of structures subjected to impacts have already been addressed in previous sections. In addition, further simple methods to determine analytically the deflections of reinforced concrete slabs are presented in [Abdel-Rohman et al., 1985]. They are called *impact factor method*, *equivalent mass method* and *continuous mass method* and rely on tests with steel balls impacting a reinforced concrete slab with different heights of fall. These methods cannot be applied for high impact velocities for which plastic material behavior is expected. With both the *equivalent mass method* and the *continuous mass method*, impacting force and loading period can be determined and thus the dynamic differential equation of the slab could be solved.

The use of systems of multiple degrees of freedom for the analysis of impact problems is shown in [CEB, 1988], [Chauvel et al., 2005], [Fujikake, 2007]. A rockfall gallery in Switzerland has also been designed by the means of such a model [Heierli, 1995].

2.7. Numerical modeling

The importance of digital computation to treat dynamic loading taking account of non linear material behavior was already recognized about 35 years ago [Stangenberg, 1973]. Major interest centred on beams and slabs of reinforced concrete subjected to loading up to failure. The systems of differential equations were integrated numerically also taking into account the rotational inertia of the respective beam or slab elements and deformations due to shear. The propagation of bending and shear waves was also considered. Constitutive laws had to be simplified by making reasonable assumptions and estimates of the order of magnitude. The influence if high strain rate was considered as far as it was known.

The behavior of concrete due to a transient dynamic load prior to and after failure was successfully modeled by a combination of the finite and the discrete element methods [Bangash et al., 2002]. To check the accuracy of the procedure, load tests of [Ammann et al., 1981] were successfully simulated.

In [Liu et al., 2004] a structural intensity approach was integrated into the finite element model and the dynamic contact-impact algorithm was solved using a Lagrangian approach. To formulate the contact-impact conditions of plates or shells, usually the *contact force method* and the *energy balance method* are used. This can be achieved by applying the Hertzian contact law. This so-called *Hertzian method* was used among others by [Sun et al., 1980], [Koller et al., 1986], [Aggour et al., 1988], [Lee et al., 1993], [Nosier et al., 1994] and [Liu et al., 1997].

To treat local effects, it is recommended in [Liu et al., 2004] to use the *Lagrange multiplier method*, the *augmented Lagrange multiplier method* or the *penalty method*. The latter allows the penetration of the impacting body into the slab offering numerical advantages.

[Ozbolt et al., 2005] demonstrated the distinct influence of the strain rate on both the ultimate load and the failure mode with a numerical simulation of an unreinforced concrete cantilever. For concrete, a strain rate sensitive micro-plane model was used and the explicit integration method was employed. It was shown that with increasing loading rates the failure mode changes from bending to diagonal shear. Due to inertial forces, which gain importance with high loading rates, the type of analysis (static or dynamic) can lead to significantly different results.

To simulate fast dynamic processes, explicit methods are more appropriate; for slower dynamical processes, however, implicit time integration algorithms are more stable.

[Noels et al., 2002] succeeded in developing a procedure that switches automatically from implicit to explicit time integration and back again, thus providing the optimal solution for problems in the high frequency range like impact.

Finite element modeling has reached such a stage that almost everything can be modeled, but the results still have to be calibrated with physical tests. For design practice, however, advanced finite element modeling is not appropriate being too complicated and time-consuming.

2.8. Guidelines and recommendations

As shown in the above sections, much knowledge has been acquired on the behavior of galleries subjected to rockfall and related phenomena on both the material and the structural level. In this section, the Swiss guidelines (see Chap. 2.8.1.) and those of Japan (see Chap. 2.8.2.) are presented providing some background information. Both Switzerland and Japan have similar levels of risk acceptance and both have made quite strong efforts concerning rockfall protection [Masuya et al., 1999]. Finally, in Chap. 2.8.3. most of the past recommendations are summarized.

2.8.1. Swiss guideline

After the incidents in 2003 mentioned in Chapter 1, an expert group was formed by the Federal Road Office (ASTRA) and charged with the decision of how to deal with rockfall as a hazard scenario on the national road network. At that time, the Swiss guideline for the design of rockfall protection galleries [ASTRA, 1998] referred to the old generation of SIA codes that were abrogated in June 2004, a proposal of the expert group was to adapt the guideline to the new generation of codes from 2003 onwards (Swisscodes). In 2008 this adaptation was carried out, but the technical content remained the same as in the previous guideline from 1998 [ASTRA, 1998].

A static equivalent force A_d to consider the impact load F_k is used according to Equations (2-1) and (2-2). The coefficient C considers either ductile ($C = 0.4$) or brittle ($C = 1.2$) failure of the structure. This approach is simpler to use but does not really cover the dynamic behavior of the structure.

$$A_d = C \cdot F_k \quad (2-1)$$

$$F_k = 2.8 \cdot e^{-0.5} \cdot r^{0.7} \cdot M_{E,k}^{0.4} \cdot \tan \varphi_k \cdot \left(\frac{m_k, v_k^2}{2} \right)^{0.6} \quad (2-2)$$

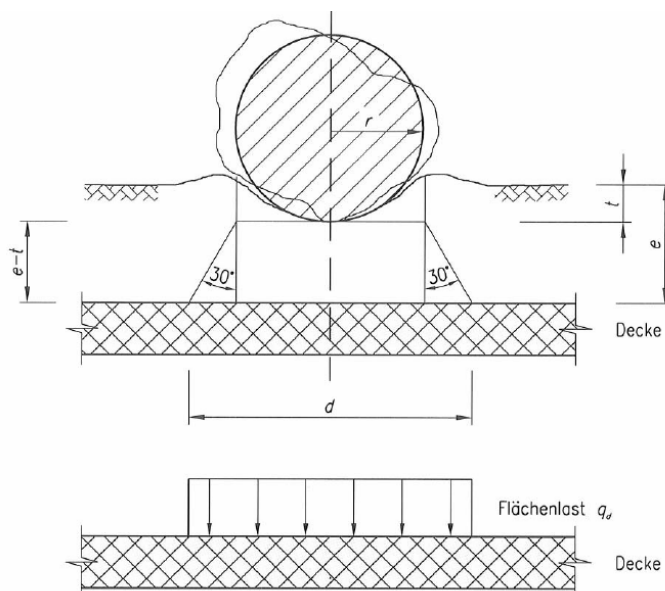


Figure 2-8: Load distribution of the equivalent static load according to [ASTRA, 2008]

Where:

- A_d Static equivalent force on design level [kN]
- C Coefficient to account for ductile or brittle failure [-]
- F_k Impact load [kN]
- e Thickness of cushion layer [m]
- r Radius of an equivalent sphere [m]
- $M_{E,k}$ Soil modulus of the cover layer [kN/m²]
- φ_k Internal friction angle of the cover layer [°]
- m_k Characteristic block mass [t]
- v_k Characteristic impact velocity [m/s]

The guideline is based on falling weight tests from 1996 that investigated the influence of the cushion layer [Montani, 1998], see Chap 2.1. The main focus was put on the penetration depth and the generated reaction forces at the supports, varying the height of fall, the mass of the block and the thickness of the cushion layer.

Numerical simulations extended the test results for impacts of higher fall energy [Bucher, 1997]. Empirical equations have been deduced from the simulations to describe the equivalent static force and the penetration depth. Local damage, especially punching, has not been considered. For the design of a gallery, the contact stresses between the cushion layer and the structural slab are of high interest. They are linked with the deformation of the slab. According to Bucher, in the investigated cases the dependence of the contact stress on the slab deformation is neglected, what is valid for soft impacts. Nevertheless, the influence of the structural stiffness on the reaction force was identified as 30%. It should be noted that the tests covered only the elastic behavior of the structure. For the numerical simulation, the reinforced concrete was modeled with linear-elastic material properties with high stiffness. The plastic deformations previous to structural failure assumed to influence the resulting load were not considered. Further inaccuracies of up to 30% are caused by the simplification of the rectangular slab with supports in the corners into a circular one supported along the circumference.

The application of the guideline is limited to a penetration depth in the cushion layer of smaller than half of the cushion thickness.

2.8.2. Japanese design recommendations

Since Japan has to deal with mountainous topography combined with a dense population, rockfall protection has been studied since the 1970s. There are numerous documents with recommendations for the design of rockfall impacts on structures. The most significant document is [Japan Road Association, 1983], a handbook containing recommendations for all types of protection measures. The great importance attached to the manual derives from the publisher being a governmental institution, even if the content is not completely accepted by most experts in this field. In the introduction, the range of application for rockfall galleries is indicated to be between 20 and 6'000 kJ. The impact load P on galleries is given by Equation (2-3), which is based on the Hertzian contact theory.

$$P = 2.455 \lambda^{\frac{2}{5}} \cdot W^{\frac{2}{3}} \cdot H^{\frac{3}{5}} \cdot i \quad (2-3)$$

$$i = \frac{P_{\max}}{P_{\max}(\lambda=100)} = \left(\frac{h}{D} \right)^{-0.5} \quad (2-4)$$

Where:

- P Impact load [tf]
- λ Lame's constant [tf/m²]
- W Block weight [tf]
- H Falling height [m]
- i Coefficient for cushion thickness [-]
- h Thickness of cushion layer [m]
- D Diameter of falling body [m]

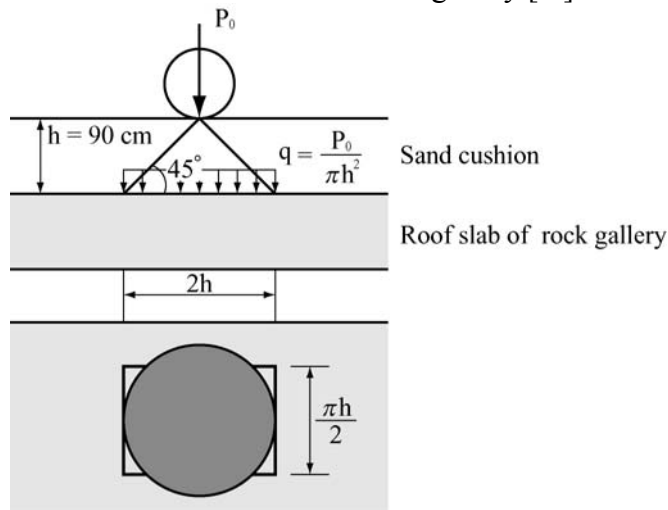


Figure 2-9: Distribution of impact load [Japan Road Association, 1983]

In 1998 the Subcommittee for Impact Problems of the Japanese Society of Civil Engineers (JSCE) published a reference book for impact resistance design of rock shed structures [JSCE, 1998]. The main difference to the handbook of 1983 is the introduction of the Lame's constant, which is integrated into Equation (2-3). In the handbook [Japan Road Association, 1983], the Lame's constant was supposed to be 100 tf/m² and the thickness of the cushion layer was suggested to be 0.9 m for sand cushion. The reference book distinguished between the impact load and the transmitted load. The increased transmitted load is supposed to be taken into account by using a value for the Lame's constant λ between 500 and 800 tf/m².

An amplification factor of 1.5 to 2 between the impact load (measured by accelerations in the impacting body) and the transmitted load (measured by load cells between cushion layer and the rigid surface below) has also been found by the [Public Works Research Institution, 1995].

A summary of the different Japanese recommendations can be found in [Ishikawa, 1999].

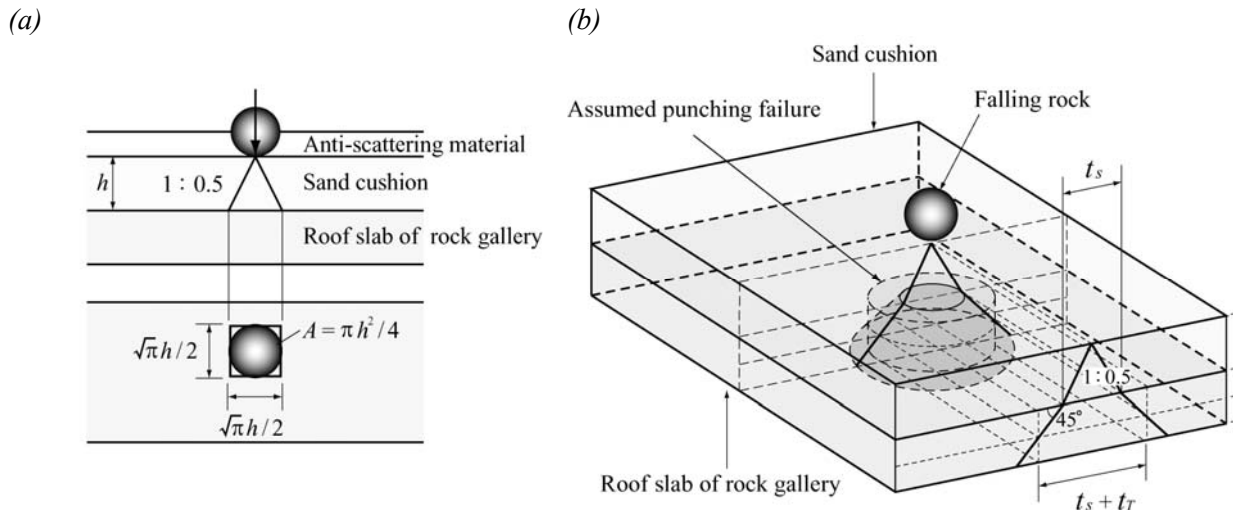


Figure 2-10: Load distribution and verification section for punching shear failure (a) section and elevation view, (b) 3-D illustration

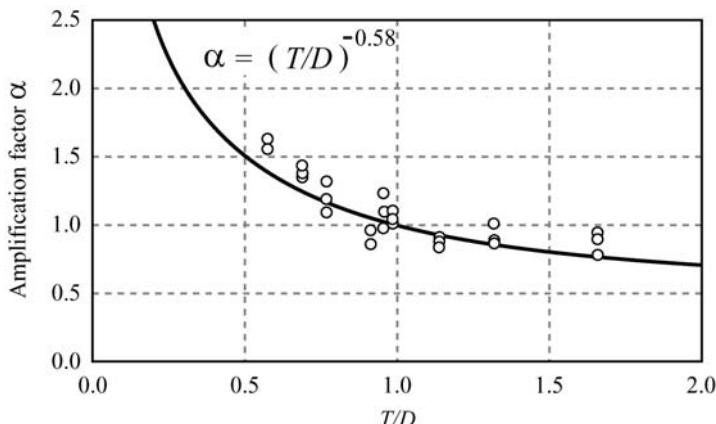


Figure 2-11: Amplification factor α for cushion thickness

A new edition of the handbook was published in the year 2000. It contains only minor changes from the previous one. Equations were adapted to SI units, Equation (2-5), and the load dispersion in the cushion layer now has to be selected using an angle of 1 : 0.5. Within the concrete slab, however, 45° is still recommended (see Figure 2-10a).

$$P = 2.108 (m \cdot g)^{2/3} \cdot \lambda^{2/5} \cdot H^{3/5} \cdot \alpha \quad (2-5)$$

$$\alpha = \frac{P_{\max}}{P_{\max(\lambda=1000)}} = \left(\frac{T}{D} \right)^{-0.5} \quad (2-6)$$

Where:

- m Mass of falling rock [t]
- g 9.81 [m/s²]
- α Amplification factor for cushion thickness [-]
- T Thickness of cushion layer [m]

2. State of the art

The Lame's constant is still proposed as $\lambda = 1'000 \text{ kN/m}^2$ ignoring the recommendations of the Subcommittee of Impact Problems of JSCE. The influence of the cushion thickness is taken into account by the amplification factor α . Figure 2-11 shows how this influence can be simplified by Equation (2-6).

An additional guideline for the design of rockfall galleries is applied by most engineers in Hokkaido area [Hokkaido Development Bureau, Ministry of Land, Infrastructure and Transportation, 2001]. Especially, recommendations on constructional issues are given. Here also Equation (2-5) is used without the amplification factor α . In Japan, several enterprises offer prefabricated rockfall protection galleries and have their own internal design guidelines.

The standards in Japan require that the galleries withstand a design event not exceeding elastic deformations. That is why the design energy is chosen to be relatively high, since the consultant engineers have to define the possible impact magnitude and take responsibility in case of an incident.

2.8.3. Other formulations

An overview of further formulations for impact forces is given in Table 2-1. The formulations are well presented in [Montani, 1998]. Most give empirical loads for impacts on soil but they are not further discussed, because they do not contribute to the physical model proposed in this thesis.

Table 2-1: Summarizing table for impact forces on soil [Montani, 1998]

Formulation	Auteur	Comportement du sol
$P = 1.995 \cdot E^{\frac{1}{2}} \cdot R^{\frac{1}{2}} \cdot W^{\frac{1}{2}} \cdot H^{\frac{1}{2}}$	Eq. 2.4 Hertz, Goldsmith	élastique
$P = 2.455 W^{\frac{1}{2}} \lambda^{\frac{1}{2}} H^{\frac{1}{2}}$	Eq. 2.5 Handbook	
$P = \sqrt{2k} \cdot \left(\frac{1}{\frac{m}{m} + 1} \right)^{0.5} \cdot (mgH)^{0.5}$	Eq. 2.7 Tonello	
$P = 2\sqrt{g} \cdot M_e^{0.5} \cdot R^{0.5} \cdot m^{0.5} \cdot H^{0.5}$	Eq. 2.9 Lang	
$P = 1.619 k^{\frac{1}{2}} W^{\frac{1}{2}} H^{\frac{1}{2}}$	Eq. 2.12 Komatsuwa	plastique
$F_{\max} = A \left(0.7 \cdot \gamma \cdot \frac{D}{2} \cdot N_r + c \cdot N_c + \gamma \cdot N_q \cdot d_{\max} \right)$	Eq. 2.15 Habib	
$F_{\max} = \frac{m \cdot v_0}{T_{imp}} \cdot \frac{1}{\lambda}$	Eq. 2.18 Heierli	
$F = Nd^n$	Eq. 2.19 Meyer	
$P = \frac{W}{g} V K^{\frac{1}{2}} e^{-\frac{X_f}{2}}$	Eq. 2.20 Sonoda	élasto-plastique
$\frac{E_1}{\frac{m}{m} + 1} = P_u d_e \left(N - \frac{1}{2} \right)$	Eq. 2.23 Tonello	
$F_{\text{res}} = P_{\text{dyn,max}} - Q \text{ avec } Q = q_d \cdot A$	Eq. 2.24 Lang	
$F_{\text{st}} = \kappa \frac{T_{imp}}{T_0} F_{\max} \text{ avec } F_{\max} = f(E)$	Eq. 2.27 Azimi	
$d_{\max} = \frac{m}{2 \cdot A} \cdot \frac{1}{b} \cdot v_0 = c \cdot m \cdot v_0$	Eq. 2.28 Poncelet	Formulations empiriques
$P = \kappa \frac{W}{g} H$	Eq. 2.29 Japan Steel Club	
$P = 2c_r \frac{W}{g \cdot T_{imp}} \sqrt{2gH}$	Eq. 2.30 Yoshida	
$P = \beta_0 \frac{W}{g \cdot T_{imp}} \sqrt{2gH}$	Eq. 2.32 Masuya	

3. Experimental research

Experimental data is required to validate an analytic treatment as well as to calibrate future numerical simulations of the rockfall impact process.

Experimental research has been carried out in three steps. First, preliminary small-scale tests under laboratory conditions with various setups to simulate rockfall impact showed that a falling weight test is the most adequate but also the most complex setup. With medium-scale tests, the performance of the measurement facilities was tested and the structural response of the specimen under rockfall impact was recorded. In large-scale tests the experience of the previous tests could be applied. Slabs with different thicknesses as well as reinforcement layouts were subjected to increasing impact loads until failure was reached. To acquire experimental data for the prediction of punching prediction of models, further tests were carried out.

For all four test series (small-scale, medium-scale, large-scale and punching tests) the test setup, specimens, cushion layer, falling weight, test program, measurements and test results are given in the following sections.

3.1. Small-scale tests

In preliminary tests three different setups are chosen to evaluate their suitability for testing rockfall impacts on the reinforced concrete slab of galleries under laboratory conditions. A weight of 825 kg is dropped on the slab from 2 m height. Since the focus is on the structural response of rockfall galleries, alternative test setups have been studied to eliminate the influence of a cushion layer. To reach this goal, impacts are reproduced by a servo-controlled actuator as well as by the backstroke of blasted water. The main focus is the evaluation of the three setups and the ability of the measuring equipment to obtain relevant data.

3.1.1. Test specimens

Since the interest is focused on the test setups and on the measurement procedure, only minor requirements for the specimens are necessary and left overs of other tests can be used. Three slabs are taken from the upper undamaged part of tested shear walls [Buzzini et al., 2006]. The specimens of 900 x 900 mm side length are named W1 to W3 according to the walls they are cut off. The sections of the slabs with a thickness of 100 mm are shown in Figure 3-1. The thickness of specimen W3 is reduced in the middle part from 520 mm width to 52 mm.

The slabs are cast with *hybrid fiber concrete* (HFC) [Stähli et al., 2007] and are additionally reinforced in one direction. HFC is designed for seismic applications and has a smooth and controlled post-peak softening behavior. HFC contains three different types of steel fibers: A, B and C (Table 3-1). Types A and B are straight fibers of 6 and 12 mm length, type C is crimped fibers of 30 mm length. The mix has been developed by increasing the total content of steel fibers starting from 2% and ending with 6%. The binder contains cement, fly ash and silica fume. W1 was cast with a 3.5% fiber content, whereas both W2 and W3 were cast with 6%. The aggregate size is limited to 1 mm, which guarantees a fine-grained matrix, ensuring the best bond between matrix and fibers.

3. Experimental research

Table 3-1: Mix design of HFC and reinforced ratios used for test specimens W1, W2 and W3 [Buzzini et al., 2006]

Component			W1	W2	W3
Matrix	Cement CEM I 52.5 R	[kg/m ³]	1000	961	961
	Fly ash	[kg/m ³]	168	161	161
	Silica fume	[kg/m ³]	95	91	91
	Aggregate 0/1 mm	[kg/m ³]	754	725	725
	Superplasticiser	[kg/m ³]	20	19	19
	Water/binder-ratio	[-]	0.17	0.18	0.18
Fibers	Type A - Short steel fibres (0.15 x 6 mm)	[Vol.-%]	1.5	3.0	3.0
	Type B - Medium steel fibres (0.2 x 12 mm)	[Vol.-%]	0.5	1.5	1.5
	Type C - Long steel fibres (0.6 x 30 mm)	[Vol.-%]	1.5	1.5	1.5
Reinforcing bars	Ratio average	[%]	1.74	1.74	2.41
	Ratio end regions	[%]	3.54	3.54	3.57
	Ratio web	[%]	0.41	0.41	0.79

In addition to the steel fibers, vertical reinforcement bars are placed in the shear walls. All specimens have the same number of reinforcing bars: Six diameter 12 mm along each edge and ten diameter 5.2 mm in between. In W2 and W3 the reinforcement is located in the center of the section. In W3 the reinforcement ratio is higher due to the different geometry.

3.1.2. Falling weight test

In the first setup, an artificial concrete boulder of diameter 800 mm and 825 kg mass is dropped from 2 m above the slab using a helicopter hook (Figure 3-2). The slab is simply supported in the four corners and has to be held horizontally to avoid instabilities. Also the load cells have to be fixed horizontally, since they can slide away once the slab fails. The diagonal span is 1103 mm. The specimen W1 is selected, because of its strongest reinforcement layout among the three test specimen. The lateral movements are blocked in both directions. The slab is covered by a cushion formed by quartz sand in a textile bag. It distributes the contact stresses and reduces the decelerations in the impacting body. The cushion layer has a thickness of 190 mm. It serves as reference material for the centrifuge

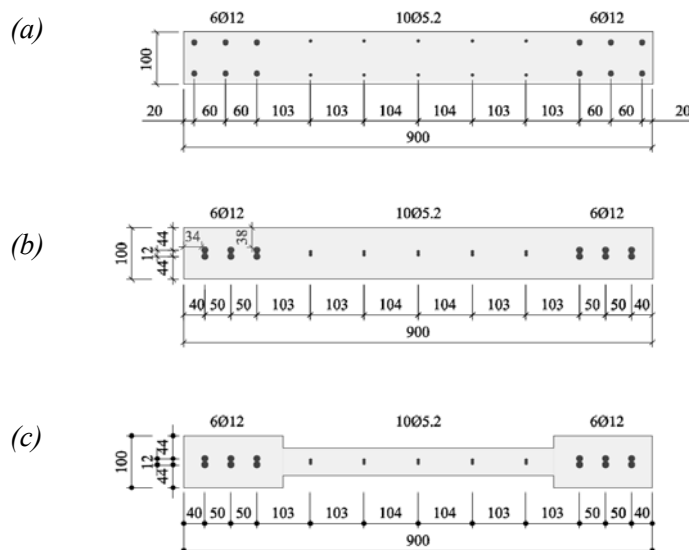


Figure 3-1: Cross section of specimens [mm] (a) W1, (b) W2 and (c) W3 [Buzzini et al., 2006].

tests for cushion materials [Chikatamarla, 2006], where the damping properties of different cushion materials were studied. The material properties of the sand are shown in Table 3-2.

The falling weight consists of two semi-shells made of fiber-reinforced high performance concrete. It is equipped with an internal acceleration measurement device [Volkwein et al., 2005].

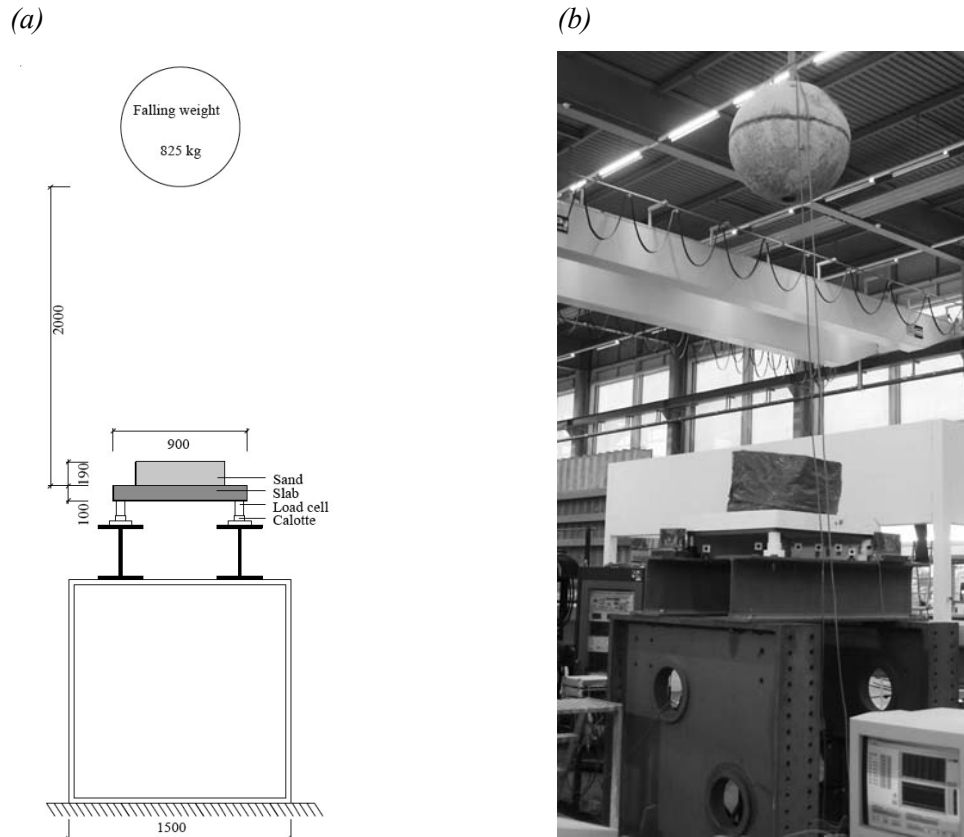


Figure 3-2: Falling weight test (a) sketch [mm], (b) photo

3.1.3. Servo-controlled actuator test

In the second setup, the actions on the slab due to an impacting rock are simulated by a servo-controlled actuator. The equipment has to produce the load in the necessary short period of time, which is limited by the valve capacity of the actuator and the pump units. The applied actuator has an oil discharge of 120 l/min and a maximum load capacity of 1000 kN. The expected cylinder velocity is 0.2 m/s. The load is reproduced by enforcing a sudden

Table 3-2: Material properties of sand used for cushion layer [Chikatamarla, 2006]

Material Property	Value
Density	[kN/m ³] 17.2
Dynamic elastic modulus (compression)	[MPa] 80-140
Dynamic shear modulus	[MPa] 29-47
Particle size	[mm] 0.5 – 1
Friction angle	[°] 33
Compressive wave velocity	[m/s] 220 – 300
Shear wave velocity	[m/s] 135 – 170
Description (SN 607008a)	Uniform soil

3. Experimental research

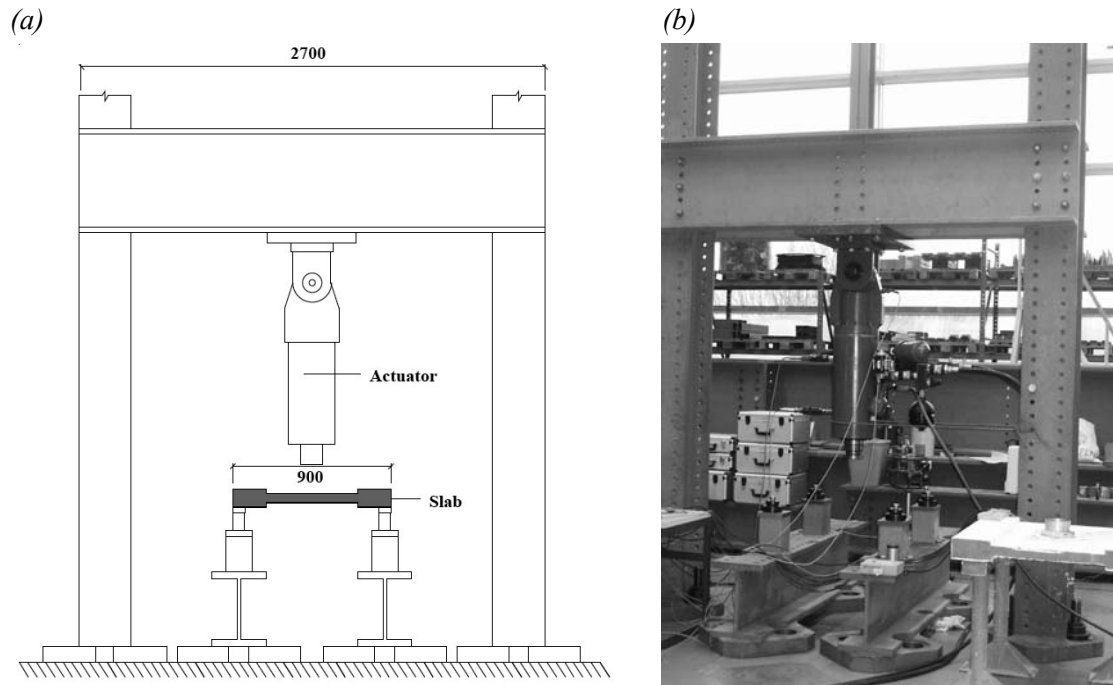


Figure 3-3: Servo-controlled actuator test (a) sketch [mm], (b) photo with test specimen removed from the simple supports in the middle

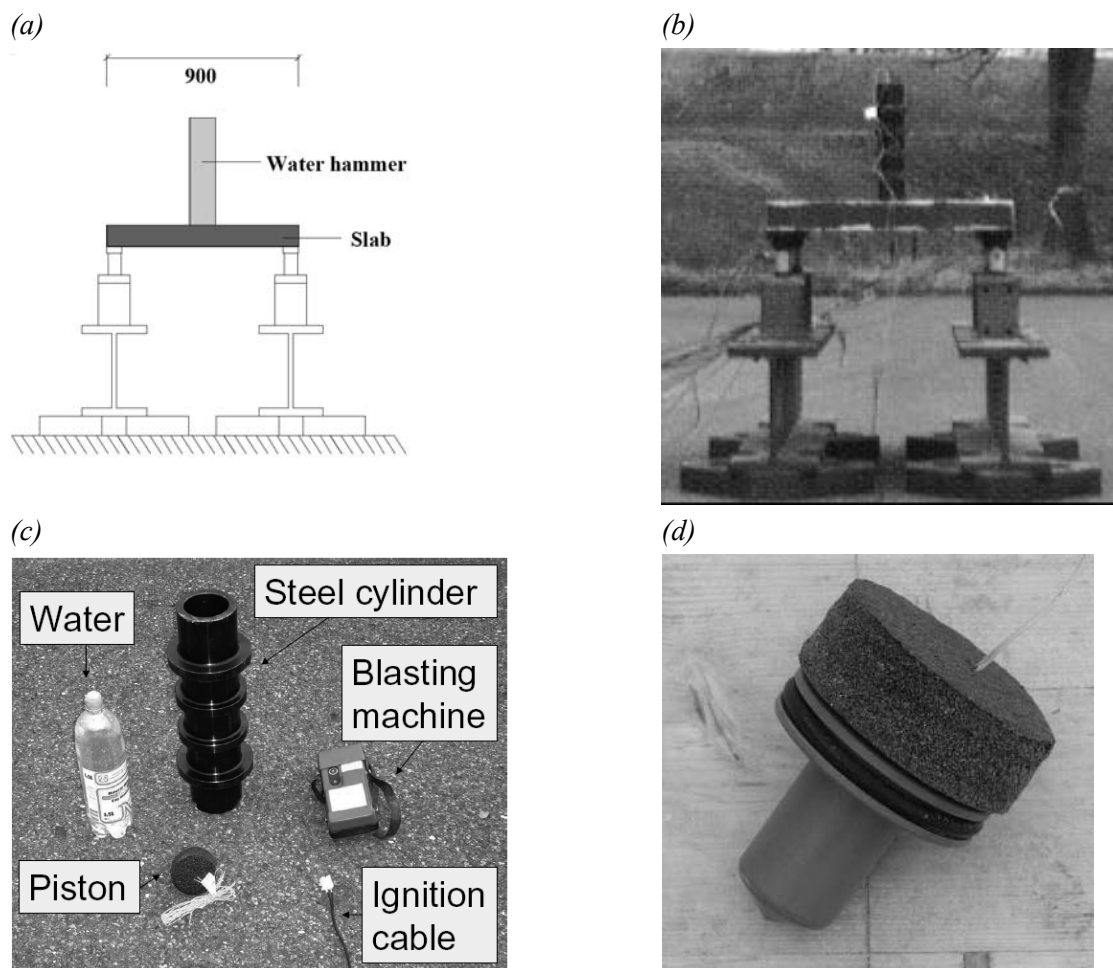


Figure 3-4: Blasting test (a) sketch [mm], (b) photo, (c) Components of the water hammer (d) piston

displacement of 20 mm. The loading time is predicted to be around 30 ms and depends on the stiffness of the slab. A storage chamber is placed between the tubes and the actuator to protect the tubes from the oil pressure shock.

The actuator is mounted in a steel frame (Figure 3-3). W3 is selected in order to keep W2 for the water hammer, where the action is supposed to be more similar to the falling weight test.

3.1.4. Blasting test

In the third setup, the impact load is applied by blasting a water column inside a steel cylinder with an explosive charge. The test is performed outdoors due to the water dispersion and the expected noise. The reaction force of the accelerated water acts on the slab W2 (Figure 3-4). The so-called *water hammer* was originally designed for police intervention units in Germany and consists of a steel tube with ribs (Figure 3-4c) that is closed at the bottom. An explosive charge is placed inside and the tube then is filled with water. The explosive charge is implemented in a piston (Figure 3-4d) displacing the water upwards after detonation. The tube weighs 20 kg and has a capacity of 1.5 liters of water. According to the manufacturer, a peak pressure of 1200 bar is reached inside, which would represent an upper limit for the impact force of 530 kN.

3.1.5. Measurements

The main focus is the evaluation of the three setups and the ability of the measuring equipment to obtain relevant data. During the impacts, the support forces, strains and accelerations in the reinforced concrete slabs are measured. The specified measurement categories should enable one to study the load capacity of reinforced concrete galleries due to rockfall impacts.

The bearing supports are four load cells (KMD 2 to 5 in Figure 3-5a). The maximum load capacity of each load cell is 300 kN and the sampling rate is 400 Hz. They are placed on spherical calottes to allow small rotations of the slab. A dowel between the load cells and the hinge avoids lateral sliding.

Accelerations are measured within the slab and the falling weight. The accelerometers of the slab are attached to the specimen's soffit (see cubes in Figure 3-5b), one in the center of the slab and the other on the diagonal at a distance of 100 mm. The boulder is equipped with eight acceleration sensors. Four sensors measure in the vertical direction and four in the horizontal direction, with two for each orthogonal direction.

Eight gages are used to measure the strains at the upper surface of each specimen (Figure 3-5a). To equip the lower surface is not appropriate because cracking would arbitrarily influence the strain measurements. A series of five gages is attached along the diagonal. In one half of the diagonal four gages (D1 to D4) are placed beginning at the center of the slab and continuing at a distance of 125 mm from each other. The fifth (D5) is placed symmetrically to D2 in order to check the symmetry of the impact. Three additional gages (D6 to D8) are positioned next to the gages (D2 to D4) in peripheral direction.

The strain gages of 20 mm length have a measure range of 4% with an accuracy of 0.001%. The sampling rate is 400 Hz and the signals are filtered by a Bessel low-pass filter with a cut-off frequency of 150 Hz.

3. Experimental research

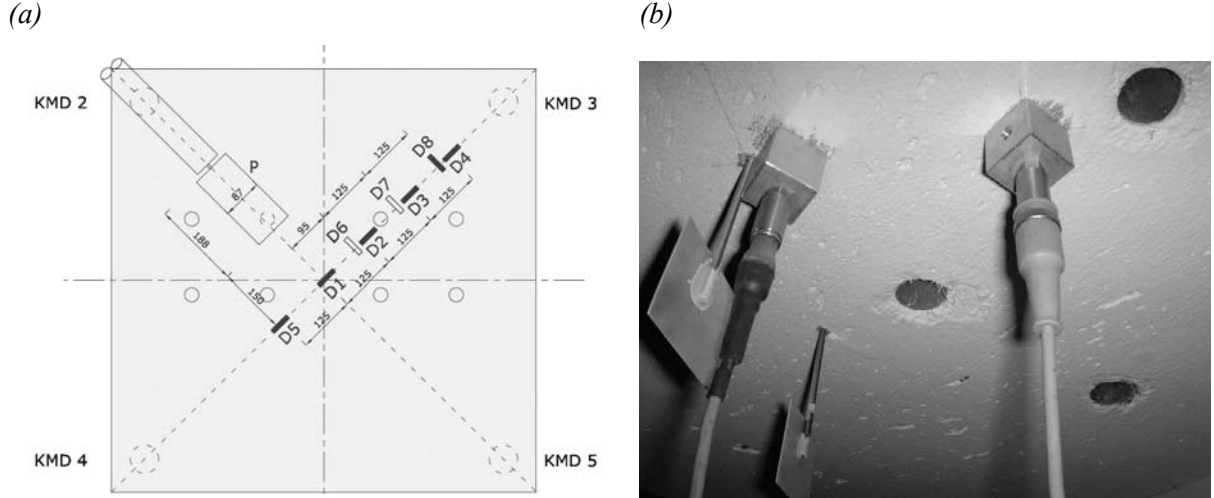


Figure 3-5: (a) Strain gages (D1 to 8), pressure cell (P) [Ebner, 2006] and (b) accelerometers on the slab soffit

A visual extensometer is evaluated for measuring the displacements of the slab. Five target points placed along the diagonal according to the strain gages on the upper surface are scanned. Two additional reference points are located at the supports. The extensometer has not performed well during the falling weight test and hence was not applied any more, neither in the actuator nor in the water hammer test. Next to the video extensometer, the displacements of the slab center are measured by an inductive displacement sensor. In the actuator test, in addition to the displacement also the loading force is measured.

An electrical earth pressure transducer (P) is placed between the cushion layer and the slab to measure the contact pressure. The transducer covers only a fraction of the contact surface. Although it was expected to allow for conclusions on the total pressure time history based on a simplified geometrical pressure distribution, the pressure transducer has been removed for further evaluation.

To enable a visual evaluation, high speed video cameras record the impact. One camera is placed on the same level as the specimen; the other is focused on the soffit to observe the cracking process.

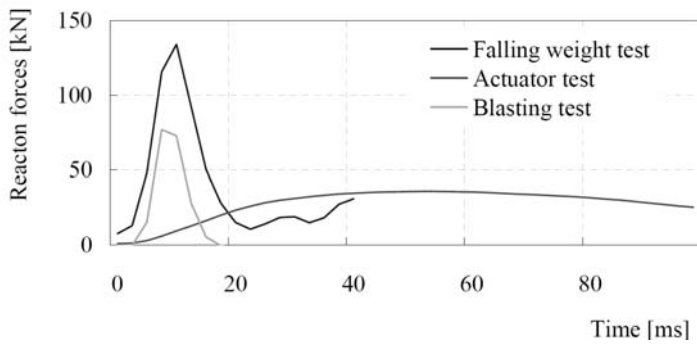


Figure 3-6: Development of the total forces in the supports over time

3.1.6. Results and conclusions

The development of the total forces in the supports over time is shown in Figure 3-6 and the slabs after the tests are shown in Figure 3-7. The actuator test seems to be the most manageable one with regard to execution but the performance of the actuators is not altogether satisfactory. The stroke is too slow and only reaches the load maximum after 45 ms. The velocity of the actuator should be at least 1 m/s. The water hammer has a short loading time of 15 ms and is partially adequate to model a rockfall impact. However, the maximum load applied to the slab is restricted by the equipment used. With some adjustments in the water capacity or in the charge, the load could be increased. By doing so, the important advantage of a balanced and approved system is lost.

The following four conclusions can be drawn from the small-scale tests:

- (1) The most complex setup is that one of the falling weight test with the cushion layer. Even so it is the most appropriate one. Concerning the test setup, only small improvements are required. The calottes should be placed between the load cells and the specimen to allow for a better rotation of the slab.
- (2) The triggering should be automated and simplified to avoid data loss in future tests.
- (3) The sampling rate of the video extensometer is too low to follow the slab displacements.
- (4) By using a sampling rate of 400 Hz it was possible to describe the shapes of the graphs in the time domain. To get better information on the beginning of the impact and in particular on the peak value, a sampling rate of at least 1 kHz should be applied.

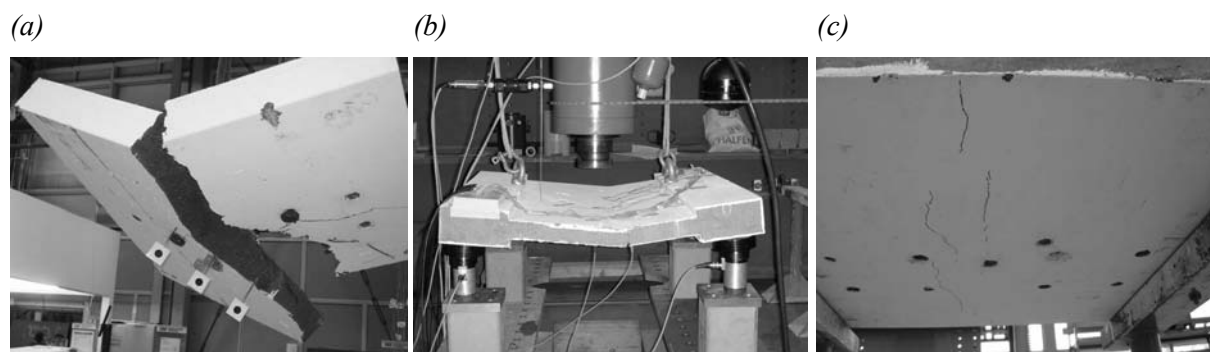


Figure 3-7: Specimens after the test (a) W1, (b) W3 and (c) W2

3.2. Medium-scale tests

After the falling weight test in small-scale, experience in measuring the slab response and especially in the reinforcement had to be improved. Thus, medium-scale tests were carried out with the aim being to obtain experimental data of the impacted reinforced concrete slab.

A series of seven rockfall impact tests was performed under laboratory conditions with three different cushion materials. The kinetics of the striking body is analyzed from measured accelerations and the dynamic response of the reinforced concrete slab is investigated.

3.2.1. Test setup

The falling weight of 825 kg (described in Chap. 3.1.2) is dropped from 2 m height released by a remote-controlled helicopter hook onto a reinforced concrete slab (Figure 3-8).

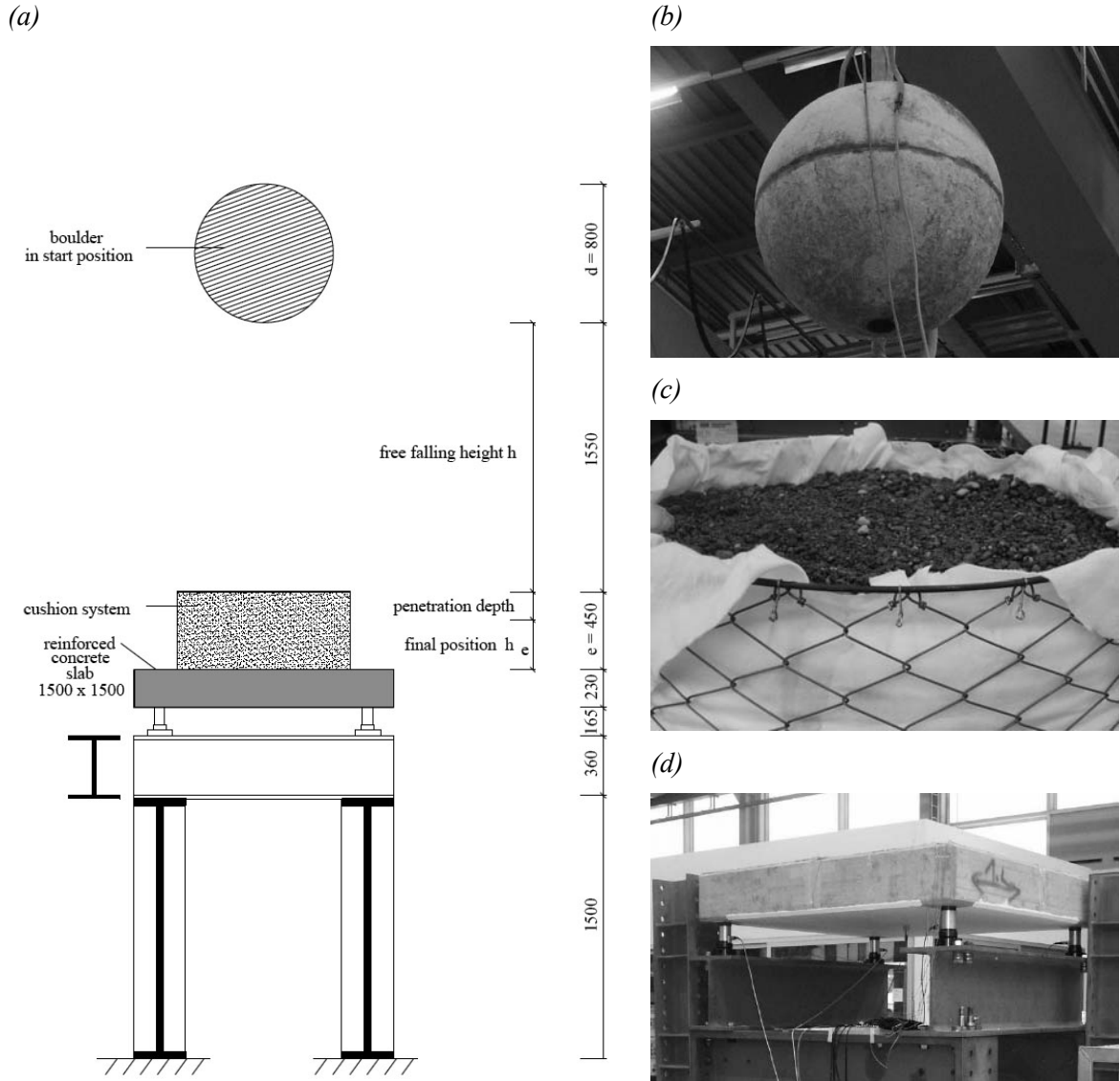


Figure 3-8: (a) Section of the test setup, (b) falling weight, (c) cushion system filled with gravel and (d) reinforced concrete slab placed on the test frame.

3.2.2. Reinforced concrete slabs

Three reinforced concrete slabs of dimensions $1.5 \times 1.5 \times 0.23$ m are simply supported at the four corners resulting in spans in the diagonal direction of 1.95 m (see Figure 3-8d). The horizontal movement of the slab is restrained. The slabs are designed according to the Swiss guidelines for an equivalent static load of 390 kN [ASTRA, 1998]. The lower reinforcement layers consist of 17 bars of 12 mm diameter in both directions (Figure 3-9).

3.2.3. Cushion layer

The cushion systems are composed of cylinders made from steel wire mesh filled with a cushion material (Figure 3-8c). The mesh cylinders restrict the lateral displacement of the material and create modular energy dissipating systems. The cylinders have a diameter of 1 m and a height of 0.5 m. The cushion layers have an initial thickness of 0.45 m. The mesh consists of 3 mm high-tensile steel wire with a tensile strength of 1770 N/mm^2 and 65 mm openings. The failure load of the mesh is 170 kN/m. In order to avoid the cushion materials

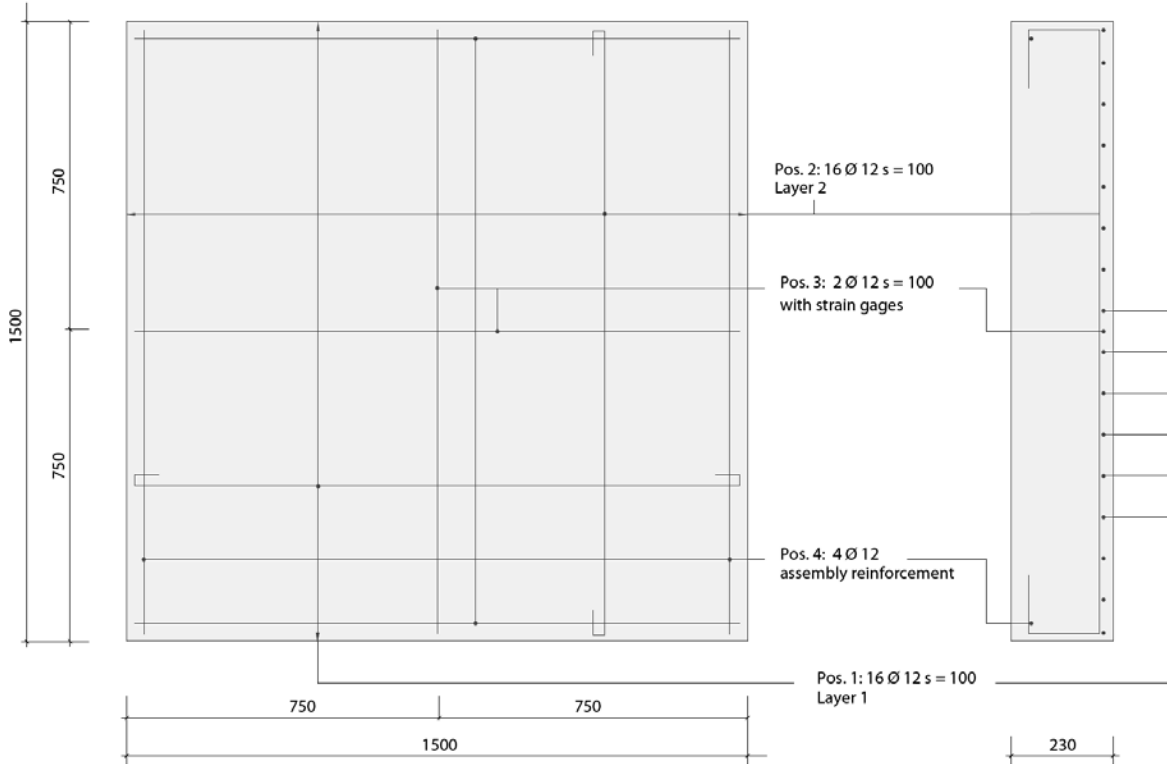


Figure 3-9: Reinforcement of concrete slabs [mm]

falling through the mesh, a geotextile is employed.

Within this test series, three different cushion materials were tested and compared: First, the sand described in Chap. 3.1.2. Second, gravel referring to the material actually used on rockfall galleries and third, a cellular glass. The cellular glass is produced from recycled glass and has a cube compressive strength of 6 N/mm^2 . The granulation of the cellular glass ranges from 10 to 50 mm and its density is 2.5 kN/m^3 . The density of the sand is 17.2 kN/m^3 and of the gravel 26 kN/m^3 , respectively.

3.2.4. Test program and measurements

Seven falling weight tests are conducted using different materials in the cushion system. Each cushion system is placed on its own reinforced concrete slab to avoid potential influence of load history.

The distance between the boulder and the slab is measured before and after each impact. After the first impact the boulder is lifted again to the original height of 2 m above the slab surface for a second impact. For the second impact, both the compaction of the cushion layer and the dent formed during the first impact are left untouched, resulting in an increased falling height. With this procedure, information on the behavior in a compacted state can be gained. For the cellular glass cushion system, a third impact with reduced falling height was performed.

Within the concrete slabs, the following parameters are measured with a sampling frequency of 1600 Hz and again filter by the Bessel filter: reaction forces at all supports, the acceleration in the center of the slab and strains at the slab upper surface as well as in the bars. Each load cell at the supports has a capacity of 300 kN. The measurement range of the acceleration sensor is $\pm 1000 \text{ m/s}^2$. Also relevant for the analysis of the dynamic processes is the measured

Table 3-3: Test results with sand (S1, S2), cellular glass (C1, C2, C3) and gravel (G1, G2)

		S1	S2	C1	C2	C3	G1	G2
Start position	h_s [m]	2.00	2.00	2.00	2.00	1.50	2.00	2.00
Final position	h_e [m]	0.26	0.24	0.20	0.15	0.13	0.21	0.18
Thickness of cushion layer	e [m]	0.45	0.26	0.45	0.20	0.15	0.45	0.21
Free falling height	H [m]	1.55	1.74	1.55	1.80	1.35	1.55	1.79
Impact velocity	v_i [m/s]	5.5	5.8	5.5	5.9	5.1	5.5	5.9
Kinetic impact energy	E_i [kJ]	12.5	14.1	12.5	14.6	10.9	12.5	14.5
Penetration depth	p [m]	0.19	0.02	0.25	0.05	0.02	0.24	0.03
Impact time	t [ms]	55.0	32.5	66.9	28.8	27.5	73.1	38.8
Max. reaction forces	F [kN]	233	491	213	374	424	236	615
Max. boulder acceleration	$a_{s,max}$ [m/s ²]	236	421	227	410	478	232	563
Max. neg. slab acceleration	$a_{p,max}$ [m/s ²]	-26	-264	-57	-135	-180	-43	-277
Max. pos. slab acceleration	$a_{p,min}$ [m/s ²]	21	180	30	80	109	28	198
Total energy	E [kJ]	14.1	14.2	14.6	15.0	11.1	14.5	14.7
Rebound height	s_{rp} [m]	0.028	0.036	0.022	0.041	0.045	0.017	0.028
Rebound energy	E_{rp} [kJ]	0.227	0.291	0.178	0.332	0.364	0.138	0.227
Energy dissipated	D [%]	98.4	98.0	98.8	97.8	96.7	99.1	98.5

acceleration of the boulder. In addition the tests are recorded with two digital high-speed video cameras with a recording rate of 125 and 250 frames per second. To synchronize the data with the boulder measurements, a reference signal is sent to all measuring units.

3.2.5. Results and conclusions

The most important values of the impact tests are summarized in Table 1. The initial position is chosen to 2 m above the slab (except for C3). The penetration depth is deduced from the final position of the boulder. The largest penetration of the first impacts is obtained with cellular glass (0.25 m) and the smallest with sand (0.19 m). These penetrations increase the free falling height of the second impacts. It is obtained by subtracting the actual thickness of the cushion layer from the height above the slab. It determines the impact velocity and together with the boulder mass the kinetic impact energy, which in the case of the cellular glass (14.6 kJ) is more than 15% higher than in the first impact (C1). The additional penetrations produced by the second impacts were between 10% (S2) to 20% (C2). For all cushion materials, the impact time of the first impact is about twice as long as for the second impact. The sand cushion layer produces shorter impacts than the cellular glass or the gravel layer.

The main result of each impact test is the peak value of the reaction forces. With cellular glass this value (213 kN) amounts to about 90% of the corresponding value with sand (233 kN) or gravel (236 kN). The second impact with cellular glass provides peak reaction forces (374 kN) on the order of 75% and 60% of the peak value with sand (491 kN) and gravel (615 kN), respectively. The measured boulder accelerations in the second impacts (S2, C2, G2) are in the range of 180 to 240% of the accelerations reached in the first impacts, which for all three amount to about 230 m/s². The accelerations in the slab show positive and negative values; the maxima and the minima of the second impacts reach between 3 and 10 times the values of the first impact. Figure 3-10 shows the time development of the accelerations in both the slab and the boulder, compared with the reaction forces in the supports for the first and the second impacts.

The three different cushion layers produced different accelerations in the boulder and different loading characteristics on the slab. The load during the first impact reaches its maximum value towards the end of the impact time. In the second impacts, where the growth of the

accelerations is clearly faster than in the first ones, the maximum is reached in the initial part of the impact. Only with cellular glass the maximum load in the second impact is also reached at the end of the impact time. A strong decrease of the boulder accelerations after a slow growth characterizes the energy dissipation during the impact. The plastic deformation of the cushion layer can be seen in the residual deformation.

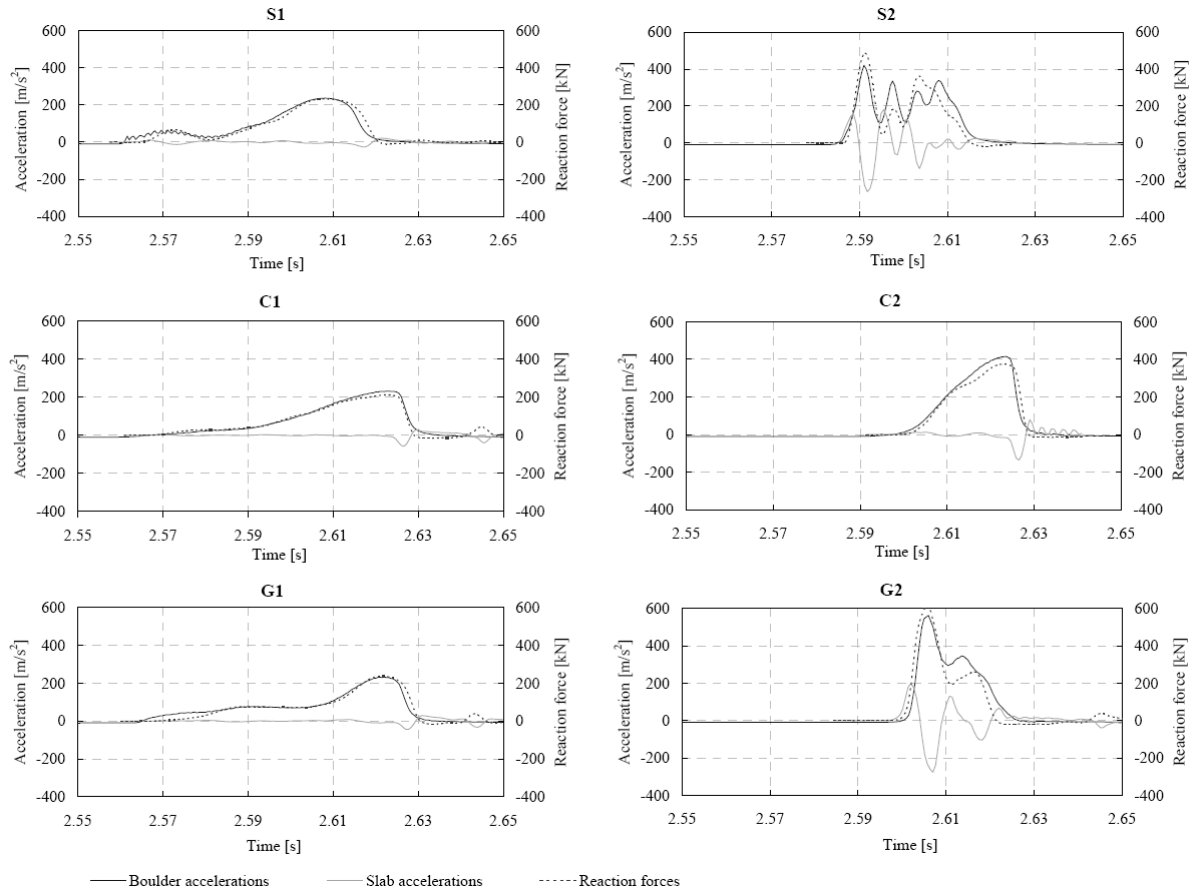


Figure 3-10: Accelerations and reaction forces for tests S1, S2, C1, C2, G1 and G2.

The time development of the reaction forces corresponds well with the measured accelerations in the boulder. Only minor discrepancies can be found, which can be explained by inertia effects.

The diagrams in Figure 3-11 visualize the results of the boulder trajectory analysis using the measured boulder accelerations. The different cushion properties of the materials are significant so that the dynamic characteristics also differ. The properties of gravel are more on the sandy side.

The acceleration curves of the three first impacts (S1, C1 and G1) look quite similar and show almost the same maximum deceleration of the boulder (Figure 3-10). For sand, the boulder's acceleration curve is not strictly increasing but shows a distinct intermediate maximum. One explanation might be a lateral expansion of the mesh. This local maximum is less distinct for cellular glass, mainly because sand is a denser material transmitting impulses better. Cellular glass absorbs small peak loads internally by plastic deformation or by crushing of the contact zones between grains during compaction. Accordingly, the velocity diagram shows a smoother retardation curve for cellular glass than for sand.

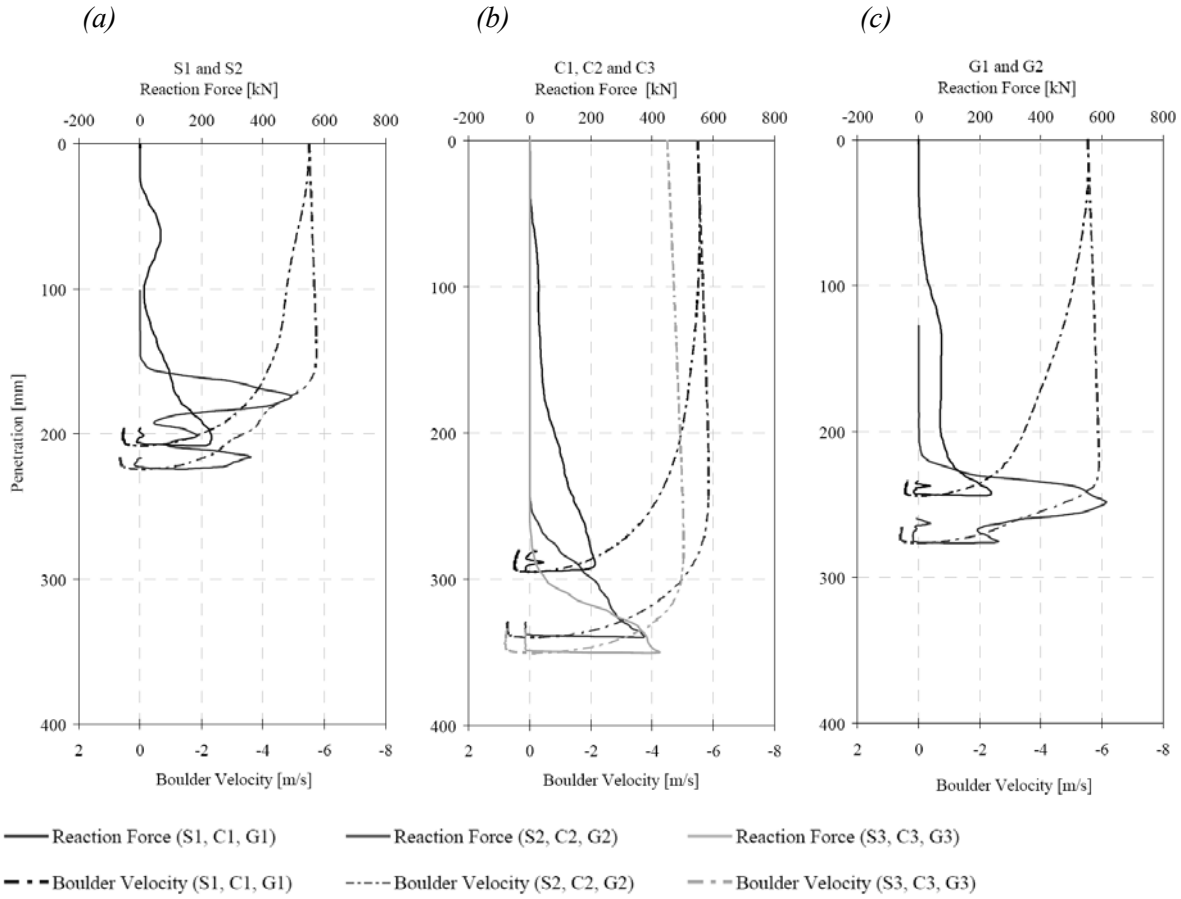


Figure 3-11: Penetration–reaction force & velocity–diagram for a) S1 and S2, b) C1, C2 and C3, c) G1 and G2

For the second experiment with sand, the observable oscillations show the interaction between the boulder and the concrete slab, which has been set in motion at the natural frequency of the system of about 160 Hz.

The interpretation of the slab accelerations is rather difficult, if they are regarded separately. Remarkable is the algebraic sign of the first significant peak, which e.g. is positive in S2 or G2 and is negative in C2 (Figure 3-10). The deflection of the slab can be deduced by integrating the measured slab acceleration twice. Figure 3-12 shows that the integration of these accelerations corresponds very well with the measured reaction forces.

The theoretical deflection by a static load of 615 kN in the slab center, which corresponds to the peak load in G2, is on the order of 1.5 mm. The maximum displacement obtained by the double integration of the slab accelerations is 2.5 mm. The reinforced concrete slabs do not show any cracking after the impacts. The strains at the slab surface as well as in the reinforcement (Figure 3-13) show that the slab mainly remains in the elastic state.

The average strain rates during the strongest increase reach values of 0.002 s^{-1} in S1 and 0.085 s^{-1} . Locally, strain rates of 0.15 s^{-1} have been measured in the reinforcement bar for the G2 impact. Impacts with strain rates of about 10^{-4} s^{-1} are classified as soft impacts. Strain rates of 10^{-1} s^{-1} are in the range of hard impacts.

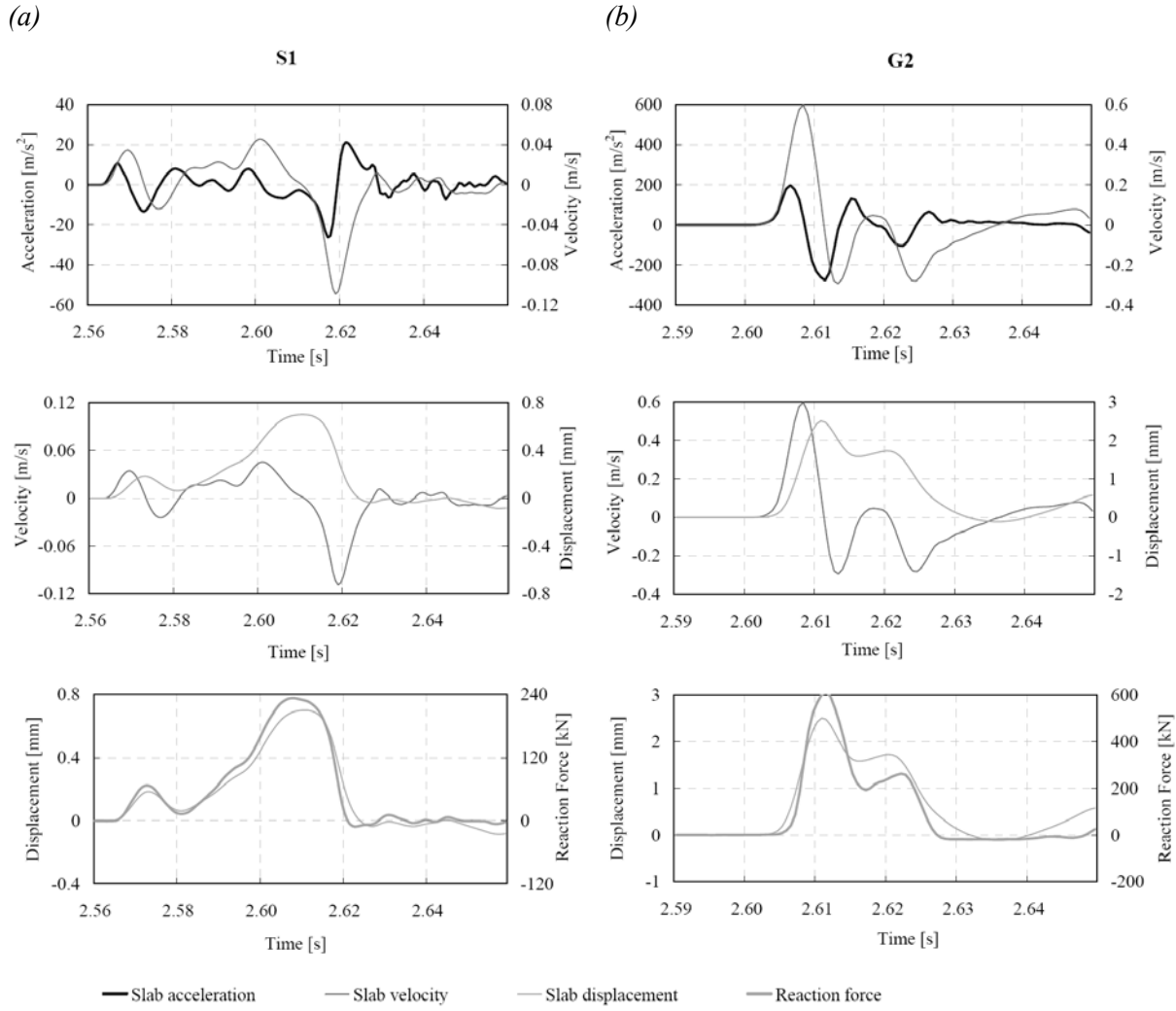


Figure 3-12: Deflection of the slab center by integrating accelerations twice for a) S1 and b) G2

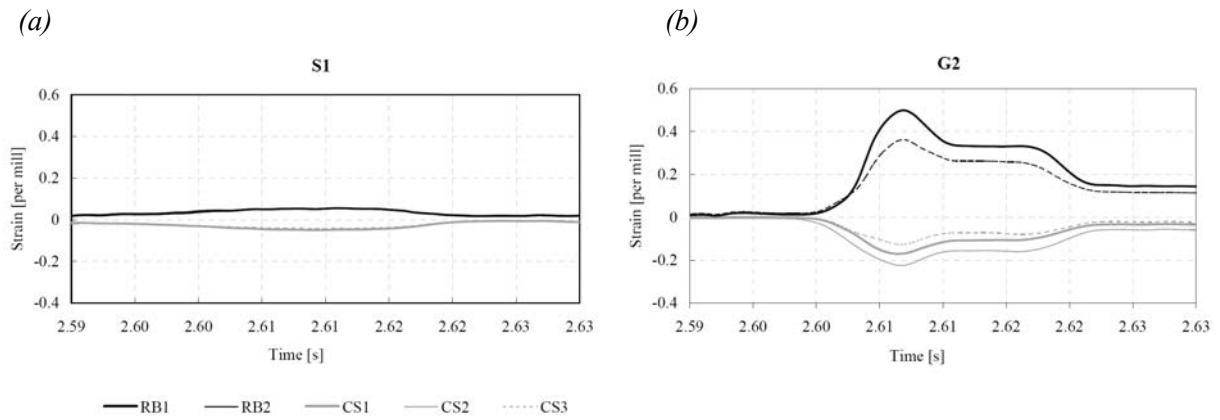


Figure 3-13: Strains at the slab surface and in the reinforcement for (a) S1 and (b) G2.

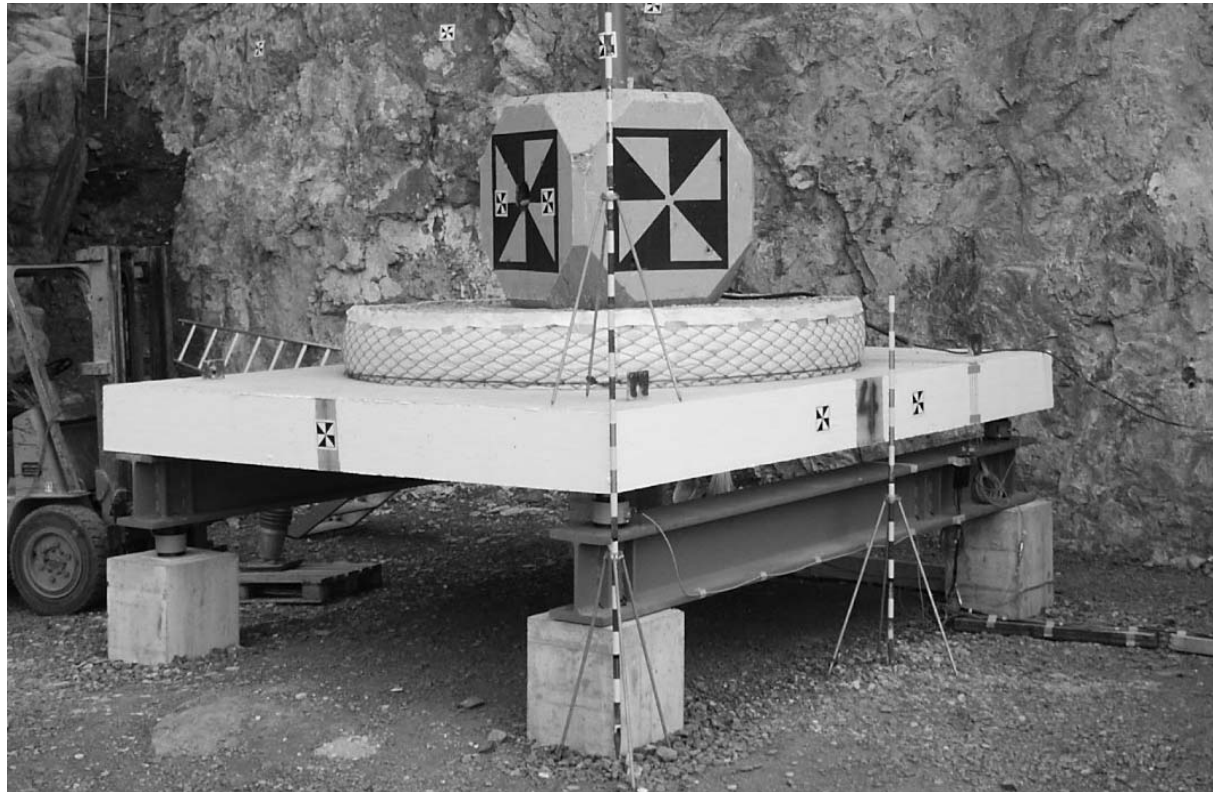


Figure 3-14: Test setup with gravel cushion and 4000 kg boulder

3.3. Large-scale tests

Large-scale field tests on reinforced concrete slabs were performed in collaboration with WSL and Geobrugg AG at the testing site Lochezen, an old quarry close to Walenstadt in the Swiss Alps. The main focus of these tests is to understand the response of the structure and the interaction between the impacting rock, the cushion layer and the reinforced concrete slab.

Six reinforced concrete slabs covered by a cushion layer are subjected to falling weight impacts. Artificial concrete boulders are dropped from different heights, ranging from 2 to 15 m, released by a remote-controlled hook. The slabs correspond to an average Swiss rockfall protection gallery (see Chap. 6) with a scale of 1:2. By using three different slab types the influence of the slab thickness and reinforcement on the impact behavior can be explored. For each slab, the impact energy is increased until failure occurs. Additional to a standard gravel cover, two special cushion systems are tested. The kinetics of the impacting body is analyzed and the dynamic response of the reinforced concrete slab is investigated by measuring accelerations, reaction forces and strains.

3.3.1. Test setup

The test unit consists of two HEM 360 beams supported by four reinforced concrete footings of 0.5×0.5 m and 0.6 m height each. Both HEM beams are 4.5 m long. One of them serves as a line support for the slabs modeling the mountain side of the gallery and is placed on two load cells (shown on the left hand side in Figure 3-14). A mortar layer of thickness about 10 mm is placed between the line support and the reinforced concrete slab. It ensures a continuous and regularly distributed support and compensates for geometrical irregularities and due to friction also allows carrying horizontal forces. The remaining two corners of the

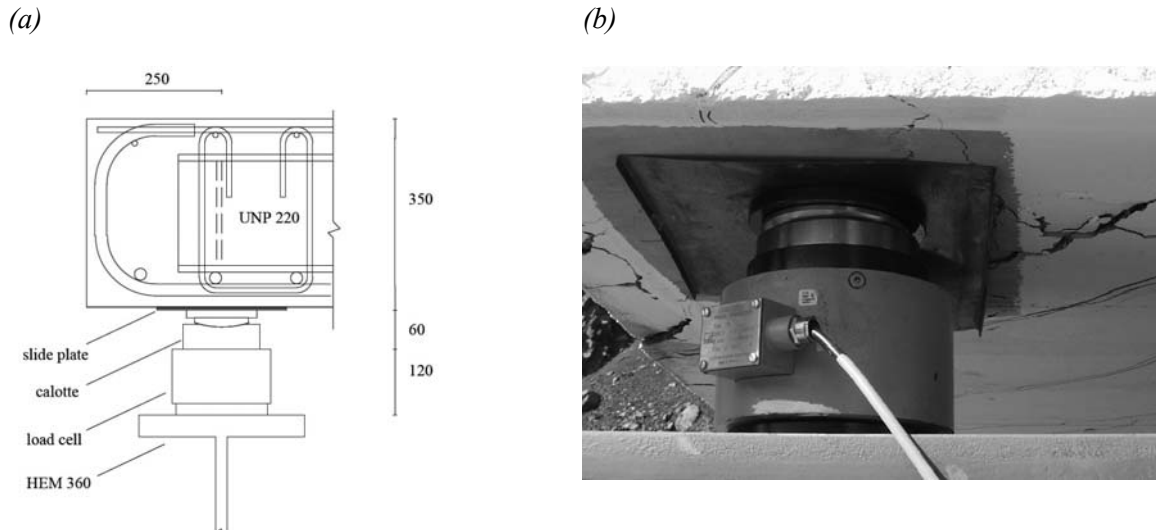


Figure 3-15: Simple support (a) technical drawing of cross section, (b) load cell with sliding plates and calotte

slabs are simply supported on the load cells modeling the valley side column supported points of the galleries. For the single supports the load cells are placed on top of the second HEM beam (shown on the right hand side in Figure 3-14). Horizontal movements of the slabs are enabled at the simple supports by Teflon laminated sliding plates (Figure 3-15). Spherical calottes placed between the slide plates and the load cells allow for rotations. Horizontal displacements of all components of the test unit are restrained by bolts. Unlike real rockfall galleries, the slabs are not restrained from lifting off the supports.

The HEM beams allow the test unit to be adjusted to other support conditions. For future tests, it could be used for two line supports, even along the short side of the testing unit.

The reinforced concrete slabs are covered by the cushion layer. The boulder is dropped onto the slab with a predefined height between cushion layer and boulder bottom surface. The boulders consist of two obtuse hexahedra (Figure 3-16), made out of fiber-reinforced high performance concrete with a weight of 800 kg and 4000 kg, respectively.

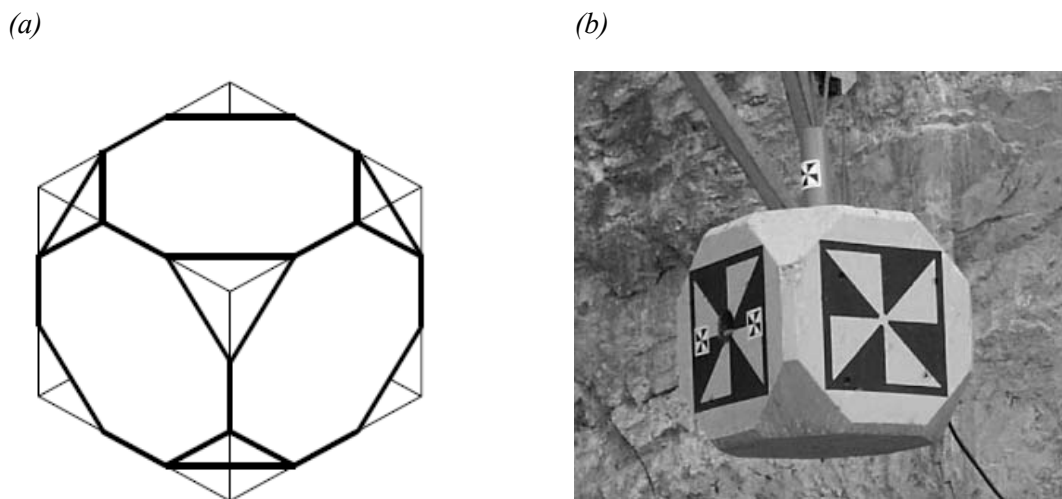


Figure 3-16: Boulder a) geometry, b) 4000 kg boulder with target points for video analysis

3.3.2. Reinforced concrete slabs

Six reinforced concrete slabs of dimensions 3.5 x 4.5 m were tested. Table 3-4 gives an overview on the three different slab types and Figure 3-17 shows the cross section along the short side. Slabs 1 and 2 have a thickness of 0.25 m, slabs 3 to 6 a thickness of 0.35 m. Slabs 5 and 6 have additional continuously distributed shear reinforcement.

To avoid shear failure near to the simple supports, two UNP 160 or 220 joists welded to an elbow are cast in at 250 mm distance from the corner. Each side of the UNP profiles has a length of 1.20 m.

Table 3-4: Slabs thickness and reinforcement

Slabs	Thickness [m]	Lower bending reinforcement [mm]	Upper bending reinforcement [mm]	Shear reinforcement [mm]
1 & 2	0.25	d = 18 s = 155/152	d = 10 s = 310/300	no
3 & 4	0.35	d = 22 s = 155/152	d = 10 s = 310/300	no
5 & 6	0.35	d = 22 s = 155/152	d = 10 s = 155	d = 10

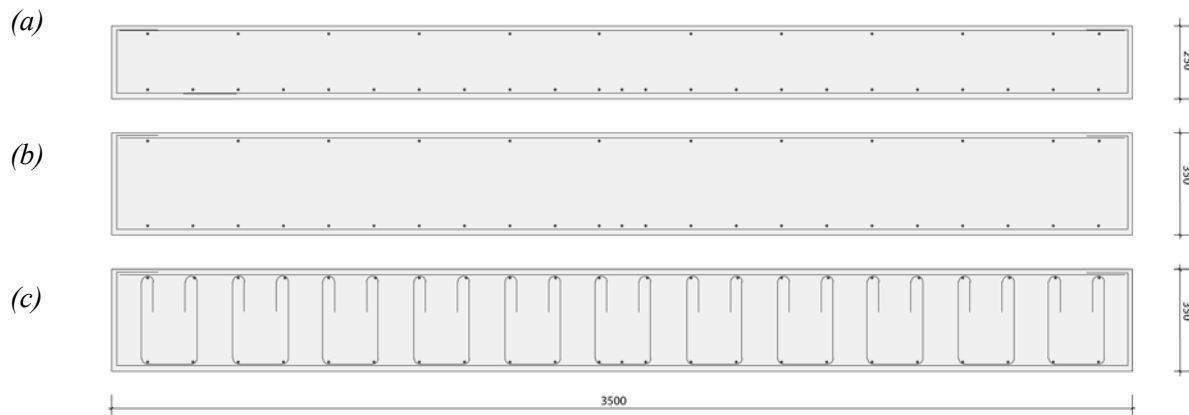


Figure 3-17: Reinforcement layout of (a) slabs 1 & 2, (b) slabs 3 & 4 and (c) slabs 5 & 6 [mm]

3.3.3. Cushion layers

For most of the tests, a gravel cushion layer is used with a thickness of 0.40 m. In the scale of 1:2 this thickness corresponds to the average layer thickness placed on typical Swiss rockfall galleries. The cushion layer is kept in place by a steel mesh cylinder of diameter 3 m. The influence of the steel mesh on the behavior of the cushion layer is assumed to be negligible considering a load spread angle of about 45°. In order to avoid the cushion materials penetrating the mesh, a geotextile is applied (Figure 3-18a).

The grain size distribution of the gravel is shown in Table 3-5. In order to quantify the energy dissipated by the gravel, rounded material is selected. After the impacts samples of the cushion layer are taken from the contact area and examined for the percentage of crushed grains. Before every test the gravel layer is compacted with a compacting machine to M_v -values of around 45 MN/m². This value corresponds to the upper range of compaction that can be expected on top of a rockfall gallery.

Table 3-5: Grain size distribution of cushion gravel

Size fraction	Mass %
0 – 4 mm	33
4 – 8 mm	11
8 – 16 mm	20
16 – 32 mm	36

Two special cushion systems with high-tensile steel wire mesh and cellular glass (described in Chap. 3.2.3.) allow analysis of the suitability and behavior of these systems as alternative cushion systems. The high-tensile steel wire mesh is a chain-link mesh with a wire diameter of 3 mm and a tensile strength of 1770 N/mm. The ultimate load of the mesh is about 170 kN/m. The cellular glass is produced from recycled glass and has a cube compressive strength of 6 N/mm². The granulation of the cellular glass ranges from 10 to 50 mm and has a bulk density of only 2.5 kN/m³.

The first setup (called Geobrugg A) consists of three layers of 40 cm of cellular glass (Figure 3-18b). Between the layers of the cellular glass and on top of the cushion, a layer of high-tensile mesh is installed in order to get an improved load distribution and to activate more cellular glass. The second setup (called Geobrugg B) is made of modular cylinders made from high-tensile mesh and filled also with cellular glass (Figure 3-18c). The cylinders have a diameter of 1 m and a height of 0.6 m. Six of them are placed around the seventh in the center

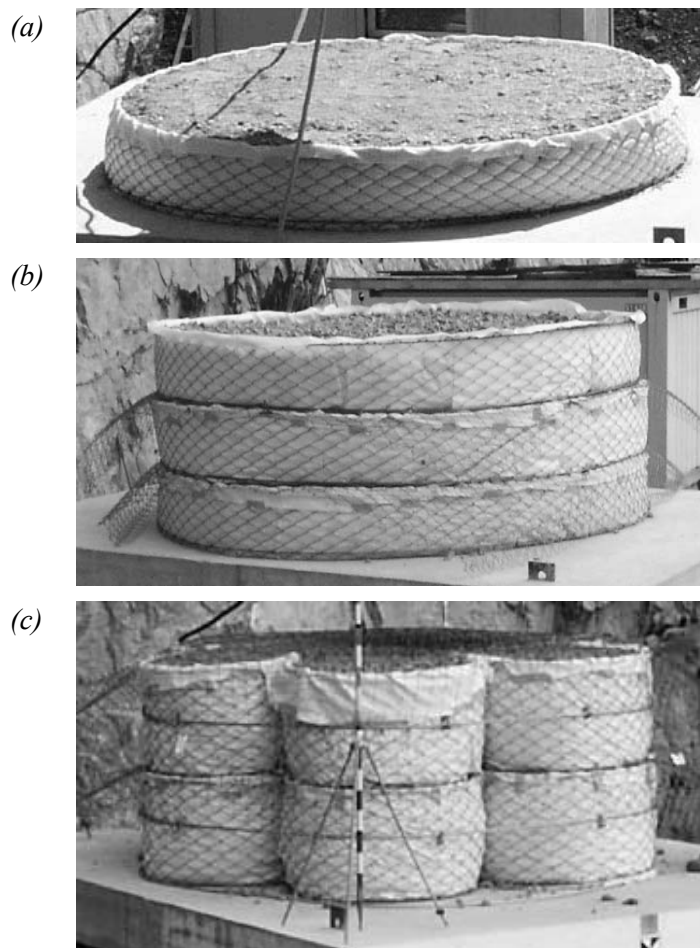


Figure 3-18: Cushion layers (a) 0.40 m gravel layer, (b) 1.20 m Geobrugg A and (c) 1.20 m Geobrugg B

and covered with a layer of high-tensile mesh. Then another seven cylinders and a top mesh layer of the high-tensile mesh are placed. The cylinders restrict the lateral displacement of the material and create a modular energy dissipating system.

3.3.4. Test program and measurements

At the beginning three identical tests (A2, A3 and A4) were carried out to identify potential systematic errors in the testing procedure. The statistical spread of the test results is of minor importance compared to the uncertainties of the event magnitude. Accordingly, each impact test is carried out only once. The test program was set up to obtain the best comparisons possible between the single impact tests.

Reaching the governing failure mode would be interesting since information on dynamic material properties and structural performance for the design can be gained. To avoid damage to the test unit and to the instrumentation, the impact loading on the slabs should not excessively exceed the ultimate load capacity. Hence the tests have been performed by increasing the falling height successively. The plastic strains in the bending reinforcement or any shear failure are the termination criterion.

The influence of the slab thickness on the impact response is the major goal of the experimental study. Additionally, the following comparisons are obtained from the test program:

- impulse variation: large mass with low impact velocity compared to small mass with high impact velocity
- slab response at different degradation states,
- load capacity of the slab with and without shear reinforcement
- conventional and special cushion layer

Neither the influence of the boulder shape nor the compaction of the cushion layer is studied during these large-scale tests. The compaction of the cushion layer has been explored parametrically in previous studies [Montani, 1998].

Using the six available slabs the test program with 38 impacts as shown in Table 3-6 is executed. The procedure for impact testing includes the following ten steps:

- 1) placing the slab on the testing unit and mounting the instrumentation,
- 2) installing the cushion layer on top of the slab,
- 3) compacting the cushion layer and measuring the compaction,
- 4) placing the boulder in a central position and measuring the position,
- 5) lifting the boulder to the predefined falling height
- 6) releasing the boulder and triggering measurements
- 7) measuring the final position after impact and removing the boulder,
- 8) measuring the amount of compaction and taking samples from the cushion layer,
- 9) tracking the cracks in the slab,
- 10) loosening the compacted cushion layer at the impact location and returning to step 3) for the next impact test.
- 11) removing the slab from the testing unit and taking drilling core samples.

The last tests F8 to F10 were carried out eccentrically. For each slab (except the last one) the tests are performed within one day.

The four load cells have a capacity of 1'000 kN each. Within the concrete slabs, acceleration and strains are measured at a sampling rate of 3'200 Hz. A Bessel low-pass filter with a cut-off frequency of 150 Hz provides the smoothed shape of the measurement. The accelerations are measured in two places: in the center of the slab and at 1.5 m distance of the center along the diagonals towards the simply supported corners. The measurement range of the acceleration sensor is $\pm 1'000 \text{ m/s}^2$.

In the center of the slab the strains within the bending reinforcement and at the slab's upper surface are measured (Figure 3-19). The reinforcement strains are measured in two additional rebars of 2 m length located orthogonally to each other in the center of the slab. There also the

Table 3-6: Test program of the 38 large scale tests

Test name	Slab No.	Cushion layer			Falling weight [kg]	Falling height [m]	Impact energy [kJ]
		Type	Thickness [m]	Compaction [GPa]			
A1	1	Gravel	0.4	53	800	2	16
A2	1	Gravel	0.4	-	800	5	39
A3	1	Gravel	0.4	46	800	5	39
A4	1	Gravel	0.4	47	800	5	39
A5	1	Gravel	0.4	43	800	7.5	59
A6	1	Gravel	0.4	36	800	10	78
A7	1	Gravel	0.4	42	800	12.5	98
A8	1	Gravel	0.4	44	800	15	118
B1	3	Gravel	0.4	48	800	5	39
B2	3	Gravel	0.4	52	800	7.5	59
B3	3	Gravel	0.4	47	800	10	78
B4	3	Gravel	0.4	56	800	12.5	98
B5	3	Gravel	0.4	54	800	15	118
B6	3	Gravel	0.4	48	4'000	2	79
B7	3	Gravel	0.4	47	4'000	5	197
C1	2	Geobrugg A	1.2	-	800	15	118
C2	2	Geobrugg A	1.2	-	800	5	39
C3	2	Geobrugg A	1.2	-	800	5	39
C4	2	Geobrugg A	1.2	-	800	5	39
C5	2	Geobrugg A	1.2	-	800	10	78
C6	2	Geobrugg A	1.2	-	800	15	118
C7	2	Geobrugg A	1.2	-	4'000	2	78
C8	2	Geobrugg A	1.2	-	4'000	5	196
D1	4	Gravel	0.4	56	4'000	2	78
D2	4	Gravel	0.4	52	4'000	5	196
E1	5	Gravel	0.4	40	800	15	118
E2	5	Gravel	0.4	38	4'000	5	196
E3	5	Gravel	0.4	46	4'000	7.5	294
F1	6	Geobrugg A	1.2	-	4'000	7.5	294
F2	6	Geobrugg A	1.2	-	4'000	7.5	294
F3	6	Geobrugg B	1.2	-	4'000	7.5	294
F4	6	Geobrugg B	1.2	-	4'000	7.5	294
F5	6	Gravel	0.2	30	800	10	79
F6	6	Gravel	0.4	16	800	15	118
F7	6	Gravel	0.4	40	800	15	118
F8	6	Gravel	0.4	35	800	15	118
F9	6	Gravel	0.4	42	4'000	5	198
F10	6	Gravel	0.4	58	4'000	7.5	295

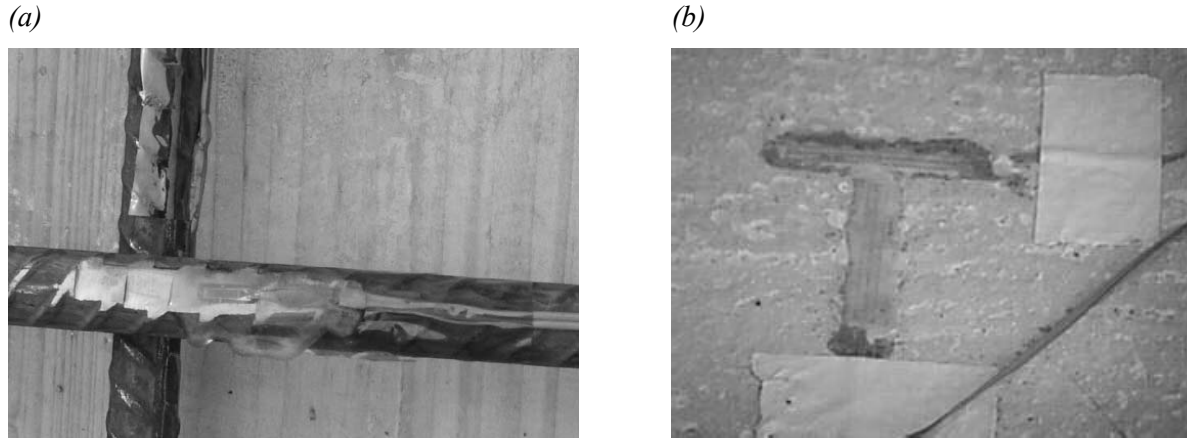


Figure 3-19: Strain gages (a) on the reinforcement and (b) at the upper slab surface

strains at the slab surface are measured. These strain gages are protected by silicon and a 0.5 cm thick mortar layer. For a better observation of crack patterns, the soffit of the slab is painted white.

The compaction of the cushion layer is measured before and after each impact. The compaction measurement is carried out by a light drop-weight device. It consists of a 10 kg weight dropping from 1 m onto a steel plate, where accelerations are measured. From the accelerations, a compaction modulus of the soil can be defined.

The boulders are equipped with four acceleration sensors measuring the vertical acceleration. The range of the sensors is $\pm 500 \text{ m/s}^2$ sampled at 10 kHz. The data from 1 s before triggering and 2 s afterwards is saved. The vertical rock velocities and movements are obtained by numerical integration of the acceleration data. Further steps are taken to increase the accuracy of this analysis: The large number of sensors allows for averaging the acceleration and the known start position and final positions allow necessary correction factors to be taken into account.

The tests are recorded by a digital video camera with a recording rate of 250 frames per second. A posterior analysis of the recorded trajectory can be done using tracking software. This redundancy in the acceleration measurements allows an additional check or further corrections, if necessary. The medium-scale tests showed that the acceleration and the time-integrated velocities taken from the acceleration sensors are very accurate. However, the best displacement curve is taken from the video recordings. The camera and the instrumentation are triggered manually.

3.3.5. Results and conclusions

An overview of the obtained maximum reaction forces at the supports is given in Figure 3-20. All measurements within the slab can be found in Appendix B. Besides the measurements, it can be observed that the boulder's impact surface is not completely horizontal at the moment of contact. This leads to a small rotation of the boulder during impact producing horizontal loads on the structure. The slabs experience a small lateral displacement. The bolts ensuring horizontal restraint of the test units need to be replaced several times.

After the tests, the cushion layer is less compacted than before. The separation of cushion layer and slab is clearly observable in the high-speed video. The lifting off of the slabs from the supports is also observed in the videos.

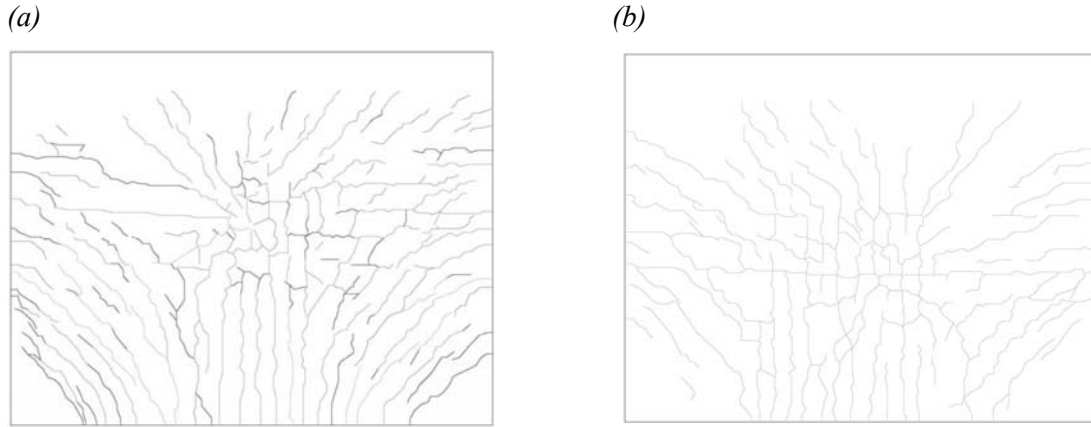


Figure 3-21: Crack pattern observed after the test a) A8 and b) D1

The crack pattern on the slabs suffit are shown in Figure 3-21 for the tests A8 and D1. The failure mode that can be observed in all slabs is a combined bending shear failure close to the simply supported corner (Figure 3-22). According to the design of the slabs for static loading, bending failure along the middle of the slab is expected. The punching resistance of the slab is close to the bending capacity.

With the cellular glass cushion layer it is possible to reduce the support forces substantially. It can be shown that the test setup produces reliable results. The obtained data is very detailed and allows an extensive analysis describing the rock impact, the behavior of the cushion system and the interaction between impacting boulder and concrete slab.

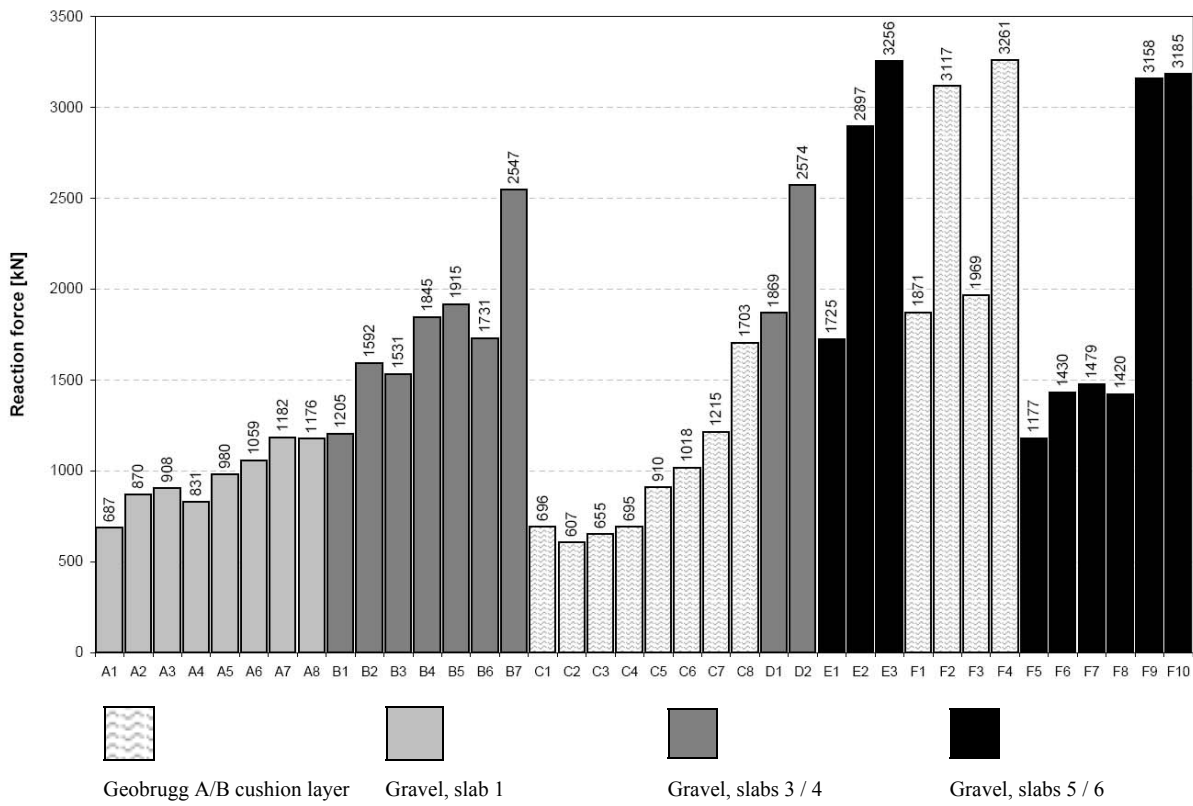


Figure 3-20: Summary of total reaction forces of large-scale tests

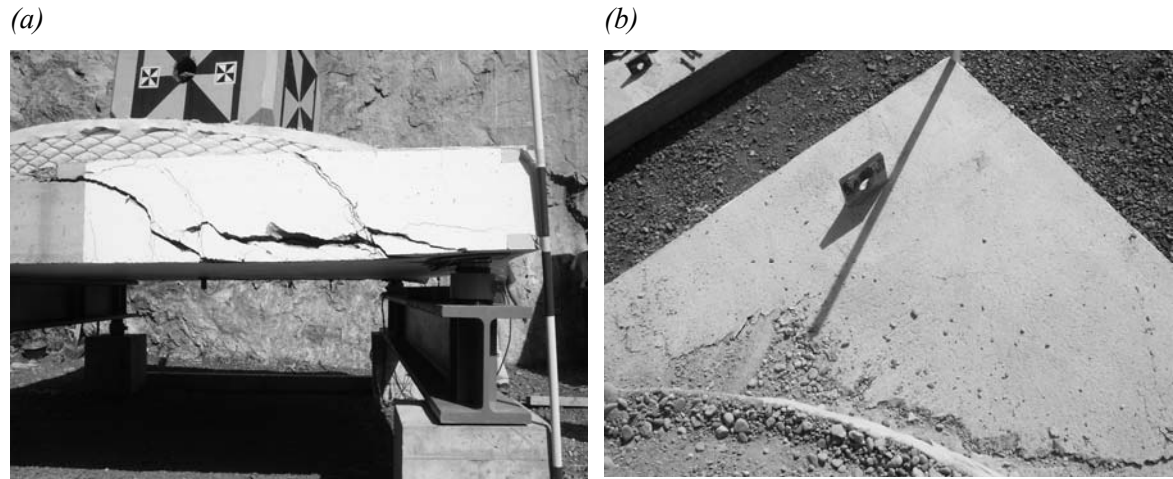


Figure 3-22: Slabs 4 after failure: (a) front view (b) chipping of concrete in the compaction zone

3.4. Punching tests

At the Muroran Institute of Technology in Japan, falling weight tests have been carried out that provide the data to verify the model's prediction of punching failure. A series of punching tests have been extended by the six tests with cushion layer. The main differences to the tests carried out in Switzerland are the boundary conditions and the concentrated loading area.

3.4.1. Test setup

Reinforced concrete slabs are subjected to falling weight impacts with predefined impact velocities. The impacts are at the centers of the slabs. The slabs are line supported and tied down along all four sides to avoid lift-off (Figure 3-23). The line supports are fixed over a reaction frame allowing small rotations. In between, load cells are distributed continuously.

3.4.2. Reinforced concrete slabs

Two identical reinforced concrete slabs are used for these punching tests. The square slabs have side lengths of 2 m and a thickness of 0.18 m (Figure 3-24). All sides are encased in U-shaped steel sections ($H = 180$; $B = 75$ mm; $t_1 = 7$ mm; $t_2 = 10.5$ mm; $I_y = 1'380 \text{ cm}^4$;

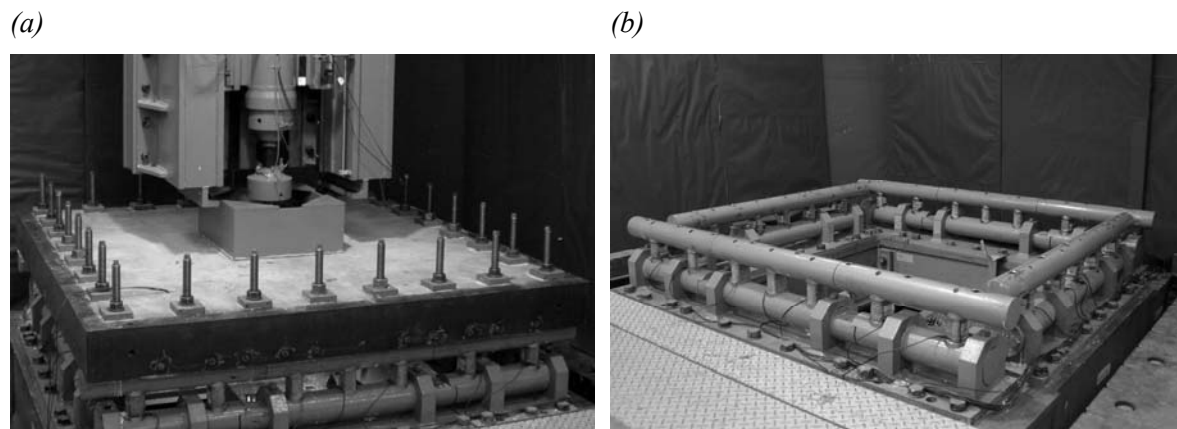


Figure 3-23: Test setup (a) concrete slab with sand cushion tied down to the line supports, (b) line supports, load cells and the reaction frame

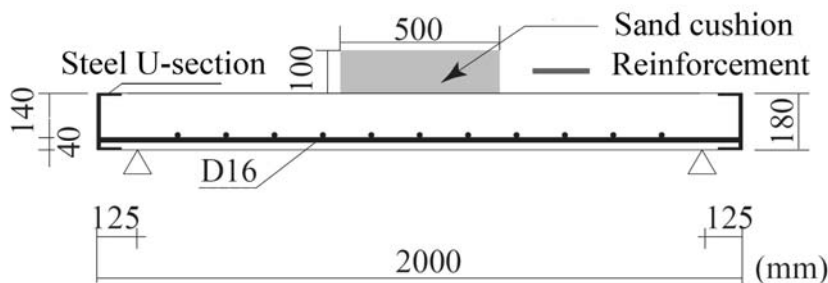


Figure 3-24: Section of reinforced concrete slab with steel U-sections and sand cushion [mm], [Kishi et al., 2008]

$I_x = 131 \text{ cm}^4$), in which the reinforcement is anchored by welding onto the steel sections. Bending reinforcement consists of 10 rebars of 16 mm diameter in each direction. Concrete strength in compression is $f_{cm} = 32.2 \text{ MPa}$.

3.4.3. Cushion layer

On top of the slabs a sand cushion layer of 100 mm thickness is placed. The thickness of the layer is limited in order to obtain punching failure. The sand corresponds to the cushion layer used for previous tests and is placed more or less compacted and slightly damp. The sand is kept in place by a 500 x 500 mm wooden box without a bottom side. To avoid intrusion of the sand into the slab after cracking, a textile is placed between the slab and the sand cushion.

3.4.4. Falling weight

A weight of 300 kg falls along a vertical guide. Due to friction between the falling weight and the guide, impact velocity determines the impact instead of the falling height. Different heads can be placed on the falling weight, allowing a selection of the contact area. For each slab a different loading diameter is used: 60 and 150 mm.

3.4.5. Test program and measurements

The first slab is impacted by the falling weight with a head of diameter of 60 mm and an impact velocity of 6 m/s, reaching punching failure. For the second slab a loading diameter of 150 mm is used. The impact velocity is increased for each test until failure occurs. For every impact, the sand cushion is prepared with the initial conditions. The test program is shown in Table 3-7.

The impact force is measured by a load cell within the falling weight. 24 load cells placed below the line supports measure the reaction force of the slab. The strains of the bending reinforcement are measured by six strain gages in the central reinforcement bar for each direction. The displacement at the center of the slab is measured by laser distance meters.

Table 3-7: Test program of punching tests

Test name	Slab nr.	Cushion layer	Diameter of loading area [mm]	Falling weight [kg]	Impact velocity [m/s]	Impact energy [kJ]
S6-6	1	Sand	60	300	6	5.40
S15-6	2	Sand	150	300	6	5.40
S15-7	2	Sand	150	300	7	7.35
S15-8	2	Sand	150	300	8	9.60
S15-9	2	Sand	150	300	9	12.15
S15-10	2	Sand	150	300	10	15.00

3.4.6. Results and conclusions

Punching failure was reached for both slabs. In Figure 3-26 the crack pattern at the slab soffit are shown for the impacts S6-6, S15-6, S15-8 and S15-10, respectively. For the smaller loading diameter, where punching resistance is lower, less bending cracks can be observed. After punching failure, both slabs have been cut though at the center revealing the shape and the angle of the punching cone (Figure 3-25).

Remarkable is that the diameter of the punching cone at the upper surface with 80 mm is clearly smaller than the loading diameter. Hence, the sand cushion did not provide the load spreading as usually assumed in design.

In Figure 3-27 the maximum impact loads, reaction forces and displacements for each test are shown. In addition, the results for the equivalent tests without a sand cushion, which were carried out previously (N6 and N15). A more detailed comparison with the test without sand cushion is given in [Kishi et al., 2008].

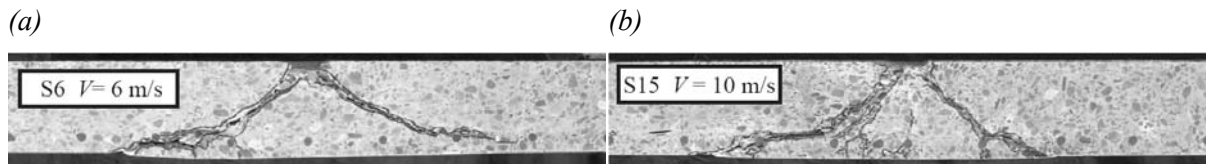


Figure 3-25: Punching cone after test (a) S6, (b) S15-10 [Kishi et al., 2008]

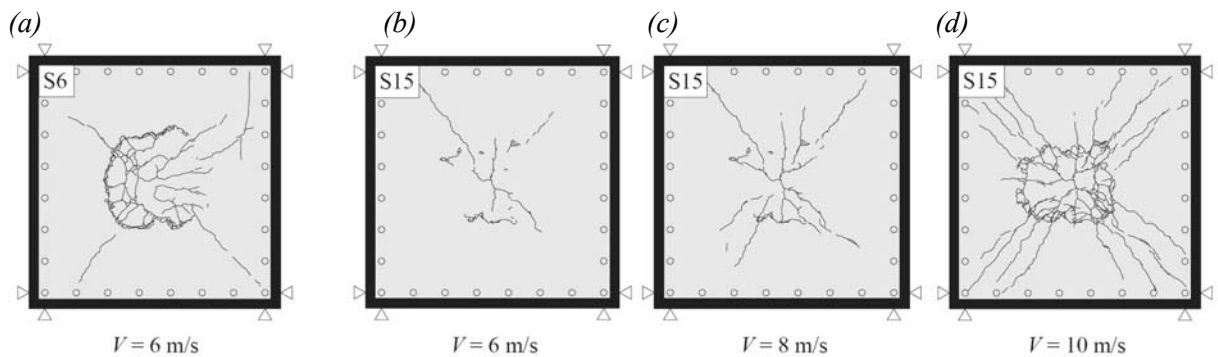


Figure 3-26: Crack pattern after the tests (a) S6, (b) S15-6, (c) S15-8 and (d) S15-10 [Kishi et al., 2008]

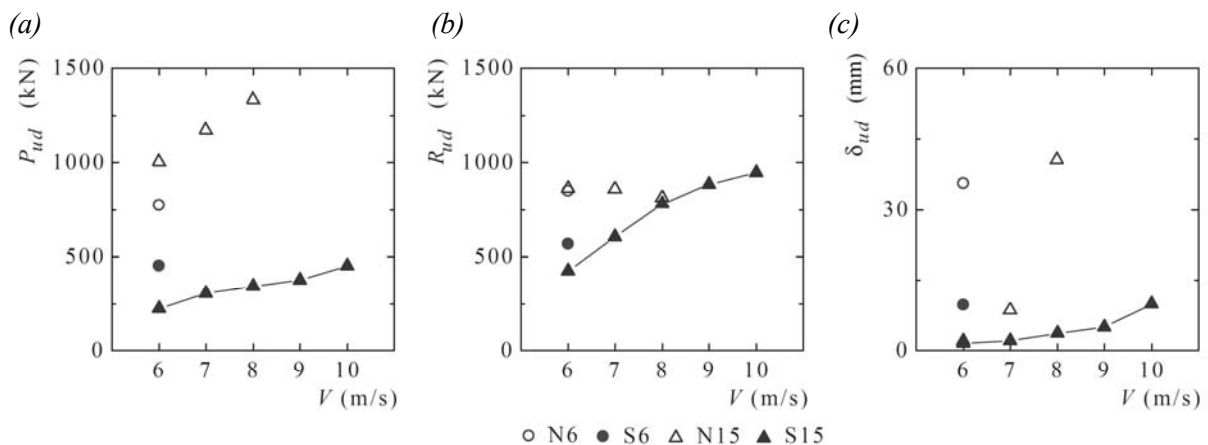


Figure 3-27: Test results (a) maximum impact forces (b) maximum reaction forces at the supports and (c) maximum displacement of the concrete slab [Kishi et al., 2008].

4. Analytical model

The dynamic process during rockfall impact on a protection gallery is a complex phenomenon. It includes not only geotechnical and structural dynamic aspects, but also includes soil-structure interaction. With regard to the dynamic impact load capacity of the reinforced concrete slab, bending and shear forces must be considered and they may depend on each other. A system of multiple degrees of freedom (SMDF) is proposed that can consider the behavior of the cushion layer, the local behavior (shear failure) and the global behavior (bending failure) at the same time. Modeling structures by masses and springs is a common way when dealing with dynamic analyses. This modeling type was widely used, especially before the era of numerical simulations, as one of the few “remaining” options for modeling. Engineers were accustomed to using their engineering judgment with regard to reasonable modeling assumptions.

Systems of multiple degrees of freedom are especially well suited to dealing with impact loads on structures, when the internal forces at predefined sections are needed, e.g. in the case of rockfall protection galleries for the determination of the reaction forces that are transferred from the slab to the columns or the forces acting between the cushion layer and the concrete slab.

Recent advances in numerical simulation methods (FE) are not necessarily a reason to reject the use of SMDF. Moreover, the advantages of both procedures should be combined. The advantage of SMDF is that due to the required simplifications a justified physical model has to be built and therefore the structural behavior of the system as a whole has to be understood. Numerical solutions enable the implementation of nonlinear properties to the SMDF, which analytically would mean an enormous increase in complexity. For the practical design of rockfall protection galleries, the use of finite elements is still too time consuming with regard

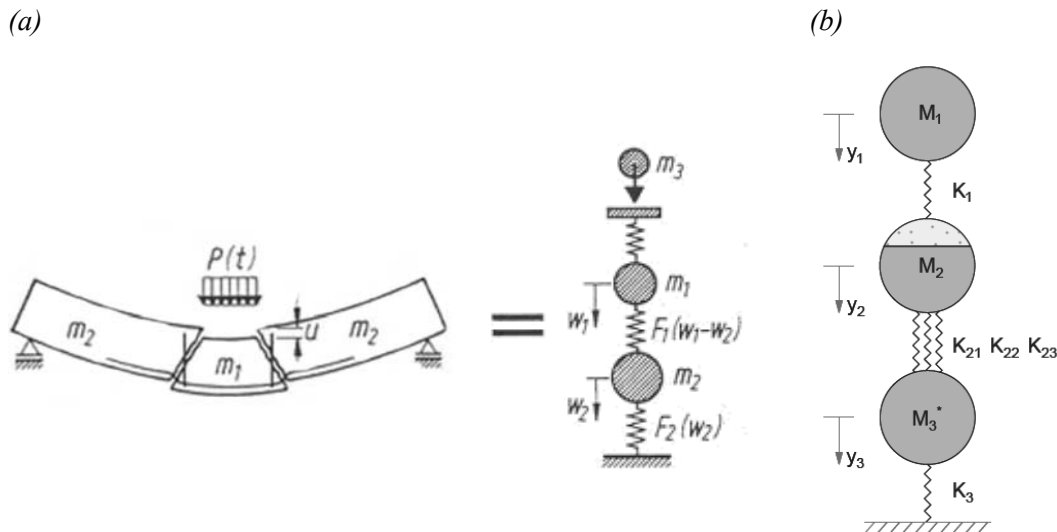


Figure 4-1: System of multiple degrees of freedom (a) for hard impacts [Eibl et al., 1988], (b) proposed for rock fall galleries

4. Analytical model

to assembling the meshes, etc. Moreover, due to the lack of calibration possibilities, the accuracy of such analyses is often uncertain. However, numerical simulations can be used for solving a nonlinear SMDF in the design procedure. But it is also much more convenient to use them in the evaluation process for the simplifying assumptions adopted within research projects or the development of guidelines.

Once the properties of the SMDF are defined, most engineers would be able to carry out a dynamic response analysis using numerical tools. Thus, recommendations for these properties are needed and could be provided by means of a design guideline. This procedure would be useful, not only for the design of new protection structures, but also for the verification of existing ones.

The chosen SMDF consists of three masses with the corresponding springs, similar to the model proposed for the analysis of aircraft collisions with reactor containments presented more than 20 years ago (Figure 4-1; Eibl et. al., 1988). For the application of this system for rockfall impact on galleries, the adequate selection of the different masses and the appropriate values for the stiffness of the springs have to be studied and investigated more precisely. Typical dimensions of the structures and loading characteristics are the main differences compared to the previous applications of this type of model. Basically, the analysis is confined to solving the equation of momentum (4-1), which due to nonlinearities and case differentiations can hardly be solved analytically.

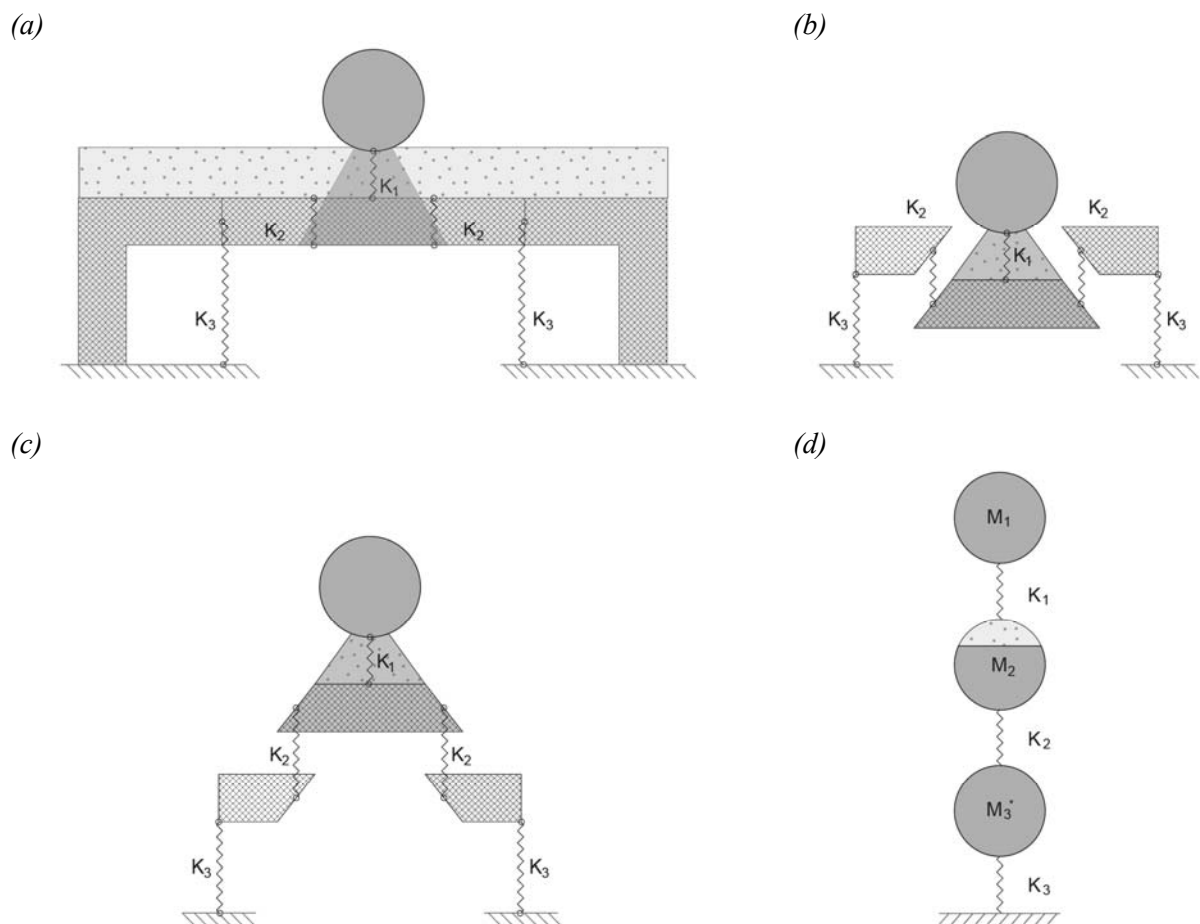


Figure 4-2: The three masses in a) the section of a gallery b) and c) intermediate steps and d) the SMDF

$$[M] \cdot \{\ddot{y}\} + [C] \cdot \{\dot{y}\} + [K] \cdot \{y\} = \{p\} \quad (4-1)$$

For the further analysis, the focus is set on the assignment of the masses and the definition of the spring properties, which are discussed in Section 4.1 and Section 4.2, respectively. In Section 4.3 the need for damping elements is discussed. The numerical solution is explained in Section 4.4 and illustrated in Appendix C. Section 4.5 describes the calculation and verification methods using the SMDF.

4.1. Assignment of the three masses

The SMDF consists of three masses as shown in Figure 4-2. The first mass M_1 is the mass of the impacting rock. The selection of the masses M_2 and M_3 has to correspond to the investigated failure mechanism for which the structure is designed. The section where shear failure is analyzed defines the theoretical masses M_2 and M_3 of the structure. M_2 corresponds to the mass of the assumed punching cone under the loading place and M_3 is the mass of the surrounding of the structure.

In addition to the concrete mass of the punching cone, the mass of the compacted soil between the impacting rock and the slab has to be included in M_2 . Therefore, the load distribution angles in the cushion layer and in the slab have to be determined first. However, the results of the model are relative insensitive to small changes of M_2 (see also Section 4.4). Nevertheless, a reasonable physical model for the definition of the distribution angle is required. Results from future investigations easily can be implemented into this model.

The load distribution angle in the cushion layer is set equal to the friction angle of the passive earth pressure ($45^\circ - \varphi/2$). For the concrete slab the angle is set to 45° . When questioning the recommendation for the design of nuclear reactors for aircraft collisions [KTA 2203 (1983)], Schlüter showed that the angle of $\beta = 57.5^\circ$ for the punching cone proposed therein was not satisfactory [Schlüter (1987)]. In KTA 2203 this value was chosen, based on static evaluations of flat slabs. An angle of 45° would be more appropriate.

Simplifying the frustums to cylinders as shown in Figure 4-3b), M_2 can be determined using Equations (4-2) and (4-3). This simplification with the cylinder is justified since it produces an insignificant error that can be quantified by Equation (4-4).

$$M_2 = \pi \cdot \left[(e - p_{\max}) \cdot \gamma_g \left(\frac{\emptyset_b + \emptyset_{sl}}{4} \right)^2 + d \cdot \gamma_c \cdot \left(\frac{\emptyset_{sl} + z}{2} \right)^2 \right] \quad (4-2)$$

with

$$\emptyset_{sl} = \emptyset_b + 2 \cdot \left[(e - p_{\max}) \tan \left(45^\circ - \frac{\varphi}{2} \right) \right] \quad (4-3)$$

$$\frac{M_{2,frustum}}{M_{2,cylinder}} = \frac{4}{3} \cdot \left(1 - \frac{r_1 \cdot r_2}{(r_1 + r_2)^2} \right) \quad (4-4)$$

4. Analytical model

Thereby are:

- \varnothing_{sl} diameter of loading area on the slab
- \varnothing_b diameter of loading area on the cushion layer
- z lever arm of internal forces in the concrete slab
- d thickness of the concrete slab
- e thickness of the cushion layer
- p_{\max} maximum penetration
- γ_c density of concrete
- γ_g density of the cushion material
- φ angle of internal friction
- $r_{1,2}$ upper and lower radius of a frustum

A more detailed evaluation of M_2 is performed when discussing the spring properties of the cushion layer (Section 4.2.1). The mass of the soil in that case corresponds to the soil cone with an angle equivalent to the passive earth pressure and therefore, the mass of the punching cone needs to be decreased in case premature punching failure occurs before the angle of passive earth pressure is reached.

Mass M_3 governs the global behavior of the gallery. It corresponds to the part of the structure that is not included in M_2 . For the following reason the mass of the cushion layer is not included in M_3 : For the design, the first oscillation of the structure is relevant because the system then yields the highest stresses. During this oscillation, accelerations in the slab of the structure are significantly higher than g , causing the cushion layer to separate from the concrete slab. This phenomenon was clearly observed during the large-scale tests (refer to Chap. 3.3).

Mass M_3 has to be reduced to the modal mass M_3^* according to the confining boundary conditions. M_3^* is defined such that the kinetic energy of the oscillating concentrated mass is equal to the kinetic energy of the oscillating slab (see Equations (4-5) to (4-8)). It is assumed, that the velocity distribution $v(x, z)$ in the slab is affine to its static deformation. For beams, α is around 0.8 in the elastic range and decreases to 0.33 for the assumption of a plastic hinge in mid span and neglecting the elastic deformations [CEB, 1988].

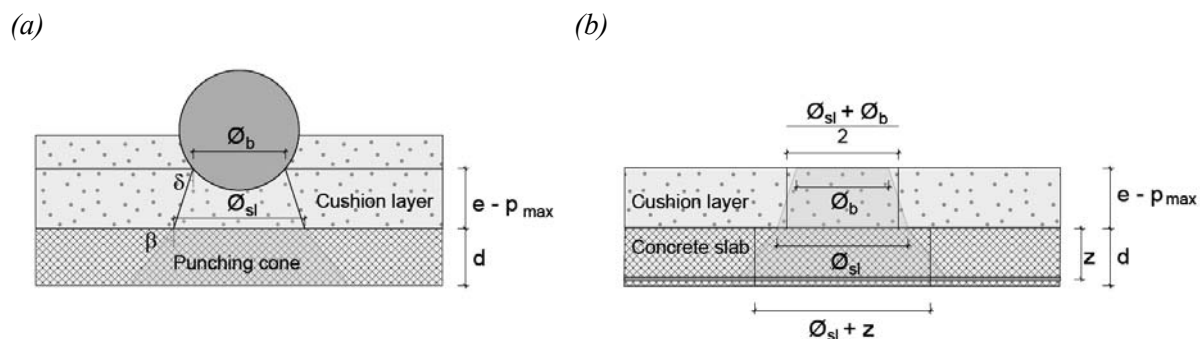
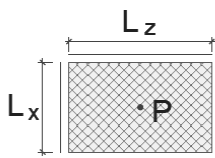
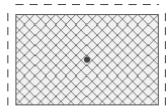
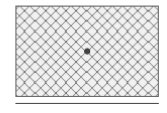
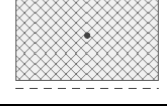


Figure 4-3: Geometry of punching cone

Table 4-1: Mass factor α for different boundary conditions and centric load [Biggs, 1964].

Boundary conditions		Mass factor α [-]			
		Elastic		Plastic	
		Ratio of spans L_x/L_z	0.6	0.8	1.0
4 restrained			0.29 0.23	0.25 0.20	0.21 0.17
4 lines			0.39 0.23	0.35 0.20	0.31 0.17
2 restrained				0.37 0.33	
1 line 1 restrained				0.43 0.33	
2 lines				0.49 0.33	

$$\frac{1}{2} M_3^* \cdot \dot{y}_3^2 = \frac{1}{2} \frac{M_3}{A} \cdot \iint_A v^2(x, z) \cdot dxdz \quad (4-5)$$

$$M_3 = L_x \cdot L_z \cdot d \cdot \gamma_c \quad (4-6)$$

$$M_3^* = \alpha \cdot M_3 - M_{2sl} \quad (4-7)$$

$$M_{2sl} = \pi \cdot \left(\frac{\varnothing_{sl} + z}{2} \right)^2 \cdot d \cdot \gamma_c \quad (4-8)$$

Thereby:

- y_3 displacement of mass M_3 in the SMDF
- A surface of concrete slab
- v velocity distribution of the concrete slab

The modal mass M_3^* can also be calculated using the factor α as shown in Equation (4-7). The mass factor α for common geometries and boundary conditions is given in Table 4-1. The values are taken from [Biggs, 1964] or [Bachmann et al., 1995].

For the equation of momentum (4-1), the mass matrix is now fully defined by the three masses as shown in Equation (4-9).

$$[M] = \begin{bmatrix} M_1 & 0 & 0 \\ 0 & M_2 & 0 \\ 0 & 0 & M_3^* \end{bmatrix} \quad (4-9)$$

4.2. Spring properties

The stiffness matrix for the gallery is described by three nonlinear springs K_1 , K_2 and K_3 (Equation (4-10)). K_1 describes the properties of the cushion layer, K_2 describes the shear behavior of an assumed critical section and K_3 describes the bending stiffness of the global system (illustrated in Figure 4-2).

$$[K] = \begin{bmatrix} K_1 & -K_1 & 0 \\ -K_1 & K_1 + K_2 & -K_2 \\ 0 & -K_2 & K_2 + K_3 \end{bmatrix} \quad (4-10)$$

4.2.1. Properties for the cushion layer

The cushion layer has been the focus of the latest research projects related to rockfall impacts on galleries [Montani, 1998], [Chikatamarla, 2006]. However, values for spring properties (K_1) applicable to the type of simplified model used herein have not yet been quantified. In the following the hardening soil behavior of the cushion layer is approximated by a hyperbola (Figure 4-4). This mathematically simple curve is defined by a vertical asymptote, where the soil reaches complete compaction and by an initial value K_{10} . During impact the soil particles cannot be pressed out of the space between the impacting rock and the slab due to the lateral pressure from the surrounding soil. This results in a maximum possible compaction of the cushion layer and consequently in a maximum penetration p_{\max} of the rock into the cushion layer.

The values for the spring stiffness at any time during the impact can be expressed as the ultimate limit state for the cushion layer according to an extension of Terzaghi's formulation considering the limited soil depth. In general, the soil behavior can be described assuming that during the initial phase of impact its behavior is similar to a triaxial compression test and at the end it is similar to an oedometer sample. For the sake of simplicity, development of the transferred forces with penetration depth is expressed in the term K_1 .

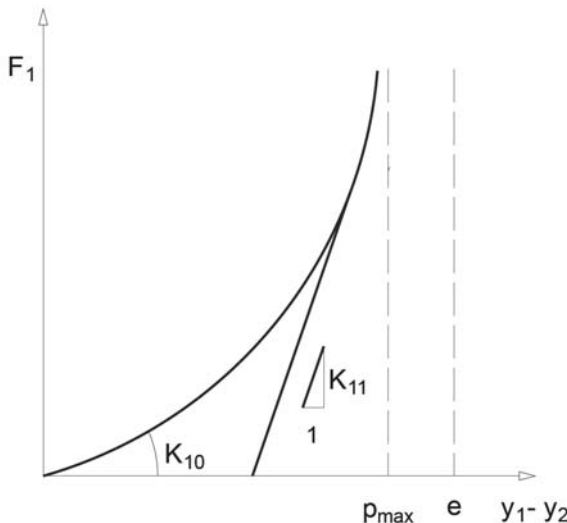


Figure 4-4: Spring properties of K_1 for the cushion layer

$$K_1 = K_{10} \cdot \left(1 - \frac{y_1 - y_2}{p_{\max}}\right)^{-1} \quad (4-11)$$

Thereby, the initial value K_{10} and the maximum possible penetration p_{\max} are functions of the soil parameters (i.e. compression modulus M_E and angle of internal friction φ) as well as functions of the structure's geometry including the loading surface A and the thickness of the cushion layer e .

$$K_{10} = f(M_E, A, e) \quad (4-12)$$

$$p_{\max} = f(A, e) \quad (4-13)$$

$$K_{11}(y_1 - y_2) = K_1(y_1 - y_2)_{\max} \quad (4-14)$$

For unloading, the spring stiffness changes from K_1 to K_{11} . K_{11} expresses the maximum stiffness that was reached during loading, Equation (4-14). The gradual increase of the stiffness K_1 in combination with the stiff unloading (K_{11}) results in a loss of potential energy in the spring. This loss simulates some of the dissipated energy within the cushion layer.

Looking at the actual impact on the cushion layer in more detail, the failure mechanism can be assumed to occur as described below (Figure 4-5):

- a) A soil cone develops due to the sliding surface built by the passive earth pressure from the rock. The cone has a load distribution angle $\delta = -(45^\circ - \varphi/2)$.
- b) The cone is pushed towards the slab and with the increase of the passive earth pressure the adjacent soil displaces laterally causing a failure mechanism similar to that associated with bearing capacity.
- c) The tip of the cone reaches the slab and the soil is compacted while the angle of load distribution increases with further compression.
- d) The distribution angle reaches the angle of passive earth pressure and the soil is compacted until complete compaction is reached.

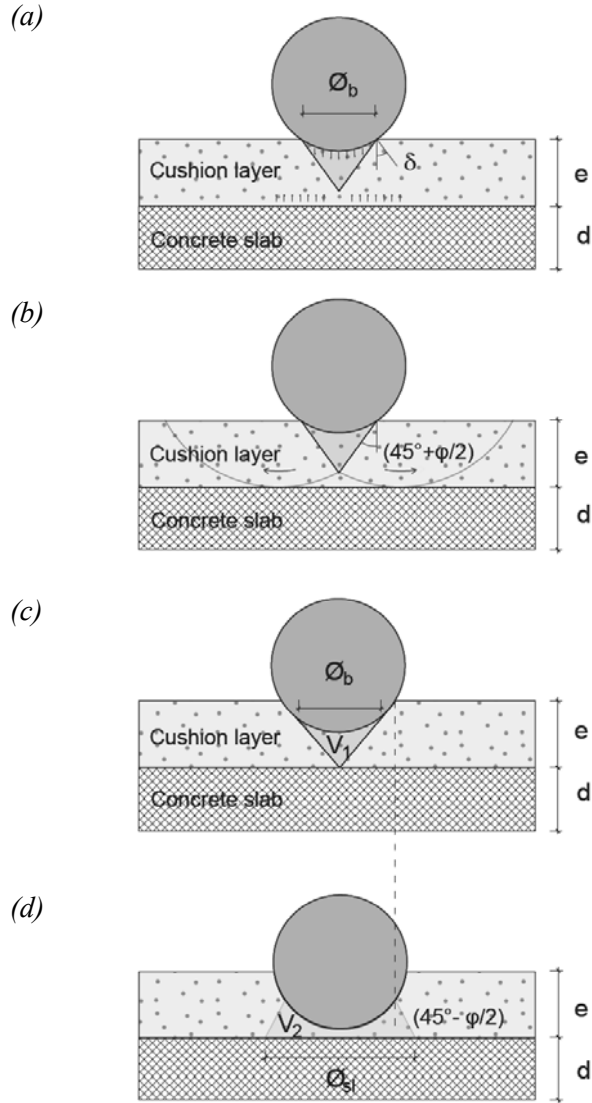


Figure 4-5: Building mechanism of the load distribution cone in the cushion layer

Assuming that the volume of the compacted active cone V_2 is equal to the volume of the passive cone V_1 , a geometrical relationship and consequently the maximum possible penetration can be determined.

$$V_1 = \frac{\pi \cdot \Ø_b^3}{24} \tan\left(45 + \frac{\varphi}{2}\right) \quad (4-15)$$

$$V_2 = \frac{\pi \cdot h}{3} \left(\frac{\Ø_{sl}^2 + \Ø_{sl}\Ø_b + \Ø_b^2}{4} \right) \quad (4-16)$$

$$p_{max} = e - h \quad (4-17)$$

Furthermore, for the described stages different load displacement characteristics can be applied. This model also allows predicting a possible premature punching failure, before maximum load distribution through the cushion layer is reached. This premature failure

depends on the time development of the loading area and the transmitted force. The resulting smaller mass M_2 of the punching cone has also to be taken into account.

4.2.2. Properties for punching behavior

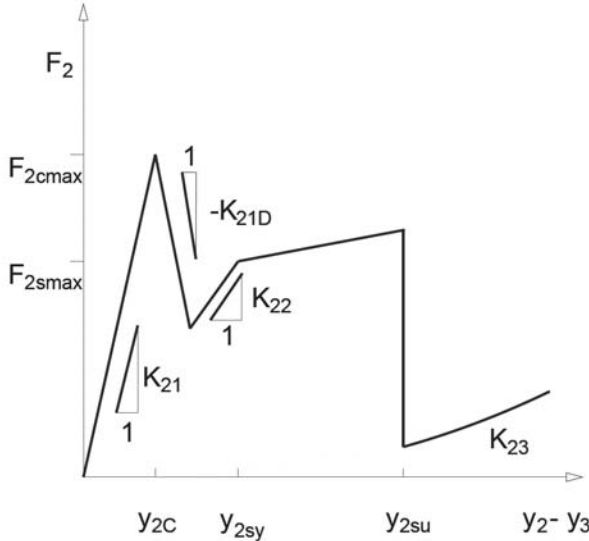


Figure 4-6: Spring properties of K_2 for the shear behavior

The spring K_2 describes the shear stiffness for the assumed shear failure of the concrete slab. With increasing relative displacements of the punching cone compared to the surrounding part of the slab, the behavior is controlled by three contributors and can therefore be substituted by three parallel springs loaded on tension:

- K_{21} : the contribution of the concrete [Schlütter, 1987],
- K_{22} : the contribution of shear reinforcement if provided and
- K_{23} : a membrane effect that acts according to the anchorage of the bending reinforcement.

These three components are illustrated in Figure 4-6 and can be formulated as shown in Equations (4-18) to (4-22).

$$K_{21} = E_c \pi (z + \emptyset_{sl}) \quad \text{for} \quad (y_2 - y_3) \leq y_{2c} = \frac{z f_{ctm}}{E_c} \quad (4-18)$$

$$K_{21D} = -E_D \pi (z + \emptyset_{sl}) \quad \text{for} \quad (y_2 - y_3) > y_{2c} = \frac{z f_{ctm}}{E_c} \quad (4-19)$$

$$K_{22} = \frac{A_{sw} E_s}{l_w} \approx \frac{A_{sw} E_s}{z} \quad \text{for} \quad (y_2 - y_3) \leq y_{2sy} = \frac{l_w f_s}{E_s} \quad (4-20)$$

$$F_2 = F_{2s\max} = f_s A_{sw} \quad \text{for} \quad (y_2 - y_3) \geq y_{2sy}. \quad (4-21)$$

$$K_{23} = \frac{M_b}{z s_w} \quad (4-22)$$

4. Analytical model

Where,

- f_{ctm} average tensile strength of concrete
- f_s yield strength of reinforcing steel
- E_c average modulus of elasticity of concrete
- E_D average modulus of elasticity of concrete for softening after cracking in tension
- E_s average modulus of elasticity of steel
- l_w anchored length of stirrups
- A_{sw} cross-sectional area of stirrups
- s_w spacing of stirrups
- M_b local bending moments

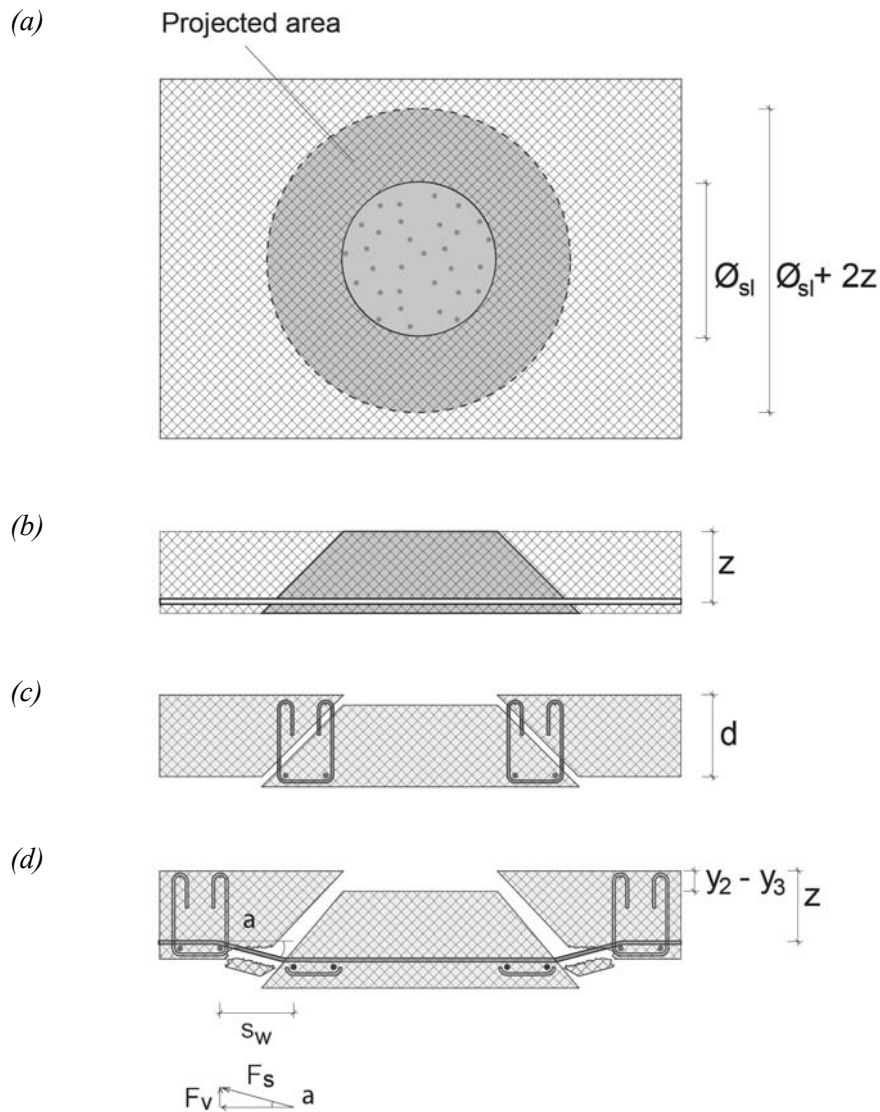


Figure 4-7: Modeling of punching failure a) top view; Contributions of b) concrete section, c) shear reinforcement and d) membrane effect of bending reinforcement.

The transition behavior between K_{21} and K_{22} has an important influence on the response of the system of multiple degrees of freedom. With a sudden decrease of the loads transmitted between the punching cone and the rest of the structure after concrete cracking, the global loading is reduced by a large amount. Therefore, after reaching concrete cracking two issues have to be taken into account. First, the softening of the concrete in tension after cracking governed by the cracking energy and second, a maximum unloading rate governed by the time that the cracks need to develop through the concrete section.

In these two aspects, a displacement-determined and a time-determined component have to be combined. The displacement-determined part is taken into account by the fictitious cracking model [Marti et al., 1999]. The softening behavior is related to the amount of elastic energy released in the concrete member G_F and is defined by Equation (4-24). For normal concrete with values of $E_c = 30 \text{ kN/m}^2$, $G_F = 100 \text{ J/m}^2$ and $f_{ct} = 3$ and 4 N/mm^2 , a critical length of the concrete member z_{cr} is about 350 or 650 mm and the denominator in Equation (4-24) becomes zero. For longer members, a snap back behavior is given, when more elastic energy is released than can be dissipated in the crack.

$$\sigma = -E_D \cdot \varepsilon \quad (4-23)$$

$$E_D = \frac{E_c f_{ctm}^2 z}{2E_c G_F - f_{ctm}^2 z} \quad (4-24)$$

From a dynamic point of view, an increased tensile strength f_{ctmd} is used in Equation (4-24) instead of f_{ctm} due to higher strain rates. For f_{ctmd} , Equation (4-25) is used as a simplification. The increase factor of 54% given in [Schmidt-Hurtienne, 2001] for a strain rate $\dot{\varepsilon} = 10^0$ is used for linearized logarithmic behavior with negligible influence for $\dot{\varepsilon} = 10^{-5}$. The modulus of elasticity E_c is assumed to be strain rate independent.

$$f_{ctmd} = f_{ctm} \cdot \left(1 + 0.54 \left(\frac{\log \dot{\varepsilon} + 5}{5} \right) \right) \quad (4-25)$$

The rapid decrease of the forces transmitted to the concrete F_{21d} , as it is the case for high values of E_D , is dynamically limited by the velocity v_{cg} of crack development; the time-determined component. An estimation of the theoretical crack velocity is based on associating the surplus of released energy (release from elastic deformation G minus the crack growth resistance R) with the kinetic energy of the opening elements behind the crack tip. Three simplifying assumptions are used [Broek, 1986]:

- Crack propagation takes place under constant stress
- The elastic energy release rate is independent of the crack speed
- The crack growth resistance R is constant

A limiting crack velocity appears to be about 0.38 times the velocity of longitudinal waves and measured crack velocities are well below the theoretical value:

$$v_{cg} \approx 0.38 \sqrt{\frac{E_c}{\gamma_c}} \quad (4-26)$$

$$t_{cg} \approx \frac{z}{0.38} \sqrt{\frac{2 \cdot \gamma_c}{E_c}} \quad (4-27)$$

4. Analytical model

Assuming that the crack length is the reference envelope line of the punching cone and neglecting three-dimensional effects, a crack growth time t_{cg} is defined in Equation (4-27). A linear transition function ξ is used to reduce K_{21} for the calculation of the force F_{21cg} in the case that the crack growth time is decisive.

$$\begin{aligned}\xi &= 0 && \text{for } t < t_0 \\ \xi &= \frac{t - t_0}{t_{cg}} && \text{for } t_0 < t < t_{cg} \\ \xi &= 1 && \text{for } t > t_{cg}\end{aligned}\quad (4-28)$$

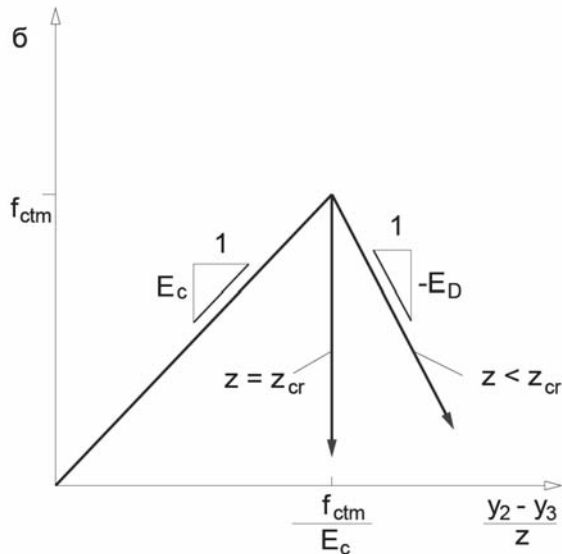
$$F_{21cg} = (y_2 - y_3)_{(t)} K_{21}(1 - \xi_{(t)}) \quad (4-29)$$

$$F_{21d(t)} = F_{21d(t-1)} + \Delta F_{21d} \quad (4-30)$$

$$\Delta F_{21d} = -\Delta(y_2 - y_3) \cdot K_{21D} \quad (4-31)$$

$$F_{21(t)} = \max(F_{21d(t)}, F_{21cg}) \quad (4-32)$$

(a)



(b)

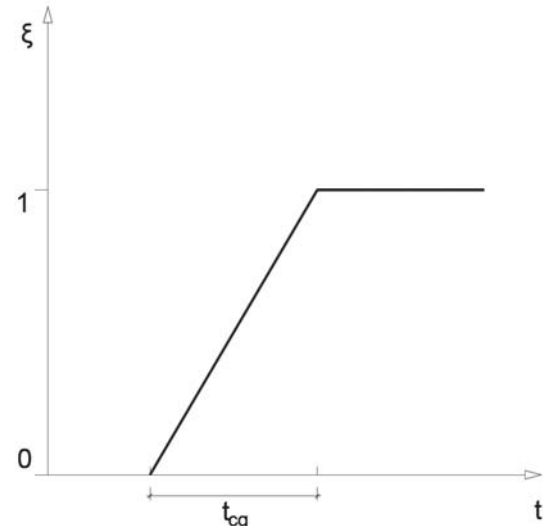


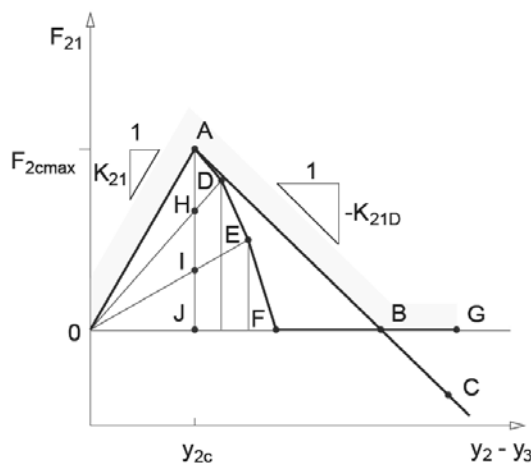
Figure 4-8: (a) Stress-strain relation of concrete in tension, (b) transition function

Numerically, both conditions (displacement and crack growth determined) can be achieved by selecting the higher value of F_{21d} or F_{21cg} in each time step, see Equation (4-32). Figure 4-9a shows the softening behavior of the concrete after having reached the dynamic tensile strength in Point A for both conditions: The displacement-determined behavior $F_{21d(t)}$ is given by the path ABC. The crack growth determined behavior F_{21cg} is given by the path ADEFG. With Equation (4-28) the linear transition function ξ reduces the stiffness and therefore divides line AJ into n equal parts, which are drawn for example with $n = 3$ in Figure 4-9 (AH, HI and IJ).

$$n = \frac{t_{cg}}{\Delta t} \quad (4-33)$$

After n integration steps, with $\xi = 1$ the stiffness K_{21} vanishes. Hence, F_{21cg} does not become negative and the graph continues along line FG.

(a)



(b)

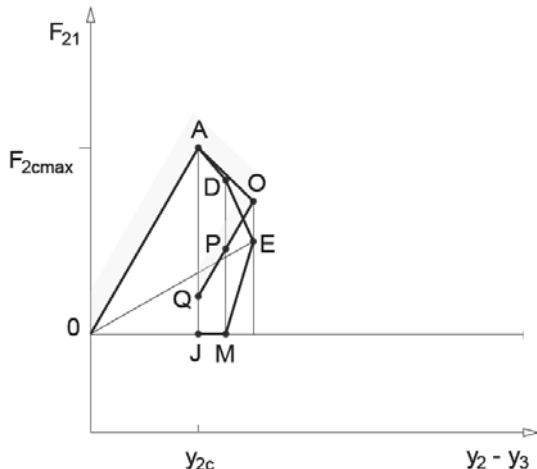


Figure 4-9: (a) Concrete behavior after cracking, (b) for unloading after cracking

For thicker slabs with a larger static depth corresponding to the length of the model concrete member in tension, the decrease (AB) is stronger and point B could be placed between the origin and point F. Consequently, only the crack growth time would determine the softening behavior. In the case shown in Figure 4-9a), the decisive line is 0ADB.

For unloading during the softening period the behavior is shown in Figure 4-9b). Assuming that unloading starts at point E, the crack growth time determined behavior follows line EM and MJ, because the stiffness of the next step is zero. For the displacement-determined path, unloading from point O would be parallel to 0A, hence OPQ.

4.2.3. Properties for bending behavior

The third spring K_3 describes the global stiffness of the concrete slab. The stiffness can be defined according to Equation (4-34). The stiffness factor k_w takes into account the ratio of the slab spans (L_x to L_z) as well as the boundary conditions [Stiglat et al., 1993].

$$K_{30} = \frac{k_w E_c z^3}{12 L_z^2} \quad (4-34)$$

The present study concentrates on impacts at mid span of the rockfall galleries. In [Sato et. al., 1999] the impact at mid span as well as close to the column of a rockfall gallery is compared. In a $\frac{1}{4}$ -scaled model test, the impact at mid span was found to be the governing one for the design. The stiffness factor k_w , though can be determined for other impact locations as well. The impact location has a strong influence on the global stiffness according to the deformation capacity of the structure. Finite element models are useful for performing parametric studies in order to recommend appropriate values.

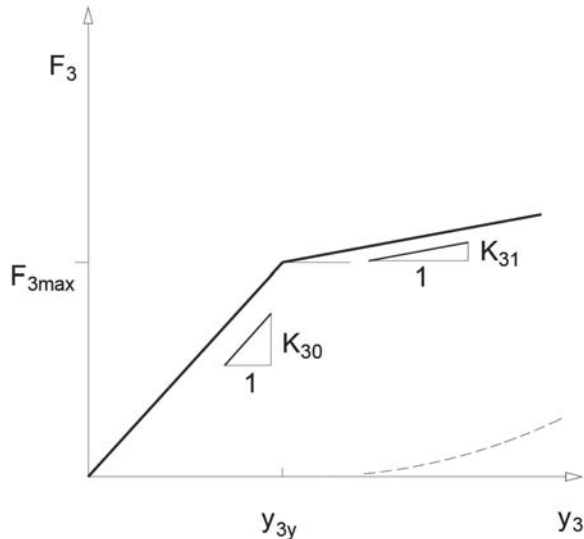


Figure 4-10: Spring properties of K_3 for the global bending stiffness.

As discussed in Section 5.1, in Equation (4-34) the static depth z is replaced by the slab thickness d , and Equation (5-2) should be used.

Plastic deformations of the slab have a large influence on the response of the system. These deformations are large in the global response in comparison to the relative displacements of the other masses and unload the springs K_1 and K_2 . This means that the yielding force has to be determined as accurately as possible. An overestimation of the yielding forces is on the safe side for the design, because the forces in the springs reach higher values. Thus the loads for punching as well as for bending are higher. Using the yield line theory [Johansen, 1962] for the upper limit state, the design procedure eliminates an unsafe load prediction. For different boundary conditions the ratio P_u/m_u is given such that the configuration of the yield

Table 4-2: Stiffness factor k_w for loading in the center [Stiglat et al., 1993]

Boundary conditions	Stiffness factor k_w [-]				
	1.4	1.2	1.0	0.8	0.6
2 restrained	122	121	117	109	89
1 line 1 restrained	87	84	79	70	58
2 lines	49	46	41	35	27
4 points				21.6	

lines is linked with the load carrying capacity of the structure.

For Table 4-3 the unit ultimate moments are used as shown in Equation (4-35). For both slab direction, the ratio of positive to negative ultimate moments is assumed to be the same.

$$m_{ux} = m_u$$

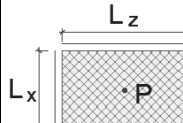
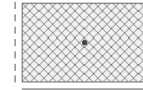
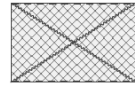
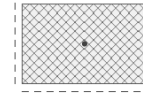
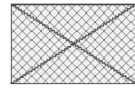
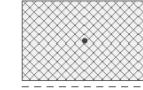
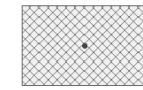
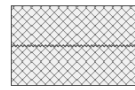
$$m_{ux}' = \lambda' \cdot m_{ux} \quad (4-35)$$

$$m_{uz} = \lambda_z \cdot m_u$$

$$m_{uz}' = \lambda' \cdot m_{uz}$$

Depending on the required degree of detailing of the system, a membrane effect of the slab can be added, which is shown in Figure 4-10 with the dashed line.

Table 4-3: Ratio ultimate load to ultimate unit moment for different boundary conditions

Boundary conditions	Yield lines	P_u/m_u [-]					
		for: $\lambda_z = \lambda' = 1$					
		0.6	0.8	1.0	1.2	1.4	
4 restrained	 	$4(\lambda' + 1) \left(\frac{L_x}{L_z} + \lambda_z \frac{L_z}{L_x} \right)$	18.13	16.4	16	16.4	18.13
2 lines 2 restrained	 	$4 \left(\frac{L_x}{L_z} + \lambda_z (\lambda' + 1) \frac{L_z}{L_x} \right)$	15.73	13.2	12	11.47	11.31
4 lines	 	$4 \left(\frac{L_x}{L_z} + \lambda_z \frac{L_z}{L_x} \right)$	9.07	8.2	8	8.2	9.07
2 restrained	 	$4 \lambda_z \frac{L_z}{L_x} (\lambda' + 1)$	13.33	10	8	6.67	5.71
1 line 1 restrained	 	$2 \lambda_z \frac{L_z}{L_x} (\lambda' + 2)$	10	7.5	6	5	4.29
2 lines	 	$4 \lambda_z \frac{L_z}{L_x}$	6.67	5	4	3.33	2.86
1 line 2 points	 	$4 \left(\frac{L_x}{L_z} + \lambda_z \frac{L_z}{L_x} \right)$	9.06	8.2	8	8.2	9.06
4 points	 	$4 \lambda_z \frac{L_x}{L_z}$	2.40	3.20	4.00	-	-

4.3. Damping elements

For the impact capacity evaluation of rockfall galleries, the first or at most the first two load peaks are relevant. Thus, for practical applications the damping properties of the structure are of minor importance. However, the damping within the cushion layer plays a decisive role, since it reduces the amount of energy that is transmitted to the structure. The damping properties of different cushion layers were focused on in [Chikatamarla 2006]. In his thesis, Chikatamarla used an equivalent damping coefficient c_1 , which is based on the dynamic stiffness of soil according to the cone model described in [Wolf et al., 2003].

$$c_1 = \gamma_g \cdot v_p \cdot A \quad (4-36)$$

With:

- c_1 : damping coefficient for cushion
- γ_g : density of cushion layer
- v_p : compression wave propagation velocity
- A : loading area

For gravel the wave propagation velocity is estimated to be between 400 and 800 m/s. For normal sizes of rock blocks the loading area could be in the range of about 1 or 2 m². With a density of 20 kN/m³, the damping coefficient would be in the range of 2 MNs/m.

In [Montani, 1998] a velocity of the wave propagation for gravel is given as $v_p = 150$ m/s. With $\gamma_g = 17$ kN/m³ and loading areas $A = 0.38$ and 1.12 m² for the small (800 kg) and the large (4'000 kg) boulders in large-scale tests, respectively, the damping coefficient c_1 results in 970'000 and 2'860'000 Ns/m. For the punching tests c_1 is 7'200 Ns/m and 45'000 Ns/m for the diameter of loading area $\mathcal{O}_b = 60$ and 150 mm, respectively.

Although damping effects are not of great importance for the analysis of rockfall impacts, damping elements are implemented in the model in order to improve numerical stability. In the concrete, damping parameters can be deduced mainly from the material damping. Therefore damping ratios of $\zeta_2 = 5\%$ or $\zeta_3 = 20\%$ are taken for the local and the global behavior, respectively, and are based on recommendations given in [Goshi, 1990].

With Equations (4-37) and (4-38) the damping matrix is now fully defined for the equation of momentum (4-1).

$$c_2 = 2 \cdot \zeta_2 \cdot \frac{M_2}{T_2} \quad (4-37)$$

$$c_3 = 2 \cdot \zeta_3 \cdot \frac{M_3^*}{T_3} \quad (4-38)$$

$$[C] = \begin{bmatrix} C_1 & -C_1 & 0 \\ -C_1 & C_1 + C_2 & -C_2 \\ 0 & -C_2 & C_2 + C_3 \end{bmatrix} \quad (4-39)$$

4.4. Numerical integration

The equation of momentum (4-1) is determined by the masses, springs and damping elements as described in the previous sections. Five sub-steps are used to analyze the new displacements, velocities, accelerations and spring forces for the following time step.

These steps are as follows and are illustrated in Figure 4-11:

1. The new displacements $y_{(t+1)}$ are calculated from all old values
2. The new state of the springs and their stiffness $K_{(t+1)}$ is determined by the new displacements $y_{(t+1)}$
3. The new spring forces $F_{(t+1)}$ or the new force increments $\Delta F_{(t+1)}$ are determined
4. The new accelerations $a_{(t+1)}$ are calculated from the spring forces $F_{(t+1)}$
5. The new velocities $v_{(t+1)}$ are calculated from all old values

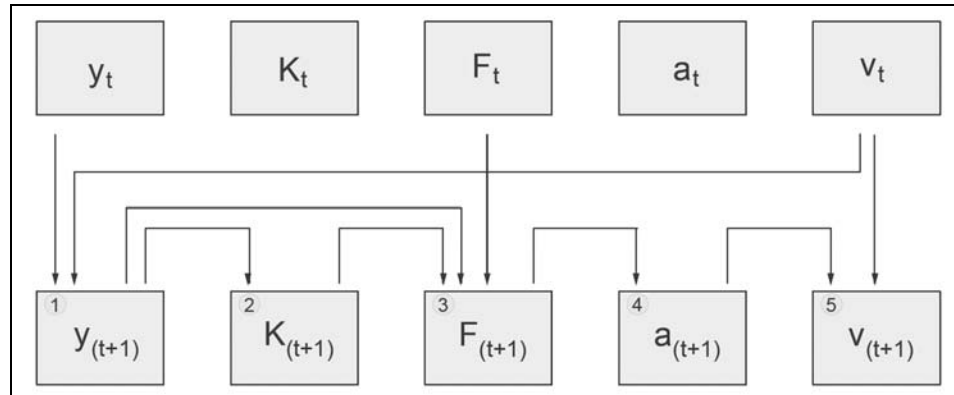


Figure 4-11: Scheme for calculating the next time step

All equations to describe these steps are listed in Appendix C and solved by means of an Excel spread sheet shown in Appendix D. In comparison to more sophisticated finite element models computation time is small. Time increments therefore can be made very small ($\Delta t < 0.1$ ms) compared to the loading time ($TF_1 \approx 12$ ms). The short time increments also allow for the use of simplified integration without compromising convergence.

$$y_{i(t+1)} = y_{it} + v_{it} \cdot \Delta t \quad (4-40)$$

$$v_{i(t+1)} = v_{it} + \Delta t \cdot a_{i(t+1)} \quad (4-41)$$

FE solutions offer an alternative way of obtaining the force-time history of the springs. The requirement for the program is to carry out a dynamic analysis with non-linear material properties. The model can be built up with three beam elements (one element for each spring) and three concentrated masses. The cross-sectional area to beam length ratio is set according to the desired stiffness.

4.5. Calculation and verification methods

The time histories of the spring forces result from the equations of motion with the given masses and spring properties described above. The peak loads are performance based results and can be compared to the resistance in the critical sections of the slab.

Compared to a static loading, the inertia forces of the different system parts are the largest deviations and they are included in the formulated SMDF. For the resistance, the static values can be applied; however they should be increased by a factor according to the strain rate. Rockfall impact with typical loading times in the range of 10 to 30 ms can lead to maximum strain rates of about 10^{-1} s^{-1} in the concrete and 5 s^{-1} in the reinforcing steel, respectively. Therefore, the concrete compressive strength and the steel tensile strength can be increased by about 20% and 5%, respectively [Goshy, 1990].

Failure criteria for punching as well as for bending failure have to be used in order to verify the section. No safety factors can be applied on the maximum forces of the model to perform a conventional design, since the new sections would lead to other spring forces. Therefore the maximum forces need to be recalculated after each change of dimensions. Instead of safety factors, relative values η_2 and η_3 are recommended for the evaluation of punching and bending failure, respectively.

$$\eta_2 = \frac{F_{2\max}}{F_{2c}} \quad (4-42)$$

$$\eta_3 = \frac{F_{3\max}}{F_{3y}} \quad (4-43)$$

For punching, F_{2c} is the ultimate punching force and defined by a critical dynamic strain of the concrete over the section of failure.

For bending, the prediction of the yield loading F_{3y} plays an important role, since the plastic deformations of the structure allow for the dissipation of a large amount of the kinetic energy and also decrease the local punching load. The upper bound solution is therefore on the safe side. Analogically, it is on the safe side to overestimate the strengthening of the global stiffness after yielding.

A ductility factor χ could be applied when assuming an ideal elastic plastic behavior of the global response. But due to the hardening behavior, it is not appropriate to limit the global response by deformation, because then the ultimate load is overestimated. Instead, the maximum force has to be limited. The increase of this force would be proportional to the increase of the bending moment due to post-yield hardening. Depending on the applied reinforcement steel it could be an increase of between 5% and 25%. A lever arm increase for the internal forces due to plasticization of the concrete can be neglected, since its influence is in the range of about 1%. The gallery latest reaches its load bearing capacity when η_3 reaching 1.3 and bending failure has to be expected definitely. Assuming that the hardening factor is not underestimated, this procedure is on the safe side.

5. Calibration of the model

The analytical model proposed in the previous section contains physically justified parameters only, i.e. no empirical or semi-empirical elements were implemented. However, the output of the model has to be verified using the test results. The model may need to be calibrated by means of the results because the input values still contain simplifications and uncertainties.

In the following sections, in order to calibrate the global response, the output of the model is compared to the reaction forces gained from the large-scale test introduced in Section 3.3. The predictions of shear loads and punching failure are evaluated for a test series introduced in Section 3.4 carried out at Muroran Institute of Technology. Then the influence of the input parameters on the model results is evaluated in a sensitivity analysis (see Section 5.3).

5.1. Global response

For the calibration of the model, series B of the large-scale tests (see Chapter 3.3) is chosen. The agreement is investigated by comparing the spring force F_3 with the total reaction force determined experimentally.

All input values are listed in Appendix D. For the first selection, mass factor α and stiffness factors k_w are set as follows:

- $\alpha = 0.8$, as the value for a beam in the elastic range.
- $k_w = 17$, as an extrapolation from the values 58 and 27 for one line support and one restrained support or for two line supports, respectively (see Table 4-2).

For the damping coefficient in the cushion layer a low value of 4000 Ns/m is defined. The concrete damping ratios ζ_2 and ζ_3 are set to 5%. The initial stiffness of the cushion layer K_{10} selected in the range of 50'000 kN/m, provides reasonable results. In a first simplification K_{10} is assumed to be proportional to the M_v values, as measured by the dynamic light drop weight device, e.g. $K_{10} = 48'000 \text{ N/mm}^2$ for B1, $K_{10} = 52'000 \text{ N/mm}^2$ for B2, etc. (see Table 3-6).

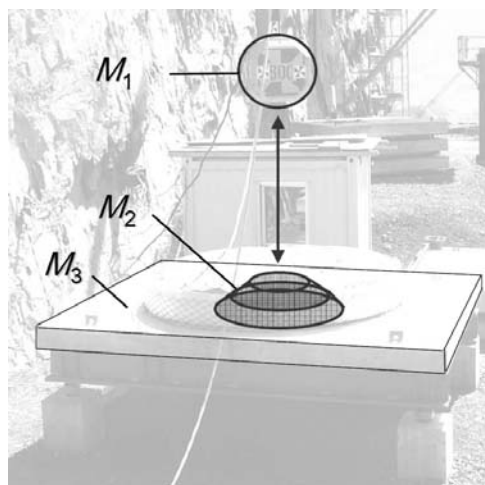


Figure 5-1: Assignment of masses for the large-scale tests

5. Calibration of the model

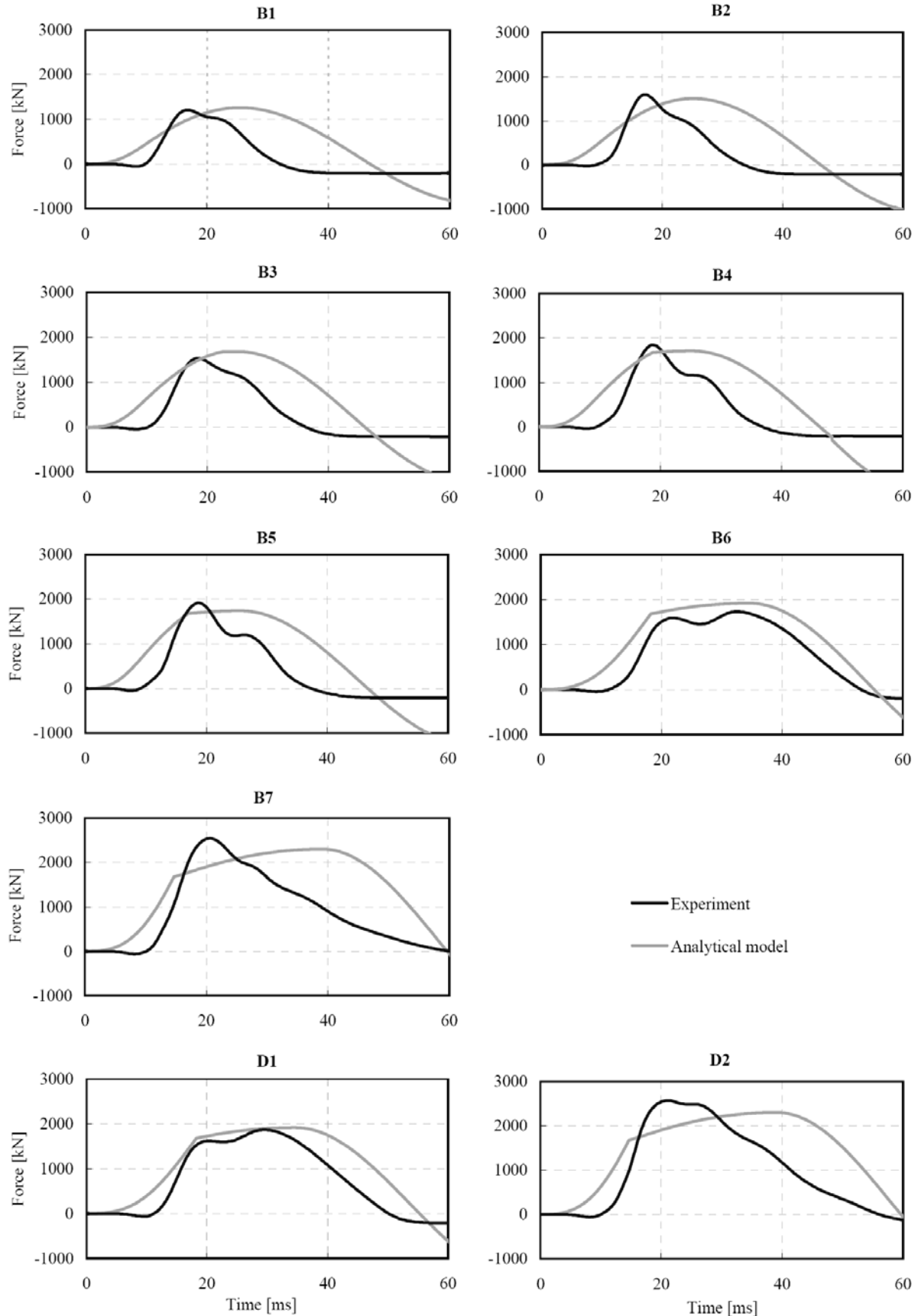


Figure 5-2: Comparison of spring force F_3 and total reaction forces of large-scale tests

Masses and spring properties have been calculated as follows:

- M_1 : 800 or 4'000 kg
- M_2 : 1'720 or 2'880 kg for the 800 or 4'000 kg boulder, respectively
- M_3^* : 10'030 or 9'320 kg for the 800 or 4'000 kg boulder, respectively
- K_{11} : maximum M_E value reached before unloading, following Equation (4-11) with $p_{\max} = 0.2$ m.
- K_{21} : 124 or 156 GN/m for the 800 or 4'000 kg boulder, respectively
- K_{30} : 79'100 kN/m
- K_{31} : 11'800 kN/m (15% of K_{30})
- $F_{2c,\max}$: force when the relative displacement $y_2 - y_3$ reaches 0.033 mm
- $F_{3,\max}$: 1'490 kN

The resulting forces in spring K_3 are compared to the results of the tests B1 to B7 and D1 to D2 (Figure 5-2). It can be observed that although the shape of the force-time histories are strongly simplified in the model, the peak load can be estimated sufficiently accurately. In general, the duration of the impact is slightly overestimated, but by an amount that is of minor importance for the design.

It is also shown that the yielding point of spring K_3 governs the global response of the system and that consequently post-yield hardening has to be considered for this spring.

Due to the satisfactory agreement of the model results with the test results, no further adjustments are made to the model. For the influence of the various parameters see Section 5.3.

The free oscillation after a short impulse at the slab's center in one large-scale test specimen (shown in Figure 5-3) is used to deduce the damping ratio ζ_3 . Based on the first six periods ($m = 6$ in Equation (5-1)), the damping ratio is determined to be of the order of 1.5%. For a

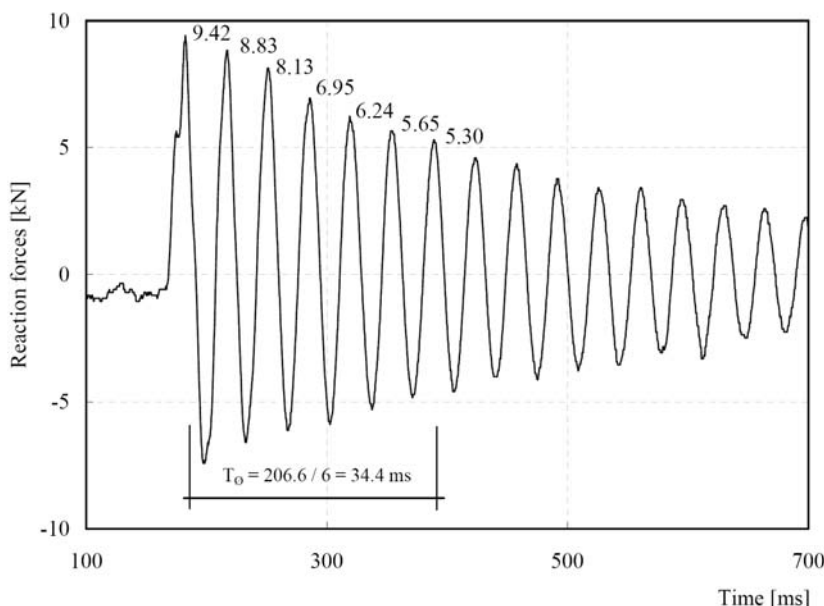


Figure 5-3: Free oscillation of slab 1 without cushion layer

5. Calibration of the model

complete rockfall gallery with different slab boundary conditions, global damping is expected to be higher.

$$\zeta = \frac{1}{2\pi m} \ln \left(\frac{x_n}{x_{n+m}} \right) \quad (5-1)$$

The measured oscillation frequency $f = 29.2$ Hz corresponds to a higher mode of motion and therefore it must not be used to verify the assumed values of the slab stiffness k_w and the factor α to reduce mass M_3 .

Figure 5-5 shows a comparison between the maximum force in the global spring F_3 and the maximum total reaction force of the large-scale tests. Only the tests with a gravel cushion layer and centric impacts are selected. In Figure 5-5a) the input values are used as described above and the corresponding calculation sheet can be found in Appendix D. Other than for the force-time-history calculations in Figure 5-2, the measured M_E values are used for the initial stiffness of the cushion layer K_{10} for every test performed. A cushion damping coefficient $c_1 = 7'000$ Ns/m and a damping ratio of $\zeta_3 = 1.5\%$ have been selected. Good agreement is seen for the tests B1 and B6, which initially were used to select the range of K_{10} . Further, it is seen that especially the test results of the series A are repeatedly underestimated. In series A the thinner slab with $d = 0.25$ m was used. It becomes clear that the assumption of using the static depth z to determine the global stiffness K_{30} in Equation (4-34) is not appropriate. Instead, the slab thickness d has to be considered.

$$K_{30} = \frac{k_w E_c d^3}{12 L_z^2} \quad (5-2)$$

The results after this change are shown in Figure 5-5b), where it may be observed that the resulting forces of those tests with their significantly higher reaction forces than the yielding load F_{3y} are still underestimated by the model. The stage after yielding of the global system is mostly determined by the hardening behavior of the global system, which is only taken into account by applying a factor γ_y that covers the hardening of bending reinforcement after yielding and the involved increase of the lever arm of the internal forces due to plasticization of the concrete compression zone. For Figure 5-5 b), $\gamma_y = 15\%$ was used.

For the tests B6, B7 and E3 the influence of γ_y is shown in Figure 5-4. For the test E3 a value of $\gamma_y = 25\%$ would lead to the corresponding model results. By applying this value the other test results would be greatly overestimated. Thus a strengthening factor of $\gamma_y = 20\%$ is chosen, which leads to the results shown in Figure 5-5c).

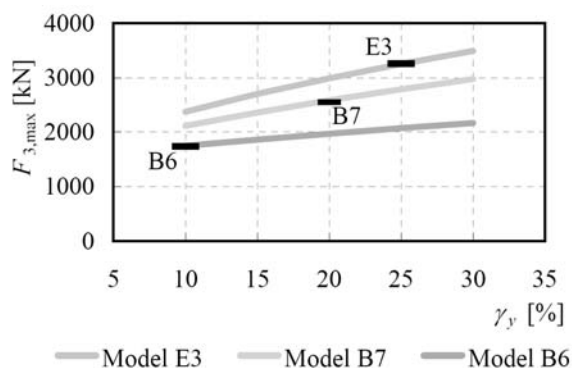


Figure 5-4: Influence of γ_y for the test B6, B7 and E3

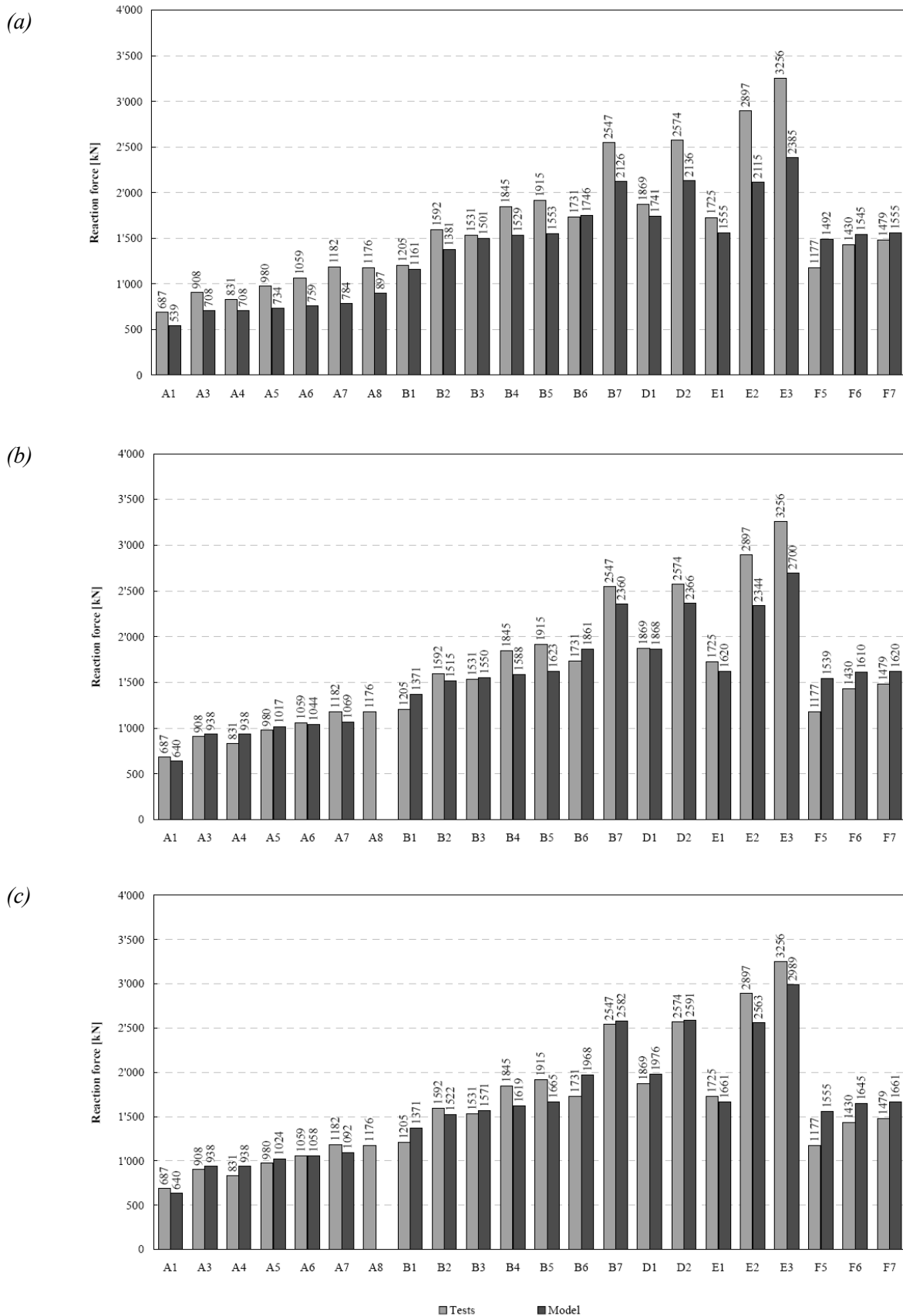


Figure 5-5: Comparison between maximum test reaction forces and model global response (a) initial values (Appendix D), (b) after adjustments in K_{30} and (c) with $\gamma_y = 20\%$

For test A8 the maximum force of the global response is not displayed in Figure 5-5, since the model predicts punching failure and therefore a comparison is not appropriate.

Figure 5-6a) shows a comparison of the maximum spring force F_1 with the maximum acceleration of the impacting body. Figure 5-6b) compares the maximum displacement y_1 of the mass M_1 with the maximum displacement of the falling body, measured from the tracking of the high speed camera. The model overestimates the impact load and therefore the results of the punching evaluation are on the safe side. This explains the punching failure prediction of test A8, where failure did not occur in the test. For test A8 the concrete strength was set to $f_{cm} = 45 \text{ N/mm}^2$ in order to obtain values of F_1 and $y_{1\max}$ for the case in which no punching failure occurs.

The prediction accuracy of the model is acceptable considering that improvements would require a much closer evaluation of the input parameters, in particular K_{10} and p_{\max} . In the present investigation, p_{\max} is set to 0.2 m for the 0.4 m thick cushion layer without more detailed evaluations.

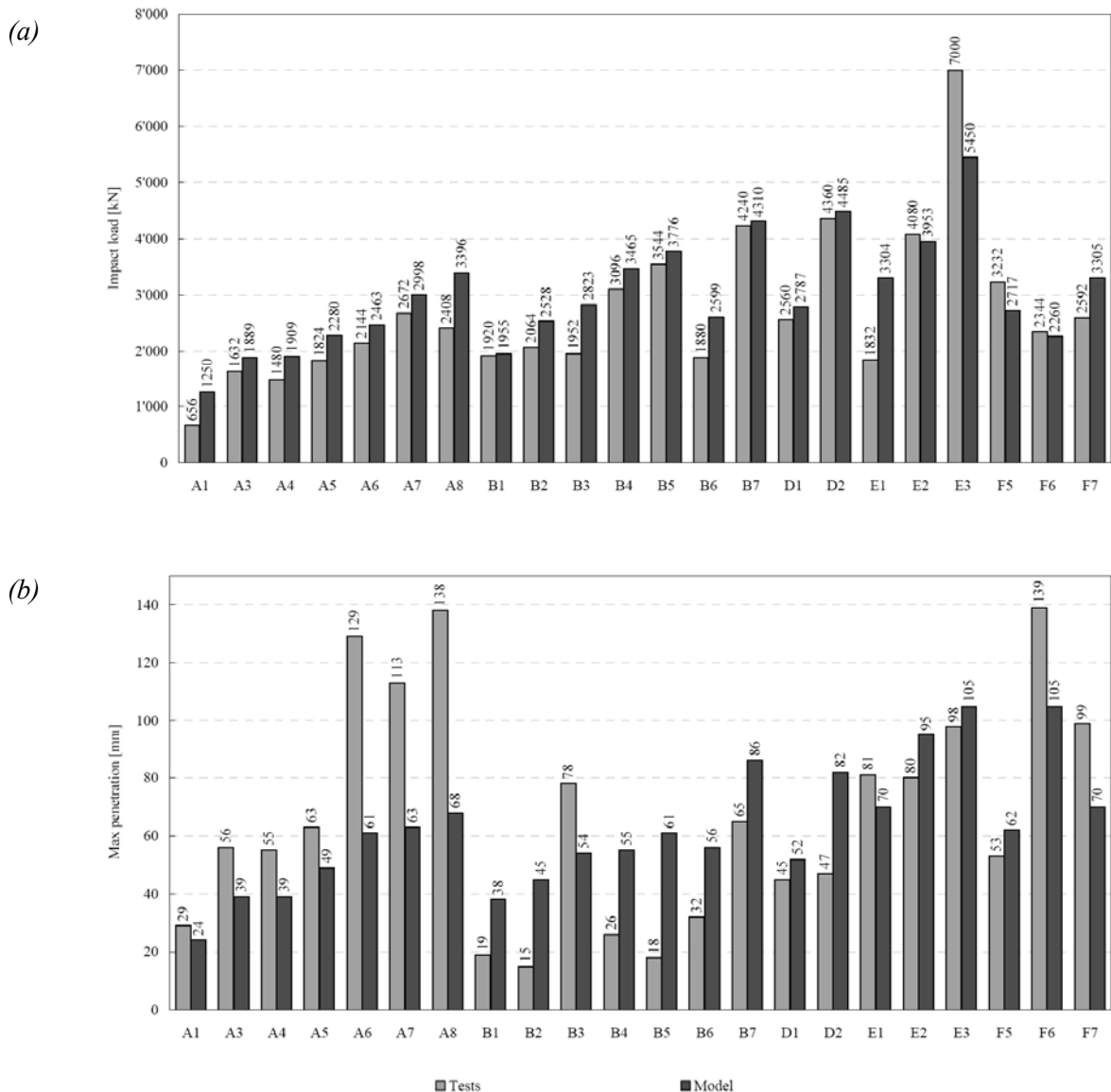


Figure 5-6: Comparison test and model of (a) impact forces and (b) maximum penetrations

The value for K_{10} was defined based on the measured M_E value, e.g. for test B1 where the modulus of elasticity was $M_E = 48'000 \text{ N/mm}^2$, $K_{10} = 48'000 \text{ N/mm}$ was used, since the order of magnitude leads to reasonable results and the simplest assumption is to use a proportional dependence of M_E .

The loading area has not been considered so far. The penetrations calculated in the model for the boulder of 4'000 kg (B6, B7, D1, D2, E2 and E3) are constantly overestimated. Most of the other tests have a smaller loading area and are therefore underestimated, in particular A6 to A8.

The dynamic stiffness of the soil can be described with Wolf's cone model [Wolf et al., 2003] as was also used in [Montani, 1998]. The dynamic soil stiffness for the initial stiffness K_{10} is calculated with Equations (5-3) to (5-7), accordingly.

$$K_{10} = \gamma_g \cdot v_p^2 \frac{A}{z_0} \quad (5-3)$$

$$v_p = \sqrt{\frac{M_E}{\gamma_g}} \quad (5-4)$$

$$v_s = \sqrt{\frac{G}{\gamma_g}} \quad (5-5)$$

$$G = \frac{M_E}{2(1+\nu)} \quad (5-6)$$

$$z_0 = \frac{\emptyset_b}{2} \cdot \frac{\pi}{4} \cdot (1-\nu) \cdot \left(\frac{v_p}{v_s} \right)^2 \quad (5-7)$$

Table 5-1: Values of the different impacting bodies for the soil model of Wolf

Boulder	\emptyset_b [m]	A_0 [m ²]	z_0 [m]	$\Delta K_{10}/M_E$ [%]
800	0.79	0.38	0.565	-32.7
4'000	1.354	1.12	0.968	+15.7

Table 5-2: K_{10} values according to the soil model of Wolf

Test name	M_E [kN/mm ²]	K_{10} [kN/mm ²]	Test name	M_E [kN/mm ²]	K_{10} [kN/mm ²]
A1	53	35.7	B1	48	32.3
A3	46	30.1	B2	52	35.0
A4	47	31.2	B3	47	31.6
A5	43	28.9	B4	56	37.7
A6	36	24.2	B5	54	36.3
A7	42	28.3	B6	48	55.6
A8	44	29.6	B7	47	54.4
D1	56	64.8	E1	40	26.9
D2	52	60.2	E2	38	44.0
F5	30	20.2	E3	46	53.2
F6	16	10.8			
F7	40	26.9			

5. Calibration of the model

The stiffness values for the large-scale tests are listed in Table 3-6. K_{10} for each test is shown in Table 5-2. The density of the cushion layer is considered to $\rho = 1'700 \text{ kg/m}^3$, the Poisson coefficient $\nu = 0.3$. In Table 5-1 the values for the different impacting bodies are shown. In comparison with the previous evaluations, the soil stiffness is reduced by 32.7% for the small falling weight of 800 kg and increased by 15.7% for the large falling weight of 4'000 kg. The new initial soil stiffness K_{10} are for the large-scale tests are shown in Table 5-2.

The agreement between the impact force of the model and the accelerations measured in the impact body is satisfactory (Figure 5-7a)). In addition, the prediction of test A8 shows no punching failure with these settings for the cushion layer. For the penetration in Figure 5-7b), the maximum displacement of spring K_1 is compared to the displacement of the boulder measured from the video tracking. In this comparison the deformation of the slab is also included. It can be seen that the actual penetrations are far smaller than the maximum possible penetration. The behavior of the cushion layer is mainly in the elastic range of the model.

The initial values of the spring displacement y_1 , y_2 and y_3 are zero. Thus, at the beginning of impact the masses are accelerated by earth gravity forces, until equilibrium is reached. This procedure increases the reaction forces of the impact by twice the weight of the masses over

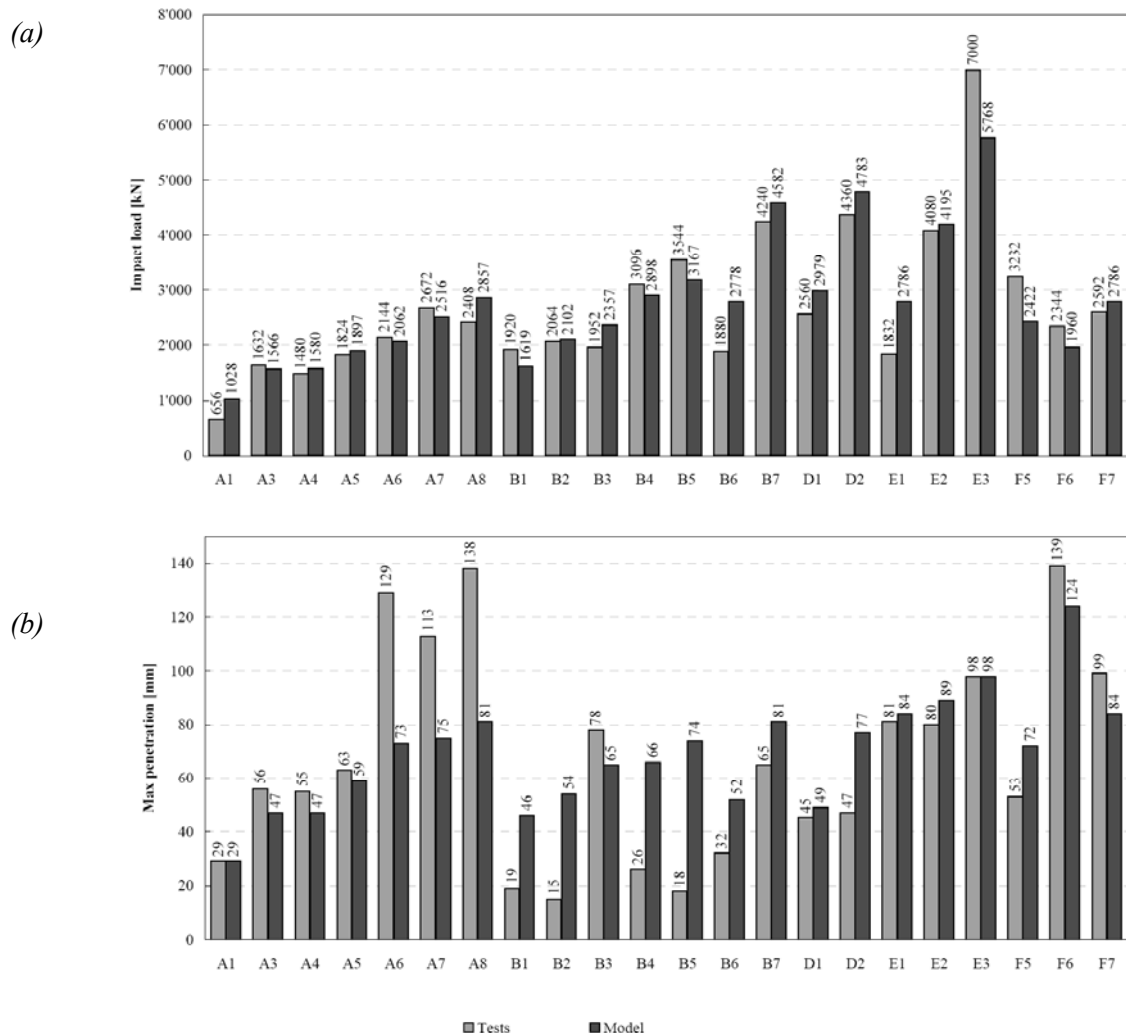


Figure 5-7: Comparison test and model of (a) impact forces and (b) maximum penetrations with soil model of Wolf

each spring. The largest influence is developed in the spring F_3 , since M_3^* is usually the dominating mass. By setting the impact velocity $v_1 = 0$ the influence can be observed (Figure 5-8). For the performed large-scale tests, the maximum forces in spring F_3 due to the dynamic effects on the dead load are summarized in Table 5-3. The peaks of the reaction forces occur between 25 and 40 ms after the start of the impact, and therefore, the peaks are not superposed.

By introducing an initial displacement of the springs, the dead load is taken into account correctly (see also Chap. 6.3).

Table 5-3: Cases for the sensitivity evaluation

Case	Series	M_1 [kg]	M_2 [kg]	M_3^* [kg]	M_{tot} [kg]	$F_{3\max}$ [kN]	$t(F_{3\max})$ [ms]
I	A	800	1'247	7'136	9'183	180	35-40
II	B, E, F	800	1'700	9'833	12'333	241	~25
III	B, D, E, F	4'000	3'802	8'567	16'369	290	35-40

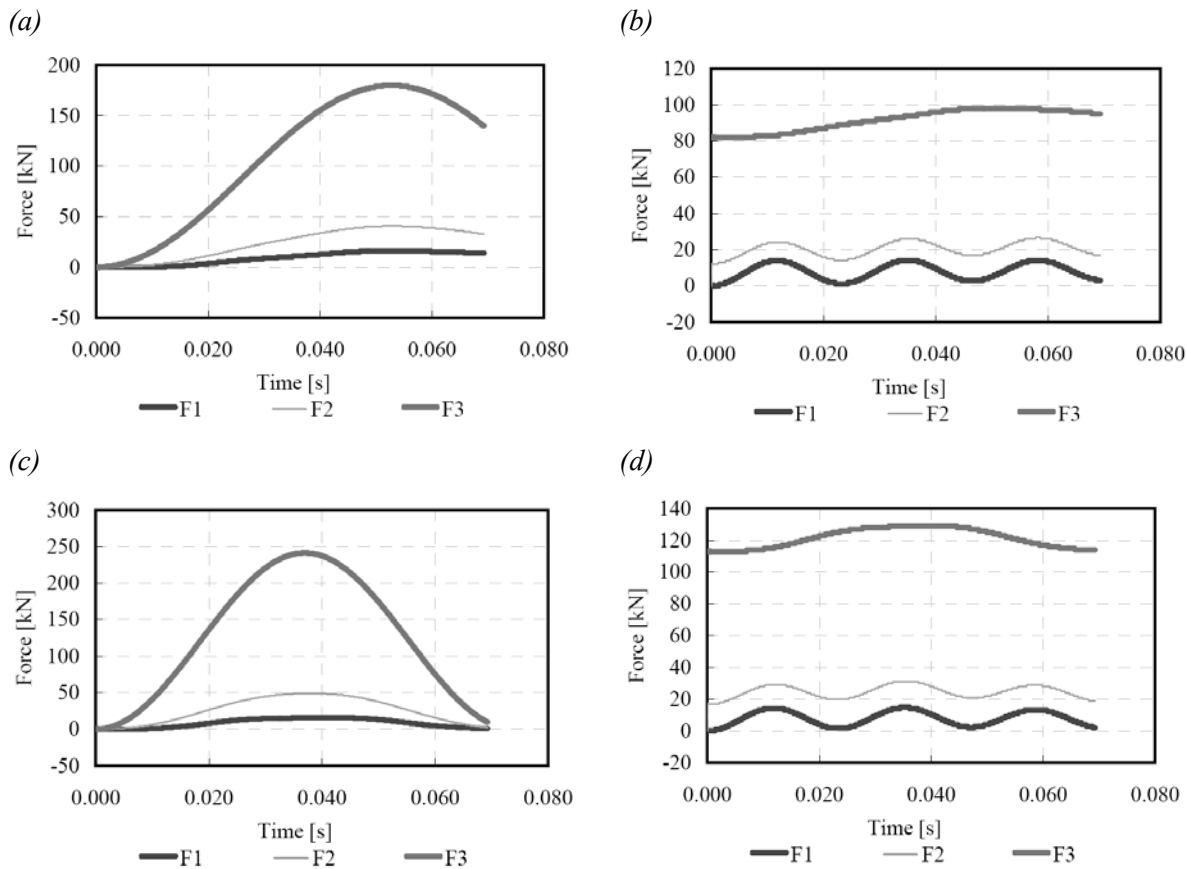


Figure 5-8: Forces in the model from gravity with $v_1 = 0$, (a) case I without and (b) with pre-deformation of the spring, (c) case II without and (d) with pre-deformation of the spring

5.2. Punching behavior

The punching tests, which are described in Chap. 3.4, are used to evaluate the punching prediction of the model, to adjust special input parameters and to adapt the model as a whole, if necessary. Prior to the tests a preliminary calculation run of the model was used to determine the impact velocities. After the impacts it was observed that immediate unloading after cracking of the concrete cannot be simplified by assuming an immediate decrease of the applied load. This led to the development of the two conditions as described in Section 4.2.2. The parameters required for the punching prediction are obtained and verified by comparing the model output of the forces F_1 and F_3 to the impact and reaction forces of the tests, respectively.

The crucial parameters that have to be determined are the following:

- effective mass factor α
- stiffness factor k_w
- modulus of elasticity M_E
- maximum penetration p_{\max}

According to Table 4-1, a mass factor of $\alpha = 0.25$ is reasonable. The influence of this selection is shown in the next section.

For the stiffness factor k_w , a value corresponding to two restrained sides is appropriate, since the boundary conditions can be assumed to be partially restrained (rotary line supports but restrained from lifting up and additional U-sections, see Chap. 3.4). Table 4-2 therefore gives a value of $k_w = 117$. However, from a previous static test on the same specimen a deflection of $y_3 = 1.76$ mm was measured under a load of $F = 200$ kN yielding to a value of $k_w = 51$.

Further definitions are $P_u/m_u = 8$ according to Table 4-3 for a slab simply supported on all sides (no reinforcement placed in the top layers of the slab).

The value of K_{10} should be determined based on the material properties of the cushion layer as well as on the loading area. The calibration of K_{10} is performed by matching the peak impact load of the model to the corresponding one in test S15-6 ($F_{\max} = 221$ kN), in which no punching failure occurred. With the following parameters a value of K_{10} of about 4000 N/mm can be selected:

- sand density $\gamma_g = 17$ kN/m³
- angle of internal friction $\varphi = 33^\circ$
- cushion thickness of $e = 100$ mm
- $p_{\max} = 85$ mm
- $c_1 = 7'200$ Ns/m according to Equation (4-36)
- $A_0 = 0.0177$ m²

For comparison purposes reference is made to the values used for the sand cushion layer in other investigations:

- $M_E = 5'000$ N/mm in the FE-simulation of previous tests with the same sand in [Bhatti et al., 2006].
- $M_E = 16'000$ N/mm for similar sand in [Chikatamarla, 2006].

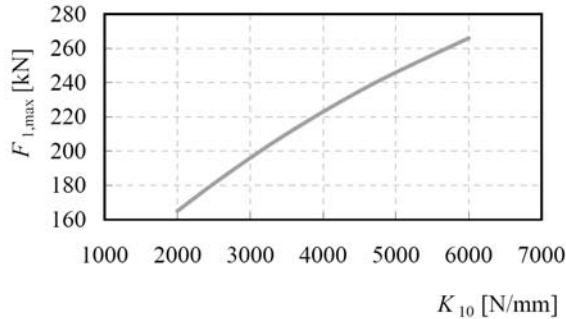


Figure 5-9: Calibration of K_{10} with test S15-6

With these values all six punching tests are calculated. The input values, intermediate and final results and the diagrams are shown in Appendix E.

The results clearly show that with these values the prediction of punching failure is satisfactory. In test S6 (loading diameter 60 mm) punching failure occurred in the slab. The model predicts punching failure but for an impact velocity $v_1 = 6.2$ m/s. In the performed test it could be observed that no load distribution took place in the cushion layer. In the model this effect can be simulated by predefining the loading area on the slab equal to the loading area on the cushion layer ($\mathcal{O}_b = \mathcal{O}_{sl}$). With this configuration punching failure can be predicted for an impact velocity of $v_1 = 6$ m/s.

For the tests S15 (loading diameter 150 mm) failure is predicted in the model already for an impact velocity of $v_1 = 9$ m/s. In the tests, failure occurred for $v_1 = 10$ m/s. By increasing the concrete strength f_{cm} in the model from 24 N/mm² to 32 N/mm² the model also predicts failure for an impact velocity of 10 m/s.

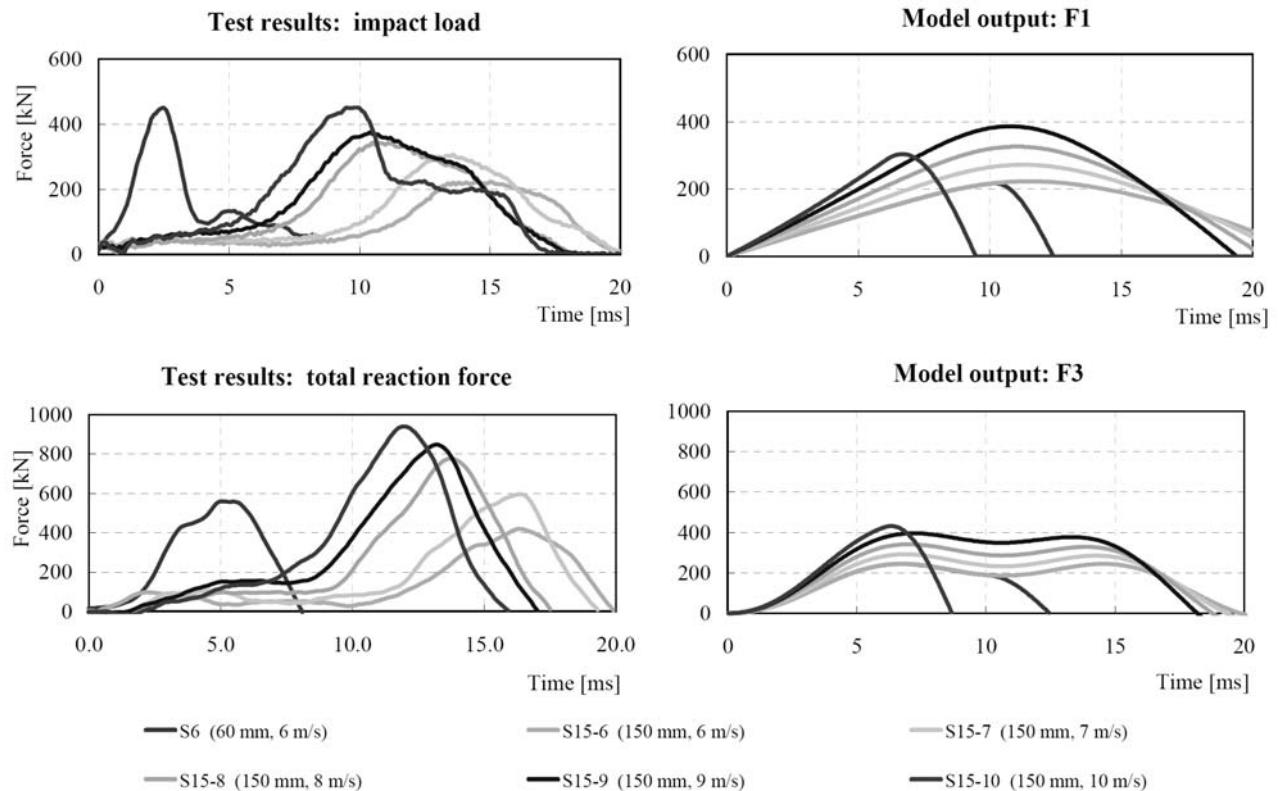


Figure 5-10: Model output and punching test results

5. Calibration of the model

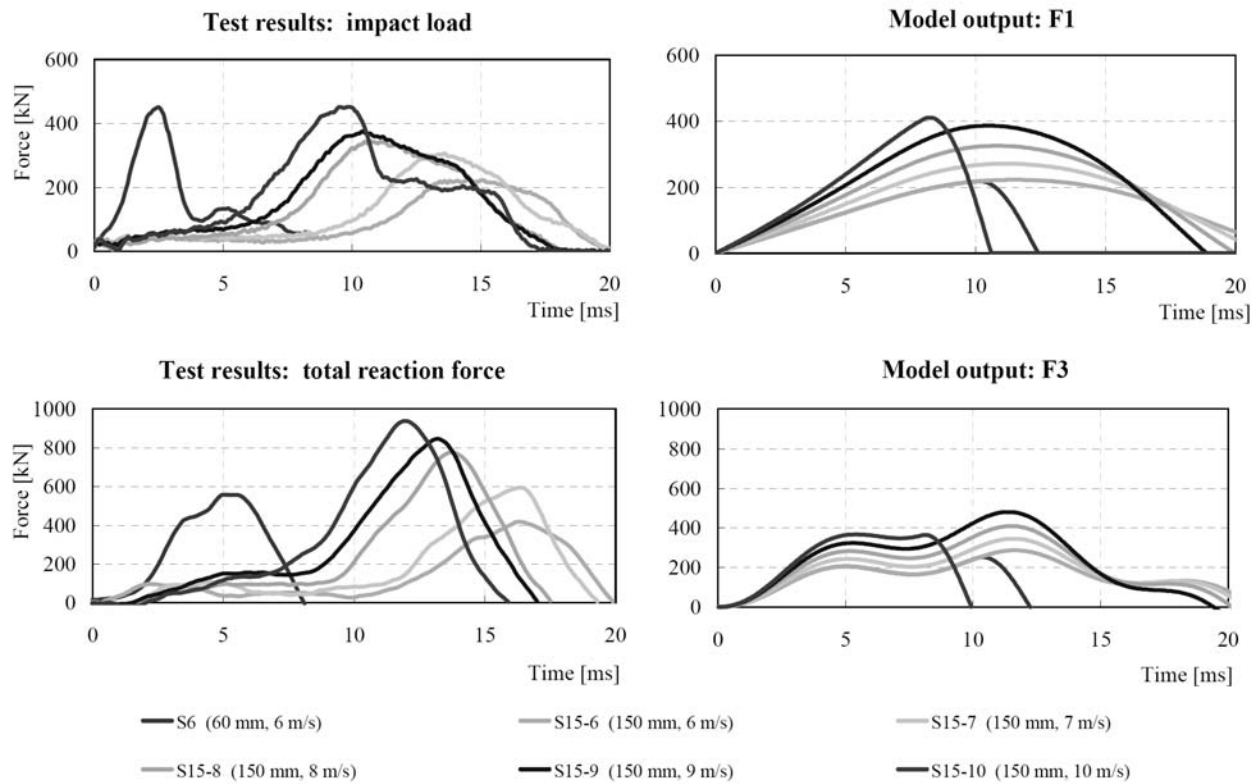


Figure 5-11: Model output and punching test results after adjustments in K_{30} using Equation (5-2)

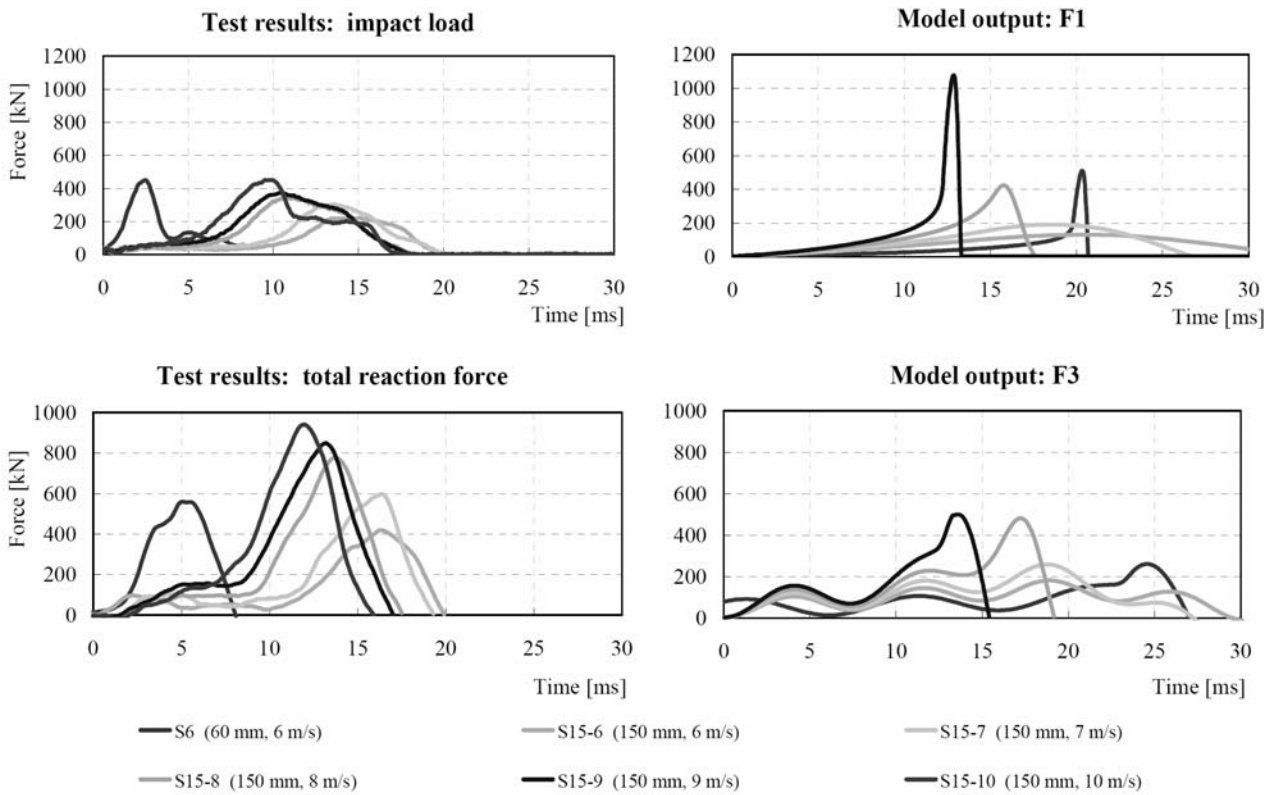


Figure 5-12: Model output and punching test results using soil model of Wolf

In the global response the reaction forces reach about 50% and 90% of the yielding load for the tests S6 and S15-10, respectively. The crack pattern shown in Figure 3-24 with several bending cracks in the diagonals of the slab also shows that the test S15-10 resulted in a higher loading in the global system.

Figure 5-10 shows a comparison of the force-time histories of both test results and the output of the model. The only reason for the different loading diameters in the model is to predict punching failure. In the test also the time of impact is shorter for S6 than for S15-6. In general, it can be seen that the reaction forces are greatly underestimated. These calculations are carried out before changing the global stiffness K_{30} which is determined according to Equation (5-2). Changing of the coefficient for hardening after yielding γ_g to 20% has no influence, since in these tests only about 95% of yield load is reached. The results of a second run considering the slab thickness d for K_{30} are shown in Figure 5-13. Here too no distribution in the cushion layer is considered by using $\emptyset_{sl} = \emptyset_b$. For a loading diameter of $\emptyset_b = 60$ mm, punching failure is already reached at an impact velocity of $v_1 = 5.8$ m/s. For $\emptyset_b = 150$ mm, the punching load is reached with the impact velocity of $v_1 = 7.7$ m/s, whereas the test S15-9 with $v_1 = 9$ m/s did not exhibit failure. In order to resist the impact with $v_1 = 9$ m/s a concrete strength of $f_{cm} \geq 34$ N/mm² would be required in the model. With this concrete strength and a loading diameter of $\emptyset_b = 60$ mm, an impact velocity of $v_1 = 7.1$ m/s would lead to failure. These load cases are summarized in Table 5-4.

The impact time and the tendencies for higher impact velocities, however, seem to be well accounted for by the model. The unloading time also seems to be of the correct order of magnitude with regard to the load decreasing after punching failure.

In order to obtain comparable load-time histories, for Figure 5-11, the impacts with the different loading diameters are simulated with different concrete strengths as follows:

- 24 N/mm² for $\emptyset_b = 60$ mm
- 35 N/mm² for $\emptyset_b = 150$ mm

The stiffness of the springs seem to be correct, especially considering impact durations and the increase of the reaction forces between 10 and 15 ms in comparison with the reaction forces shown in Figure 5-10. Trying to vary the input parameters in order to obtain higher reaction forces would only be possible by first increasing the concrete strength, since the model does not transmit high enough forces to the spring F_3 after punching failure. Dowel effects of the bending reinforcement are not considered in the model. The influence of these effects on the test results are difficult to quantify.

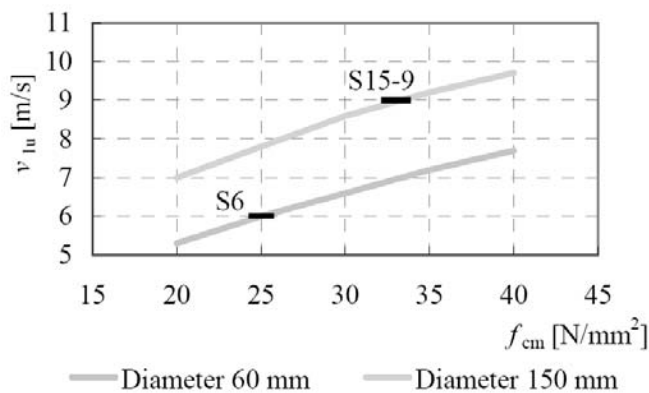


Figure 5-13: Influence of concrete strength on failure prediction

Table 5-4: Influence of concrete strength on the prediction of punching failure

\varnothing_b [mm]	v_{1u} [m/s]	
	f_{cm} [N/mm ²]	
	24	34 N/mm ²
60	5.8	7.1
150	7.1	9.1

By applying the soil model of Wolf, the force time histories of the tests S6 and S15-6 differ from each other. Using a modulus of elasticity of $M_E = 5'000$ N/mm² for the diameters of loading area $\varnothing_b = 60$ mm and $\varnothing_b = 150$ mm the initial stiffness results in $K_{10} = 330$ and 825 N/mm, respectively. The results of the model using this initial stiffness are shown in Figure 5-12. For a modulus of elasticity of $M_E = 16'000$ N/mm², the correspondent values are $K_{10} = 1'050$ and 2'640 N/mm.

5.3. Sensitivity of the single parameters

For the present evaluation the important parameters are varied individually, keeping all the others unchanged. The influence of these different variations on the three maxima of the forces F_1 , F_2 and F_3 provides a good knowledge of the model sensitivity with regard to the following parameters.

- Impact velocity v_1
- Impacting mass M_1
- Static depth z
- Stiffness factor k_w
- Mass factor α
- Cushion thickness e
- Initial stiffness of cushion K_{10}
- Angle of internal friction of cushion φ
- Damping coefficient of cushion c_1

This evaluation is carried out mainly in the linear range, which means that none of the springs undergo significant changes in their properties. Three cases have been selected with different geometries and the results are summarized in Table 4-6:

- Case 1: large-scale test B2
- Case 2: punching test S15-6
- Case 3: typical rockfall gallery in Switzerland

Due to the strong nonlinearity of the system, not only should the force maxima be paid attention to, but also the range in which the springs are working. Thus a detailed output of the model can be found in Appendix F. The percentages of the maximum loads compared to the limit of the linear state are given and allow the identification of the loading range.

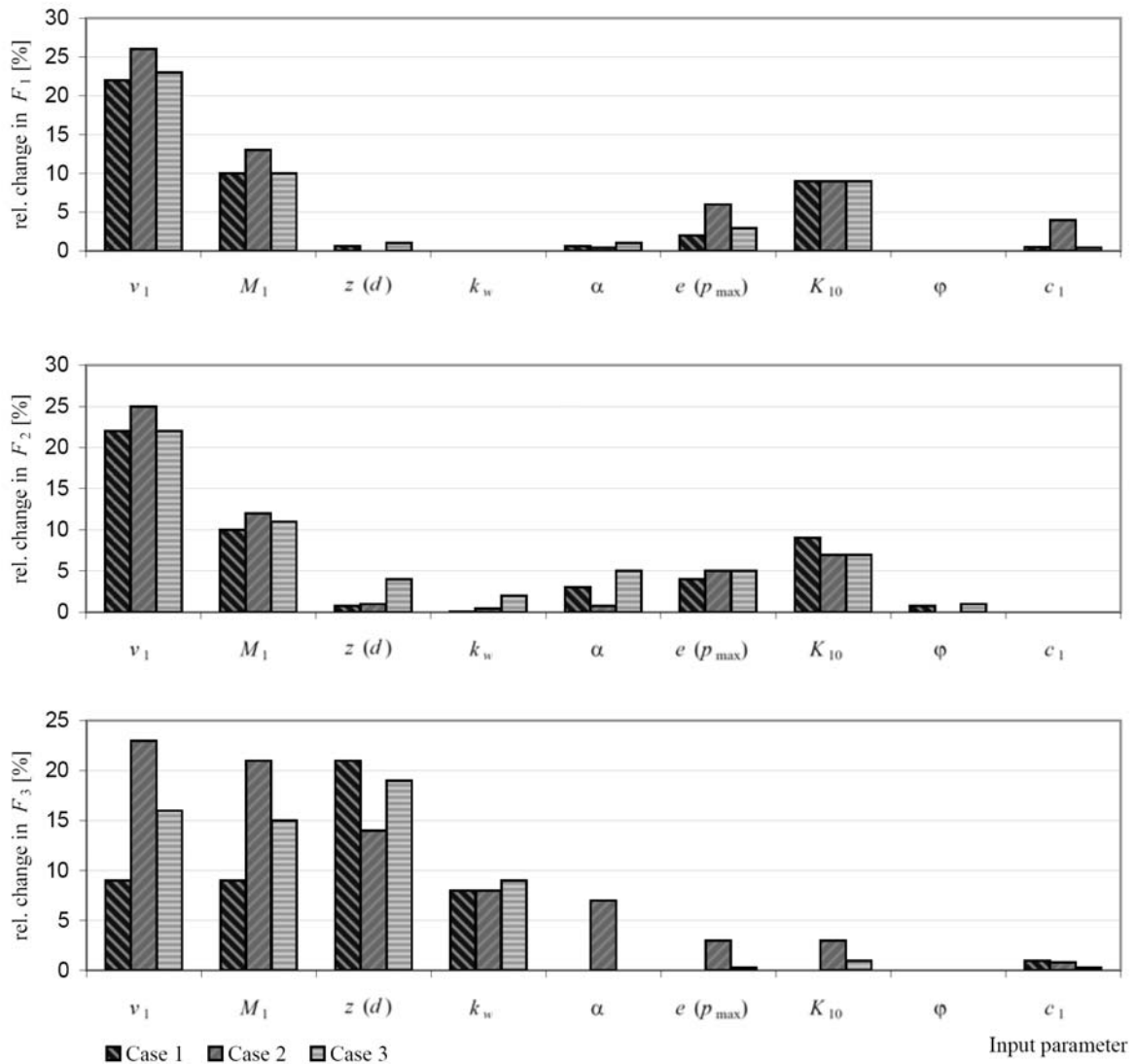


Figure 5-14: Influence of individual parameters on the spring forces (sensitivity analysis)

Figure 5-14 summarizes the values of Table 5-5 showing the relative change of the spring after having changed the input parameters by 20%. Only the positive values are shown, since this makes it easier to read the diagram. Negative values can be taken from Table 5-5.

In general, the different cases seem to be affected similarly under changes of single parameters. Only the global behavior shows a smaller increase in F_3 . The explanation for this behavior is that globally the structure starts to deform plastically during impact. Moreover, it becomes very clear, that v_1 and M_1 have the greatest influence on the response of the gallery. Additionally, the global behavior depends more on the static depth than on small changes in the factor for the global stiffness k_w and small changes of the mass factor α . The values for the cushion layer can influence the punching behavior but have little influence on the global response.

5. Calibration of the model

Table 5-5: Cases for the sensitivity analysis

		Parameters								
		Impact velocity	Striking mass	Static depth (Slab thickness)	Stiffness factor	Mass factor	Cushion layer thickness	Initial stiffness of cushion layer	Angle of internal friction	Damping coefficient
		v_1 [m/s]	M_1 [kg]	$z (d)$ [m]	k_w [-]	α [-]	$e (p_{max})$ [m]	K_{10} [N/mm]	ϕ [°]	c_1 [Ns/m]
Case 1: Large-scale test B2										
initial value		12.14	800	0.31 (0.35)	17	0.8	0.4 (0.2)	56000	33	7000
new value		14.6	960	0.37 (0.42)	20.4	0.96	0.32 (0.16)	67200	40	5600
rel. change	[%]	+20	+20	+20	+20	+20	-20	+20	+20	-20
$F_{1,old}$	[kN]	2'618	2'618	2'618	2'618	2'618	2'618	2'618	2'618	2'618
$F_{1,new}$	[kN]	3'203	2'877	2'633	2'618	2633	2'673	2'853	2'617	2'632
rel. change in F_1	[%]	+22	+10	+0.6	0	+0.6	+2	+9	0	+0.5
$F_{2,old}$	[kN]	2'356	2'356	2'356	2'356	2'356	2'356	2'356	2'356	2'356
$F_{2,new}$	[kN]	2'883	2'588	2'375	2'358	2'436	2'452	2'572	2'375	2'351
rel. change in F_2	[%]	+22	+10	+0.8	+0.1	+3	+4	+9	+0.8	
$F_{3,old}$	[kN]	1'382	1'382	1'382	1'382	1'382	1'382	1'382	1'382	1'382
$F_{3,new}$	[kN]	1'512	1'510	1'679	1'491	1'313	1'380	1'383	1'382	1'396
rel. change in F_3	[%]	+9	+9	+21	+8	-5	-0.1	+0	+0	+1
Case 2: Punching test S15-6										
initial value		6	300	0.15 (0.18)	51	0.25	0.1 (0.085)	4000	33	7220
new value		7.2	360	0.18 (0.22)	61	0.3	0.08 (0.07)	4800	40	5780
rel. change	[%]	+20	+20	+20	+20	+20	-20	+20	+20	-20
$F_{1,old}$	[kN]	223	223	223	223	223	223	223	223	223
$F_{1,new}$	[kN]	282	253	223	223	224	237	242	223	231
rel. change in F_1	[%]	+26	+13	0	0	+0.4	+6	+9	0	+4
$F_{2,old}$	[kN]	262	262	262	262	262	262	262	262	262
$F_{2,new}$	[kN]	328	293	265	263	264	276	281	262	261
rel. change in F_2	[%]	+25	+12	+1	+0.4	+0.8	+5	+7	0	-0.4
$F_{3,old}$	[kN]	245	245	245	245	245	245	245	245	245
$F_{3,new}$	[kN]	302	296	280	265	262	253	253	245	247
rel. change in F_3	[%]	+23	+21	+14	+8	+7	+3	+3	0	+0.8
Case 3: Case study Gallery Axen-Süd										
initial value		25	2500	0.51 (0.55)	33	0.20	0.8 (0.6)	44000	33	7000
new value		30	3000	0.61 (0.66)	40	0.24	0.64 (0.48)	53000	40	5600
rel. change	[%]	+20	+20	+20	+20	+20	-20	+20	+20	-20
$F_{1,old}$	[kN]	8'569	8'569	8'569	8'569	8'569	8'569	8'569	8'569	8'569
$F_{1,new}$	[kN]	10'535	9'399	8'663	8'575	8'648	8'822	9'318	8'568	8'602
rel. change in F_1	[%]	+23	+10	+1	+0	+1	+3	+9	-0	+0.4
$F_{2,old}$	[kN]	6'763	6'763	6'763	6'763	6'763	6'763	6'763	6'763	6'763
$F_{2,new}$	[kN]	8'275	7'479	7'034	6'873	7'068	7'121	7'269	6'819	6'763
rel. change in F_2	[%]	+22	+11	+4	+2	+5	+5	+7	+1	0
$F_{3,old}$	[kN]	9'045	9'045	9'045	9'045	9'045	9'045	9'045	9'045	9'045
$F_{3,new}$	[kN]	10'465	10'432	10'779	9'823	8'586	9'073	9'138	9'051	9'074
rel. change in F_3	[%]	+16	+15	+19	+9	-5	+0.3	+1	+0	+0.3

6. Results

In order to evaluate the potential enhancements for the design by the proposed model, the results are compared to the values given in the Swiss guideline in addition to the results of the large-scale impact tests (Chap. 6.1). The results of an evaluation for the impact load capacity of a reinforced concrete slab are shown for the example of a large-scale test in Chap. 6.2. The structural evaluation of an existing rockfall gallery as a case study is shown in detail in Chap. 6.3. The aim of presenting these results is to show the importance of considering the structural behavior in the design and in particular to show the advantages in the evaluation of existing structures by means of the presented model, simultaneously considering shear and bending loads.

6.1. Comparison with guideline

In order to improve the design procedure of rockfall galleries a comparison of the model's spring forces, the test results and the design recommendation of the recent guidelines is given in Figure 6-1.

As mentioned in Chap. 2.8.1, the Swiss guideline [ASTRA, 2008] allows one to determine a static equivalent force from the kinetics of the impacting body and the properties of the cushion layer. This static equivalent force F_k is compared in Figure 6-1a) with the impact load from the tests (deceleration of the boulder) and the spring force F_1 of the model.

More significant may be the comparison of the design values. For brittle failure the guideline uses a coefficient $C = 1.2$ and these values can be compared to F_2 , which is the actual shear load for punching failure in the model. Since these forces cannot be determined experimentally, in Figure 6-1b) only the model forces F_2 and the values from the guideline are compared.

Figure 6-1c) shows the total reaction forces for the tests compared to the model global forces F_3 and the design values for ductile failure, using a value of the coefficient C of 0.4.

In general, it is not easy to define a static equivalent load for a given impact. The aim, obviously, is that by applying the static equivalent force the static design provides dimensions that would withstand the impact dynamically. Thus, these comparisons of the maximum values of the spring forces (impact force, shear force and reaction force) with the design values from the guideline has to be interpreted carefully. However, the static equivalent force for brittle failure lies in a reasonable range. Only for the tests B7, D2, E2 (196 kJ) and E3 (294 kJ) does the equivalent force lead to too high values. The guideline is based on tests with impact energies up to 100 kJ (1'000 kg from 10 m) [Montani, 1998] and was extrapolated by means of FE simulations (see Chap. 2.8.1). Apparently, the extrapolation was performed conservatively.

6. Results

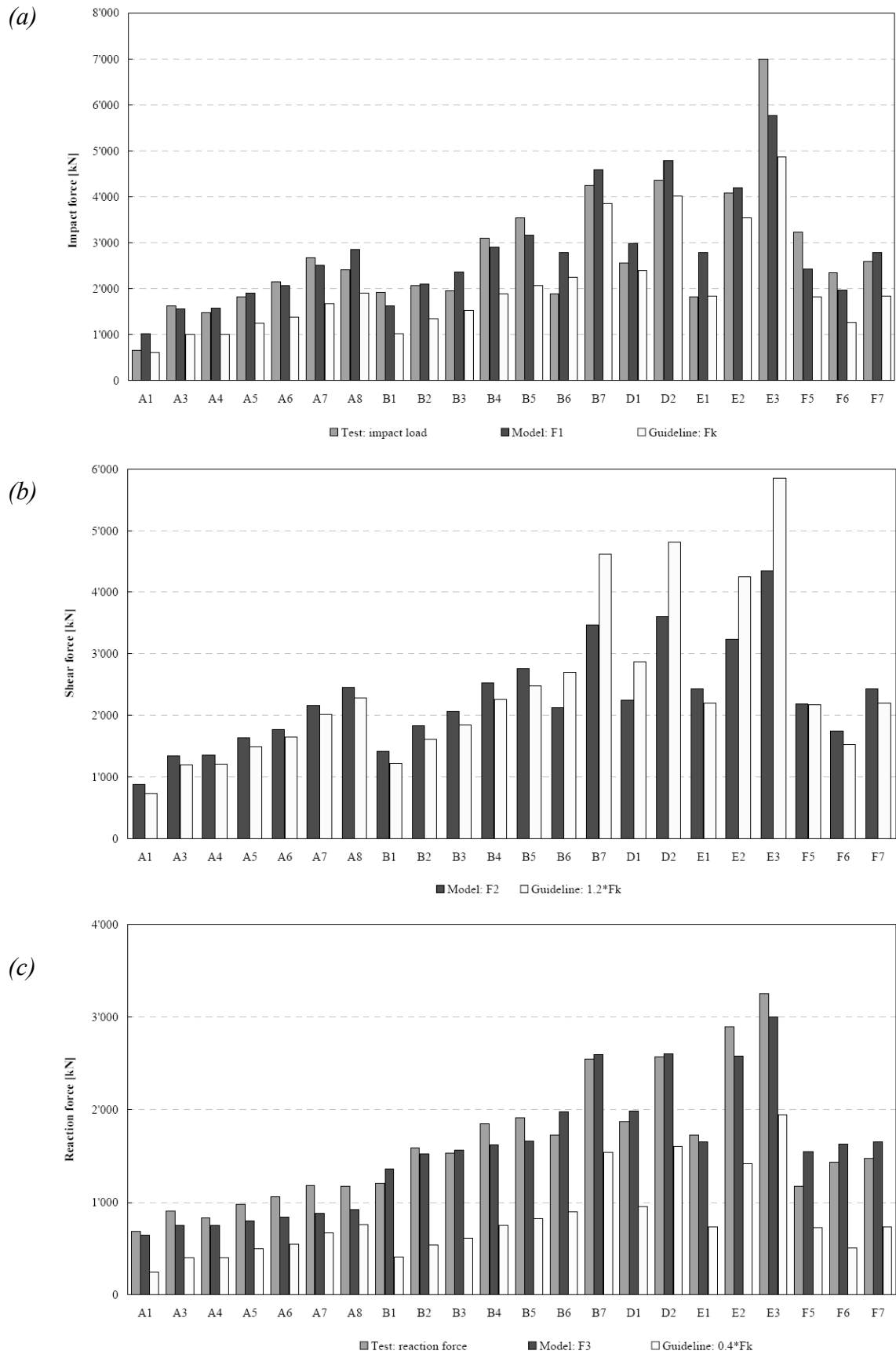


Figure 6-1: Comparison of model results with tests and values taken from the Swiss guidelines (a) impact forces, (b) shear force on punching cone and (c) reaction forces

The design values for ductile failure based on the guideline are much lower than the measured reaction forces. But the equivalent load must not be understood to be a prediction of the load given by this impact. The pertinent question is, would a thinner slab designed for the lower equivalent force reach the ultimate state under the given impact? Obviously, if the ultimate state was not reached, the design load has to be lower.

Accordingly, the best comparison is given for test A8. Bending reinforcement in test A8 reached a strain of $\varepsilon = 0.5\%$ (see Appendix B) and the slab exhibited a well developed crack pattern (Figure 3-21). The global force of the model reaches a value almost 30% higher than the yielding load (see Appendix D, $\eta_3 = F_{3\max}/F_{3y} = 1.29$) and bending capacity can be assumed to be reached. F_{3y} reached 690 kN, which is calculated by an upper bound solution giving a lower limit for a static load that would result in these dimensions of the slab.

Since the static equivalent load according to the guideline is independent of the structure, the values with the same loading have to be the same: A3 = A4 = B1 or A8 = B5. Here the problem of design by a static equivalent force becomes clear: If the section is defined by the punching loading, then this thicker slab will perform stiffer and give higher loads for bending design.

6.2. Evaluation of ultimate load capacity

The presented model is suitable for reproducing the reaction forces and also for quantifying the ultimate state of the structure for defining punching of bending failure, since the model is performance-based. In addition, the model also allows an evaluation of the influence of different dimensions on the impact behavior, which is not taken into consideration in the current design procedure.

Punching shear resistance and bending capacity both increase with the thickness of the slab. For the case of the large-scale tests, Figure 6-2 shows the forces in the springs F_2 and F_3 for impacts of a boulder with a mass $M_1 = 800$ kg falling from different heights while varying the slab thickness d . The ultimate loads for punching F_{2u} and bending F_{3u} are determined for the ratios $\eta_2 = 1.0$ and $\eta_3 = 1.3$, respectively. The slab thicknesses $d = 0.25$ m and $d = 0.35$ m correspond to the performed tests, with falling heights of 5, 10 and 15 m. For Figure 6-2 all other parameters, apart from the slab thickness and the static depth, are unchanged. In

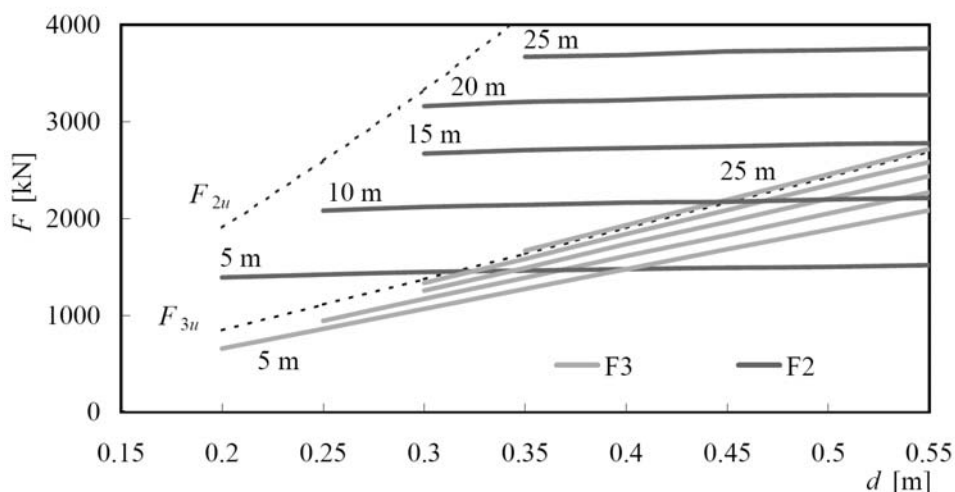


Figure 6-2: Influence of slab thickness on the spring forces F_2 , F_3 and load capacity

6. Results

particular, the reinforcement does not increase with slab thickness. A reinforcement cross-section $A_s = 2'030 \text{ mm}^2/\text{m}$ is used for all calculations. This value corresponds to an average of the reinforcement content in the test series A and B. This selection is admissible, while the minimal reinforcement ratio for thick slabs and the depth of the concrete compression zone are complied with.

As seen in Figure 6-2, the global reaction forces and the capacity of the slab F_{3u} increase with slab thickness almost by the same amount. The resulting shear loads are not greatly influenced by the thickness of the slab. For slab thicknesses with more than $d = 0.35 \text{ m}$ bending failure is relevant.

6.3. Case study

The rockfall protection gallery Axen-Süd is located on the Axenstrasse between Sisikon and Flüelen, a very important north-south connection in the Swiss Alps built between 1975 and 1977. On the mountain side of the gallery, the slab is flexurally rigidly connected with the back wall (Figure 6-3). The valley side is simply supported by columns every 7.5 meters. The span of the gallery is 8.6 meters and the slab thickness varies between 0.40 and 0.70 m. The gallery is about 225 m long and was originally dimensioned for the impact of a 2'500 kg rock falling from a height of 70 m (1'717 kJ).

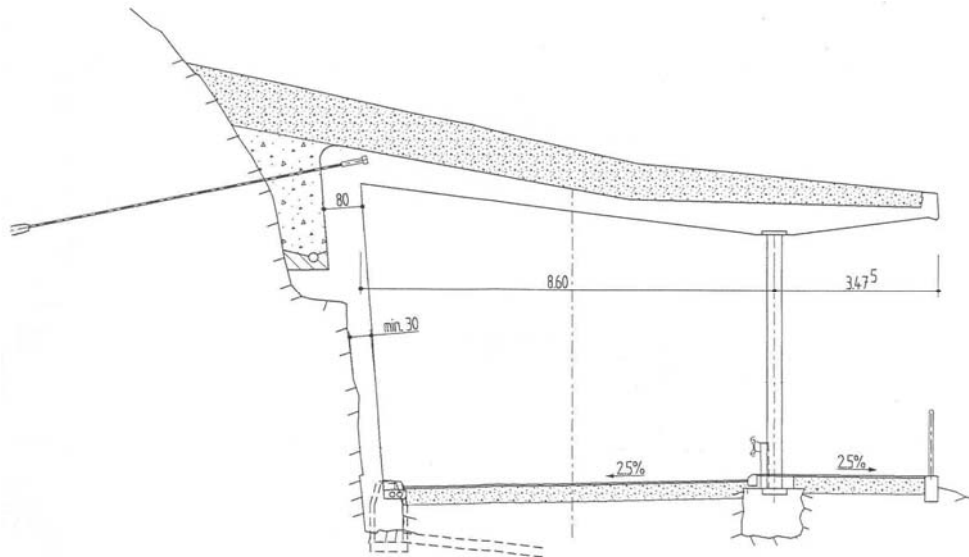


Figure 6-3: Rockfall gallery Axen-Süd

The design from 1974 (exemplary for that time) considered a completely inelastic impact according to Equation (6-1) and is described in a structural evaluation [ARP, 2003] carried out later. The effective mass M_3^* was determined by assuming a one-way load-bearing slab of 5 m width, 8.8 m span and totally restrained at one support. A mass factor $\alpha = 0.43$ was selected and the weight of the cushion layer was considered over the whole slab. Only the mass of the impacting block was neglected in determining the mass of the structure.

$$P = \frac{M_1^2 \cdot H}{y_e \cdot (\chi - 0.5) \cdot M_3^*} \quad (6-1)$$

Where:

- P Impact load
- M_1 Mass of impacting block
- H Falling height
- y_e Elastic deflection
- χ Ductility factor: $(y_e + y_{pl})/y_e$
- M_3^* Equivalent weight of gallery slab

Since the impact load depends on the elastic deflection y_e , some iteration steps were needed, resulting in a ductility factor $\chi = 2.6$, $y_e = 15.7$ mm and an impact load $P = 2'500$ kN. Punching failure was not taken into consideration. The impact load P is statically used for the design in bending using the theory of plasticity, where the one-way load-bearing slab required an effective slab width of 5.5 m to mobilize enough deformation energy.

The analysis by means of the proposed model is explained in detail below, allowing for easy comprehension.

The gallery is simplified to a slab with constant thickness $d = 0.55$ m and a constant cushion layer thickness $d = 0.80$ m. In order to consider the dead load of the gallery and to avoid the dynamic effect (increase factor $\alpha = 2$) on the dead loads, initial displacement $y_{10} = y_{20} = 1.0268$ mm and $y_{30} = 1.0265$ mm are selected according to Equations (6-2) and (6-3).

$$y_{10} = y_{20} = y_{30} + \frac{g \cdot M_2}{K_{21}} \quad (6-2)$$

$$y_{30} = \frac{g \cdot (M_2 + M_3^*)}{K_{30}} \quad (6-3)$$

For the soil, the initial stiffness $K_{10} = 37'200$ N/mm is determined according to Equation (5-3), with the values: soil's modulus of elasticity $M_E = 30'000$ N/mm², Poisson's ratio $\nu = 0.3$, cushion density $\gamma_g = 17$ kN/m² and loading area of $A = 1.13$ m². The maximum possible penetration $p_{max} = 0.57$ m results by assuming a ratio of the compacted volume V_2 of 80% of the volume of the active cone under the boulder V_1 . With V_1 and V_2 , according to Equations (4-15) to (4-17) the height of the passive cone $h = 0.23$ m results for the ratio of $V_2 / V_1 = 0.8$.

The factor for global stiffness is calculated by the most simplified case of assuming a one-way slab with one restrained and one simple support. This results in a spring constant of $K_{30} = 146$ MN/m, which corresponds to $k_w = 33$. The prediction of punching failure depends on the selected value of k_w . To check the importance of this influence, in Figure 6-4 the falling height that produces punching failure is shown for different values of k_w without having defined all other values yet.

6. Results

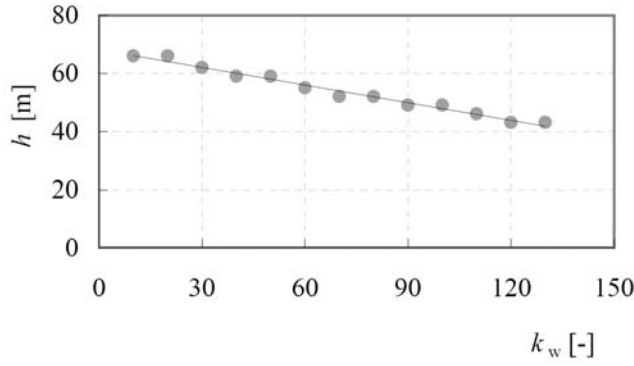


Figure 6-4: Falling height producing punching for different values of k_w

As boundary conditions, a middle span of the gallery is considered with three restrained sides and the fourth side free. The yielding load F_{3y} is calculated according to the upper bound solution shown in Figure 6-5 and results in Equation (6-4).

$$F_{3y} = 2m_{u1} \cdot \frac{L_z}{L_{x0}} + 2m_{u2} \cdot \frac{L_z}{L_{x0}} + 4m_{u3} \cdot \frac{L_x}{L_z} + 4m_{u4} \cdot \frac{L_x}{L_z} \quad (6-4)$$

For the reinforcement placed at the sections 1 to 4, m_{u1} to m_{u4} are determined as shown in Table 6-1. With $L_x = 10$ m, $L_{x0} = 8.5$ m and $L_z = 7.5$ m, the ultimate load is $P_u = 10'340$ kN. In the model an effective reinforcement diameter of $\emptyset_1 = 30$ mm with spacing $s = 150$ mm and a static depth of $z = 0.51$ m results in $m_u = 1'110$ kNm/m and thus $P_u/m_u = 9.3$ is selected in order to obtain the same ultimate load as the gallery.

In the region of small impacting masses with high impact velocities, the damping properties of the cushion layer become important. The value for c_1 was assumed to be 7'000 Ns/m, but this value has not been verified.

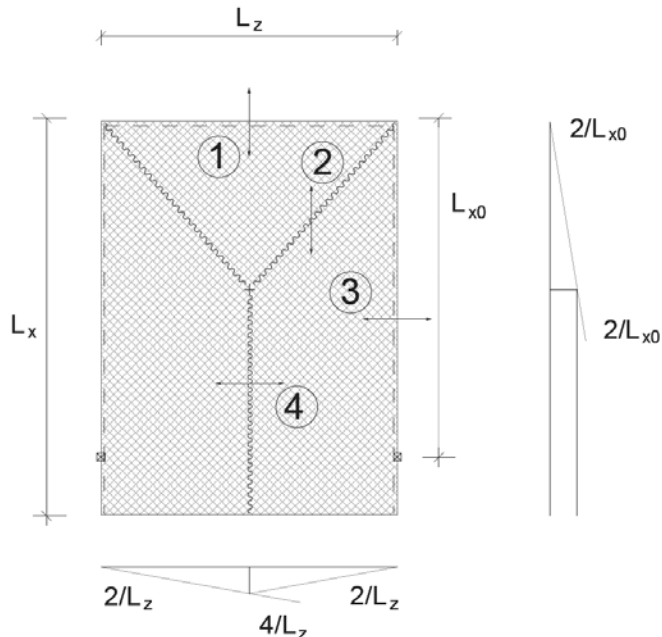
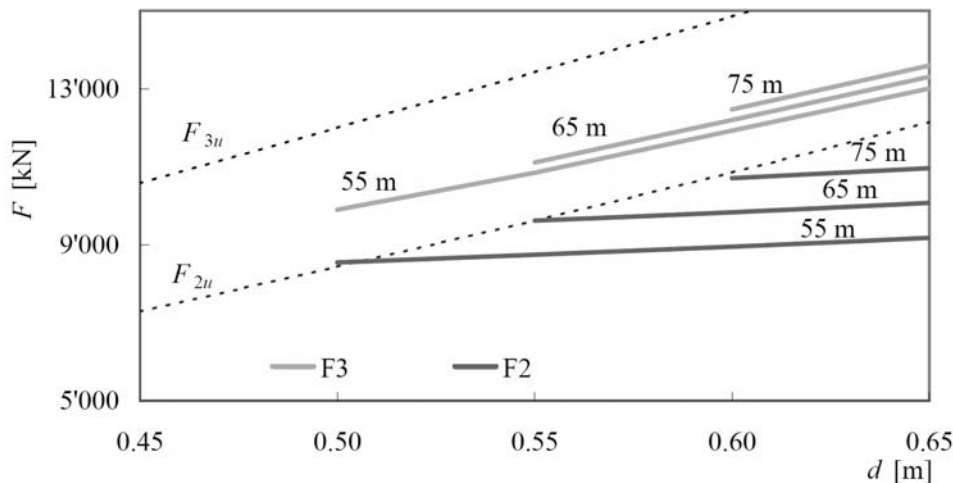


Figure 6-5: Falling height producing punching for different values of k_w

Table 6-1: Bending reinforcement in the slab of the protection gallery Axen-Süd

Section	Slab thickness d [m]	Reinforcement \varnothing [mm] @ [cm]	Cross-section A_s [mm ² /m]	Unit ultimate moment m_u [kNm/m]
Section 1	0.70	$\varnothing 30 @ 30$ $\varnothing 26 @ 30$ $\varnothing 22 @ 30$	5'393	1'712
Section 2	0.55	$\varnothing 30 @ 30$ $\varnothing 26 @ 30$	4'127	1'005
Section 3	0.55	8 x $\varnothing 30$ 6 x $\varnothing 20$ 31 x $\varnothing 18$ (in 10 m)	1'541	391
Section 4	0.55	15 x $\varnothing 30$ 40 x $\varnothing 22$ 5 x $\varnothing 15$ (in 10 m)	2'657	659

The same evaluation of the impact capacity as explained for the large-scale test is shown in Figure 6-6. The forces obtained in the springs F_2 and F_3 as well as the punching and bending capacity are shown for various values of slab thickness. Here, it is seen that for a rock of 2'500 kg, with the given diameter of the loading area, punching is relevant for all thicknesses and that the punching load increases slightly with increasing slab stiffness.

Figure 6-6: Influence of slab thickness on the spring forces F_2 , F_3 and load capacity

In general, for given geometries of the gallery (slab thickness $d = 0.55$ m) the falling height for various impacting masses can be determined that results in a certain state of the structure. For this case study the ultimate state of the slab is defined by $\eta_2 = 1$ for punching failure and $\eta_3 = 1.2$ for the flexural capacity. Figure 6-7 shows that punching is relevant for smaller rocks up to 4'500 kg mass. For higher masses bending failure is predicted. The loading area is related to the volume of the rock and has more influence than the mass itself. The corresponding maximum penetration p_{max} and the initial stiffness K_{10} for different falling masses are summarized in Table 6-2.

6. Results

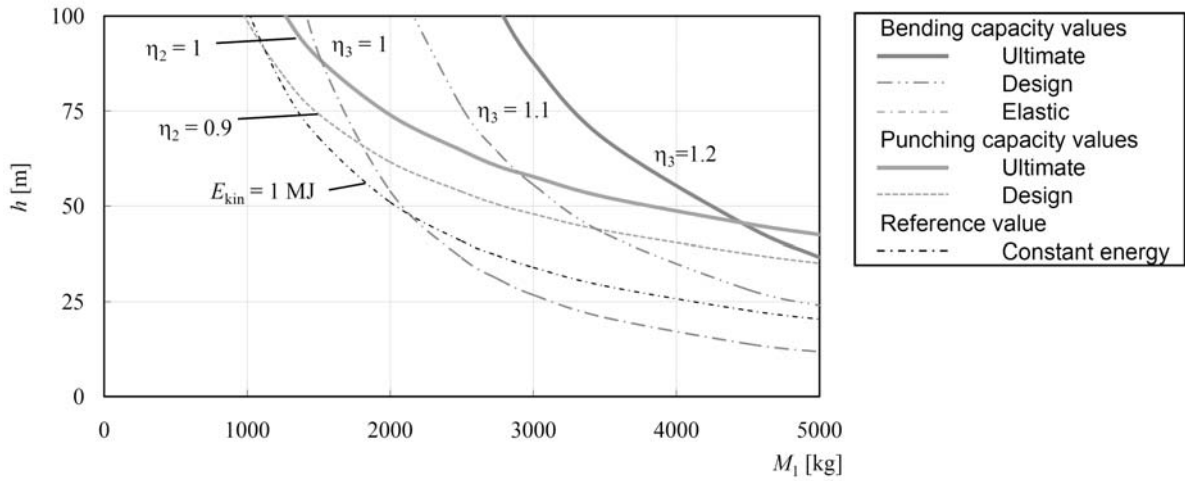


Figure 6-7: Loading capacity of protection gallery Axen-Süd for different impacting masses

In addition, the falling heights leading to a ratio $\eta_3 = 1$ are shown in Figure 6-7 and represent the state when the structure reaches the yield load. These values could be used to determine the serviceability state of the gallery for impacts with a short return period that should not cause any structural damage. In this case, punching failure is dominant, while the flexural behavior would still have enough reserves of strength. It is evident, that the ultimate load capacity could have been significantly improved with shear reinforcement distributed continuously through the slab.

Since no safety factor can be applied in this performance-based design procedure, the ratios of acting force to the ultimate load capacity can be used. For example, the values for $\eta_2 = 0.9$ and $\eta_3 = 1.1$ are shown in Figure 6-7.

For reference purposes, the falling height for impacts with a kinetic energy of $E_i = 1 \text{ MJ}$ are included. It is usual to give the impact energy for both the expected loading and the protection level of a gallery. Here, it is shown that punching failure occurs for lower impact energies for smaller rocks with higher impact velocities.

Table 6-2: Values of cushion layer for different impacting masses and determined falling height for different states of the concrete slab

Impact body M_1 [kg]	\varnothing_b [m]	Cushion layer	Falling height H [m]					
			$\eta_2 = 0.9$	$\eta_2 = 1$	$\eta_3 = 1$	$\eta_3 = 1.1$	$\eta_3 = 1.2$	$E_i = 1 \text{ MJ}$
500	0.661	21'791	0.67	163.6	195.9			203.9
850	0.789	26'011	0.64	110.9	133.4			119.9
1000	0.836	27'560	0.63	98.7	118.4			101.9
1250	0.897	29'571	0.62	84.4	101.2	127.0		81.5
1500	0.953	31'418	0.61	74.2	88.8	89.9		68.0
2000	1.049	34'582	0.59	61.6	73.9	53.8	112.0	51.0
2500	1.130	37'253	0.57	53.8	64.6	36.5	75.9	42.0
2750	1.166	38'440	0.57	50.4	60.5	31.0	64.2	37.1
3000	1.201	39'593	0.56	47.9	57.7	26.7	55.6	34.0
3500	1.264	41'670	0.55	43.6	52.4	20.8	42.8	29.1
4500	1.375	45'330	0.52	37.5	45.3	13.9	28.2	22.7
5000	1.424	46'945	0.51	35.0	42.5	11.8	24.0	20.4

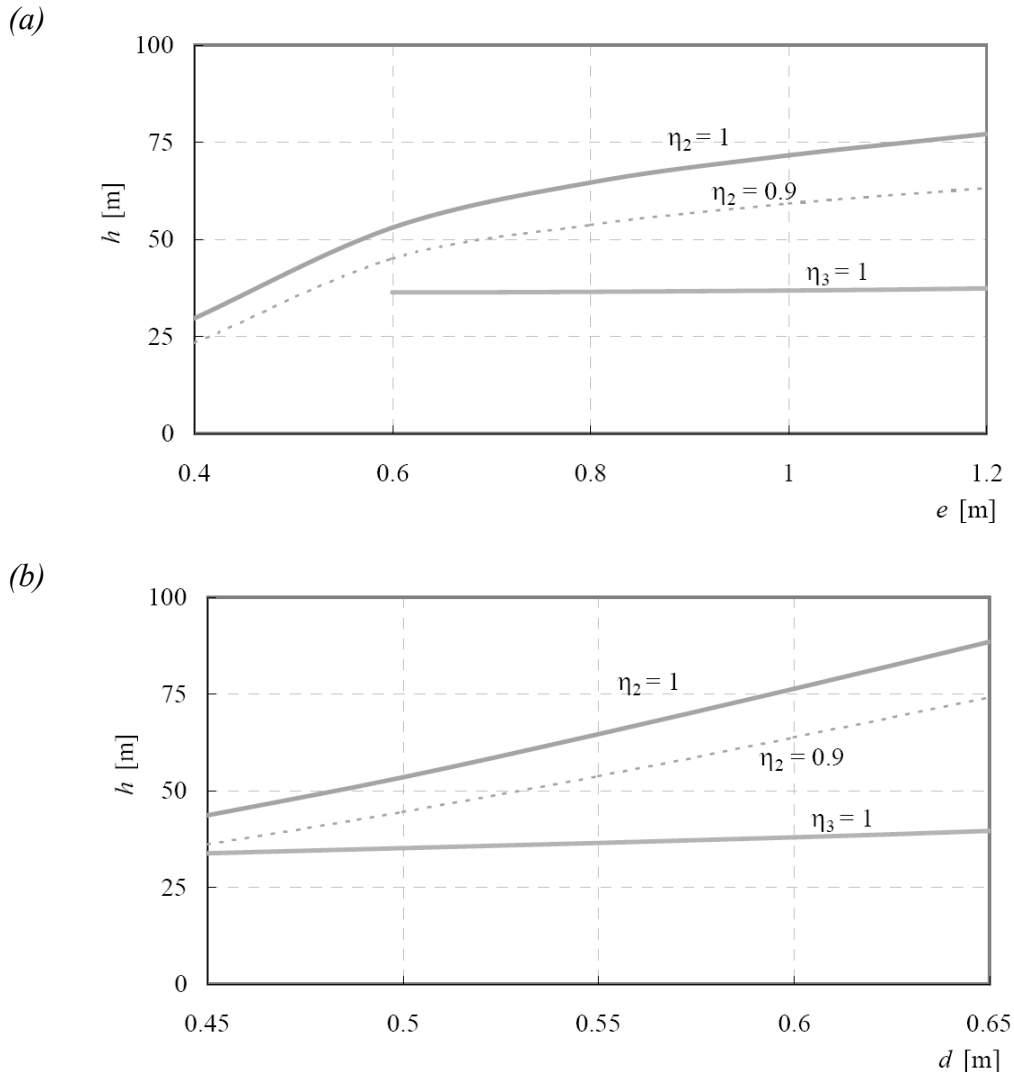


Figure 6-8: Influence of (a) cushion thickness and (b) slab thickness on the ultimate falling height for the given impact mass

Interesting for the design is the influence of the thickness of the slab or of the cushion layer on the load capacity, shown in Figure 6-8 in terms of the falling height for the design impact mass of 2'500 kg. In future such a diagram could readily be applied for the design of rockfall galleries to determine which rocks have to be removed from the slope above of an existing gallery.

A numerical simulation for this case study carried out by Chikatamarla and described in [Chikatamarla, 2006] resulted in a triangular-shaped load impulse transmitted from the cushion layer to the slab, which exhibited a peak value of 10'400 kN and a duration of 13 ms. Compared to the values shown in Figure 6-6, this value is in an interesting range. The loaded area on the slab was approximately 1 m².

It has to be mentioned that the original design of the gallery Axen-Süd for an impact mass of 2'500 kg falling from 70 m was quite satisfactory from the point of view of the results of this evaluation, which predicts punching failure with a falling height of about 64 m.

6. Results

Following the Swiss guideline [ASTRA (2008)] the static equivalent load F_k given by Equation (2-1) is approximately 4'630 kN. As mentioned above, in Equation (2-1) the static load amounts $A_d = 5'560$ kN for punch failure (brittle failure with $C = 1.2$) or $A_d = 1850$ kN for the ultimate flexural resistance (ductile failure with $C = 0.4$). It has to be questioned, however, whether a gallery designed by the current guideline would perform as well as in a dynamic evaluation.

7. Conclusions

Protection galleries belong to the most important structures with regard to risk reduction in the case of rockfall impacts. They provide protection against high energy impact and compared with other measures, they provide a suitable solution with low maintenance for more frequent events of low energy. Additionally, galleries limit the risk due to uncertainties in the trajectory prediction, since they are placed directly above the object that has to be protected. For establishing rational risk acceptance criteria for the design of such structures it is necessary to estimate the ultimate load capacity as accurately as possible. An optimization of design is needed to mobilize the structural reserves due to the high erection costs.

Rockfall events are going to be more frequent in the future as a consequence of global warming and the retreat of the permafrost in the mountainous regions. Therefore, the risk assessment of existing structures is of great importance. Whenever a decision is to be made on whether a gallery still meets the requirements, has to be strengthened or replaced, the response characteristics and the dynamic soil-structure interaction analyses are crucial. Taking them into account will lead to a better balance between the required structural safety and economic aspects of an eventual intervention. A simplified design procedure should be implemented in the governing guidelines, to allow engineers in practice to deal with the complex mechanisms involved.

Furthermore, a deeper knowledge of the impact processes by means of a physical model rather than by employing empirical formulas will allow further progress to be made and scientists of various disciplines can contribute by providing solutions for parts of the model.

The cushion layer has a large influence on the impact behavior. However, for the design of the structure, the structural behavior cannot be neglected. The interaction between rock, cushion layer and slab has to be considered. An analytical model consisting of three masses and three non-linear springs is able to provide all relevant quantities for the design. Due to simplifications based on engineering judgment, the model allows an easy and efficient way to carry out a performance based design.

The properties of the three non-linear springs are defined by the geometrical and the material properties as well as by the deformation state at every time step. For the cushion layer, the soil model of Wolf provides adequate values for the dynamic stiffness. An increase of soil stiffness with penetration gives an alternative for design instead of a limitation of the penetration to a certain range, as it is proposed in the current guidelines.

In the case of stiff galleries, the punching load is only slightly influenced by the global response. Moreover, it follows the impact loading, which occurs within the first 10 to 20 ms. The global response is in the range of around 50 ms. Yielding of the global structural system has an influence on the impact load, by either increasing the impact forces or not. Since punching failure is dominant for usual geometries, it is recommended to use shear reinforcement in the whole slab, in particular when the global yielding load is below the ultimate resistance of the shear reinforcement. In addition, the ductility of reinforcing steel is of great importance.

7. Conclusions

Failure can be predicted, when the ultimate tensile strain of concrete is reached in the section of punching failure considering strain rate effects. For the global structure an upper bound solution is on the safe side, since impact loads decrease with increasing plastic displacements.

Large-scale tests provided experimental data to evaluate and calibrate the analytical model and future numerical models. Based on the combination of the acceleration measured in the impacting body and the high-speed cameras, the boulder-soil-structure interaction can be completely described. The data is available for further investigations.

It can be seen that the static equivalent load F_k according to the guideline without coefficients is of the same order of magnitude as the measured impact load (deceleration forces of the impacting body). However, for impact energies higher than 100 kJ the guideline seems to have been conservatively extrapolated.

The evaluation of an existing protection gallery shows that punching failure governs. Furthermore, for the same impact energy the loading diameter plays a crucial role for the performance of the structure.

8. Outlook

The proposed model enables a simple design procedure and also evaluation of protective structures. The practical applicability of the model was achieved by making several simplifications. In some cases the simplifications are introduced as a first attempt and their influence needs to be examined in more detail for further applications. Some of these assumptions are as follows:

- the horizontal component of impact can be regarded separately,
- the loading surface is plane,
- the damping coefficient of the soil is not evaluated in detail,
- the soil stiffness is independent from the impact velocity,
- direct shear failure in soil is not considered,
- concentrations of the transmitted forces do not exhibit premature punching failure,
- the angle of the punching cone in the slab is 45° ,
- shear forces are carried by tension in the projected area,
- three dimensional effects of crack propagation velocity are not considered,
- scale effects are not taken into consideration,
- the weight of the cushion layer is only considered between the boulder and the slab,
- the diameter of the punching cone is conservatively determined with the maximum possible penetration

The next step from a structural point of view is follow-up research, which was already started in 2007. This research will evaluate the range of the input parameters for the structure, e.g. mass factor α , stiffness factor k_w , by means of FE simulations. The FE model can be calibrated with the performed large-scale and punching tests. Figure 8-1 shows the mesh of such a full model compiled at Muroran Institute of Technology. By means of FE analyses the presented model can be validated for extrapolations out of the range of the performed tests. The FE simulations will also allow extrapolation to other boundary conditions and in particular to different loading positions. For example, they could identify the relevant load cases for different types and dimensions of galleries and also the influence of the load distribution.

As expected, the cushion layer is of great importance. The potential enhancement of the loading capacity of existing structures by the use of alternative materials also demonstrated in the large-scale tests (cushion system Geobrugg A/B) was beyond the scope of this thesis. Characteristics of soil behavior (e.g. K_{10} and p_{max} , or other values for better models) have still have to be quantified. Then, the model output can be compared with other approaches for the penetration [Montani, 1998], [Heidenreich, 2004], etc. Also the amount of dissipated or transmitted energy could be quantified.

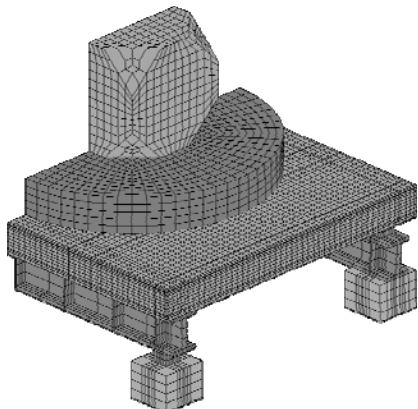


Figure 8-1: Mesh of the finite element model for the large-scale test, compiled at Muroran Institute of Technology

For the goal of this thesis the Interdisciplinary Workshop on Rockfall Protection 2008 was organized [Volkwein et al., 2008]. Collaboration between the researchers of the different disciplines involved has to be promoted. These disciplines also include all geological aspects of events, geotechnical and risk evaluation of trajectory calculations that lead to risk mapping, the basics for the decision to adopt the protection measure and for the analysis of the protective structures. The workshop succeeded in bringing together most of the active researchers, so that gaps in our knowledge not only within the various disciplines but also in the interactions between the disciplines were pin-pointed.

The next step toward a verification of these results would be a falling weight test on a real gallery. This impact does not necessarily need to reach the load bearing capacity of the gallery, since it would correct the model for the real conditions. Even an impact in the elastic range would show whether the assumptions, which lead to ultimate load predictions, are correct. The test could be performed on any existing gallery, ideally before rehabilitation works take place. In this case, the reaction forces of the gallery cannot be measured, but bending reinforcement could be equipped with strain gages. By measuring the acceleration the predominant mode of motion could be obtained, which will be needed to evaluate the effective mass. Furthermore, the acceleration measurements would allow one to obtain the deflection of the gallery by double integration, which would be the most important value to calibrate the global response.

Notation

Roman capital letters

A	Loading area
A_{sw}	Cross-section area of stirrups
C	Coefficient for brittle or ductile failure
D	Dissipated energy, diameter of falling body
E	Energy
E_c	E-modulus of concrete
E_D	E-modulus for softening of concrete in tension after cracking
E_i	Kinetic impact energy
E_{rp}	Rebound energy
E_s	E-modulus of reinforcing steel
$F_{1,2,3}$	Force in springs $K_{1,2,3}$
F_{3y}	Yield loading
G	Shear modulus
G_F	Release energy from elastic deformation
H	Falling height of the impacting body
$I_{x,y}$	Moment of inertia
$K_{1,2,3}$	Stiffness of springs for cushion, shear and bending properties
K_{10}	Initial stiffness of cushion layer
$K_{21,22,23}$	Stiffness of punching for components of concrete, shear reinforcement and membrane effects
$L_{x,z}$	Span of concrete slab
M_b	Local bending moments
M_E	E-modulus of cushion layer
$M_{1,2,3}$	Mass of the impacting body, punching cone with part of cushion and rest of slab
M_{2sl}^*	Mass of the concrete of the punching cone
M_3	Modal mass for the rest of the slab
P	Impact loading
P_u	Concentrated load in ultimate state
R	Radius of impacting body, crack growth resistance
T	Thickness of cushion layer
$T_{2,3}$	Period of masses M_2 and M_3
V_1	Volume of active cone in cushion layer
V_2	Volume of passive cones in cushion layer
W	Weight of block

Roman small letters

$a_{1,2,3}$	Accelerations of masses M_1, M_2 and M_3
$c_{1,2,3}$	Damping coefficient for cushion, shear and bending properties

d	Slab thickness
e	Thickness of cushion layer
f	Frequency
f_{cm}	Mean strength of concrete
f_{ctm}	Mean tensile strength of concrete
f_{ctmd}	Mean dynamic tensile strength of concrete
f_s	Yielding strength of reinforcing steel
g	Earth constant of acceleration
h	Height of passive cone with volume V_2 , thickness of cushion layer
$h_{e,s}$	Final, starting position of the boulder
i	Coefficient for cushion layer
k_w	Coefficient for bending stiffness
l_w	Length of shear reinforcement
m	Number of periods, mass of block
m_u	Ultimate unit moment
n	Number of time steps for cracking through the slab section
p_{\max}	Maximum possible penetration
$r_{1,2}$	Upper and lower radius of a frustum
s	Spacing of bending reinforcement
s_{rp}	Rebound height
s_w	Spacing of shear reinforcement
t	Time, impact time
t_0	Start time of cracking
t_{cg}	Crack growing time
v	Velocity
v_1	Impact velocity
v_{1u}	Ultimate impact velocity
$v_{p,s}$	Compression and shear wave velocities
v_{cg}	Velocity of crack growing
x	Slab coordinate
$y_{1,2,3}$	Displacement of impacting body, punching cone and global system
y_e	Elastic deflection
z	Static depth, slab coordinate
z_0	Distance between tip of cone and cushion surface in Wolf's soil model
z_{cr}	Critical static depth

Greek letters

α	Factor for modal mass, dynamic increase factor, amplification factor for cushion layer
β	Angle of punching cone
γ_y	Newmark constant of Integration
$\gamma_{c,g}$	Density of concrete, gravel
Δt	Time step of integration

δ	Angle of load distribution in cushion layer
ε	Strain
$\zeta_{2,3}$	Damping ratio for punching cone, for bending behavior
η	Relative value
λ	Lame's constant
ν	Poisson's ratio
ξ	Transition function
ρ_w	Geometric reinforcement ration for shear
ν	Radical strain coefficient
φ	Angle of internal friction
χ	Ductility factor

Special symbols

\emptyset_b	Diameter of loading area on the cushion layer
\emptyset_{sl}	Diameter of loading area on the slab
\emptyset_w	Diameter of shear reinforcement
\emptyset_1	Diameter of bending reinforcement

Abbreviations

ASTRA	Federal Road Office (FEDRO)
ETH	Swiss Federal Institute of Technology
FE	Finite Element
IBK	Institute of Structural Engineering, ETH Zurich
IGT	Institute for Geotechnical Engineering, ETH Zurich
JSPS	Japanese Society for Promotion of Science
SBB	Swiss Federal Railways
SMDF	System of multiple degrees of freedom
WSL	Federal Institute for Forest, Snow and Landscape Research

Acknowledgements

I want to thank the highway authorities of the different cantons and the infrastructure divisions of the railways that provided access to their archives and for the transfer of valuable knowledge concerning rockfall galleries. Especially, I want to thank the highway authorities of the cantons Grisons and Uri, which financially supported the large-scale tests. Thanks also to the Federal Road Office (FEDRO) for funding the research project.

A sincere debt of gratitude is owed to Dr. A. Volkwein in appreciation of his most gracious assistance and for the exemplary collaboration within the different parts of the ETH Domain that allowed carrying out the experiments at the three different scales.

The ETH Zurich internal cooperation with related research topics of Dr. R. Chikatamarla and M. Schubert were highly appreciated. Also I would like to thank our former graduate students C. Ebner, R. Hess and D. Caduff, for their great efforts in conducting and evaluating tests. My special thanks are also addressed to the technical support of M. Baumann, C. Gisler and T. Jaggi (IBK), H. Richner (IfB), E. Bleiker and M. Iten (IGT) as well as B. Fritschi (WSL) and A. Müller.

The contributions of R. Gava and R. Hofmann (Kantonspolizei Zürich), C. Ambühl (AC-Sicherheitsdienst) and M. von Ah (Gasser Felstechnik AG) to the water hammer test are also gratefully acknowledged. Sincere thanks are addressed also to the companies Crestageo AG (Chur) for the casting of the slabs and Misapor AG (Landquart) for providing the cellular glass as well as to A. Roth and M. Denk (Geobrugg Protection Systems) for the productive cooperation during the experiments and for providing the special cushion systems in the medium and large scale tests, to H. Kienast (EMPA) for the falling weight device, to J. H. Schellenberg for his contribution to the successful performance of the large-scale tests and to W. Gerber (WSL) for providing and evaluating the high speed cameras.

I thank also Prof. Dr. A. Dazio (IBK), Dr. J. Laue (IGT), K. Bucher (Ernst Basler & Partner), Dr. W. Heierli and Prof. Dr. T. Krauthammer for the interesting discussions and for the willingness to productively criticize my ideas during the development of the model. My sincere appreciation goes also to Prof. em. Dr. N. Ishikawa and Prof. Dr. K. Fujikake (NDA, Japan) for the exchange of ideas and to Prof. Dr. H. Masuya and Prof. Dr. N. Kishi for the technical discussions that I really enjoyed.

The Japanese Society for Promotion of Science (JSPS) supported my research stay at Muroran Institute of Technology and allowed me to carry out the punching tests.

Special thanks are also addressed to A. Merkli and R. Arn for the notable contribution in reviewing my figures and the manuscript.

For the excellent time together at the Institute and their daily support, I want to acknowledge my current and former colleagues, Dr. I. Müllers, R. Bargähr, S. Fricker, S. Ghadimi, P. Fehlmann and T. Wolf.

I also wish to gratefully thank Prof. Thomas Vogel for backing this work all the way.

Acknowledgements

References

- Abdel-Rohman, M., Sawan, J. (1985). *Impact Effect on R.C. Slabs: Analytical Approach*, Journal of Structural Engineering, Vol 111, No. 7, ASCE, Paper No. 19863.
- Aggour, H., Sun, C.T. (1988). *Finite element analysis of a laminated composite plate subjected to circularly distributed central impact loading*, Comput Struct, 28, pp. 729-736.
- Ali, M.M. (2002). *Protective design of concrete buildings under blast loading*, Structures Under Shock And Impact VII, pp. 23-33.
- Ammann, W., Mühlmutter, M., Bachmann, H. (1981). *Untersuchungen über das Bruch- und Verformungsverhalten stossbelasteter Stahlbeton- und Spannbetontragwerke*, IBK Bericht Nr. 115, Birkhäuser, Basel, 39 pp.
- Ammann, W. (1983). *Stahlbeton- und Spannbetontragwerke unter stossartiger Belastung*, Dissertation, IBK Bericht Nr. 142, Birkhäuser, Basel, 285 pp.
- ARP (2003). *Galerien im Eingangsbereich von Tunnels, Sisikon-Flüelen Gruppe 6a-6c*, Technischer Bericht, Phase: Überprüfung, Projektverfasser: André Rotzetter + Partner, März 2003.
- ASTRA, SBB (1998). *Einwirkungen auf Steinschlagschutzgalerien*, Richtlinie, Bundesamt für Strassen, Baudirektion SBB, Eidgenössische Drucksachen- und Materialzentrale, Bern.
- ASTRA (2003). *"Steinschlag": Naturgefahr für die Nationalstrassen*; Schlussbericht der ASTRA-Expertengruppe.
- ASTRA (2008). *Einwirkungen infolge Steinschlags auf Schutzgalerien*, Richtlinie, Bundesamt für Strassen, Baudirektion SBB, Eidgenössische Drucksachen- und Materialzentrale, Bern.
- Bachmann, H., Ammann, W.J., Deischl, F., et al. (1995). *Vibration problems in structures: Practical guidelines*, Birkhäuser, Basel; Boston; Berlin, pp. 234.
- Bangash, T., Munjiza, A. (2002). *FEM/DEM modelling of R.C. beams under impact*, Structures Under Shock And Impact VII, pp. 519-528.
- Barr, P., Carter, P.G., Howe, W.D., Neilson, A.J. (1982). *Replica Scaling Studies of Hard Missile Impacts on Reinforced Concrete*, Symposium on Concrete Structures under Impact and Impulse Loading, Berlin, pp. 329-344.
- Bhatti, A.Q., Kishi, N., Konno, H. and Okada, S. (2006). *Effective mesh size distribution for numerical method of prototype RC girders under falling-weight impact loading*. 2nd International Conference on Design and Analysis of Protective Structures, Singapore, Nov. 13-15, pp. 261-272.

References

- Bažant, Z. P. (2004). *Scaling theory for quasibrittle structural failure*, PNAS, vol. 101, no. 37, pp. 13'400-13'407.
- Berner, K. (1981). *Der Einfluss der Dehngeschwindigkeit auf das mechanische Verhalten von Betonstählen*, 12. Forschungskolloquium des Deutschen Ausschusses für Stahlbeton, BAM, Berlin.
- Berhet-Rambaud, P. (2004). *Structures rigides soumises aux avalanches et chutes de blocs: modélisation du comportement mécanique et caractérisation de l'interaction "phénomène-ouvrage"*, Thèse doctoral, Université Grenoble 1, 286 pp.
- Biggs J.M. (1964). *Introduction to structural dynamics*. McGraw-Hill, New York, pp.341.
- Bischoff, P.H., Bachmann, H., Eibl, J. (1991). *Microcrack development during high strain rate loading of concrete in compression*, Eurodyn'90 European Conf. on Struct. Dynamics, Rotterdam, The Netherlands, Vol. 1, pp. 59–66.
- Bischoff, P.H., Perry, S.H. (1995). *Impact behavior of plane concrete loaded in uniaxial compression*, J. Eng. Mech. ASCE, Vol. 121, pp. 685-693.
- Block, K. (1983). *Der harte Querstoss - Impact - auf Balken aus Stahl, Holz und Stahlbeton*, Dissertation, Universität Dortmund, 141+11 pp.
- Brandes, K. und Limberger, E. (1985). *Zur Beeinflussung der Festigkeitskennwerte von Betonstahl durch die Dehngeschwindigkeit*. Beton- und Stahlbetonbau, 80:90-94 und 128-133.
- Broek, D. (1986). *Elementary engineering fracture mechanics*, Martinus Nijhoff Publishers, Dordrecht, 501 pp.
- Bucher, K. (1997). *Dynamische Berechnung von Steinschlageinwirkungen*, Proceedings, Schweizerische Gesellschaft für Boden und Felsmechanik, Montreux.
- Buzaud, E., Don, D., Chapelle, S., Gary, G., Bailly, P. (1999). *Perforation studies into MB50 concrete slabs*, Workshop 99: Material Test Procedures in Support of Dynamic Material Modelling.
- Buzzini, D., Dazio, A., Trüb, M., (2006). *Quasi-Static Cyclic Tests on Three Hybrid Fibre Concrete Structural Walls*, IBK Report Nr. 297, Institute of Structural Engineering, ETH Zurich.
- CEB - Comité-Euro-International du Béton (1988). *Concrete Structures under Impact and Impulsive Load*, Bulletin d'information N° 187, Draft TG V/14, Lausanne.
- Chauvel, D., Touret, J.-P., Stangenberg, F., Borgerhoff, M., Zinn, R. (2005), *Non-linear impact analysis of a concrete building*, Proceedings, 18th International Conference on Structural Mechanics in Reactor Technology (SMiRT 18), August 7-12, Beijing, pp. 1-8.
- Chikatamarla, R., Laue, J., Springman, S.M. (2004a). *Rock fall on protection galleries*. SEMC 2004, Cape Town, South Africa. 5-7 July 2004.

-
- Chikatamarla, R., Laue, J., Springman, S. M. (2004b). *Rockfall impact on protection galleries*, in Zingoni, A. (ed.): Progress in Structural Engineering, Mechanics and Computation, Tylor&Francis, London, pp. 1139-1144.
- Chikatamarla, R., (2006). *Optimisation of cushion materials for rockfall protection galleries*, Dissertation, Diss. Nr. 16315, ETH Zurich.
- Descoedres F., Montani, S. (1996). *Etude expérimentale de la chute de blocs impactant une dalle en béton armé recouverte par des matériaux amortissants*, Laboratoire de mécanique des roches, EPFL, VSS Bericht No. 524.
- Drake, J.L., Twisdale, L.A., et al. (1989). *Protective Construction Design Manual*, TR-87- 57, Air Force Engineering & Services Center, Tyndall Air Force Base Florida.
- Ebner, C. (2006), *Versuche zur dynamischen Tragfähigkeit von Stahlbetonplatten*, Diplomarbeit, IBK, ETH Zurich.
- Eibl, J., Keintzel, E., Charlier, H., (1988). *Dynamische Probleme im Stahlbetonbau, Teil II, Stahlbetonteile und -bauwerke unter dynamischer Beanspruchung*, Heft 392, Berlin, Deutscher Ausschuss für Stahlbetonbau, 1988.
- Eibl, J., Curbach, M. (1989). *An attempt to explain strength increase due to high loading rates*, Nuclear Engineering and Design, Vol. 112, pp. 45-50.
- Eibl, J. Klein, E. Kobler, G. (1994). *Verhalten von Betonkonstruktionen bei harten Stössen – Teil I: Betonverhalten bei hoher hydrodynamischer Beanspruchung*, Forschungsbericht, Institut für Massivbau und Betontechnologie, Universität Karlsruhe.
- Fujikake, K. (2007). *Response Analysis of RC Beams Subjected to Impact Loads*, Proceedings, Structures under Extreme Loading (Protect 2007), Whistler, Canada, p. 22 and CDROM file JPN07.pdf, pp. 1-10.
- Gholipour, Y. (2004). *Impact resistance of composite plate*, Structural Concrete, Vol. 5, 2, pp. 57-60.
- Goschy, B. (1990). *Design of buildings to withstand abnormal loadings*, Butterworths, London, 197 pp.
- Heidenreich, B. (2004). *Small- and half-scale experimental studies of rockfall impacts on sandy slopes*, Ph. D. thesis n° 3059, Ecole Polytechnique Fédérale de Lausanne.
- Heierli, W. (1995). Ingenieurbüro Heierli AG, Zurich, unpublished project documents.
- Hjorth O. (1976). *Ein Beitrag zur Frage der Festigkeit und des Verbundverhaltens von Stahl und Beton bei hohen Beanspruchungsgeschwindigkeiten*, Dissertation, TU Braunschweig, 188 pp.
- Hokkaido Development Bureau, Ministry of Land, Infrastructure and Transportation (2001). *Guideline for the design of structures to resist rockfall impacts* (in Japanese).

References

- Ishikawa, N. (1999). *Recent Progress on Rock-Shed Studies in Japan*, Proceedings of the Joint Japan-Swiss Scientific Seminar on Impact Load by Rock Falls and Design of Protection Structures, Ed. Masuya, H. and Labious, V., October 4-7, Kanazawa, Japan.
- Jacquemoud, J. (1999). *Swiss guideline for the design of protection galleries: background, safety concept and case histories*, Joint Japan-Swiss Scientific Seminar on Impact by Rock Falls and Design of Protection Structures, Kanazawa, Japan.
- Japan Road Association (1983). *Manual for anti-impact structures against falling rocks* (in Japanese).
- Japan Road Association (2000). *Manual for anti-impact structures against falling rocks* (in Japanese).
- Johansen, K.W. (1962). *Yield Line Theory*, Cement and Concrete Association, London, 181 pp.
- Johnson, W. (1972). *Impact Strength of Materials*, Edward Arnold, London, 361 pp.
- JSCE (1998). *Impact Resistant Design of Rock-Shed Structures*, Ed. H. Kobayashi, Subcommittee of Impact Problems, Japan Society of Civil Engineers (in Japanese).
- JSCE (2004). *Practical Methods for Impact Test and Analysis*, Ed. N. Kishi, Subcommittee of Impact Problems, Japan Society of Civil Engineers (in Japanese).
- KTA 2203 (1983) (aus [Brandes et al. 1985]): *Schutz von Kernkraftwerken gegen Flugzeugabsturz. Auslegung der baulichen Anlagen (bei vorgegebenen Lastannahmen)*. Entwurf.
- Kishi, N., Konno, H., Ikeda, K., Matsuoka, K.G. (2002a). *Prototype impact tests on ultimate impact resistance of PC rock-sheds*, International Journal of Impact Engineering, 97, pp. 969-985.
- Kishi, N., Mikami, H., Matsuoka, K.G., Ando T. (2002b). *Impact behavior of shear-failure-type RC beams without shear rebar*, Int J Impact Eng, Vol. 27, pp. 955-968.
- Kishi, N., Okada, S., Konno, H., Ikeda, K. (2003). *A consideration for constitutive model of sand element for estimation of impact analysis*, Journal of Structural Engineering, Vol. 49A 2003.3, pp.1323-1332. (in Japanese).
- Kishi, N., Mikami, H., Okada, S., Yoshida, H., Schellenberg, K. (2008). *Effects of sand cushion on impact resistant behavior of RC slabs under falling-weight impact test*. Proceedings of annual meeting of Hokkaido section of JSCE, 2008 (in Japanese).
- Kobarg, J. (1986). *Ein inkrementelles Stahl-Betonverbundgesetz unter Berücksichtigung von Stahldehnung und Querdruck*, Fortschritt-Berichte VDI, Nr. 76, Düsseldorf, 197 pp.
- Koller, M.G., Busenhart, M. (1986). *Elastic impact of spheres on thin shallow spherical shells*, Int J Impact Eng, Vol. 4, pp. 11-21.
- Korenev, B.G., Rabinovic, I.M. (1980). *Baudynamik*, VEB Verlag für Bauwesen Berlin, 628 pp.

-
- Kupfer, H., Zelger, C. (1973). *Das Verhalten des Betons unter mehrachsiger Kurzzeitbelastung unter besonderer Berücksichtigung der zweiachsigen Beanspruchung*, DAfStb, Heft 229, Berlin.
- Labrouse, V.; Descoedres, F. (1999). *Possibilities and Difficulties in predicting Rockfall Trajectories*, Proceedings of the Joint Japan-Swiss Scientific Seminar on Impact Load by Rock Falls and Design of Protection Structures; Kanazawa, Japan, 4-7 October 1999, pp. 29-36.
- Lee, D.I., Kwak, B.M. (1993). *An analysis of low-velocity impact of spheres on elastic curved-shell structures*, Int J Solids Struct, Vol. 30, pp. 2879-93.
- Lee, W.S., Lin, C.F. (2001). *Impact properties and microstructure evolution of 304L stainless steel*, Materials science and engineering, A38, pp. 124-135.
- Leppänen, J. (2002). *Dynamic Behaviour of Concrete Structures Subjected to Blast and Fragment Impacts*, Thesis, Chalmers University of Technology, Göteborg, 71 pp. & annexes.
- Liu, Z.S., Swaddiwudhipong, S. (1997). *Response of plate and shell structures due to low velocity impact*, J Eng Mech ASCE, Vol 123, 12, pp. 1230-1237.
- Liu, Z.S., Lee, H.P., Lu, C. (2004). *Structural intensity study of plates under low-velocity impact*, International Journal of Impact Engineering 31, 957-975.
- Marti, P., Alvarez, M., Kaufmann, W., Sigrist, V. (1999). *Tragverhalten von Stahlbeton*, IBK Publikation SP-008, Institut für Baustatik und Konstruktion, ETH Zürich, 301 pp.
- Masuya, H. , Labrouse, V. (Editors, 1999). *Impact Load by Rock Falls and Design of Protection Structures*, Proceedings Joint Japan-Swiss Scientific Seminar, October 4-7, 1999, Kanazawa, Japan.
- Masuya, H. (2005). *Impact problem concerning rock falls and research activities in related field in Japan*, Keynote Paper, Proceedings, 6th Asia-Pacific Conference on SHOCK & IMPACT LOADS ON STRUCTURES (SI05), December 7-9, 2005, Perth, Western Australia.
- Montani, S., Descoedres, F., (1996). *Etude expérimentale de la chute de blocs impactant une dale en béton armé recouverte par des matériaux amortissants*, EVED, Bundesamt für Strassen, Forschungsbericht Nr. 524, VSS, Zürich, 93 pp. & annexe.
- Montani, S. (1998). *Sollicitation dynamique de la couverture des galeries de protection lors de chutes de blocs*, Dissertation, Nr. 1899, École Polytechnique Fédérale de Lausanne, 190 pp.
- Mougin, J.-P., Perrotina, P., Mommessina, M., Tonnelob, J., Agbossou, A. (2005). *Rock fall impact on reinforced concrete slab: an experimental approach*, International Journal of Impact Engineering, Volume 31, Issue 2, February 2005, Pages 169-183.
- Muttoni, A. (2003). *Schubfestigkeit und Durchstanzen von Platten ohne Querkraftbewehrung*, Beton- und Stahlbetonbau, Band 98, Heft 2, pp. 74-84.
- Muttoni, A., Fernández Ruiz, M. (2008). *Shear strength of members without transverse reinforcement as function of critical shear crack width*, ACI Structural Journal, V. 105, No 2, pp. 163-172, Farmington Hills, USA.

References

- Newmark, N. M., (1959). *A Method of Computation for Structural Dynamics*, ASCE Journal of the Engineering Mechanics Division, Vol. 85 No. EM3.
- Newmark, N. M. (1962). *Air Force Design Manual: Principles and Practices for Design of Hardened Structures*, TDR 62-138, Air Force Special Weapons Center, Kirkland Air Force Base, New Mexico.
- Noels, L., Stainier, L., Ponthot, J.-P., Bonini, J. (2002). *Implicit-explicit time integration algorithms for the numerical simulation of blade/casing interactions*, Structures Under Shock And Impact VII, pp. 179-188.
- Norris, C.H., Hansen, R.J., Holley, M.J., Biggs, J.M., Namyet, S., Minami, J.K. (1959). *Structural Design for Dynamic Loads*, McGraw-Hill Civil Engineering Series, New York, Toronto, London, 453 pp.
- Nosier, A., Kapania, R.K., Reddy, J.N. (1994). *Low-velocity impact of laminated composites using a layerwise theory*, Comput Mech, Vol. 13, pp. 360-379.
- Ockert, J. (1997). *Ein Stoffgesetz für die Schockwellenausbreitung in Beton*, Schriftenreihe Inst. für Massivbau u. Baustofftechnologie, Heft 30, Dissertation Universität Karlsruhe.
- Ozbolt, J., Reinhardt, H.-W. (2005). *Dehnungsgeschwindigkeitsabhängiger Bruch eines Kragträgers aus Beton*, Bauingenieur, 06/2005, pp. 283-290.
- Pfaffinger, D. (1989). *Tragwerksdynamik*, Springer-Verlag, Wien, 327 pp.
- Public Works Research Institution (1995). *Report of the Impact Test on Rock Impact Force*, Report of PWRI, No. 3340.
- Reinhardt, H.W., Vos, E. (1980). *Bond Resistance of Deformed Bars, Plain Bars and Strands under Impact Loading*, Report Number 5-80-6, Delft University of Technology, Department of Civil Engineering
- Reinhardt, H. W. (1982). *Concrete under impact loading, tensile strength and bond*, Heron, Vol. 27, pp. 1-48.
- Rossmannith, H.P., Uenishi, K. (2005). *The Mechanics of Spalling and Scabbing in Concrete And Rock - A Reconsideration*, The 4th Kumamoto International Workshop on Fracture, Acoustic Emission and NDE in Concrete, p. 5.
- Sato, H., Mabuchi, T., Ishikawa, N., Enrin, H., Wakabayashi, O. (1999). *Study on impact resistance of rock-shed section model*, Joint Japan-Swiss Scientific Seminar on Impact Load by Rock Falls and Design of Protection Structures, 4-7 October 1999, Kanazawa, Japan. Ed. H. Masuya, V. Labiouse, pp. 59-64.
- Schaedler, S. (2004). *Ermittlung dreidimensionaler Starrkörperbewegungen anhand von Beschleunigungsdaten*, Diplomarbeit Fachhochschule Weingarten.
- Schellenberg, K., Vogel, T. (2005). *Swiss Rockfall Galleries - Impact Load*. Proceedings IABSE Symposium Lisbon 2005, 'Structures and Extreme Events', IABSE Zurich, 2005, pp. 302/303 and CD-ROM file LIS099.PDF, pp. 1-8.

Schellenberg, K. (2006). *Impact load tests on reinforced concrete slabs*, Proceedings, 6th International PhD Symposium in Civil Engineering 2006, Zurich, August 23-26, pp. 130/131 and CD-ROM file 230_Schellenberg.pdf, pp. 1-8.

Schellenberg, K., Volkwein, A., Roth, A., Vogel, T. (2006). *Rockfall – Falling weight tests on galleries with special cushion layers*, Proceedings, 3rd International Conference on Protection of Structures Against Hazards, September 28–29, Venice, pp. 251-258.

Schellenberg, K., Volkwein, A., Roth, A., Vogel, T. (2007a). *Large-scale impact tests on rock fall galleries*, Proceedings of 7th Int. Conference on Shock & Impact Loads on Structures, 17-19 October 2007, Beijing, pp. 497-504.

Schellenberg, K., Vogel, T. (2007b). *Tests and analytical model of rockfall impacts on galleries*, Proceedings of Protect2007, Structures under Extreme Loading, Aug. 20-22, Whistler, p. 27 and CD-ROM file SWO04_Schellenberg.pdf, pp. 1-10.

Schlüter, F.H. (1987). *Dicke Stahlbetonplatten unter stossartiger Belastung – Flugzeugabsturz*, Dissertation, Schriftenreihe des Instituts für Massivbau und Baustofftechnologie, Heft 2. Karlsruhe.

Schmidt-Hurtienne, B. (2001). *Ein dreiaxiales Schädigungsmodell für Beton unter Einschluss des Dehnrateneffektes bei Hochgeschwindigkeitsbelastung*, Massivbau Baustofftechnologie Karlsruhe, Heft 42, 259 pp.

Schubert, M., Straub, D., Faber, M.H. (2005). *Reliability of rock-fall protection galleries – A case study with a spezial focus on the uncertainty modeling*. Submitted paper to ICOSSAR 05, Rome.

Schwieger, H. (1973). *Vereinfachte Theorie des elastischen Balkenquerstosses und ihre experimentelle Überprüfung*. Konstruktiver Ingenieurbau, Berichte, Aus dem Institut für Konstruktiven Ingenieurbau der Ruhr-Universität Bochum, Heft 17, Vulkan-Verlag, Essen, pp. 25-53.

Soroushian, P., Choi, K.-B., Alhamad, A. (1986). *Dynamic Constitutive Behavior of Concrete*, ACI Journal Proceedings, Volume 83, Issue 2, pp. 251-259.

Stangenberg, F. (1973). *Berechnung von Stahlbetonbauteilen für dynamische Beanspruchung bis zur Tragfähigkeitsgrenze*, Konstruktiver Ingenieurbau, Berichte, Aus dem Institut für Konstruktiven Ingenieurbau der Ruhr-Universität Bochum, Heft 16, Vulkan-Verlag, Essen, 76 pp.

Stähli, P., van Mier, J. G. M. (2007). *Manufacturing fibre anisotropy and fracture of hybrid fibre concrete*, Engineering Fracture Mechanics, 74: 223-242.

Stiglat, K., Wippel, H. (1993). *Platten*, 3. Aufl., Berlin, München, Ernst & Sohn Verlag, 267 pp.

Studer, J.A., Laue, J., Koller, M.G. (2007). *Bodendynamik*, Springer, 3. Auflage.

Sun, C.T., Yang, S.H. (1980). *Contact low and impact response of laminated composite*, NASA CR-159884, Washington, DC.

References

- Süper, W. (1982). *Rechnerische Untersuchung stossartig beanspruchter Stahlbetonplatten*, Dissertation, Universität Dortmund, 193 pp.
- Tang, T., Malvern, L. E., Jenkins, D. A. (1992). *Rate effects in uniaxial dynamic compression of concrete*, J Eng. Mech., Vol. 118, pp. 108-124.
- Tang, Z.-P. , Xu, S.-L., Dai, X.-Y., Hu, X.-J. , Liao, X.-L., Cai, J. (2005). *S-wave tracing technique to investigate the damage and failure behavior of brittle materials subjected to shock loading*, International Journal of Impact Engineering, Vol. 31, 9, pp. 1172-1191.
- TM 5-1300, Joint Department of the Army, the Navy, and the Air Force (1990). *Structures to Resist the Effect of Accidental Explosions*, TM 5-1300/NAVFAC P-397/AFR 88-22.
- Toutlemonde, F., Rossi, P., et al. (1995). *Dynamic behaviour of concrete: tests of slabs with a shock tube*, Materials and Structures, Vol. 28, pp. 293-298.
- Volkwein, A (2004). *Numerische Simulation von flexiblen Steinschagschutzsystemen*, IBK Bericht Nr. 289, vdf Hochschulverlag an der ETH Zürich, 134 pp.
- Volkwein, A., Schädler, S., Fritschi, B., Grassl, H. (2005). *Spatial tracking of a falling rock using internal acceleration sensors*, EGU, Vienna.
- Volkwein, A., Labiouse, V., Schellenberg, K. (Organizers) (2008). Proceedings of Interdisciplinary workshop on rockfall protection, June 23-25, 2008, Morschach., 124 pp.
- Weerheim, J. (1992). *Concrete under impact tensile loading and lateral compression*, PhD Thesis, Delft University of Technology, 157 pp.
- Wolf, J.P. (1985). *Dynamic soil-structure interaction*, Englewood Cliffs, N.J., Prentice-Hall, ISBN 0-13-221565-9, pp. 466.
- Wolf, J.P., Preisig, M. (2003). *Dynamic stiffness of foundation embedded in layered halfspace based on wave propagation in cones*, Earthquake Engineering and Structural Dynamics, 32, pp. 1075-1098.
- Zielinski, A.J. (1982). *Fracture of concrete and mortar under uniaxial impact tensile loading*, PhD Thesis, Delft University of Technology, 148 pp.
- Zielinski, A.J., Reinhardt, H.W. (1982). *Impact Stress-Strain Behaviour of Concrete in Tension*, Symposium on Concrete Structures under Impact and Impulse Loading, Berlin, pp. 112-124.
- Zukas, J.A., Nicholas, T., Swift, H.F., Greszczuk, L.B., Curran, D. (1982). *Impact Dynamics*, John Wiley & Sons, New York, 452 pp.

Appendices

A. Structures considered in the survey

It was seen that to handle the large amount of information a well prepared questionnaire is indispensable. This questionnaire was filled for all considered structures from the archive of the structures owner

Additionally to the data, collected sketches of cross section, longitudinal section and situation are added into the database. Where available also pictures are added and the gallery is localized on a Swiss map.

Survey questionnaire	107
Example of the database	108
List of considered galleries	109

 Eidgenössische Technische Hochschule Zürich Swiss Federal Institute of Technology Zurich	Institut für Baustatik und Konstruktion ETH Hönggerberg CH-8093 Zürich Kristian Schellenberg dipl. Bauing. ETH +41-1-633 30 80 schellenberg@ibk.baug.ethz.ch www.ibk.ethz.ch																																				
Projektinterne Nummer Kanton <input type="text"/> Nr. <input type="text"/> Erfasst am: <input type="text"/>																																					
<u>Bestandesaufnahme der Steinschlagschutzgalerien</u>																																					
<table border="1" style="width: 100%; border-collapse: collapse;"> <tr> <td style="width: 50%;">Name: <input type="text"/></td> <td style="width: 50%;">BW: <input type="text"/></td> <td style="width: 50%;">Landeskarte 1:25000</td> </tr> <tr> <td>Gemeinde: <input type="text"/></td> <td>Kanton: <input type="text"/></td> <td>Nr.: <input type="text"/></td> </tr> <tr> <td colspan="2"> Strassen <input type="checkbox"/> Nationalstrasse <input type="checkbox"/> Kantonstrasse km: <input type="text"/> Bezeichnung: <input type="text"/> Strecke: <input type="text"/> </td> <td> Bahn km: <input type="text"/> Gesellschaft: <input type="text"/> Strecke: <input type="text"/> </td> </tr> <tr> <td colspan="3">Baujahr: <input type="text"/></td> </tr> <tr> <td colspan="3"> Typ: <input type="checkbox"/> Tunnelportal <input type="checkbox"/> vorgespannt <input type="checkbox"/> aufgelöster Querschnitt <input type="checkbox"/> Stahl-Betonverbund <input type="checkbox"/> Gewölbe <input type="checkbox"/> vorfabriziert <input type="checkbox"/> auskragende Konstruktion <input type="checkbox"/> Überdeckung Stärke: <input type="text"/> bis <input type="text"/> USCS-Klassifikation: <input type="text"/> Foto: <input type="text"/> Normalquerschnitt: <input type="text"/> Situation: <input type="text"/> </td> </tr> <tr> <td colspan="3"> Abmessungen Länge: <input type="text"/> Lichte Breite: <input type="text"/> Plattenstärke: <input type="text"/> Stützenabstand in Galerierichtung: <input type="text"/> </td> </tr> <tr> <td colspan="3"> Bewehrung Biegebewehrung in Galerierichtung: <input type="text"/> in Querrichtung: <input type="text"/> <input type="checkbox"/> Durchstanzbewehrung: <input type="text"/> </td> </tr> <tr> <td colspan="2"> Einwirkung Blockgrösse: <input type="text"/> Fallhöhe: <input type="text"/> </td> <td style="text-align: center;">Kommentar <input type="text"/></td> </tr> <tr> <td colspan="3"> Vorhandene Bauakten <input type="checkbox"/> Katasterplan <input type="checkbox"/> Projektpläne <input type="checkbox"/> Geologisch-geotechnische Gutachten <input type="checkbox"/> Statik <input type="checkbox"/> Ausführungspläne <input type="checkbox"/> Weiteres: <input type="text"/> Projektierender Ingenieur: <input type="text"/> </td> </tr> <tr> <td colspan="3"> Bemerkung <input type="text"/> </td> </tr> <tr> <td colspan="3"> Erfahrungen <input type="text"/> </td> </tr> <tr> <td colspan="3"> Ereignisse <input type="text"/> </td> </tr> </table>		Name: <input type="text"/>	BW: <input type="text"/>	Landeskarte 1:25000	Gemeinde: <input type="text"/>	Kanton: <input type="text"/>	Nr.: <input type="text"/>	Strassen <input type="checkbox"/> Nationalstrasse <input type="checkbox"/> Kantonstrasse km: <input type="text"/> Bezeichnung: <input type="text"/> Strecke: <input type="text"/>		Bahn km: <input type="text"/> Gesellschaft: <input type="text"/> Strecke: <input type="text"/>	Baujahr: <input type="text"/>			Typ: <input type="checkbox"/> Tunnelportal <input type="checkbox"/> vorgespannt <input type="checkbox"/> aufgelöster Querschnitt <input type="checkbox"/> Stahl-Betonverbund <input type="checkbox"/> Gewölbe <input type="checkbox"/> vorfabriziert <input type="checkbox"/> auskragende Konstruktion <input type="checkbox"/> Überdeckung Stärke: <input type="text"/> bis <input type="text"/> USCS-Klassifikation: <input type="text"/> Foto: <input type="text"/> Normalquerschnitt: <input type="text"/> Situation: <input type="text"/>			Abmessungen Länge: <input type="text"/> Lichte Breite: <input type="text"/> Plattenstärke: <input type="text"/> Stützenabstand in Galerierichtung: <input type="text"/>			Bewehrung Biegebewehrung in Galerierichtung: <input type="text"/> in Querrichtung: <input type="text"/> <input type="checkbox"/> Durchstanzbewehrung: <input type="text"/>			Einwirkung Blockgrösse: <input type="text"/> Fallhöhe: <input type="text"/>		Kommentar <input type="text"/>	Vorhandene Bauakten <input type="checkbox"/> Katasterplan <input type="checkbox"/> Projektpläne <input type="checkbox"/> Geologisch-geotechnische Gutachten <input type="checkbox"/> Statik <input type="checkbox"/> Ausführungspläne <input type="checkbox"/> Weiteres: <input type="text"/> Projektierender Ingenieur: <input type="text"/>			Bemerkung <input type="text"/>			Erfahrungen <input type="text"/>			Ereignisse <input type="text"/>		
Name: <input type="text"/>	BW: <input type="text"/>	Landeskarte 1:25000																																			
Gemeinde: <input type="text"/>	Kanton: <input type="text"/>	Nr.: <input type="text"/>																																			
Strassen <input type="checkbox"/> Nationalstrasse <input type="checkbox"/> Kantonstrasse km: <input type="text"/> Bezeichnung: <input type="text"/> Strecke: <input type="text"/>		Bahn km: <input type="text"/> Gesellschaft: <input type="text"/> Strecke: <input type="text"/>																																			
Baujahr: <input type="text"/>																																					
Typ: <input type="checkbox"/> Tunnelportal <input type="checkbox"/> vorgespannt <input type="checkbox"/> aufgelöster Querschnitt <input type="checkbox"/> Stahl-Betonverbund <input type="checkbox"/> Gewölbe <input type="checkbox"/> vorfabriziert <input type="checkbox"/> auskragende Konstruktion <input type="checkbox"/> Überdeckung Stärke: <input type="text"/> bis <input type="text"/> USCS-Klassifikation: <input type="text"/> Foto: <input type="text"/> Normalquerschnitt: <input type="text"/> Situation: <input type="text"/>																																					
Abmessungen Länge: <input type="text"/> Lichte Breite: <input type="text"/> Plattenstärke: <input type="text"/> Stützenabstand in Galerierichtung: <input type="text"/>																																					
Bewehrung Biegebewehrung in Galerierichtung: <input type="text"/> in Querrichtung: <input type="text"/> <input type="checkbox"/> Durchstanzbewehrung: <input type="text"/>																																					
Einwirkung Blockgrösse: <input type="text"/> Fallhöhe: <input type="text"/>		Kommentar <input type="text"/>																																			
Vorhandene Bauakten <input type="checkbox"/> Katasterplan <input type="checkbox"/> Projektpläne <input type="checkbox"/> Geologisch-geotechnische Gutachten <input type="checkbox"/> Statik <input type="checkbox"/> Ausführungspläne <input type="checkbox"/> Weiteres: <input type="text"/> Projektierender Ingenieur: <input type="text"/>																																					
Bemerkung <input type="text"/>																																					
Erfahrungen <input type="text"/>																																					
Ereignisse <input type="text"/>																																					

Appendices

FileMaker Pro - [Bestandesaufnahme]

File Edit View Insert Format Records Scripts Window Help

Datenbank der auf Steinschlag gefährdeten Galerien der Schweiz

K. Schellenberg
IBK, ETH Zürich

Projektinterne Nummer: SZ 201

Name: Galerie und Auskragung Ölberg Nord

BW: 524

Gemeinde: Morschach

Kanton: Schwyz

Erfasst am: 9. März 2005

Baujahr: 1994 - 96

Koordinaten: 689 320 / 202 800

Landeskarte Nr: 1171

Nationalstrasse: ja

Kantonsstrasse:

Bezeichnung: A4/N4

Bahngesellschaft:

Strecke: Brunnen - Altdorf

km: 131.100

Bild

Type:

- Tunnelportal: ja
- Gewölbe: nein
- vorgespannt: ja
- vorfabriziert: ja
- aufgelöster Querschnitt: nein
- auskragende Konstr.: ja
- Stahl Beton Verbund: nein
- Überdeckung: ja

Stärke der Überdeckung: 0.50 - 3.50

USCS Klassifikation:

Abmessungen:

- Länge: 146
- Lichte Breite: 14.35
- Plattenstärke:
- Stützenabstand:

Bewehrung:

- in Galerierichtung:
- in Querrichtung:
- Durchstanzbewehrung:

Einwirkung:

- Blockgröße:
- Fallhöhe:
- Kommentar:

Vorhandene Bauakten:

Projektiertender Ingenieur:

Erfahrungen:

Ereignisse:

Bemerkung:

Normalquerschnitt

Querschnitt 1:100

Situation

Ölberg SZ 201

Fruttlis Tord.

Wurmis Schellä Hint. Zingel 812

Stalden 775

835 835

SZ 202

Tannen 903

Schifserenegg 700

Schifseren SZ 203 Läntigen 679 655,9

Kartenausschnitt

Projektinterne...	Landes...	Name	Bauja...	Länge	Lichte Breite	Plattenstärke
SG 201	1134	Galerie Churfirsten	1977	150	8.10 bis 11.10 m	60 bis 70 cm
SG 202	1134	Galerie Mattstock	1981	110	8.10 - 11.10 m	0.70 m
SG 203	1114	Tunnel Chsellobel		23.25	11.25 m	1.15 m
UR 201	1171	Steinschlaggalerie Axen Süd	1975	225	8.60 m	0.40 bis 0.70 m
NW 201	1170	Steinschlagschutzbauten Galerie	1981	39.7	16 m	2.40 bis 1.50, dann
NW 202	1170	Steinschlagschutzbauten Galerie	1981	61	9 m bis 13.3 m	von 1.50 m abnehmend bis
NW 203	1170	Steinschlagschutzbauten Galerie	1981	20.15	9.20 m	bis 0.5 m
NW 204	1170	Steinschlagschutzbauten Galerie	1987	267	14.00 bis 20.00 m	HEB 360 + 0.25
NW 205	1170	Portal Acheregg (KWT-Nord) /	1964	30	20 m	
NW 206	1170	Portal Kirchwaldtunnel Süd	im Bau			
NW 207	1170	Portal KWT	im Bau			
NW 208	1170	Steinschlagschutzbauten	1981	34.5	ca. 9 m	von ca. 1.50 m auf 0.50 m
BE 201	1230	Galerie Marzoltitunnel	1985	42	8.5 m	0.5 m
BE 202	1210	Steinschlaggalerie Fuhren	1983/8	68.85	6.40 bis 9.80 m	Träger: 0.85 m ,
BE 203	1230	Steinschlaggalerie Schlagbächli	1974	32.65	6.50 m	0.30 m + 0.65 Träger alle
BE 204	1230	Lawinen- und Steinschlaggalerie	1980	59.20	8.40 m	Träger: 0.65 m (alle 5 m,
UR 202	1212	Galerie Güetli	1975	422	10.10 m + 11.80 m	0.65 bis 1.00 m
UR 203	1211	Galerie Fedenwald	1978	ca. 685		0.40 bis 0.70 m
UR 204	1212	Galerie Breitlau	1995	82.75	7.80 m	0.60 m
UR 205 MGB	1232	Oberalpsee	1913 /	740	Str. 7 m MGB 4.30	NP 38
UR 206	1211	Oberplattiflüe	1994	62	7.50 m	0.7 m
UR 207	1171	Galerie Schiltegg		152.50	8 m	HEA 400 + 0.25 m
UR 208	1171	Galerie 1, Südportal		18.45	8.00 m	HEA 400 + 0.25 m
UR 209	1171	Steinschlaggalerie Nordportal		60.28	~ 8 m	0.50 m (inkl. HEB300 in
UR 210	1171	Rekonstruktion Portal Süd	1999			
TI 201	1251	Galleria Ganne S. Antonio	1964	705		Vorfabrizierter Träger 0.90
TI 202	1251	Galleria Banchi	1968	41.50	9.50	Vorfabrizierter Träger 0.90
TI 203	1231	Galleria Scaglioni	1971/7	440	9.50	Vorfabrizierter Träger 0.90
TI 204	1353	Galleria Zona Sassa		32.60	8.40 Kragarm	Einpannung 0.90, bis 0.40
TI 205	1292	Galleria artificiale Ganna		80	oben 9.10 m	
BE 205	wo ?	Tunnel Sous les Roches, Portal	1997	17.5		0.4 - 0.9 m
BE 206	wo ?	Rugentunnel Portal West (Lea)	1979	11		0.45 m
BE 207	1227	Simmenfluhstollen Portal Port	2003	90		0.40 m
BE 208	1227	Simmenfluhstollen Portal Wimmis	2003	24.50		0.50 m
BE 209	1209	Chüebalmstollen Portal West	1980	43		0.45 - 1.50 m
BE 210	1209	Chüebalmstollen Portal Ost	1980	39.80		0.45 m
SBB 201	1168	Galerie Wiggentunnel	1950	7.25	8 m	0.80 m
SBB 202	1212	Galerie Bristenlau	1981	88.11	12.9 m	0.70m Vorfabri.
SBB 203	1212	Galerie Aecheribach	1946	47.82	9.81 m	Tot 89 cm
SBB 204	1212	Galerie Märchlisbach Nord		30.5	10.99	1.11
SBB 205	1212	Galerie Märchlisbach Süd	1989	30.5	10.99	1.11
SBB 206	1211	Galerie Hägggriger Nord	1978	30.15	10.8	1.11
SBB 207	1211	Galerie Hägggriger Süd	1978	30.15	10.8 m	1.11 m
SBB 208	1211	Galerie Kohlplatz	1970	33.26	11.55	0.8
SBB 209	1211	Galerie Rorbach	1983	29.81	11.8 / 10.8	1.05
SBB 211	1211	Galerie Rorbach Nord	1984	47.3	10.02	0.65
SBB 213	1211	Galerie Chohrlroneritikele	1988	46.35	10.83 m	1.06 m
SBB 214	1211	Galerie Steinchäle	1987	229.02	10.85 m	1.06 m
SBB 215	1211	Galerie Laubchäle	1989	85	15.5 m	1.06 m
SBB 216	1088	Galerie Hardwald	1998	36	6.05 ?	
SBB 217	1162	Galerie de protection				
GR 201	1274	Galleria Gorda Süd	1975	24.60	ca. 9.70	0.50 m
GR 202	1274?	Galleria Gorda Nord	1975			
GR 203	1274	Galleria Cozz	1967/7	424	9.50	0.75
GR 204	1274	Galleria Seda	1967/7	608	9.50	0.70 bis 0.85
GR 205	1274	Tunnel Land	1967/7	231	9.5 / 11.5	0.85
GR 206	1274	Galleria Cianca Pressella	1967/7	332.30	9.5	0.60 bis 0.85
GR 207	1274	Galleria Gei Süd	1967	17.2	7.5	0.50
GR 208	1274	Galleria Gei Nord	1966	33.6	7.5	0.5
GR 209	1234	Lawinengalerie Hohe Brücke	1977/8	225	7	0.675
GR 210	1235	Galerie Traversa Süd	1970	15.2	9.7	
GR 211	1235	Galerie Rofla Nord	1970	60	7.50	6
GR 212	1235	Galerie Rofla	1967	302		
GR 213	1235	Galerie Wegerhaus	1967			
GR 214	1235	Galerie Bargias Süd	1967	18		
GR 215	1215	Galeria Viamala Nord	1967	63		

Appendices

Projektinterne...	Landes...	Name	Bauja...	Länge	Lichte Breite	Plattenstärke
GR 216	1215	Galerie Trögli				
GR 217	1176	Galerie Chlus Ost	1986/8	40.50	9.70	var. 1.10
GR 218	1236	Lawinengalerie Sera	1987	54.26	9.30	0.70
GR 219	1256	Steinschlaggalerie Marmorera	1951/6	121.10*	7.15	0.50*
GR 220	1215	Galerie Rongellen 2 Nord	1967	30	8	0.42
GR 221	1215	Galerie Viamala 1	1937/3	91.2	7	0.7
GR 222	1215	Galerie Viamala 1 Verlängerung	1995/9	26.5	6 bis 6.6 m	
GR 223	1235	Galerie Viamala 2	1952	71	8.1	0.80
GR 224	1199	Steinschlaggalerie Tasna	1956	50	8 - 9	0.70
GR 225	keine,	Galerie Val Mundin - Val Zipla	1965/6	360	9.8	0.70 - 0.50
GR 226	keine,	Galerie Val Funtana	1969/7	77.50	8.8	0.70
GR 227	1215	Galerie West Passmal	1966	20.23	7	0.44
GR 228	1215	Galerie Ost Passmal	1966	9.80	7	0.44*
GR 229	1215	Galerie West Solistunnel	1971	15.8	7.8	0.75
GR 230	1216	Galerie Ostportal	1972	10	7	0.50
GR 231	keine,	Galerie Val Chasté	1975	63	7.05	0.75 - 0.50
GR 232	keine,	Galerie Val Pischöt				
GR 233	keine,	Galerie Val Alpetta	1973	37.50	7 - 8	0.75
GR 234	keine,	Galerie Val Sablunera	1965/6	31.4	7.28 - 7.39	0.45*
GR 235	1179	Galerie Laubtal	?	31.55	7	0.7
GR 236	1294	Lawinengalerie Tiieda	1988	20.3	7.6	0.75 - 0.50
GR 237	1294	Lawinengalerie Segheria Buseno	1989/9	56.80	7.60	0.75 - 0.60
GR 238	1274	Galleria antivalanga Santa	1986/8	80	7	0.90
GR 239	1235	Lawinengalerie Val Verda	1976	48.60	6.80	0.70
GR 240	1255	Galerie Val Digi Uors	1956/7	50 +	6.75	0.65
GR 241	1255	Valle di Lei Stutz, Galerie 1	1962	16.50		Träger alle 0.494
GR 242	1214	Val da Pruastg				
GR 243	1214	Rieinertobel 2A	1981/8	43.20	7	0.35*
GR 244	1214	Rieinertobel 2B		123	7	0.35*
GR 245	1214	Rieinertobel 2C		76.50	7	0.35*
GR 246	1234	Galerie Hundsschipfe 2	1971	30.50	7 m	0.50 - 0.40 m
GR 247	1234	Galerie Hundsschipfe 1	1970/7	62.80		
GR 248	1234	Galerie Steintöbeli 2	1972	36	7	50
MGB 201	wo ?	Schafgraben	1966	262		
MGB 202	1348	Luegelwang	1932	322		
MGB 203	1328	Schusslaui	1933	236		
MGB 204	wo ?	Kalter Boden - Schilten	1933	730		
MGB 205	1250	Täschwang	1932	642	4.70 m (Verl. 89)	0.40 m (Verl. 89)
MGB 206	1270	Jungbach	1970/7	290	4.70 m	0.27 m
MGB 207	1269	Tschong (-bach)	1962	115	Geschl.: ca. 4.50; Offen 5 m	0.45 m (Rückwand 0.50
MGB 208	1270	Niederwald	1975	160		
MGB 210	wo ?	Calmot I	1913/2	412		
MGB 211	wo ?	Calmot II	1913/2	412		
MGB 212	1231	Steinli Ia	1969	155	4.30 m	0.12 m
MGB 213	1231	Steinli Ib	1988	92	ca. 4.30	0.12 m + HEA220 alle 1.5
MGB 214	1231	Steinli II	1988	38	ca. 4.30	0.12 m + HEA220 alle 1.5
MGB 215	1231	Steinlikehr		184	ca. 5.60 bis 8.70 (in	0.60 m inkl. HEA alle 2m
MGB 216	1231	Spränggi	1913	113	ca. 6 m	Tot 0.65 m, inkl HEB 400;
MGB 217	1231	Brüggwald	1913	136	5.60	0.14 m Platte +
MGB 218	1231	Urnerloch	1972	61	5.70	0.28 Platte + HEB 450
MGB 219 UR	1231	Urnerloch II	1970/7	65	var.	0.25 m
MGB 220 UR	1231	Nasse Kehle	1983	253.2	15	0.26
BLS 201	1247	Fuerten Steinschlaggalerie		22.50	R= 4.70	1.35
BLS 202	1247	Steinschlaggalerie	1986/8	98	10	25 cm Stahlbeton +
BLS 203	1288	Steinschlaggalerie Schmalholz	1954	42	5,15	0.55 m
BLS 204	1288	Steinschlaggalerie im äusseren	1952	106	4.80	0.50
BLS 205	1288	Marchgrabengalerie	1955	38		
BLS 206	1288	Steinschlaggalerie Lipenplatten	1965	39	8.90 m	
GR 219a	1256	Steinschlaggalerie Marmorera	1962	14.50		0.50 + Rahmenträger
GR 249	1234	Galerie Steintöbeli 1	1970			
GR 250	1234	Galerie Im Schmiedeli	1969	96*	7	0.50**
GR 251	1235	Galerie Bagn de Ferrera 1	1956	49.50	5.80	0.12*
GR 252	1235	Galerie Bagn de Ferrera 2	1956	82.50	5.80	0.12*
GR 253	1213	Galerie Caschlatsch	1956	19.20	8 - 8.50	0.6
GR 254	1213	Galerie Tuf	1956/5	61	8.55	
GR 255	1213	Galerie las Ruinas	1971	127.95	9 - 9.80	0.90*

A. Structures considered in the survey

Projektinterne...	Landes...	Name	Baujahr	Länge	Lichte Breite	Plattenstärke
GR 256	1213	Galerie Val Zagrendra I	1953	21	7.50 - 8.30	0.60
GR 257	1213	Galerie Val Zagrendra II	1954	31.70	7.90 - 8.30	0.60
VS 201	1304	Galerie du Contour Noir	1985	87.3	6	50 cm mit Unterzügen de
VS 202	1328	Lawinengalerie Zen Meiggern	P	200.8	6.5	
VS 203	1270	Galerie du Laubach	1987	75.83	5.5	Galerie semi ouverte B.A.
VS 204	1309	Pradetschgalerie	-	24	3.5	0.30 m
VS 205	1309	Lärtschigrabengalerie	1995	115	4.3	Dalle pleine en b.a sur
VS 206	1309	Egggrabengalerie 1	1971	24	3.4	0.30 m
VS 207	1309	Egggrabengalerie 2 A	1974	72	4.6	Dalle pleine en béton armé
VS 208	1309	Egggrabengalerie 2 C	1974	8.1	5.25 m	Dalle en BA
VS 209	1286	Galerie des Rousses 3	-	25	5.2	Aval 7 HEB 300/300/19,
VS 210	1286	Galerie de la Tenache 1	-	27.5	4.25	Aval 12 HEB 300/300/19,
VS 211	1286	Galerie de la Tenache 4	-	35	6.5	aval :17 poteaux HEB
VS 212	1327	Galerie de la Combe 1 Forclaz	1956	22	4.65	Sommiers en b.a. H = 65
VS 213	1327	Galerie de la Combe 2 Forclaz	1956	17	4.65 m	Sommiers en b.a. H = 65
VS 214	1268	Schluchlauigalerie Goppenstein	1959	230	6.10	0.30 - 0.50
VS 215	1268	Ritigalerie 1 Schwere	1988	88	7	0.70 - 0.90
VS 216	1268	Ritigalerie 2 Mittlere	1988	161.5	7	0.80
VS 217	1268	Faldumgalerie 1	1967	20.52	6.5	0.42 m
VS 218	1268	Faldumgalerie 2	1967	85.99	6.5	Dalle en b.a. 42 cm
VS 219	1268	Faldumgalerie 3	1967	89.85	6.5	0.42
VS 220	1268	Golmbachgalerie 1 A	1971	16.5	6.5	Dalle pleine en b.a.
VS 221	1268	Golmbachgalerie 1 B	1974	63.5	6.5	Dalle pleine encastree en
VS 222	1268	Golmbachgalerie 1 C	1974	40	6.5	Dalle en b.a. ép. 42 cm
VS 223	1268	Golmbachgalerie 2 A	1972	36.4	6.5	Dalle pleine en b.a. ép. 42
VS 224	1268	Golmbachgalerie 2 B + C	1969	100	6.5	0.42 m
VS 225	1268	Golmbachgalerie 2 D + E	1969	88	6.5	0.42 m
VS 226	1268	Golmbachgalerie 3	1975	72	6.5	0.42 m
VS 227	1268	Blötzagalerie	1993	264.65	7	0.75 m
VS 228	wo ?	Galerie (Mauvoisin-Col de	-			
VS 229	1287	Trittjigalerie Albinen	1981	86.47	6.5	0.5 m
VS 230	1267	Galerie du Portail nord Flaschen	1978	32.8	6.8	0.50 m
VS 231	wo ? (P)	Galerie Aval des Croisettes	P	55	6	
VS 232	1307	Galerie Amont des Croisettes	1947	60.7	6	0.20 m
VS 233	1307	Galerie Sous Torrent de Vissioie	1951	10.7	6.2 m	0.35 m
VS 234	1307	Galerie de la Loverêche	2002	70	7 m	Dalle ba 70 à 85 cm
VS 235	1307	Galerie de Pralong	P	100		
VS 236	1306	Galerie des Cretaux Est	1989	5.8	6	im Scheitel 0.40 m
VS 237	1306	Galerie des Cretaux Ouest	1989	7.8	6	im Scheitel 0.40 m
VS 238	1305	Galerie de Roselin	1979	24	7	0.55 m
VS 239	1306	Galerie de Mourty	1981	253.06	7 m	0.50 m
VS 240	1327	Galerie de Petit-Pont	2002	43.6	7.15 m	0.80 m
VS 241	1327	Galerie d'entrée du tunnel	1970	43	4.37	Dalle préfabriquées en b.a
VS 242	1327	Galerie centrale du tunnel	1959	24.4	5.2	0.30 m
VS 243	1327	Galerie de sortie du tunnel	-	65.65	4.72 m	Dalle en b.a. sur 16
VS 244	1327	Prolongation Galerie de sortie du	2002	37.3	6.6	0.70 m
VS 245	1327	Galerie de Perire	1995	143	6.6	0.50 bis 0.70 m
VS 246	1327	Galerie La Savanne	P	71.5	7.6 m	0.60 m
VS 247	1327	Galerie de Zano	1971	140.2	6 m	Dalle préfabriquée sur 34
VS 248	1327	Galerie de Zano II	P			
VS 249	1306	Galerie de l'Aa	1990	170	7	0.80 m
VS 250	1286	Galerie de Fonjalles 2	1961	20.8	5 m	Tunnel en béton en 4
VS 251	1286	Galerie de Fonjalles 3	1963	10.5	6 m	Tunnel en béton
VS 252	1286	Galerie de Fonjalles 4	1991	36	6 m	Tunnel en béton
VS 253	1286	Galerie de la Lozde Grimisuat	1999	54	7.5 m	0.50 m
VS 254	1305	Galerie du Cherrier	1983	35	7 m	0.60 m
VS 255	1305	Galerie de liaison Cherrier-Metin	1986	37.7	7 m	0.60 m
VS 256	1305	Galerie du Metin	1982	25	7	0.50 m
VS 257	1305	Galerie de la Crête	1982	40	7 m	0.50 m
VS 258	1305	Galerie des Combes	1979	115	6.5 m	0.40 m ?
VS 259	1305	Galerie de Villy	1982	62.5	6.5 m	
VS 260	1345	Galerie de la Sasse	1970	120.8	7 m	Dalle en b.a. sur multi-
VS 261	1289	Tunnel Brig-Naters	1996	146	9 m	0.60 bis 0.80 m
VS 262	1270	Galerie de Niederwald	1972	163	7 m	0.50 m
VS 263	1270	Galerie de Wilerbach à Blitzingen	P	178	7.5 m	
VS 264	1270	Hilperbachgalerie Blitzingen	1973	250	7	0.47 m

Appendices

Projektinterne...	Landes...	Name	Bauja...	Länge	Lichte Breite	Plattenstärke
VS 265	1250	Mühlebachgalerie 1 West	1993	570	7.5	0.65 m
VS 266	1250	Mühlebachgalerie 1a Wendeplatte	1993	42	15 m	0.40 m
VS 267	1250	Mühlebachgalerie 2 Ost	1993	470	7.5 m	0.82 m
VS 268	1250	Jostbachgalerie 1	1990	105	7.5 m	0.60 m
VS 269	1250	Jostbachgalerie 2	1990	195	7.5 m	0.60 m
VS 270	1324	Galerie de Tête-Noire 1 Aval	1965	28.78	7 m	0.50 m
VS 271	1324	Galerie de Tête-Noire 2 Amont	1965	26.2	7	0.50 m
VS 272	1325	Portail Nord du tunnel	1991	60	7.50 m	0.35 m
VS 273	1325	Portail Sud du tunnel	1991	63	7.50 m	0.50 m
VS 274	1325	Galerie de protection du Lavanchy	2005	75	11.5 m	
VS 275	1325	Galerie du Tiercelin	1969	62.4	10.9 m	Aval galerie légère sur 5
VS 276	1325	Galerie de la Monnaie	1976	98.98	8 m	0.40 m
VS 277	1325	Galerie de la Ravennaz	1984	170	10.5 m	0.80 m
VS 278	1325	Galerie du Lavanchet	1986	128.5	10.5 m	0.80 m
VS 279	1345	Galerie de Sorevy 1	1982	80	7.5 m	0.50 m
VS 280	1345	Galerie de Sorevy 2	1982	280	7.5	0.75 m
VS 281	1345	Galerie de Sorevy 3	1982	160	7.5 m	0.75 m
VS 282	1345	Gal. N1 Valsorey 0-36	1962	1075	8 m	Aval:sommier sur piliers
VS 283	1345	Gal. R2 Mottey 36-38	1962	60	8 m	
VS 284	1345	Gal. N3 Mottey 38-41	1962	90	8 m	
VS 285	1345	Gal. R4 Mottey 41-43	1962	60	8 m	
VS 286	1345	Gal. N5 Mottey 43-45	1962	60	8 m	
VS 287	1345	Gal. R6 Fourtse 45-47	1963	60	8 m	
VS 288	1345	Gal. S7 Fourtse 47-47B	1974	10	8 m	
VS 289	1345	Gal. N8 Fourtse 47B-49	1974	55	8 m	
VS 290	1345	Gal. R9 Fourtse 47-51	1962	60	8 m	
VS 291	1345	Gal. N10 Petacrot 51-57	1962	180	8 m	Aval et amont sommiers
VS 292	1345	Gal. R11 Petacrot 57-58	1962	30	8 m	Aval et amont sommier su
VS 293	1345	Gal. L12 Petacrot 58-68	1962	280	8 m	0.35 m
VS 294	1345	Gal. R13 Les Toules 68-70	1962	60	8 m	Aval sommier sur piliers
VS 295	1345	Gal. N14 Les Toules 70-72	1962	60	8 m	Sommiers en b.a. sur
VS 296	1345	Gal. R15 Les Toules 72-74	1962	50	8 m	Sommier sur piliers
VS 297	1345	Gal. L16 Les Toules 74-77e	1962	120	8 m	Aval sommier sur piliers e
VS 298	1345	Gal. NS 17 Les Toules 77e-80	1962	70	8 m	0.60 m total ?
VS 299	1345	Gal. RS 18 Les Toules 80-81a	1991	37	8 m	0.60 m total ?
VS 300	1345	Gal. RS19 Les Toules 83-87	1986	130	8 m	xx + 0.60 m Ortbeton
VS 301	1365	Gal. N20 Matcheby 87-89	1962	60	8 m	Aval et Amont :sommier
VS 302	1365	Gal. R21 Matcheby 89-90	1962	30	8 m	Aval et amont sommier su
VS 303	1365	Gal. N22 Matcheby 90-93	1962	90	8 m	Aval et amont sommier su
VS 304	1365	Gal. R23 Matcheby 93-96	1962	90	8 m	Aval et amont sommier e
VS 305	1365	Gal. N24 Ballerones 96-101	1962	150	8 m	Aval et amont piliers et
VS 306	1365	Gal. R25 Ballerones 101-113	1962	350	8 m	Aval et amont piliers et
VS 307	1365	Gal. L26 Ballerones 113-115	1962	70	8 m	Aval sommier en b.a sur
VS 308	1365	Gal. R27 Pieudet 115-123	1962	240	8 m	Aval et Amont sommier su
VS 309	1365	Gal. R28 de Petemont 123-126	1962	90	8 m	Aval et amont sommiers e
VS 310	1365	Gal. R29 Petemont 126-128	1962	60	8 m	Aval et amont sommier er
VS 311	1365	Gal. N30 Petemont 128-147	1962	570	8 m	Aval : piliers en b.a. Amor
VS 312	1365	Gal. R31 Plan du Jea 147-155	1962	240	8 m ? (aussen 11 wie die	
VS 313	1365	Gare routière 165 - tunnel	1962	200	11 m	
VS 314	1365	Gal. de Bourg - St. Bernard	1987	90	4.5 m	0. 60 m
VS 315	1308	Guggeligrabengalerie	1961	48	5.85 m	
VS 316	1308	Deibfelsgalerie 1 Aval	1961	44.3	6.85 m	0.45 m ca.
VS 317	1308	Deibfelsgalerie 2 Amont	1961	4.55	6.55 m	0.30 m
VS 318	1308	Fallauinengrabengalerie	1957	52.5	7.1 m ? < Largeur de chaussée	
VS 319	1308	Butzigrabengalerie	1955	48	6.7 m	0.38 m
VS 320	1308	Eistbachgalerie 1	1954	24.6	7.1 m	0.42 m
VS 321	1308	Eistbachgalerie 2	1954	47.7	7.25 m	0.38 m
VS 322	1308	Fluhgrabengalerie 4	1971	22.5	7.5 m	0.55 m
VS 323	1308	Fluhgrabengalerie 1	1971	27.8	7.5 m	0.52 m
VS 324	1308	Fluhgrabengalerie 3	1971	67.5	7.5 m	0.55 m
VS 325	1308	Fluhgrabengalerie 2	1971	18	7.5 m	0.52 m
VS 326	1308	Fluhgrabengalerie 6	1972	58.5	7.5 m	0.55 m
VS 327	1308	Fluhgrabengalerie 5	1972	31.5	7.5 m	0.55 m
VS 328	1308	Hutegggalerie	1953	69	7.1 m	0.38 m
VS 329	1308	Dreikreuzgalerie	1956	49.2	5.5 m	0.34 m
VS 330	1308	Sonnegggraben gallerie	1961	48.5	5.6 m	dalle pleine en b.a.

Projektinterne...	Landes...	Name	Bauja...	Länge	Lichte Breite	Plattenstärke
VS 331	1308	Zen-Walkengalerie 0	P	40		
VS 332	1308	Zen-Walkengalerie 1	1989	212	8.55 m	dalle pleine en b.a.
VS 333	1308	Zen-Walkengalerie 2	1985	36.6	8.55 m	dalle pleine en b.a.
VS 334	1308	Zen-Walkengalerie 3	1985	92.4	8.55 m	dalle supérieure pleine en
VS 335	1308	Zen-Walkengalerie 4	1985	34.8	8.55 m	dalle pleine en b.a.
VS 336	1308	Galerie Martiswald	P	78		
VS 337	1308	Gal. Stägjitschuggen Prol. Nord	1978	.1		
VS 338	1308	Gal. Stägjitschuggen Prol. Sud	P	.1		
VS 339	1308	Galerie de Stägjitschuggen	1976	116	7 m	0.40 m = Balken +
VS 340	1308	Grossergrabengalerie	1968	59.5	8.2 m	0.60 bis 0.90 m
VS 341	wo ?	PI Galerie de la Torma	2001	51	9.4 m	0.75 m
VS 342	1288	Portail Nord Mittal	1985	132	7.5 m	0.40 m
VS 343	1288	Lawinengalerie Mittal 1	1987	225	7.5m	0.65 m
VS 344	1288	Lawinengalerie Mittal II A	1990	150	7.5 m	0.60 m
VS 345	1288	Lawinengalerie Mittal II B	1990	290	7.5 m	0.60 m
VS 346	1288	Lawinengalerie Mittal II C	1990	100	7.5 m	0.60 m
VS 347	1288	Schintigrabengalerie	2003	184.5	7.5 m	Dalle b.a.
VS 348	1268	Stockgrabengalerie Verlängerung	2000	50	7.5 m	0.75 m
VS 349	1268	Stockgrabengalerie	1988	115	7.5 m	0.75 m
VS 350	1268	Rotlauigalerie II Verlängerung	1988	65.5	7 m	0.66 m
VS 351	1268	Rotlauigalerie I	1961	217.8	6.6 m	0.65 m
VS 352	1289	Alpen Galerie No 092	1967	180		
VS 353	1289	Beichtstuhlgalerie No 088-2	1972	128		
VS 354	1289	Brücke Untere Galerie No 099	1967	10		
VS 355	1309	Casermettagalerie No 089	1960	347		
VS 356	1309	Engigalerie No 065	1967	201		
VS 357	1289	Fiqinen Galerie No 093	1973	75		
VS 358	1289	Furrirabengalerie No 080	1982	300		
VS 359	1289	Galerie Kapf-Schallbett No 053	1966	260		
VS 360	1289	Galerie Schallbett-Kulm No 054	1969	70		
VS 361	1309	Hohsteg Galerie No 088-1	1957	91		
VS 362	1289	Jodigu-Hittini Galerie No 085	1983	250		
VS 363	1289	Josefsgalerie No 057	1965	270		
VS 364	1289 ?	Kapfgalerie 1 No 052	1967	45		
VS 365	1289	Meggerigalerie No 051	1969	410		
VS 366	1309	Ober Gondo Galerie No 097	1967	140		
VS 367	1289	Schreindgalerie No 088-3	1958	125		
VS 368	1289	Unt. Mittenbächgalerie No 047	1966	279		
VS 369	1309	Untere Gondogalerie No 099	1967	187		
VS 370	wo ?	Galerie Couv. St.-Maurice N 004	1984	1160		
VS 371	wo ?	Ouvr.Prot.Canal-Fuite EOS 104	1987	5.3		
VS 372	1365	GAL. N32 PLAN DU JEU 155 - 162	1962	210		
VS 373	1365	GARE ROUTIERE 165 - Tunnel	1962	200		
VS 374	1324	GAL. DE PROTEC. DU TRIENT 1	0	99	3.9 m	
VS 375	1324	GAL. DE PROTEC. DU TRIENT 2	0	65.7	4.1 m	
VS 376	1309 ?	PONT GALERIE EGGGRABEN 2 B	1974	22.75	5.3 m	nicht bekannt
VS 377	1325	GALERIE AVAL DE GUEUROZ	1972	21		0.30 m
VS 378	wo ?	GAL. DE PROT. SOUS LE MONT	1975	32	5 m	0.20 m
VS 379	1328	GALERIE TÄSCHWANG 1 Leicht	1990	60.8	6.5 m	0.40 m
VS 380	1328	GALERIE TÄSCHWANG 2 Schwer	1990	130.8	6.5 m	0.40 m
VS 381	1328	GALERIE TÄSCHWANG 3 Leicht	1990	70.8	6.5 m	0.40 m
SBB 212	1211	Galerie Rorbach Süd	1984	43.45	10.72	0.65
UR 214	1231	Untere Lawinengalerie Heuegg	1968 /	251 /	7.23	0.20 / 0.25 / 0.30
UR 215	1231	Ob. Lawinengalerie Tanzenbein	1984	44	7.23 m	0.20 m
UR 216	1231	Ob. Lawinengalerie Tanzenbein	1962 /	79.40	7.23	0.25
UR 217	1231	Ob. Lawinengalerie Tanzenbein	1966	195.6	7.23 m bis 7.65 m	0.25 m
UR 218	1231	Ob. Lawinengalerie Tanzenbein	1969	230	7.40 bis 8.14	0.16 / 0.24 / 0.29
UR 219	1231	Obere Lawinengalerie Tanzenbein	1952 *	80	ca. 7 m	0.30 m
UR 220	1231	Obere Lawinengalerie Tanzenbein	1985	59	7.55 m	0.20
BE 205a	wo ?	Tunnel Sous les Roches, Portal	1997	57.5		0.4 - 0.9 m
BE 206a	wo ?	Rugentunnel Portal West (Rita)	1979	16.35		0.45 m
GR 245a	1214	Rieinertobel D		61.80	7	0.35*
UR 221	1231	Galerie Brüggwaldboden (Teil A)		ca. 160	var. ca. 7.20 m	0.25 m
UR 222	1231	Galerie Brüggwaldboden (Teil B)		ca. 216	var. ca. 7.20	0.25
UR 223	1171	Lawinengalerie Buggital	1982	67.5 m	var. max. 11.6 m	0.70 m
UR 224	1171	Leichte Galerie Buggital	1982	69.5 m	7 - 7.50 m	0.55 m

Appendices

Projektinterne...	Landes...	Name	Baujahr...	Länge	Lichte Breite	Plattenstärke
UR 225	1171	Galerie Tellspalte	1991	144.8	var. 7 bis 9	0.90
UR 226	1171	Steinschlaggalerie Zarenkopf	1982	ca. 68	8.4	0.65
UR 227	1172	Steinschlaggalerie Geissrücken	1978	56.8	9	0.6 - 0.8
UR 228	1191	Lawinengalerie Fischlauwi	1979	90.64	10.94 + 10.94	0.35
UR 229	1212	Lawinengalerie Wilerplanggen	1975	601.6	9.48 m + 11.4 m	0.24
UR 230	1211	Lawinengalerie Ripplistal	1975	562.6	9.48 m + 11.4 m	0.24 resp. 0.34
UR 231	1211	Lawinengalerie Pfaffensprung	1974	374.6	9.57 m + 11.49 m	0.30
UR 232	1211	Galerie Schöni	1977	160	9.50 m + 11.60 m	0.30 / 0.34
UR 233	1231	Tagbautunnel Steglau	2000	178.09	9.40	0.90
UR 234	1231	Steinschlaggalerie	2000	147.31	9.50 - 15.00	0.85 - 1.00
SZ 201	1171	Galerie und Auskragung Ölberg	1994 -	146	14.35	
SZ 202	1171	Steinschlaggalerie Ölberg Süd bis	1968 -	815	9 bis 12 m	0.20
SZ 203	1171	Steinschlaggalerie Schiferelegg	1968 -	260	9 bis 12 m	0.20
SZ 204	1171	Steinschlaggalerie Dorni Nord	1968 -	25	9 bis 12 m	0.20
SZ 205	1171	Steinschlaggalerie Dorni Süd	1968 -	40	9 bis 12 m	0.20
SZ 206	1171	Galerie Fallenbach	1985 -	240	12	0.80 - 0.95
MOB 201	1264	Rapes de Jor VI - Galerie	1895	122		
MOB 202	1245	La Tine - Galerie		124	4.6	0.60
MOB 203	1264	Galerie des 5000	1971	53	Kragarm 2.60, davon bis	0.18
MOB 204	1264	Galerie Pare - neige (entre	1971	21	3.6	0.20
MOB 205	1264	Galerie Gardiol	1929,	54		Ergänzung 0.14
MOB 206	1264		1966	62		0.20
MOB 207	1264	Galerie avant tunnel	1993	186	5	HEA 200 + Holzschwellen

B. Test results of large-scale tests

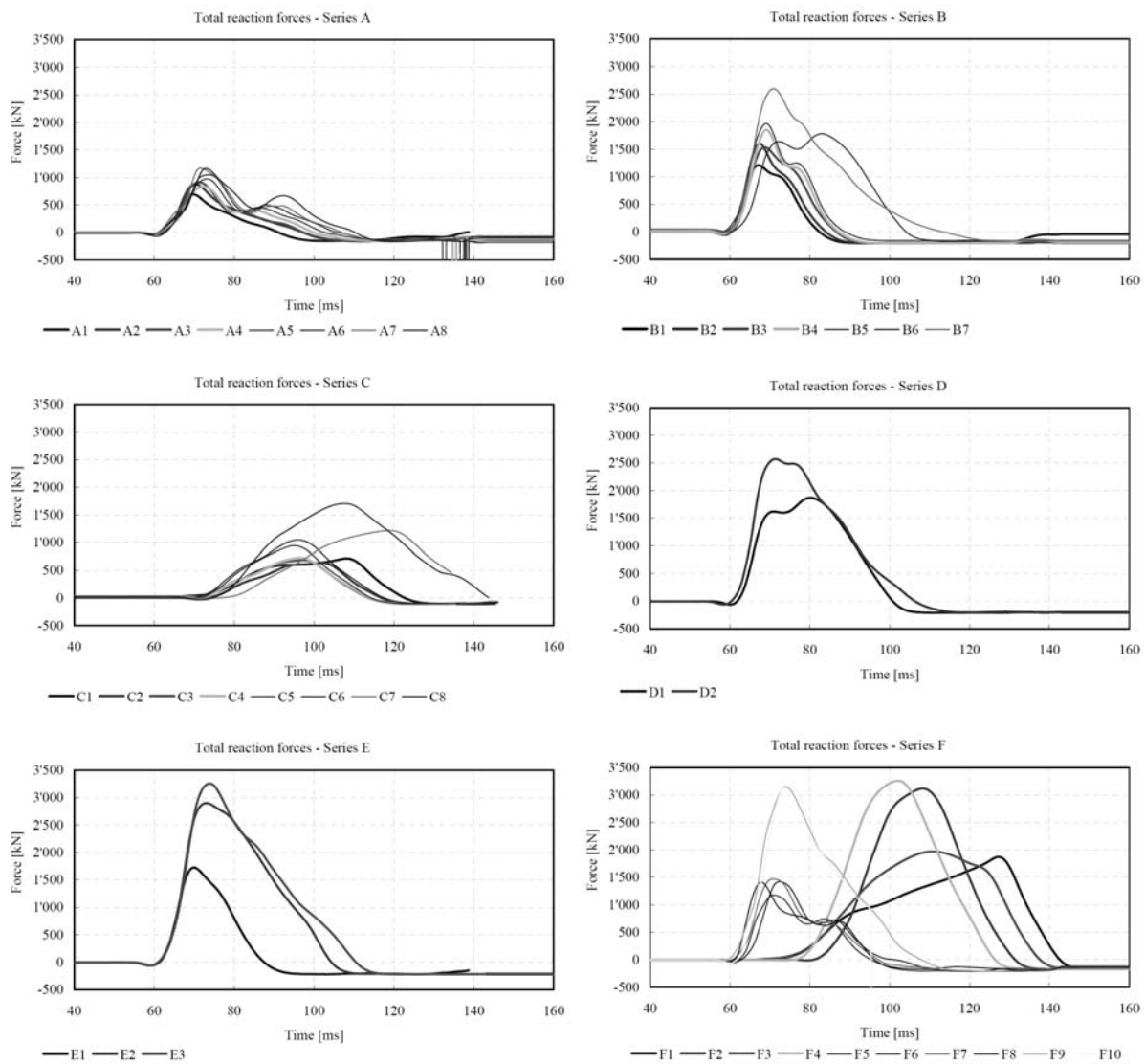
In this appendix the time histories of the measured reaction forces and the strains of large-scale tests are presented. First an overview of the reaction forces of the complete series is shown. Then for each test, the total reaction forces over 400 ms and over 120 ms are illustrated. The shape of the reaction forces strongly depends on the addition of the reaction forces of the single supports. Thus these are shown, too. Additional the strain in reinforcement and concrete surface are shown.

Due to the different falling heights, time had to be shifted for comparison reasons. Reference time is when the boulder contacts the cushion layer and therefore the acceleration defers from g . This point in time has been set to 50 ms for all impacts.

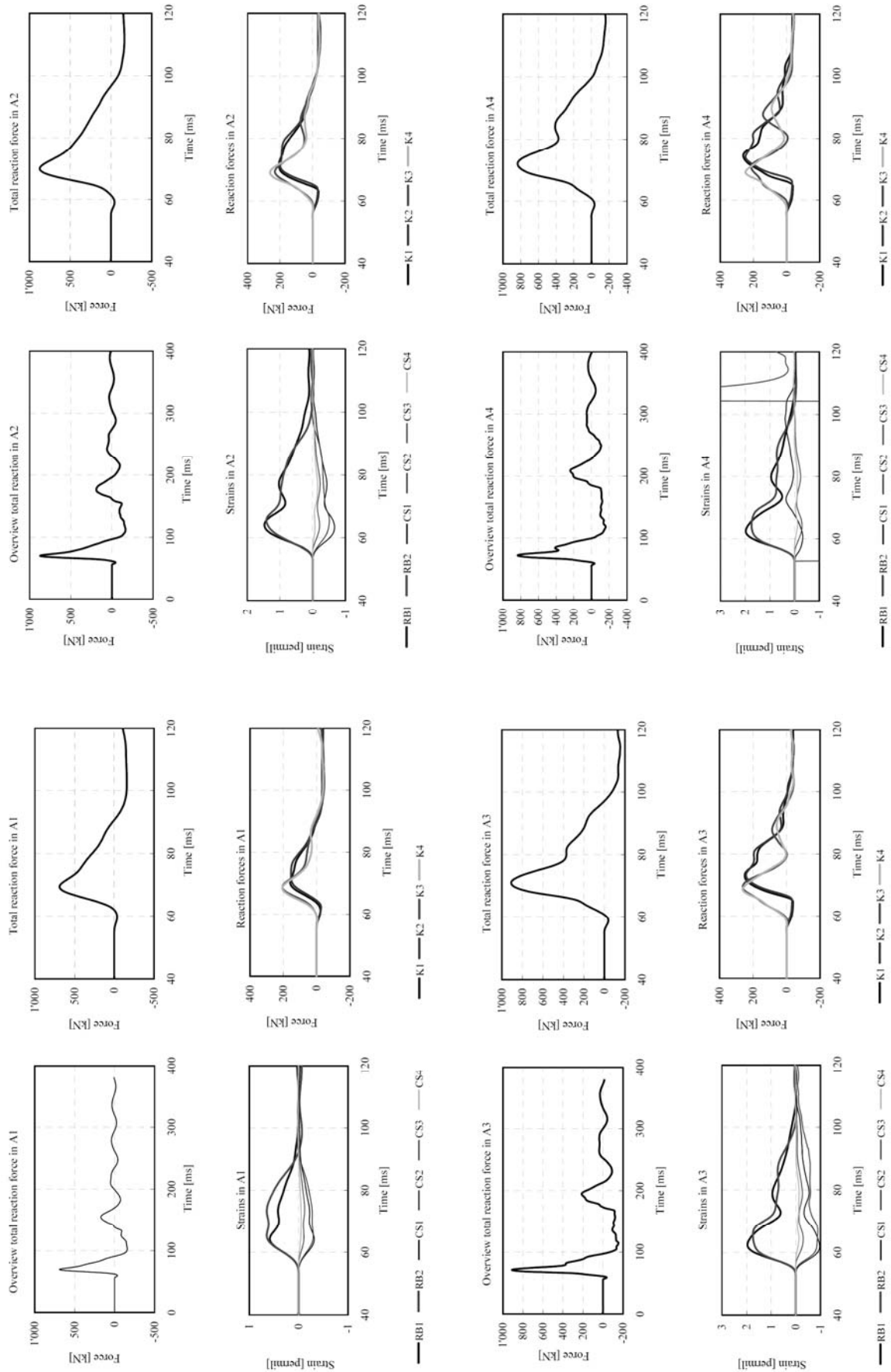
Overview of total reaction forces	116
Test series A	117
Test series B	119
Test series C	121
Test series D	123
Test series E	124
Test series F	125

Appendices

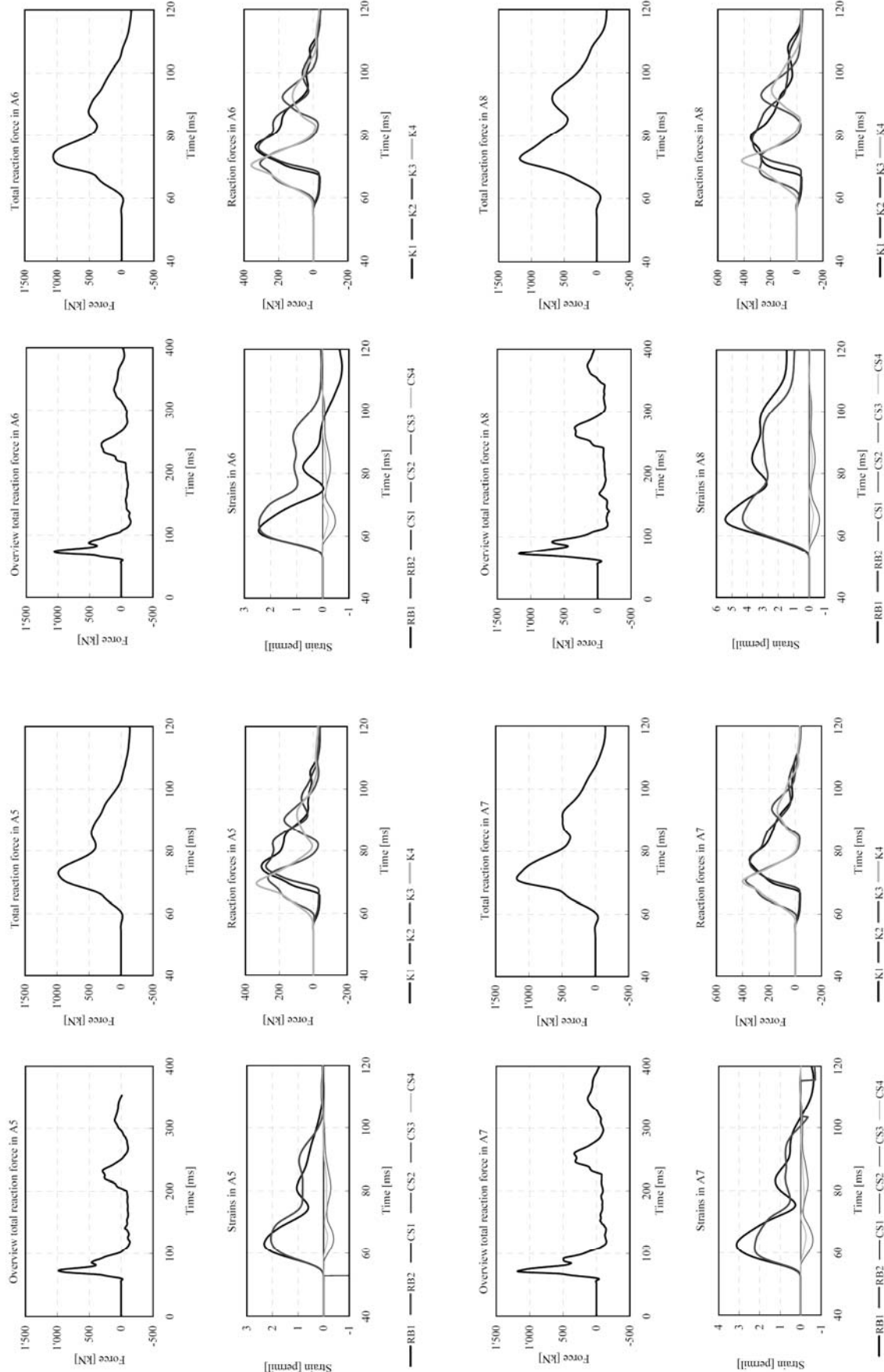
Overview of total reaction forces:



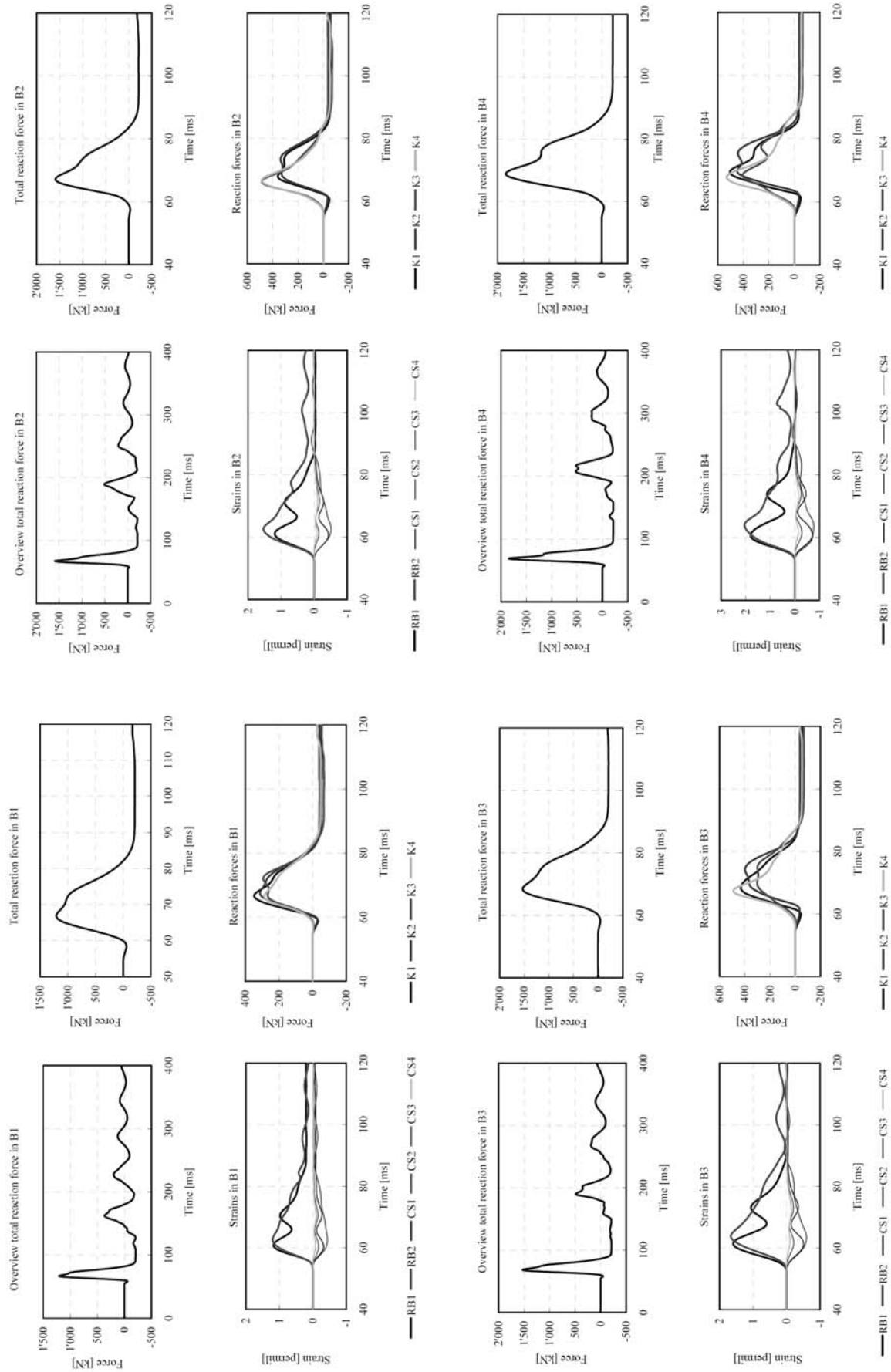
Results of tests A1-A4



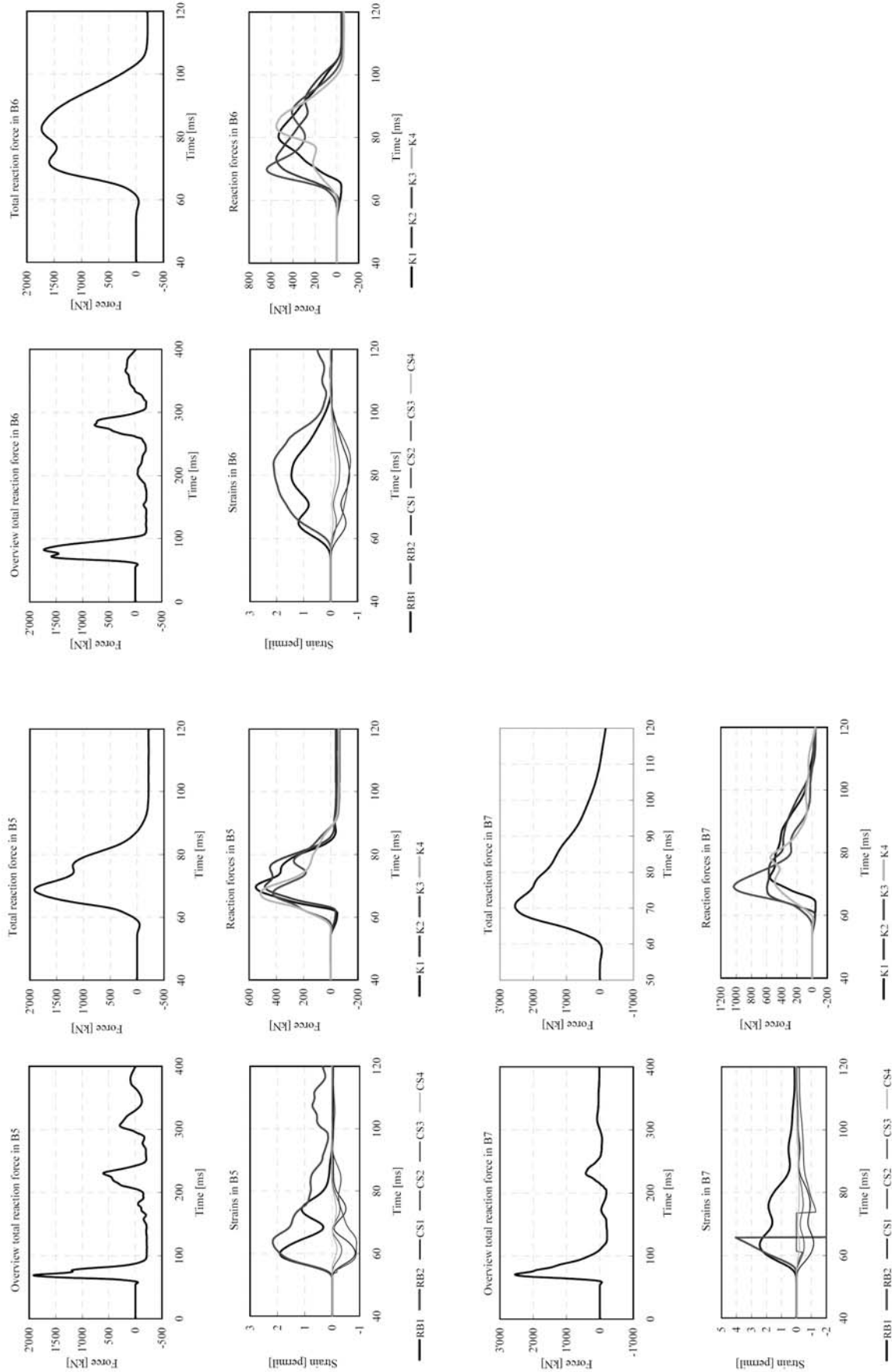
Results of tests A5-A8



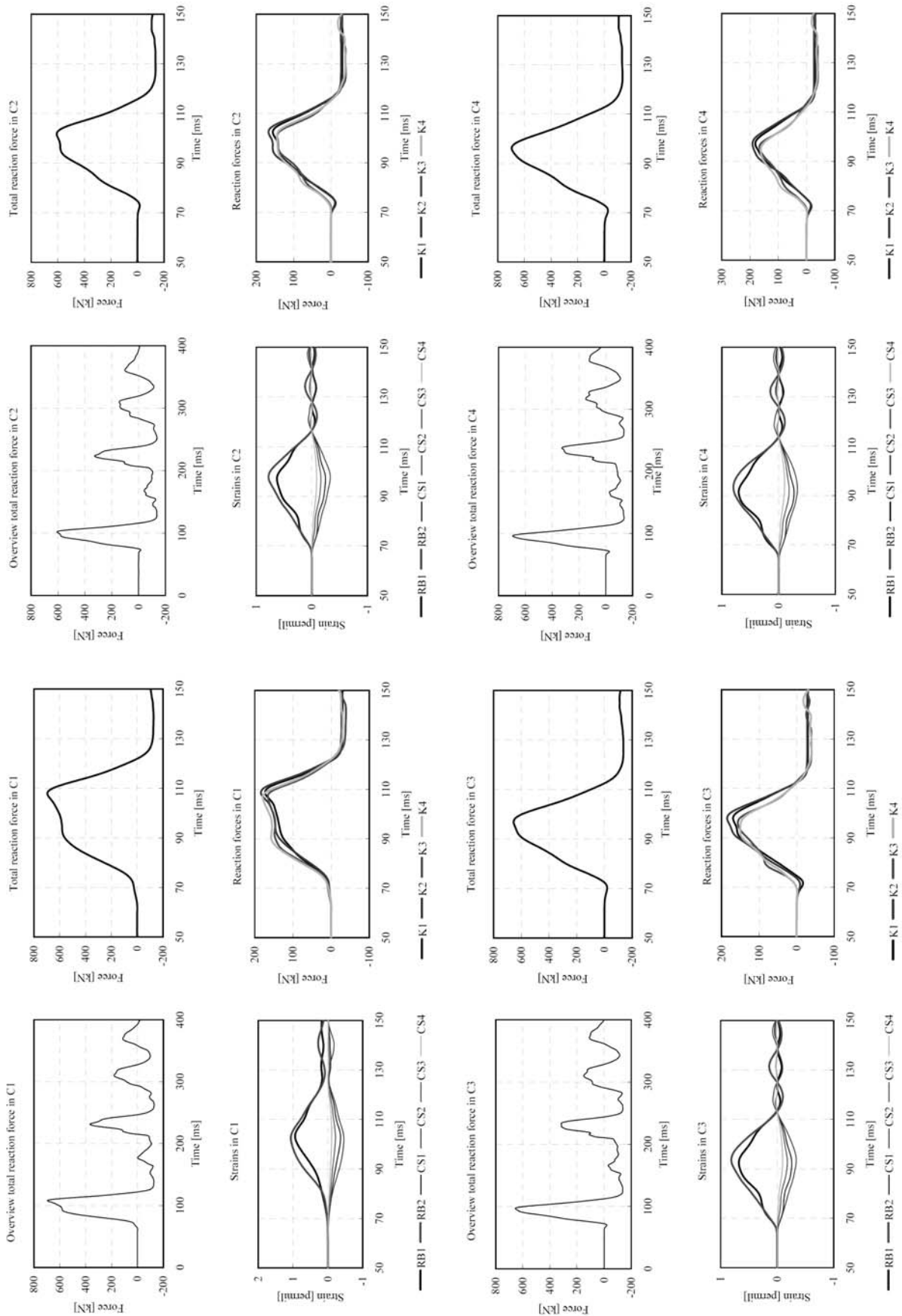
Results of tests B1-B4



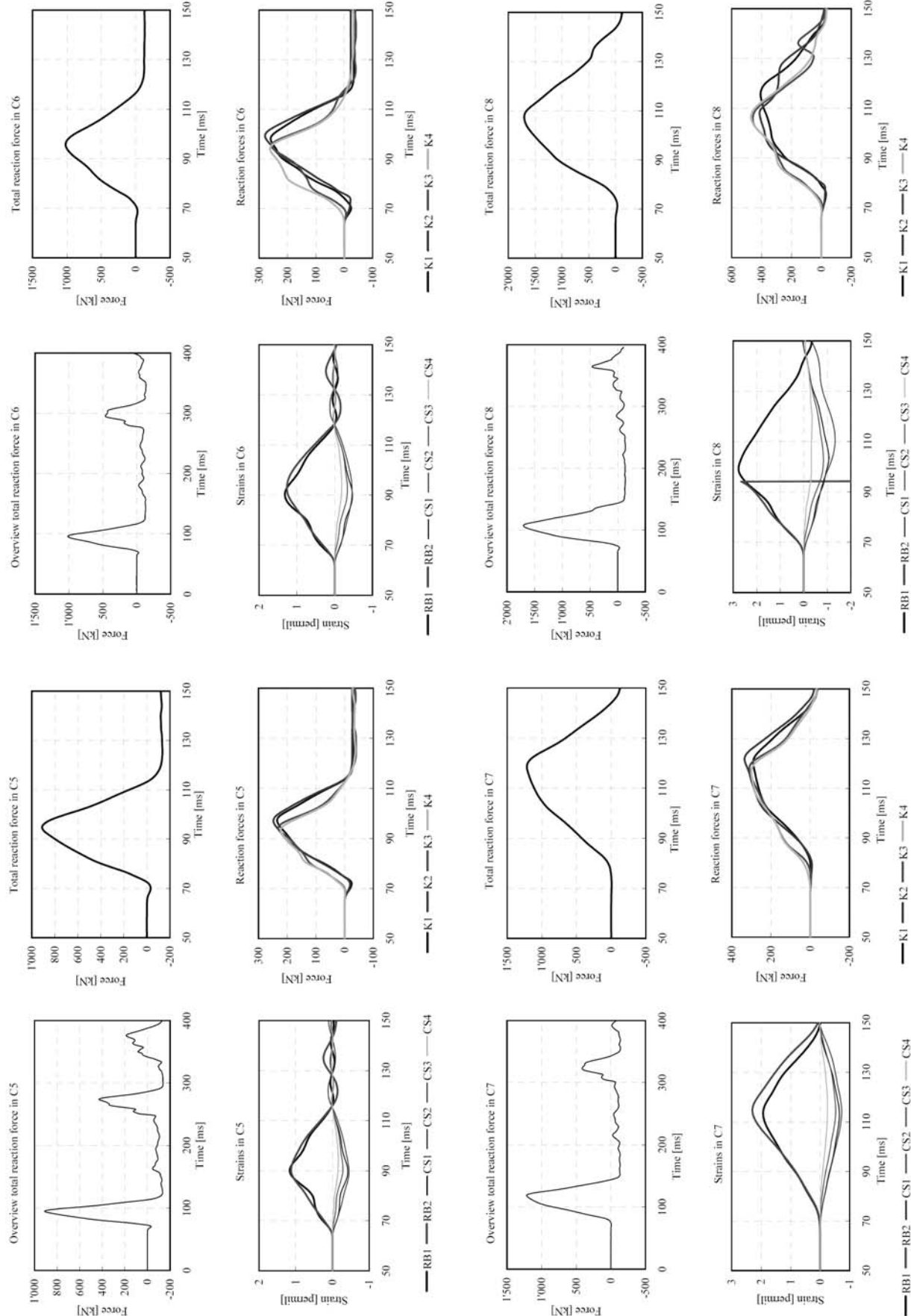
Results of tests B5-B7



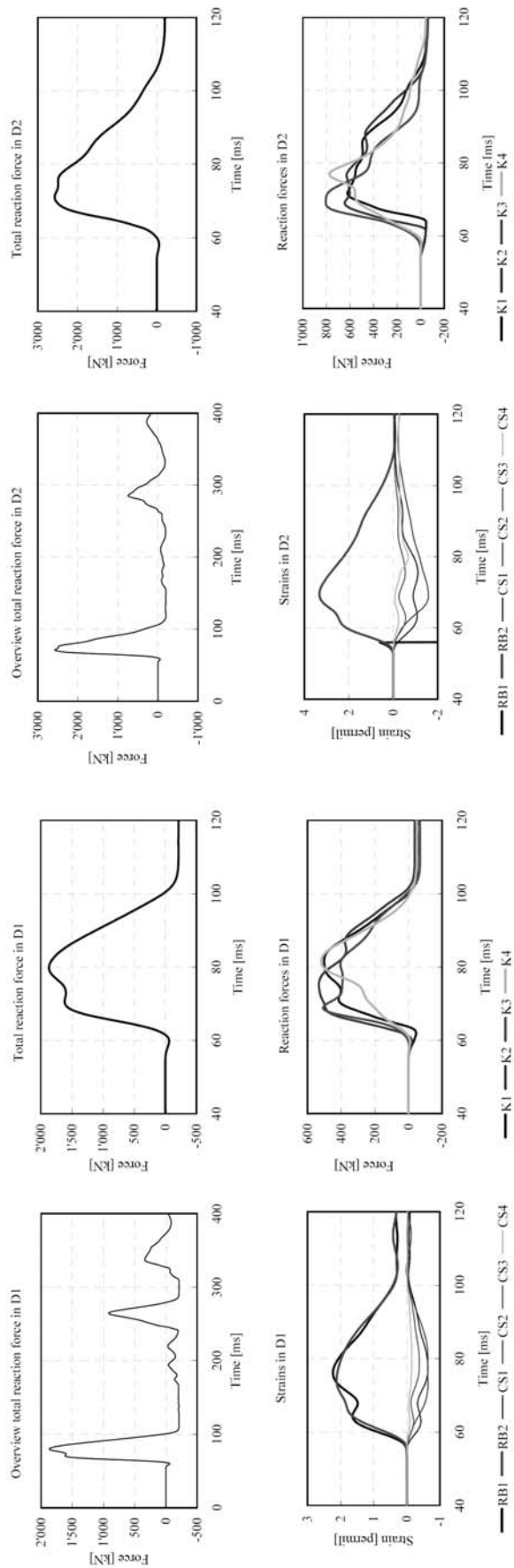
Results of tests C1-C4



Results of tests C5-C8

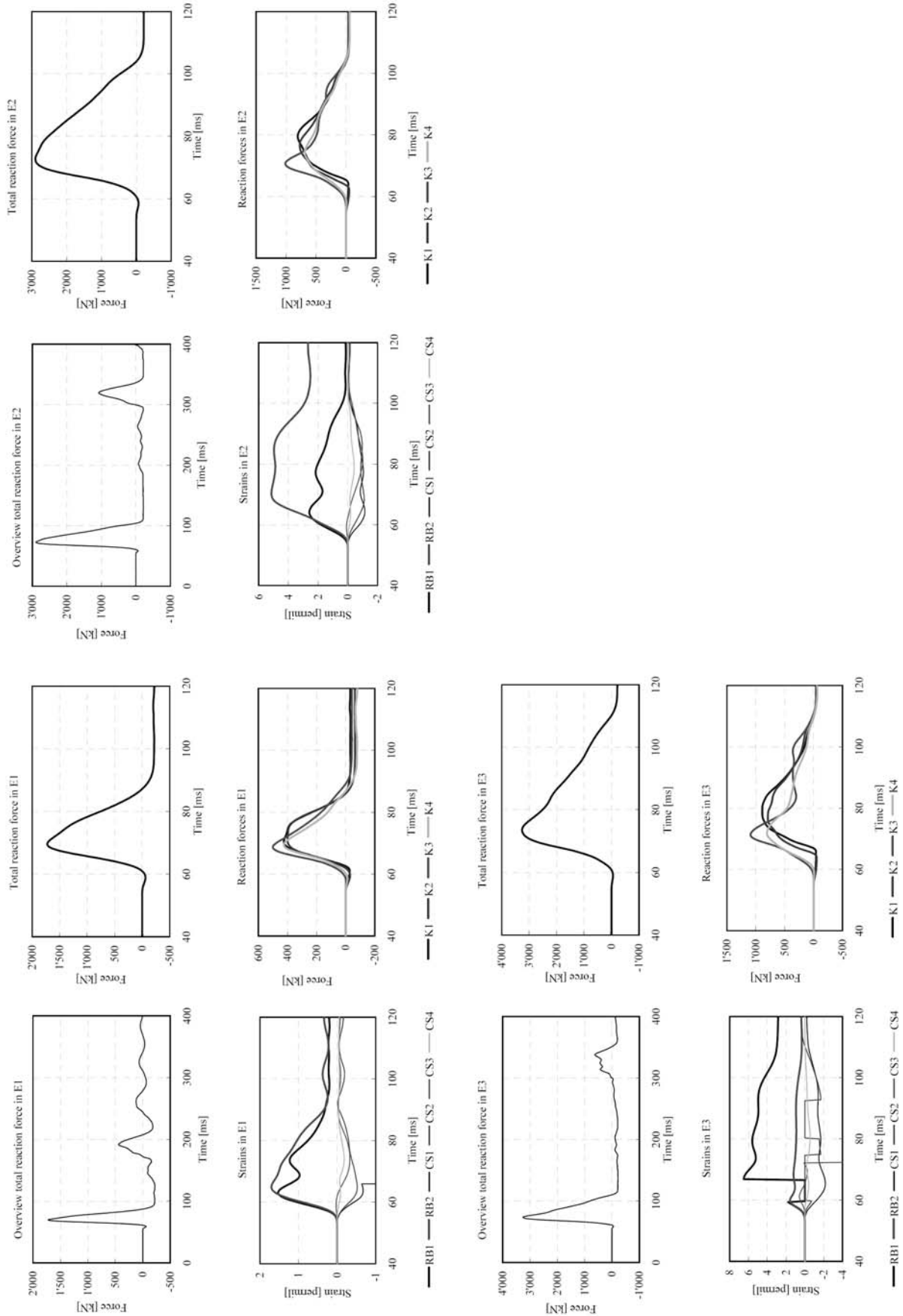


Results of tests D1-D2

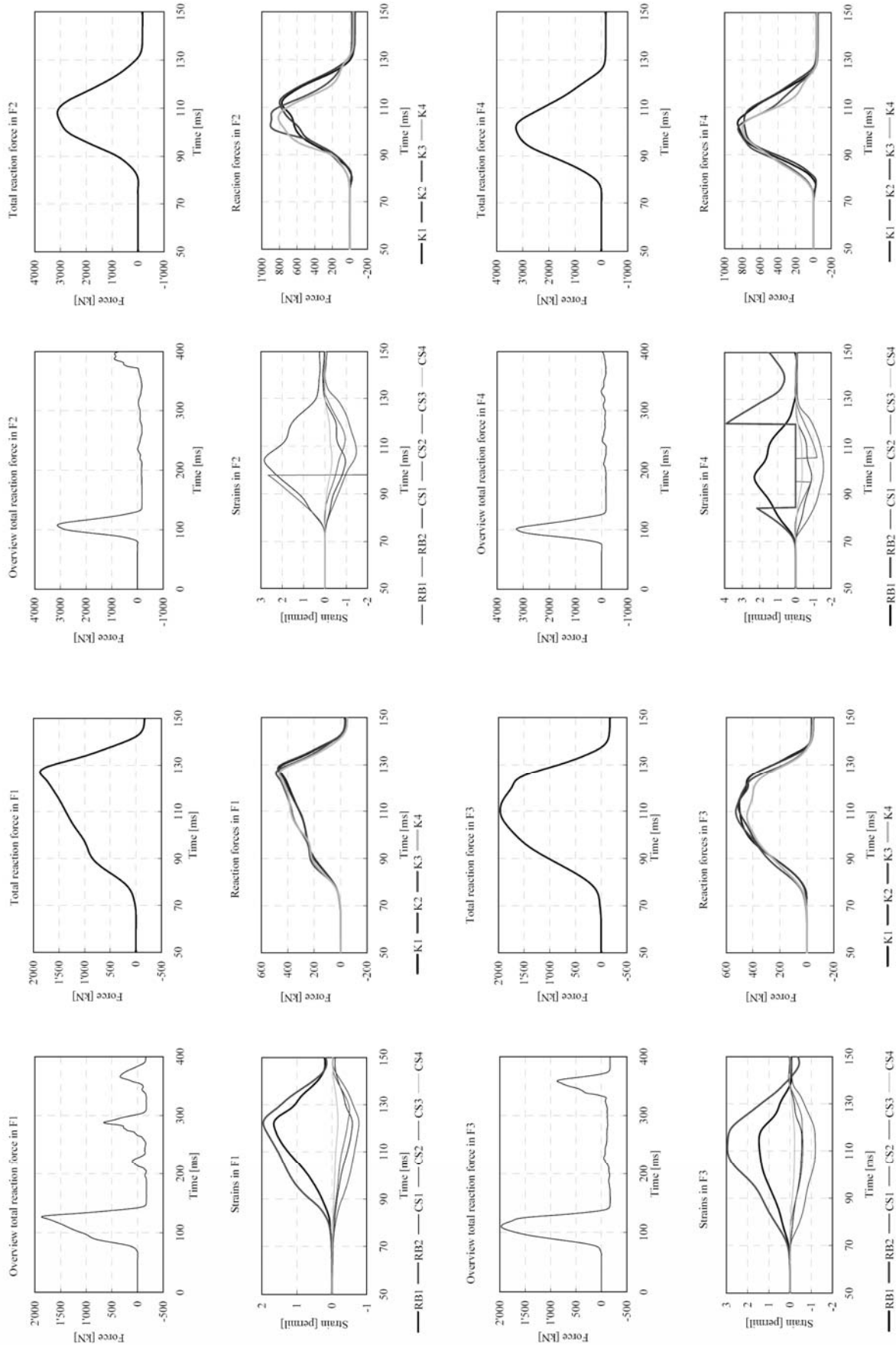


Appendices

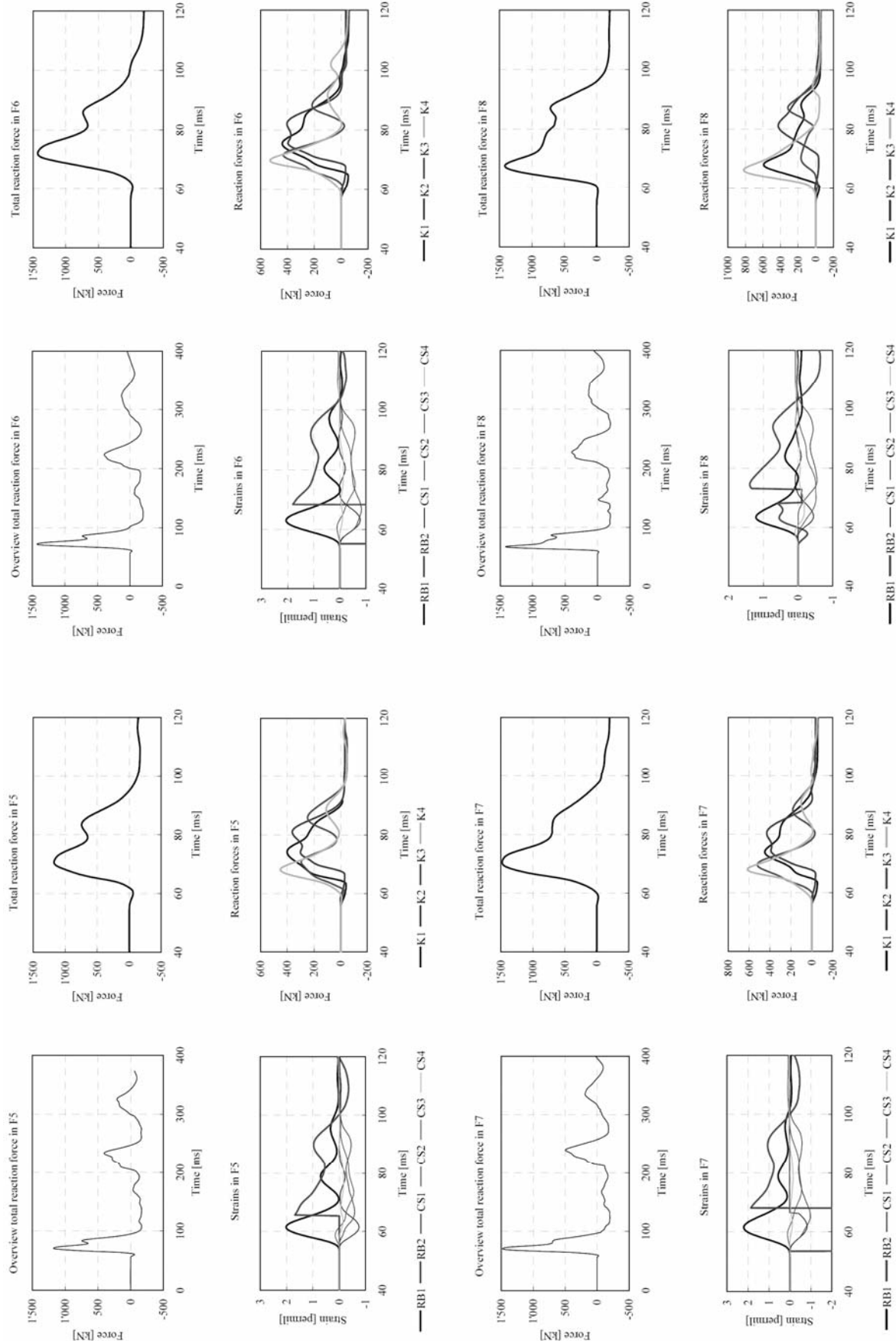
Results of tests E1-E3



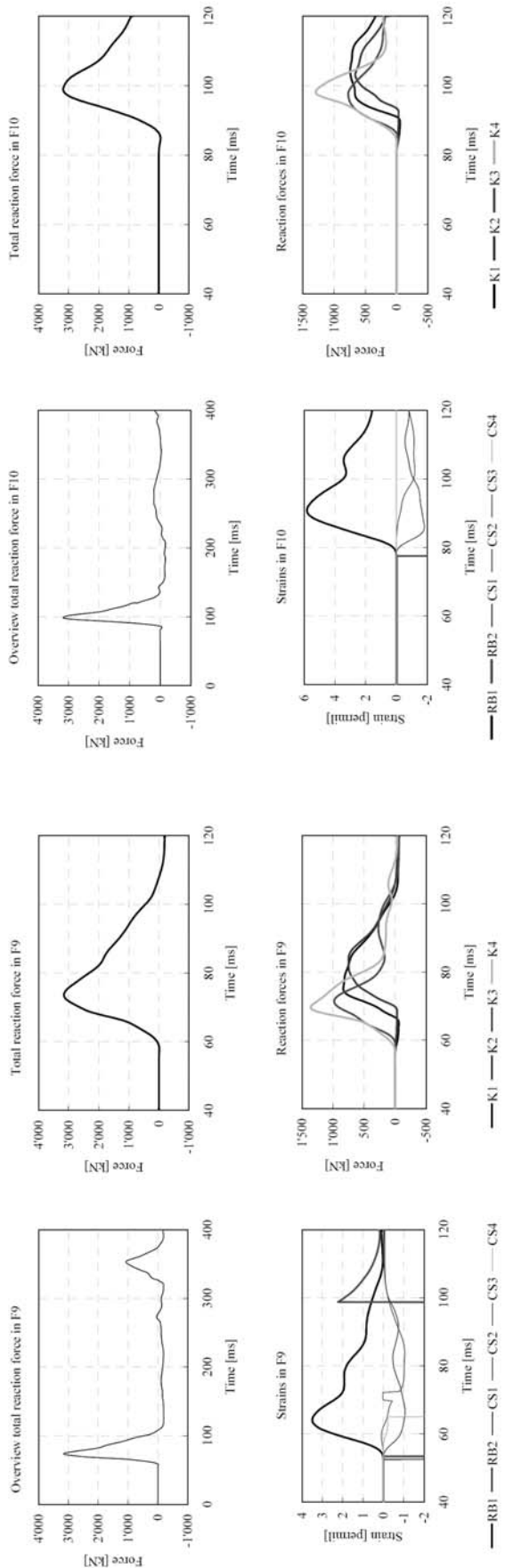
Results of tests F1-F4



Results of tests F5-F8



Results of tests F9-F10



C. Numerical solving of the SMDF

The system of multiple degrees of freedom (SMDF) is solved numerically as described below.

Input data are the following parameters:

Integration

Time step of integration	Δt
--------------------------	------------

Loading

Impact velocity	v_1
Mass of the impacting body	M_1
Diameter of impacting body	\emptyset_b
Earth constant of acceleration	g

Slab

Side length of concrete slab	L_x
Side length of concrete slab	L_z
Slab thickness	d
Static depth	z
Coefficient for bending stiffness	k_w
Coefficient for effective mass	α
Concrete cover lower and upper side	\ddot{u}, \ddot{u}'
Diameter of bending reinforcement lower and upper side	$\emptyset_1, \emptyset_1'$
Spacing of bending reinforcement lower and upper side	s, s'
Diameter of shear reinforcement	\emptyset_w
Spacing of shear reinforcement	s_w
Damping constant for punching cone	ζ_2
Damping constant for bending behavior	ζ_3

Cushion layer

Density of gravel	γ_g
Initial stiffness of cushion layer	K_{10}
Thickness of cushion layer	e
Maximum penetration	p_{\max}
Angle of internal friction	φ
Maximum possible cushion stiffness	$K_{1\max}$
Damping coefficient	c_1

Material properties

Ultimate strain of shear reinforcement	A_{sg}
Concrete strength	f_{cm}
Yielding strength of reinforcing steel	f_s
E-modulus of concrete	E_c
E-modulus of reinforcing steel	E_s
Density of concrete	γ_c
Release energy from elastic deformation	G_f
Factor for global strengthening after yielding	γ_y
Maximum diameter of aggregates	D_{\max}

The calculation procedure consists of five steps (Figure C-1). Initial values are

$$v_{1(t=0)} = v_{10}$$

$$v_{2(t=0)} = v_{3(t=0)} = 0$$

$$a_{1(t=0)} = a_{2(t=0)} = a_{3(t=0)} = 0$$

$$F_{1k(t=0)} = F_{2k(t=0)} = F_{3k(t=0)} = 0$$

$$y_{10} = y_{20} = y_{30} + \frac{g \cdot M_2}{K_{21}} \quad (6-2)$$

$$y_{30} = \frac{g \cdot (M_2 + M_3^*)}{K_{30}} \quad (6-3)$$

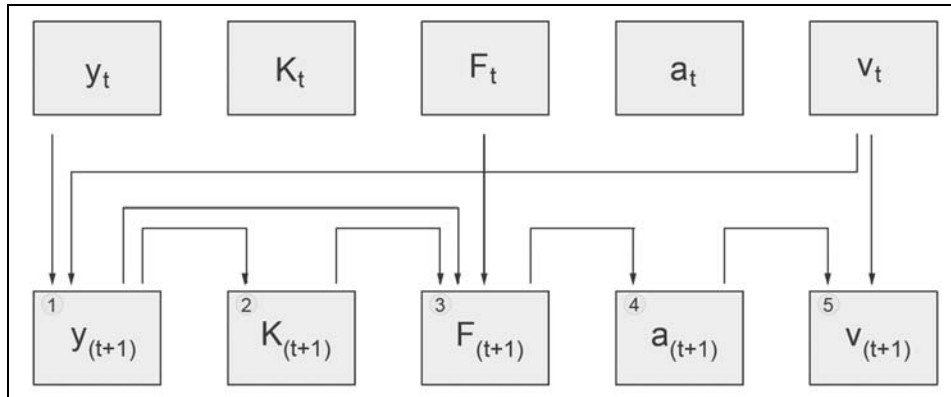


Figure C-1: Scheme for calculating the next time step

Step 1: The new displacements $y_{(t+1)}$ are calculated from all old values

$$y_{i(t+1)} = y_{i(t)} + v_{i(t)} \cdot \Delta t \quad (4-40)$$

Step 2: The new state of the springs and their stiffness $K_{(t+1)}$ are conditioned by the new displacements $y_{(t+1)}$

$$K_{1(t+1)} = K_{1(t)} \quad \text{for} \quad K_{10} \cdot \left(1 - \frac{(y_1 - y_2)_{(t+1)}}{p_{\max}}\right)^{-1} < K_{1(t)} \quad (4-11)$$

$$K_{1(t+1)} = K_{10} \cdot \left(1 - \frac{(y_1 - y_2)_{(t+1)}}{p_{\max}}\right)^{-1} \quad \text{for} \quad K_{1(t)} \leq K_{10} \cdot \left(1 - \frac{(y_1 - y_2)_{(t+1)}}{p_{\max}}\right)^{-1} < K_{1\max} \quad \text{see also (4-17)}$$

$$K_{1(t+1)} = K_{1\max} \quad \text{for} \quad K_{10} \cdot \left(1 - \frac{(y_1 - y_2)_{(t+1)}}{p_{\max}}\right)^{-1} \geq K_{1\max}$$

$$K_{10} = \gamma_g \cdot v_p^2 \frac{A}{z_0} \quad (5-3) \text{ to } (5-7)$$

Appendices

$$K_{2(t+1)} = K_{21} \cdot (1 - \xi_{(t+1)}) + K_{22(t+1)} + K_{23(t+1)}$$

$$K_{21} = \pi \cdot E_c \cdot (z + \emptyset_{sl})$$

$$\emptyset_{sl} = \emptyset_b + 2 \cdot (e - p_{\max}) \cdot \tan\left(45^\circ - \frac{\varphi}{2}\right)$$

$$\xi_{(t+1)} = 0 \quad \text{for} \quad (y_2 - y_3)_{(t+1)} < \frac{z \cdot fctmd_{(t+1)}}{E_c} \quad (4-3)$$

$$\xi_{(t+1)} = \xi_t + \frac{1}{n} \quad \text{for} \quad (y_2 - y_3)_{(t+1)} \geq \frac{z \cdot fctmd_{(t+1)}}{E_c} \quad (4-28)$$

$$\xi_{(t+1)} = 1 \quad \text{for} \quad \xi_t \geq 1$$

$$n = \frac{z}{0.38 \cdot \Delta t} \cdot \sqrt{\frac{2\gamma_c}{E_c}} \quad (4-27) \text{ and } (4-33)$$

$$f_{ctmd(t+1)} = f_{ctm} \cdot \left(1 + 0.54 \left(\frac{\log \dot{\varepsilon} + 5}{5} \right) \right) \text{ for } \dot{\varepsilon}_{2(t+1)} > 0 \quad (4-25)$$

$$f_{ctmd(t+1)} = f_{ctm} \quad \text{for} \quad \dot{\varepsilon}_{2(t+1)} \leq 0$$

$$\dot{\varepsilon}_{2(t+1)} = \frac{(y_2 - y_3)_{(t+1)} - (y_2 - y_3)_{(t)}}{z \cdot \Delta t}$$

$$K_{21D(t+1)} = -\pi \cdot E_{D(t+1)} \cdot (z + \emptyset_{sl}) \quad (4-18)$$

$$E_{D(t+1)} = \frac{E_c f_{ctmd(t+1)}^2 z}{2E_c G_F - f_{ctmd(t+1)}^2 z} \quad (4-24)$$

$$K_{22(t+1)} = \gamma_y \cdot K_{22}$$

$$\text{when } (y_2 - y_3)_{(t+1)} - (y_2 - y_3)_{(t)} > 0 \quad \text{and} \quad F_{2k(t)} > F_{2y} \quad \text{instead of (4-21)}$$

$$K_{22(t+1)} = K_{22}$$

$$\text{when } (y_2 - y_3)_{(t+1)} - (y_2 - y_3)_{(t)} \leq 0 \quad \text{or} \quad F_{2k(t)} \leq F_{2y}$$

$$K_{22} = \frac{A_{sw} \cdot E_s}{l_w} \approx \frac{A_{sw} \cdot E_s}{z} \quad (4-20)$$

$$A_{sw} = \pi \cdot \rho_w \cdot (z^2 + z \cdot \emptyset_{sl})$$

$$\rho_w = \pi \cdot \left(\frac{\emptyset_w}{2 \cdot s_w} \right)^2$$

$$K_{23(t+1)} \approx \frac{F_{3kt}}{\left(\frac{Q_u}{m_u} \right) \cdot z \cdot s_w} \quad \text{instead of (4-22)}$$

$$K_{3(t+1)} = \gamma_y \cdot K_{30} \quad \text{when } y_{3(t+1)} - y_{3(t)} > 0 \text{ and } F_{3k(t)} > F_{3y}$$

$$K_{3(t+1)} = K_{30} \quad \text{when } y_{3(t+1)} - y_{3(t)} \leq 0 \text{ or } F_{3k(t)} \leq F_{3y}$$

$$K_{30} = \frac{k_w E_c d^3}{12 L_x^2} \quad (5-2)$$

Step 3: The new spring forces $F_{(t+1)}$ or the new force increments $\Delta F_{(t+1)}$ are determined

$$F_{1k(t+1)} = F_{1k(t)} + \Delta F_{1k(t+1)} \quad \text{for} \quad F_{1k(t)} + \Delta F_{1k(t+1)} > 0 \quad (4-14)$$

$$F_{1k(t+1)} = 0 \quad \text{for} \quad F_{1k(t)} + \Delta F_{1k(t+1)} < 0$$

$$\Delta F_{1k(t+1)} = K_{1(t+1)} \cdot ((y_1 - y_2)_{(t+1)} - (y_1 - y_2)_{(t)}) \quad (4-31)$$

$$F_{2k(t+1)} = F_{21k(t+1)} + F_{22k(t+1)} + F_{23k(t+1)}$$

$$F_{21k(t+1)} = F_{21cg(t+1)} \quad \text{for} \quad F_{21cg(t+1)} > F_{22d(t+1)} \quad (4-32)$$

$$F_{21k(t+1)} = F_{21d(t+1)} \quad \text{for} \quad F_{21cg(t+1)} \leq F_{22d(t+1)}$$

$$F_{21cg(t+1)} = (y_2 - y_3)_{(t+1)} \cdot K_{21} \cdot (1 - \xi_{(t+1)}) \quad (4-29)$$

$$F_{21d(t+1)} = F_{21d(t)} + \Delta F_{21d(t+1)} \quad (4-30)$$

$$\Delta F_{21d(t+1)} = ((y_2 - y_3)_{(t+1)} - (y_2 - y_3)_{(t)}) \cdot K_{21}$$

$$\text{when } (y_2 - y_3)_{(t+1)} - (y_2 - y_3)_{(t)} < 0 \quad \text{or} \quad \xi_{(t+1)} = 0$$

$$\Delta F_{21d(t+1)} = ((y_2 - y_3)_{(t+1)} - (y_2 - y_3)_{(t)}) \cdot K_{21D}$$

$$\text{when } (y_2 - y_3)_{(t+1)} - (y_2 - y_3)_{(t)} > 0 \quad \text{and} \quad \xi_{(t+1)} \neq 0$$

$$F_{22k(t+1)} = F_{22k(t)} + ((y_2 - y_3)_{(t+1)} - (y_2 - y_3)_{(t)}) \cdot K_{22(t+1)}$$

$$F_{23k(t+1)} = F_{23k(t)} + ((y_2 - y_3)_{(t+1)} - (y_2 - y_3)_{(t)}) \cdot K_{23(t+1)}$$

$$F_{3k(t+1)} = F_{3k(t)} + (y_{3(t+1)} - y_{3(t)}) \cdot K_{3(t+1)}$$

$$F_{ic(t+1)} = c_i \cdot v_{i(t)}$$

$$c_2 = 2 \cdot \zeta_2 \cdot \frac{M_2}{T_2}$$

$$T_2 = 2 \cdot \pi \sqrt{\frac{M_2}{K_{21}}}$$

$$M_2 = \pi \cdot \left[(e - p_{\max}) \cdot \gamma_g \left(\frac{\emptyset_b + \emptyset_{sl}}{4} \right)^2 + d \cdot \gamma_c \cdot \left(\frac{\emptyset_{sl} + z}{2} \right)^2 \right] \quad (4-2)$$

$$c_3 = 2 \cdot \zeta_3 \cdot \frac{M_3^*}{T_3}$$

$$T_3 = 2 \cdot \pi \sqrt{\frac{M_3^*}{K_{30}}}$$

$$\dot{M}_3 = \alpha \cdot M_3 - M_{2sl} \quad (4-7)$$

$$M_3 = L_x \cdot L_z \cdot d \cdot \gamma_c \quad (4-6)$$

$$M_{2sl} = \pi \cdot \left(\frac{\emptyset_{sl} + z}{2} \right)^2 \cdot d \cdot \gamma_c \quad (4-8)$$

Step 4: The new accelerations $a_{(t+1)}$ are calculated from the spring forces F_t

$$a_{1(t+1)} = -\frac{F_{1k(t+1)} + F_{1c(t+1)}}{M_1} + g \quad \text{for} \quad F_{1k(t+1)} > 0 \quad (4-1)$$

$$a_{2(t+1)} = \frac{F_{1k(t+1)} + F_{1c(t+1)} - F_{2k(t+1)} - F_{2c(t+1)}}{M_2} + g$$

$$a_{3(t+1)} = \frac{F_{2k(t+1)} + F_{2c(t+1)} - F_{3k(t+1)} - F_{3c(t+1)}}{M_3^*} + g$$

Step 5: The new velocities $v_{(t+1)}$ are calculated from all old values

$$v_{i(t+1)} = v_{i(t)} + \Delta t \cdot a_{i(t+1)} \quad (4-41)$$

D. Input and output of SMDF for large-scale test

This appendix shows the input parameters and the output of the model for the calculation of series B of the large-scale tests. This is the base for calibrating the model in its global behavior.

In the diagrams the time histories of the spring forces, mass velocities and mass displacements are shown in the first row. Then, the time histories of the spring stiffnesses are shown in the middle row and the force displacement curves can be found in the lower row. All those diagrams allow for surveying the calculation and to judge its plausibility.

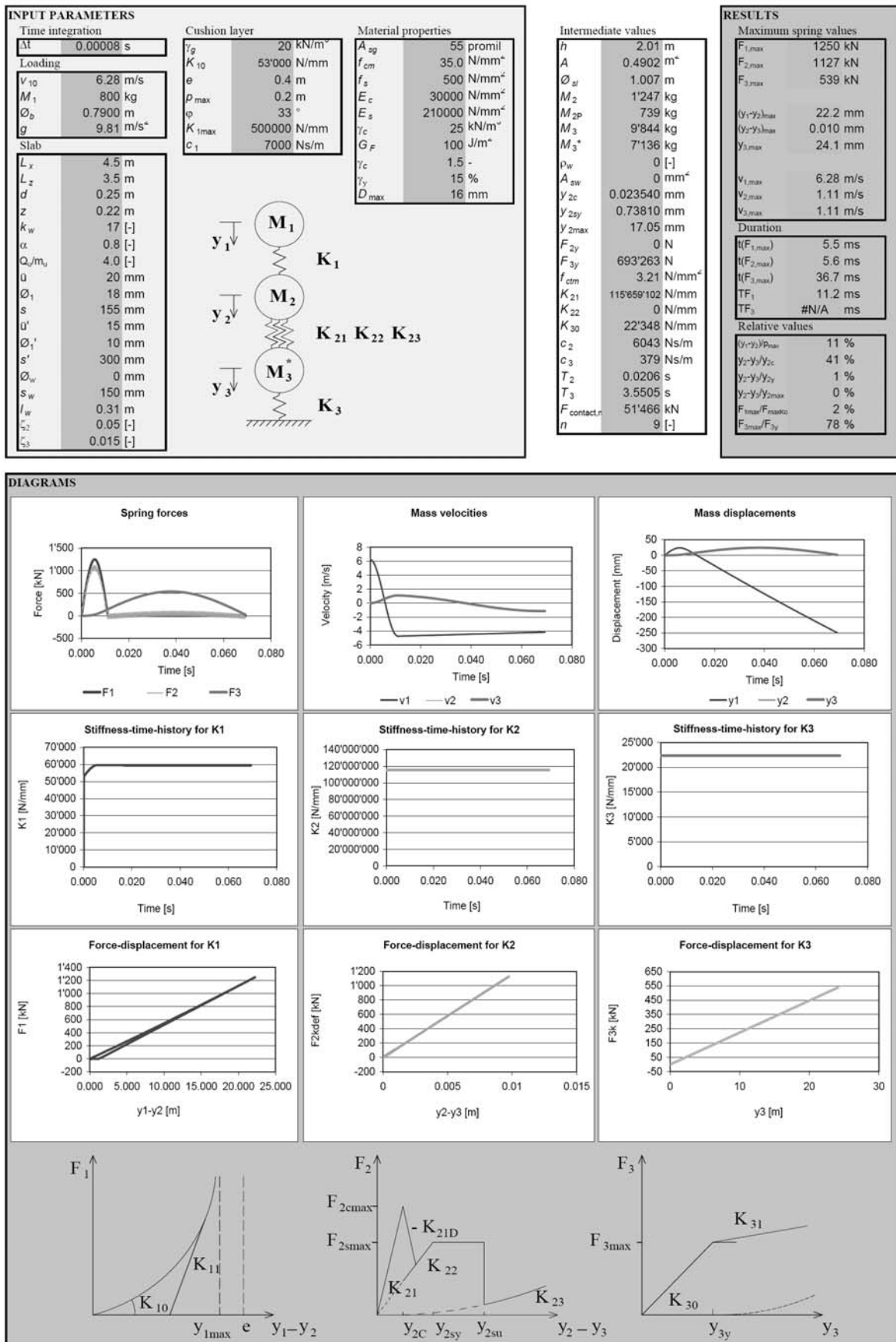
Values for tests

Test A1	134
Test A3	135
Test A4	136
Test A5	137
Test A6	138
Test A7	139
Test A8	140
Test B1	141
Test B2	142
Test B3	143
Test B4	144
Test B5	145
Test B6	146
Test B7	147
Test D1	148
Test D2	149
Test E1	150
Test E2	151
Test E3	152
Test F5	153
Test F6	154

Appendices

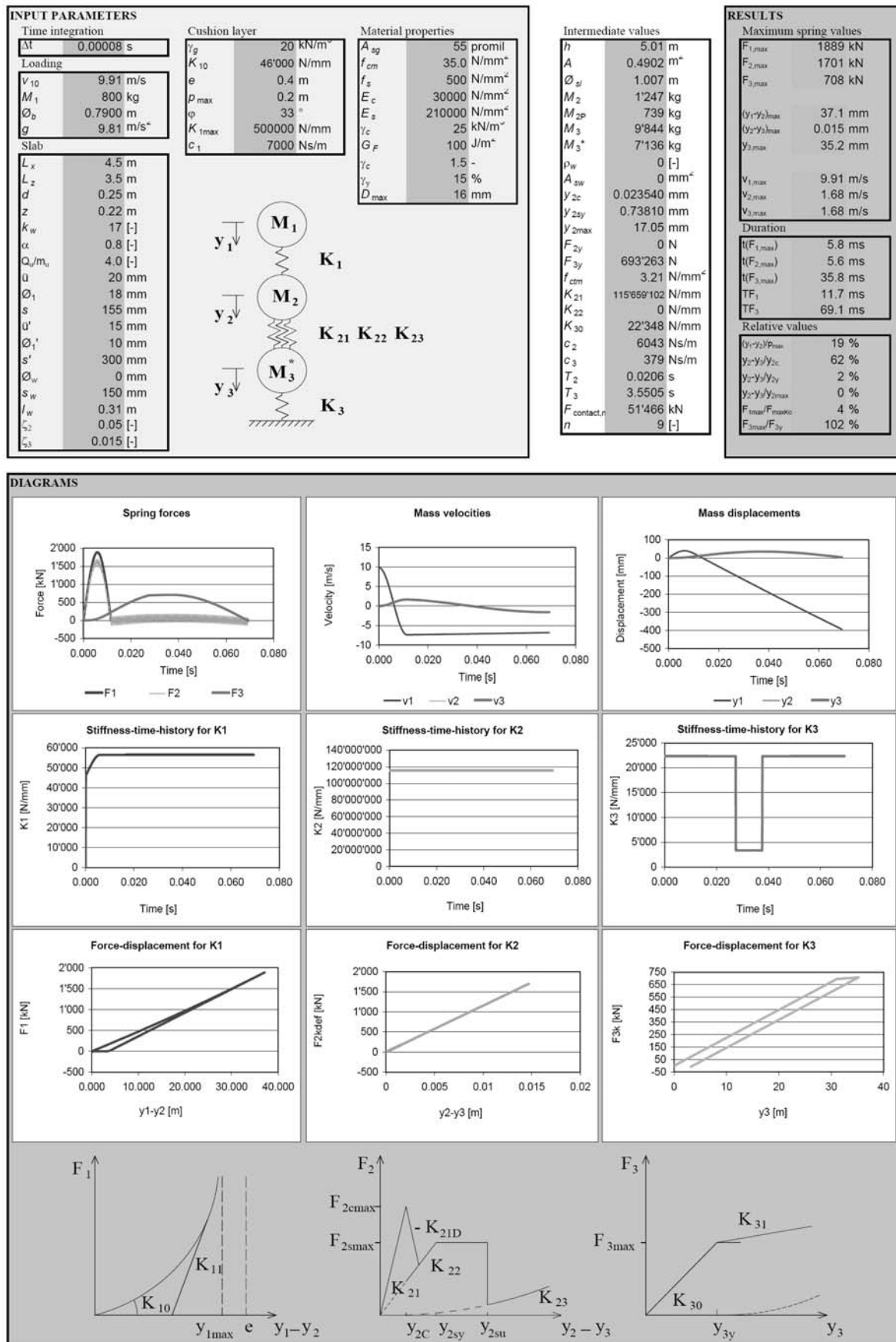
Values for test A1

Analytical model (System of multiple degrees of freedom)



Values for test A3

Analytical model (System of multiple degrees of freedom)

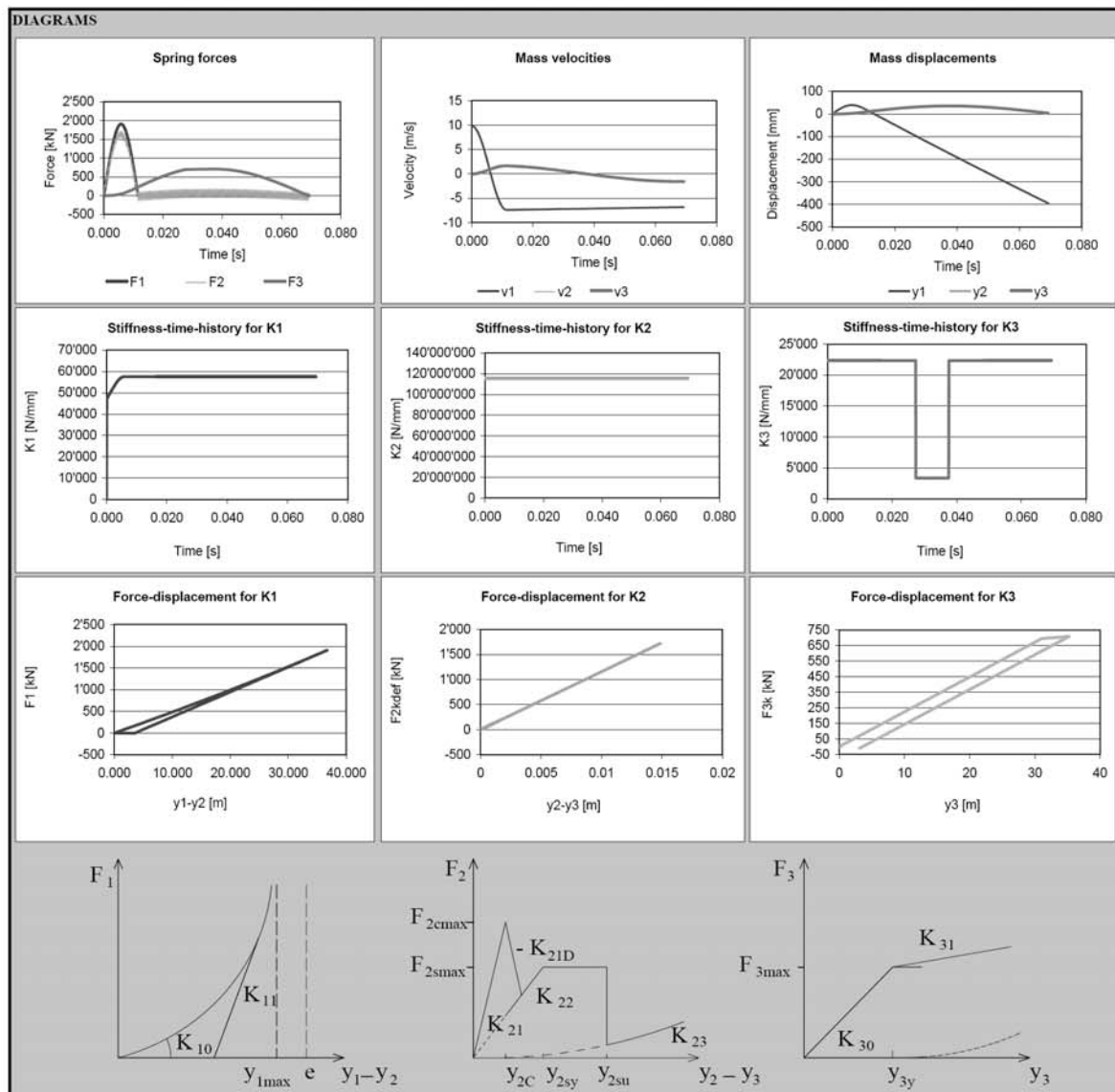
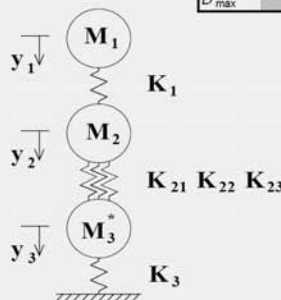


Appendices

Values for test A4

Analytical model (System of multiple degrees of freedom)

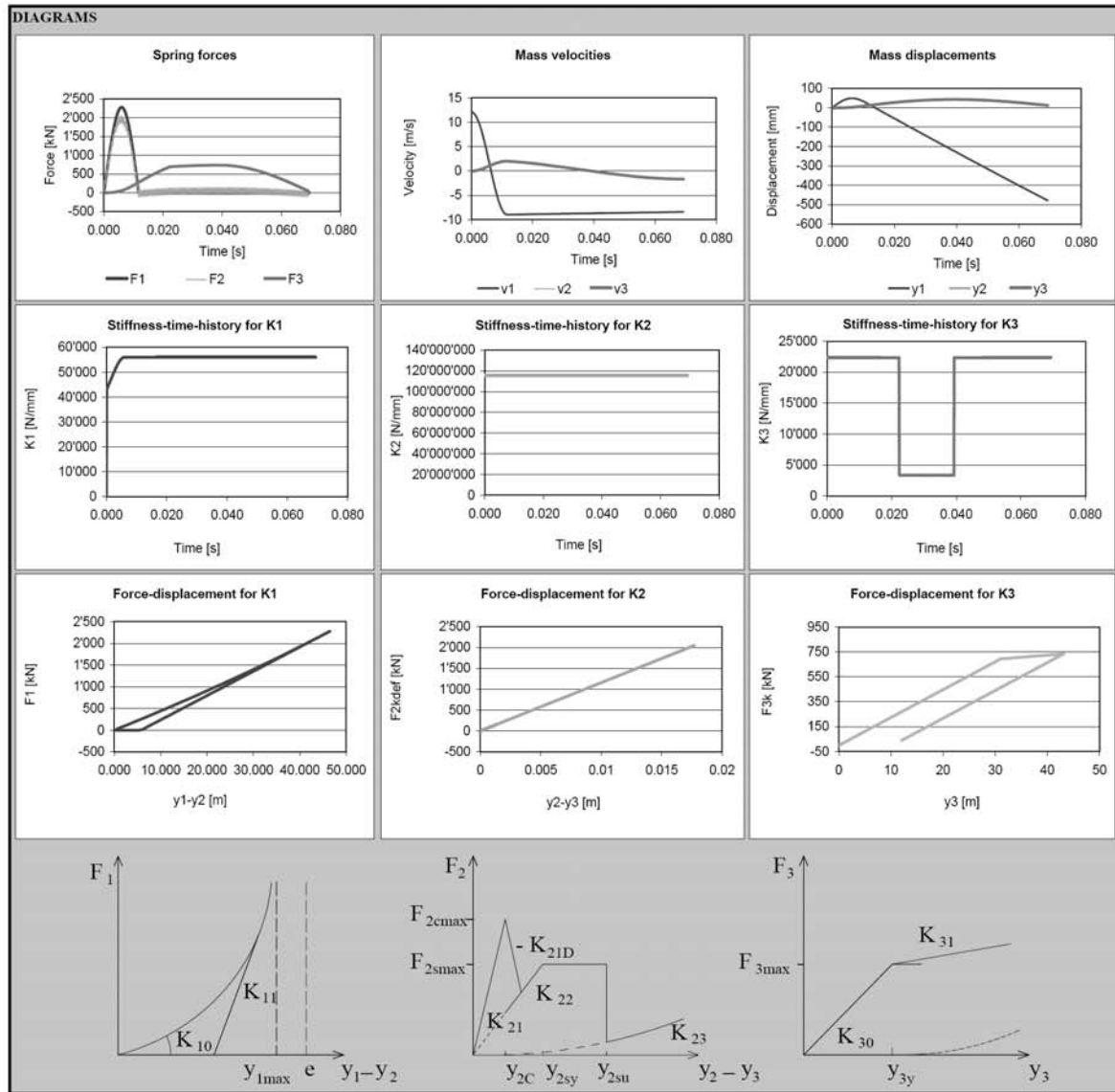
INPUT PARAMETERS		Material properties		Intermediate values		RESULTS	
Time integration	$\Delta t = 0.00008 \text{ s}$	$y_g = 20 \text{ kN/m}^2$	$A_{sg} = 55 \text{ promil}$	$h = 5.01 \text{ m}$	$F_{1,max} = 1909 \text{ kN}$		
Loading	$V_{10} = 9.91 \text{ m/s}$	$K_{10} = 47'000 \text{ N/mm}$	$f_{cm} = 35.0 \text{ N/mm}^2$	$A = 0.4902 \text{ m}^2$	$F_{2,max} = 1719 \text{ kN}$		
M_1	800 kg	$e = 0.4 \text{ m}$	$f_s = 500 \text{ N/mm}^2$	$\emptyset_{sl} = 1.007 \text{ m}$	$F_{3,max} = 708 \text{ kN}$		
\varnothing_b	0.7900 m	$p_{max} = 0.2 \text{ m}$	$E_c = 30000 \text{ N/mm}^2$	$M_2 = 1'247 \text{ kg}$			
g	9.81 m/s ²	$\varphi = 33^\circ$	$E_s = 210000 \text{ N/mm}^2$	$M_{2P} = 739 \text{ kg}$			
Slab		$K_{1max} = 500000 \text{ N/mm}$	$G_F = 100 \text{ J/m}^2$	$M_3 = 9'844 \text{ kg}$			
L_x	4.5 m	$c_1 = 7000 \text{ Ns/m}$	$\gamma_c = 1.5 -$	$M_{3*} = 7'136 \text{ kg}$			
L_z	3.5 m		$\gamma_y = 15 \%$				
d	0.25 m		$D_{max} = 16 \text{ mm}$				
z	0.22 m						
k_w	17 [-]						
a	0.8 [-]						
Q_0/m_0	4.0 [-]						
u	20 mm						
\varnothing_1	18 mm						
s	155 mm						
\bar{u}'	15 mm						
\varnothing_1'	10 mm						
s'	300 mm						
\varnothing_w	0 mm						
s_w	150 mm						
l_w	0.31 m						
ζ_2	0.05 [-]						
ζ_3	0.015 [-]						



Values for test A5

Analytical model (System of multiple degrees of freedom)

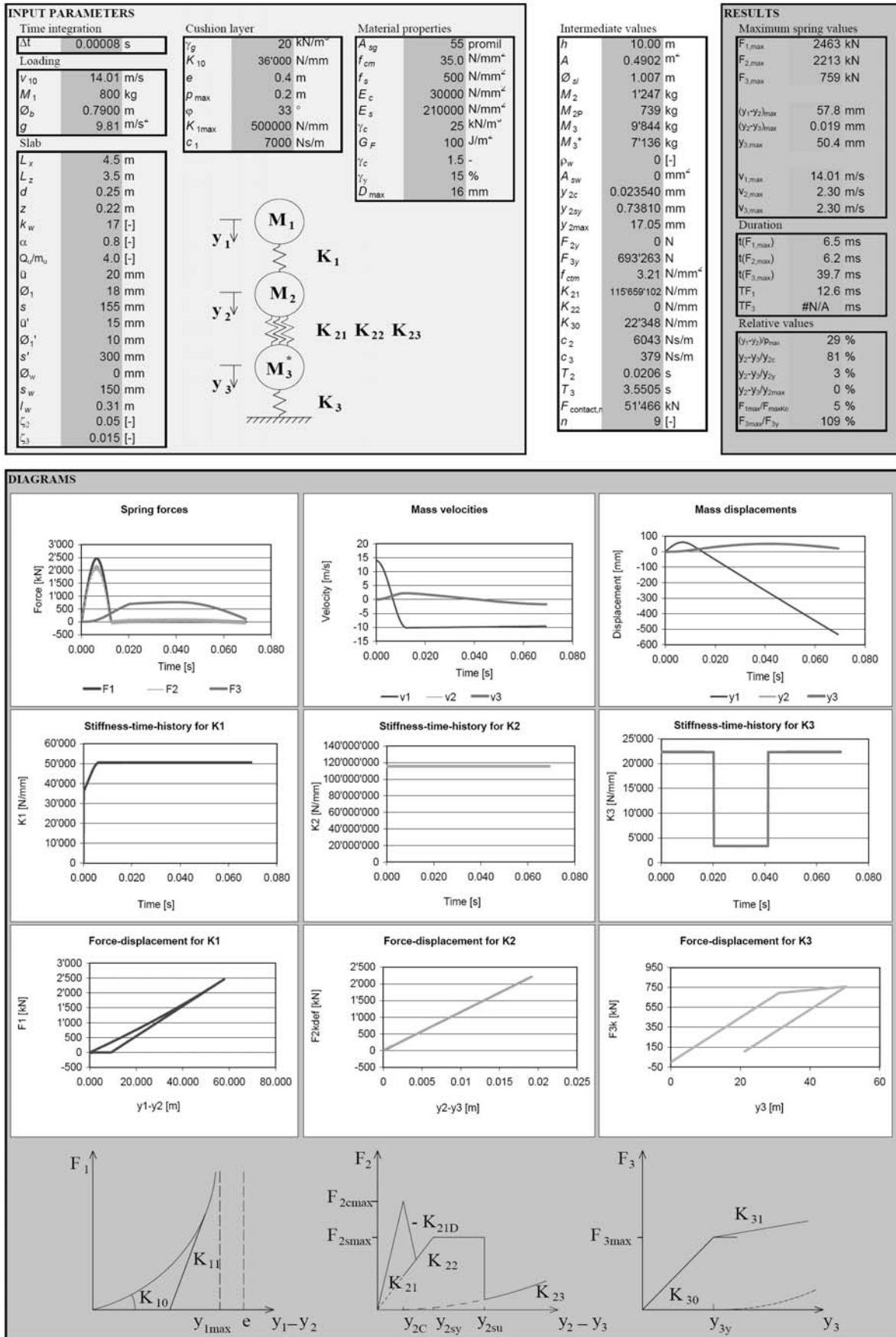
INPUT PARAMETERS		RESULTS	
Time integration	$\Delta t = 0.00008 \text{ s}$	Intermediate values	Maximum spring values
Loading	$V_{10} = 12.14 \text{ m/s}$ $M_1 = 800 \text{ kg}$ $\varnothing_b = 0.7900 \text{ m}$ $g = 9.81 \text{ m/s}^2$	$h = 7.51 \text{ m}$ $A = 0.4902 \text{ m}^2$ $\varnothing_{sl} = 1.007 \text{ m}$ $M_2 = 1'247 \text{ kg}$ $M_{2P} = 739 \text{ kg}$ $M_3 = 9'844 \text{ kg}$ $M_3^* = 7'136 \text{ kg}$ $\rho_w = 0 \text{ [-]}$ $A_{sw} = 0 \text{ mm}^2$ $y_{2c} = 0.023540 \text{ mm}$ $y_{2sy} = 0.73810 \text{ mm}$ $y_{2max} = 17.05 \text{ mm}$ $F_{2y} = 0 \text{ N}$ $F_{3y} = 693'263 \text{ N}$ $f_{cm} = 3.21 \text{ N/mm}^2$ $K_{21} = 115'659'102 \text{ N/mm}$ $K_{22} = 0 \text{ N/mm}$ $K_{30} = 22'348 \text{ N/mm}$ $c_2 = 6043 \text{ Ns/m}$ $c_3 = 379 \text{ Ns/m}$ $T_2 = 0.0206 \text{ s}$ $T_3 = 3.5505 \text{ s}$ $F_{contact,n} = 51'466 \text{ kN}$ $n = 9 \text{ [-]}$	$F_{1,max} = 2280 \text{ kN}$ $F_{2,max} = 2048 \text{ kN}$ $F_{3,max} = 734 \text{ kN}$ $(y_1-y_2)_{max} = 46.5 \text{ mm}$ $(y_2-y_3)_{max} = 0.018 \text{ mm}$ $y_{3,max} = 43.1 \text{ mm}$ $V_{1,max} = 12.14 \text{ m/s}$ $V_{2,max} = 2.03 \text{ m/s}$ $V_{3,max} = 2.03 \text{ m/s}$
Slab	$L_x = 4.5 \text{ m}$ $L_z = 3.5 \text{ m}$ $d = 0.25 \text{ m}$ $z = 0.22 \text{ m}$ $k_w = 17 \text{ [-]}$ $a = 0.8 \text{ [-]}$ $Q_0/m_0 = 4.0 \text{ [-]}$ $u = 20 \text{ mm}$ $\varnothing_1 = 18 \text{ mm}$ $s = 155 \text{ mm}$ $u' = 15 \text{ mm}$ $\varnothing_1' = 10 \text{ mm}$ $s' = 300 \text{ mm}$ $\varnothing_w = 0 \text{ mm}$ $s_w = 150 \text{ mm}$ $l_w = 0.31 \text{ m}$ $\zeta_2 = 0.05 \text{ [-]}$ $\zeta_3 = 0.015 \text{ [-]}$	Duration	
		Relative values	
		$(y_1-y_2)/p_{max} = 23 \%$ $y_2-y_3/y_{2c} = 75 \%$ $y_2-y_3/y_{2y} = 2 \%$ $y_2-y_3/y_{2max} = 0 \%$ $F_{1max}/F_{maxK_2} = 4 \%$ $F_{3max}/F_{3y} = 106 \%$	



Appendices

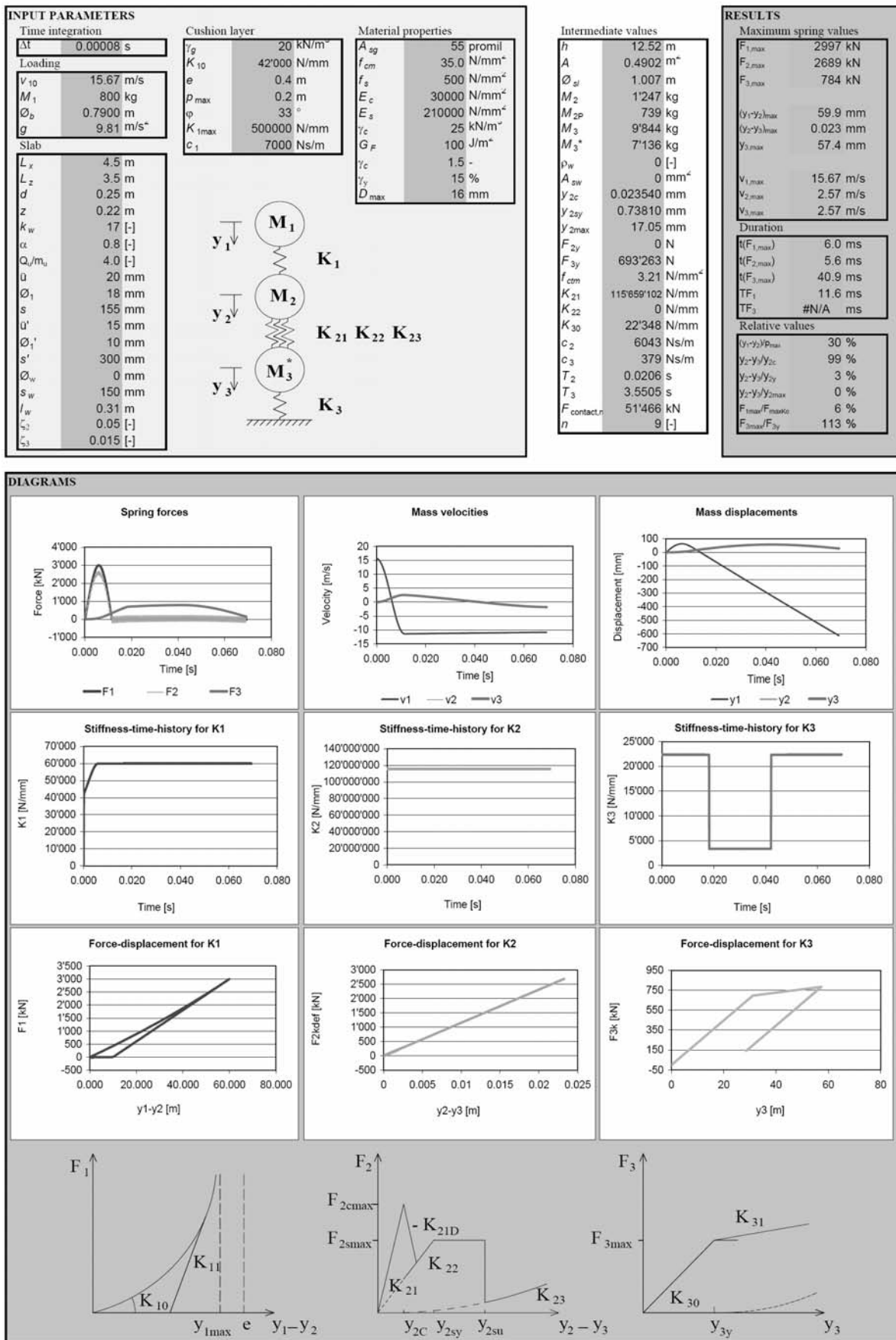
Values for test A6

Analytical model (System of multiple degrees of freedom)



Values for test A7

Analytical model (System of multiple degrees of freedom)

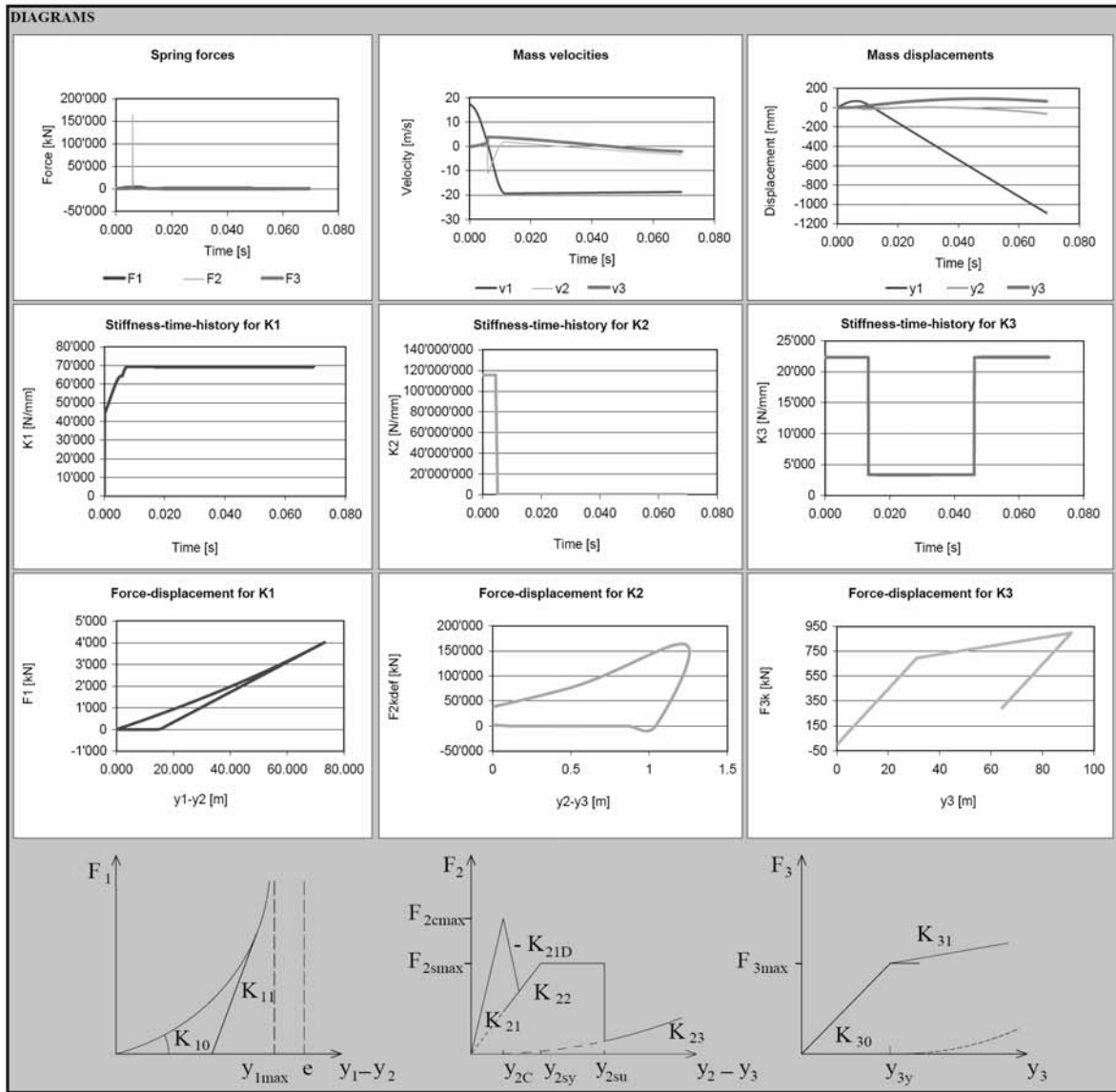
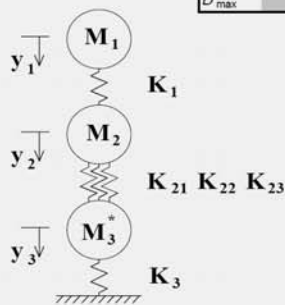


Appendices

Values for test A8

Analytical model (System of multiple degrees of freedom)

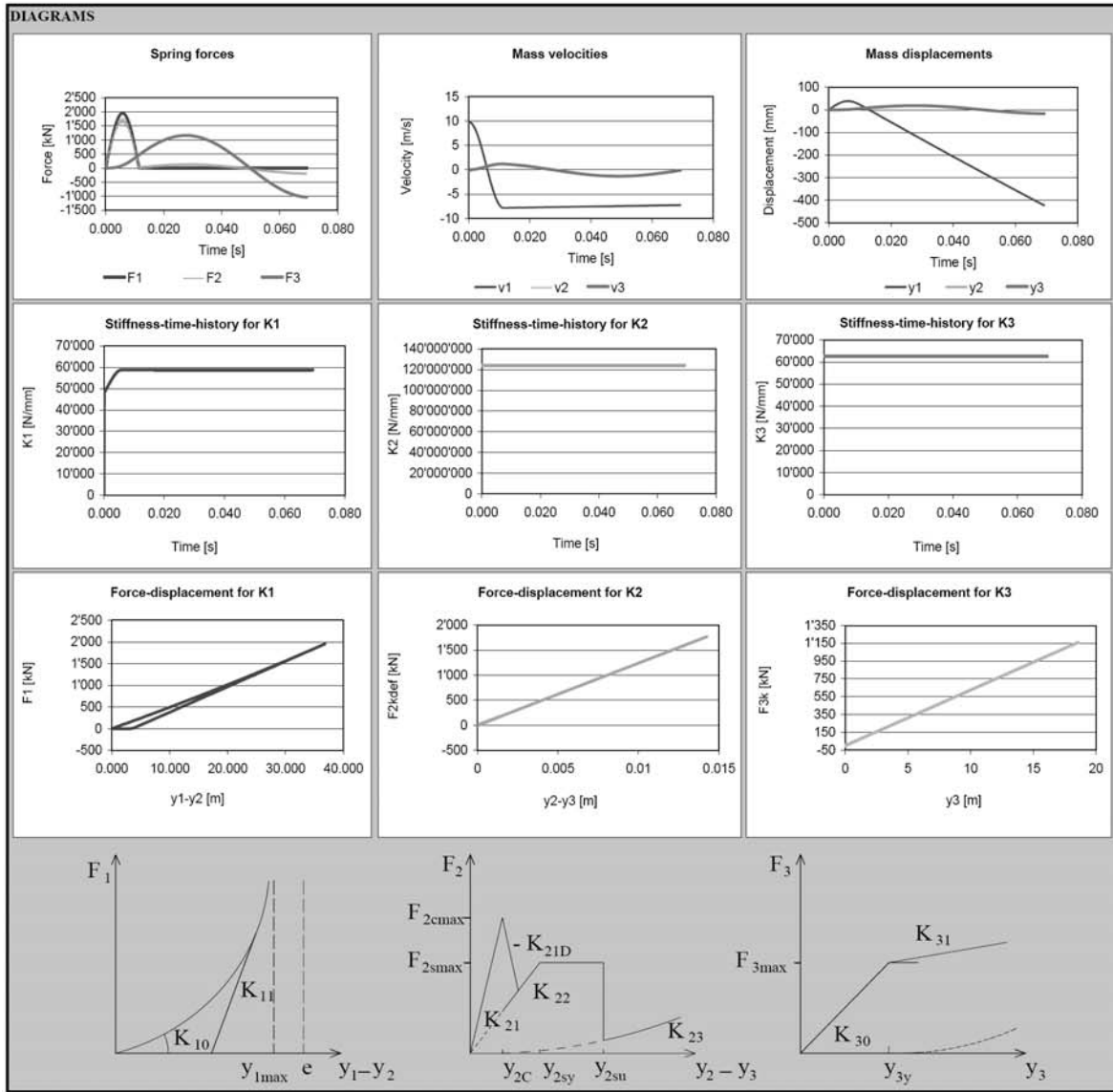
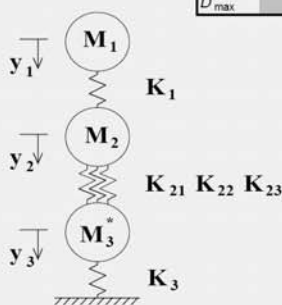
INPUT PARAMETERS		Cushion layer		Material properties		Intermediate values		RESULTS	
Time integration		γ_g	20 kN/m ²	A_{sg}	55 promil	h	15.03 m	Maximum spring values	
Δt	0.00008 s	K_{10}	44'000 N/mm	f_{cm}	35.0 N/mm ⁴	A	0.4902 m ²	$F_{1,max}$	4016 kN
Loading		e	0.4 m	f_s	500 N/mm ⁴	\varnothing_{sl}	1.007 m	$F_{2,max}$	162647 kN
V_{10}	17.17 m/s	p_{max}	0.2 m	E_c	30000 N/mm ²	M_2	1'247 kg	$F_{3,max}$	897 kN
M_1	800 kg	ϑ_p	33 °	E_s	210000 N/mm ²	M_{2P}	739 kg	$(y_1-y_2)_{max}$	73.1 mm
\varnothing_b	0.7900 m	K_{1max}	500000 N/mm	γ_c	25 kN/m ²	M_3	9'844 kg	$(y_2-y_3)_{max}$	1.235 mm
g	9.81 m/s ²	c_1	7000 Ns/m	G_F	100 J/m ²	M_3^*	7'136 kg	$y_{3,max}$	91.2 mm
Slab				ρ_w	0 [-]	ρ_w	0 [-]	$v_{t,max}$	17.17 m/s
L_x	4.5 m			A_{sw}	0 mm ²	$v_{2,max}$	3.61 m/s	$v_{3,max}$	3.84 m/s
L_z	3.5 m			y_{2c}	0.023540 mm	$y_{2z,y}$	0.73810 mm		
d	0.25 m			y_{2max}	17.05 mm				
z	0.22 m			F_{2y}	0 N				
k_w	17 [-]			F_{3y}	693'263 N				
α	0.8 [-]			f_{cm}	3.21 N/mm ⁴				
Q_u/m_u	4.0 [-]			K_{21}	115'659'102 N/mm				
u	20 mm			K_{22}	0 N/mm				
\varnothing_1	18 mm			K_{30}	22'348 N/mm				
s	155 mm								
u'	15 mm								
\varnothing_1'	10 mm								
s'	300 mm								
\varnothing_w	0 mm								
s_w	150 mm								
l_w	0.31 m								
γ_2	0.05 [-]								
γ_3	0.015 [-]								



Values for test B1

Analytical model (System of multiple degrees of freedom)

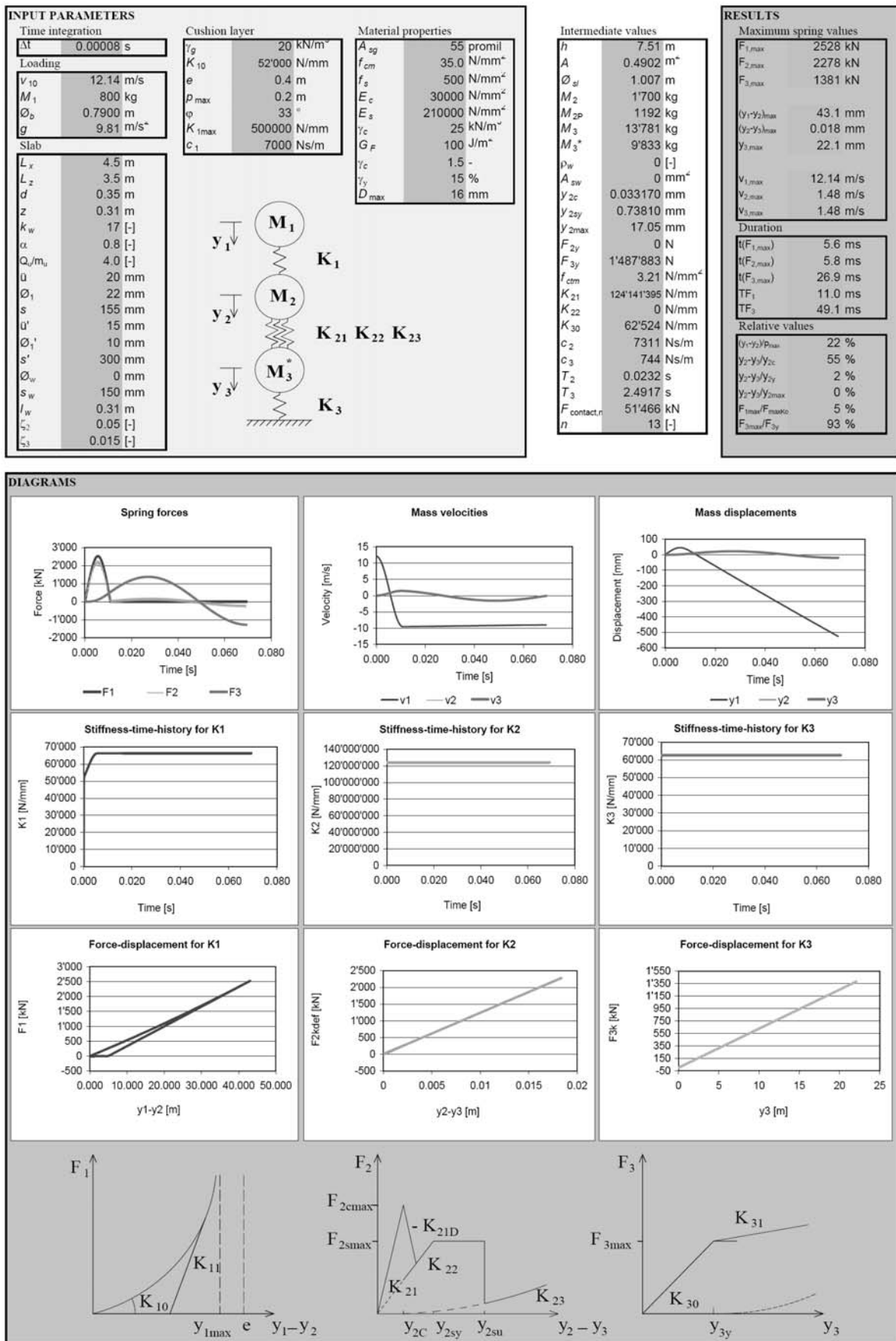
INPUT PARAMETERS		Cushion layer		Material properties		Intermediate values		RESULTS	
Time integration	$\Delta t = 0.00008 \text{ s}$	$\gamma_g = 20 \text{ kN/m}^2$	$K_{10} = 48'000 \text{ N/mm}$	$A_{sg} = 55 \text{ promil}$	$f_{cm} = 35.0 \text{ N/mm}^2$	$h = 5.01 \text{ m}$	$A = 0.4902 \text{ m}^2$	$F_{1,max} = 1954 \text{ kN}$	
Loading	$v_{10} = 9.91 \text{ m/s}$	$e = 0.4 \text{ m}$	$\rho_{max} = 0.2 \text{ m}$	$f_s = 500 \text{ N/mm}^2$	$E_c = 30000 \text{ N/mm}^2$	$\varnothing_{sl} = 1.007 \text{ m}$	$M_1 = 1700 \text{ kg}$	$F_{2,max} = 1768 \text{ kN}$	
M_1	800 kg	$\phi = 33^\circ$	$K_{1max} = 500000 \text{ N/mm}$	$E_s = 210000 \text{ N/mm}^2$	$E_c = 25 \text{ kN/m}^2$	$M_2 = 1192 \text{ kg}$	$M_3 = 13'781 \text{ kg}$	$F_{3,max} = 1161 \text{ kN}$	
\varnothing_b	0.7900 m	$c_1 = 7000 \text{ Ns/m}$		$G_F = 100 \text{ J/m}^2$	$\gamma_c = 1.5 -$	$M_3^* = 9'833 \text{ kg}$		$(y_1-y_2)_{max} = 36.8 \text{ mm}$	
g	9.81 m/s ²			$\gamma_y = 15 \%$	$y_{zc} = 0.033170 \text{ mm}$			$(y_2-y_3)_{max} = 0.014 \text{ mm}$	
Slab				$D_{max} = 16 \text{ mm}$	$y_{2sy} = 0.73810 \text{ mm}$			$y_{3,max} = 18.6 \text{ mm}$	
L_x	4.5 m				$y_{2max} = 17.05 \text{ mm}$				
L_z	3.5 m								
d	0.35 m								
z	0.31 m								
k_w	17 [-]								
a	0.8 [-]								
Q/m_u	4.0 [-]								
\hat{u}	20 mm								
\varnothing_1	22 mm								
s	155 mm								
u'	15 mm								
\varnothing_1'	10 mm								
s'	300 mm								
\varnothing_w	0 mm								
s_w	150 mm								
l_w	0.31 m								
ζ_1	0.05 [-]								
ζ_3	0.015 [-]								



Appendices

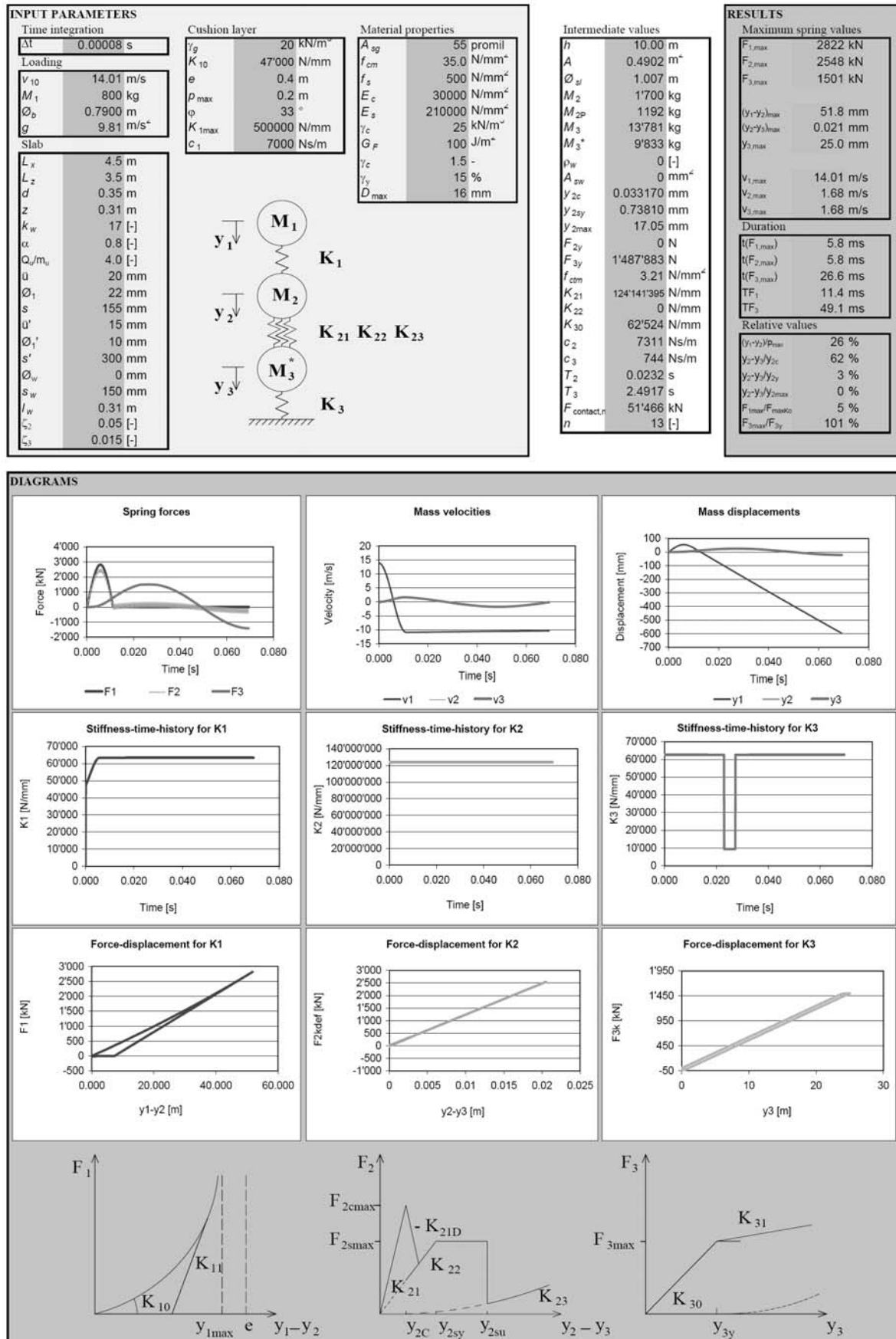
Values for test B2

Analytical model (System of multiple degrees of freedom)



Values for test B3

Analytical model (System of multiple degrees of freedom)

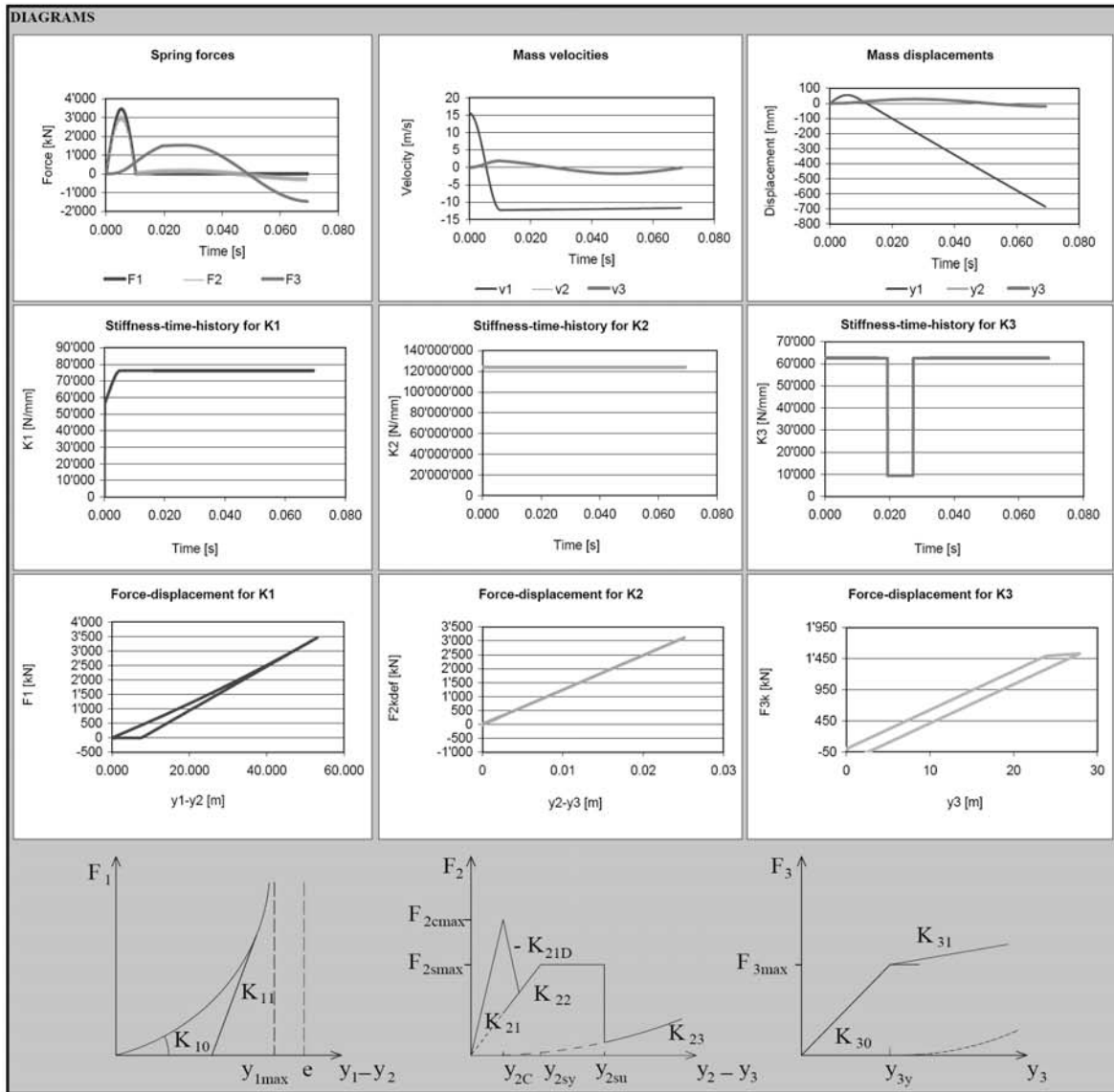
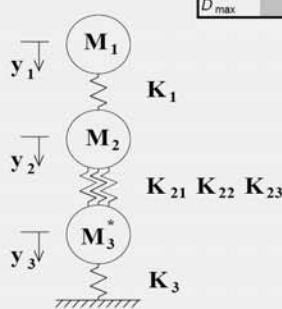


Appendices

Values for test B4

Analytical model (System of multiple degrees of freedom)

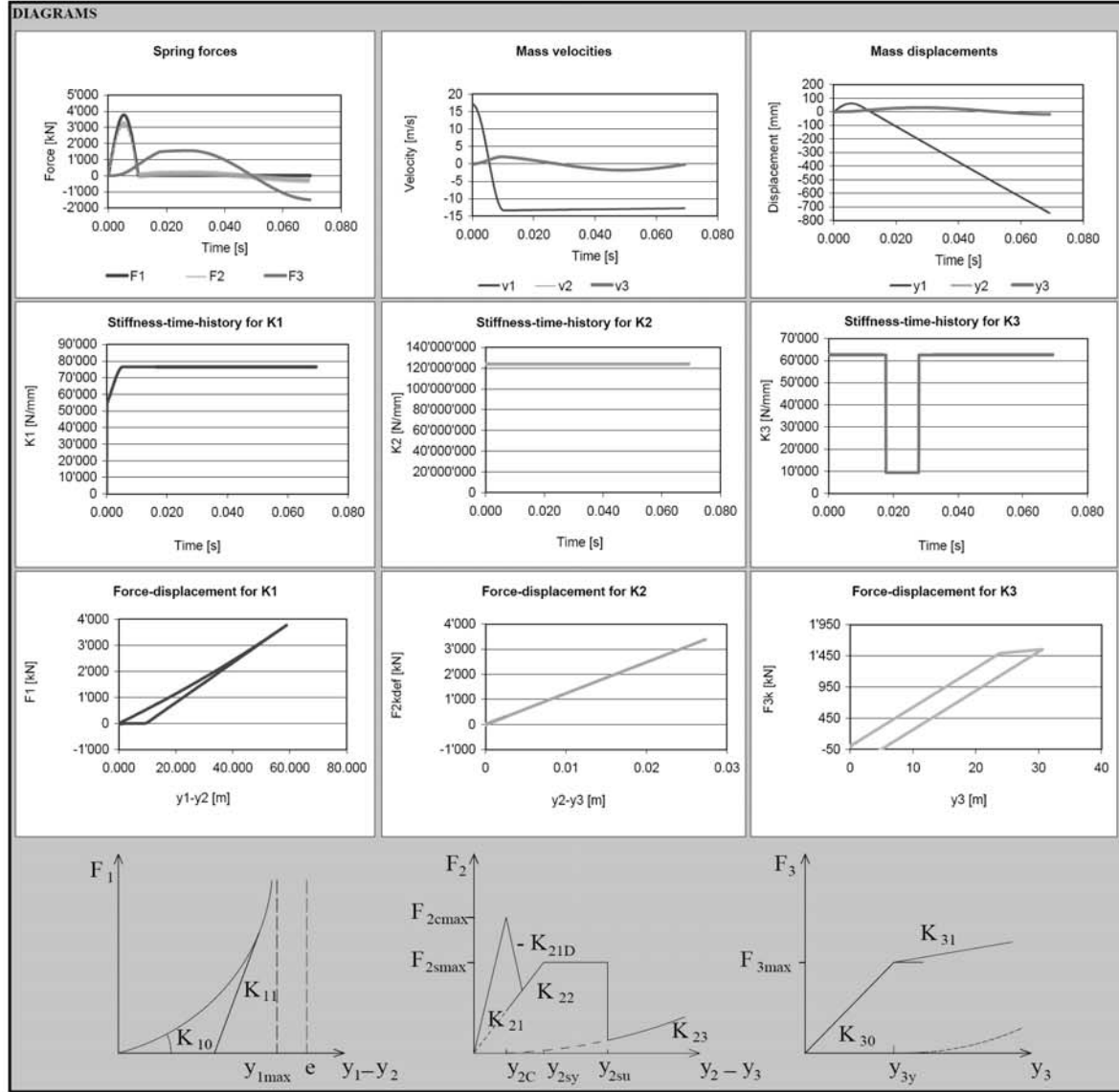
INPUT PARAMETERS		Cushion layer		Material properties		Intermediate values		RESULTS	
Time integration		γ_g	20 kN/m ²	A_{sg}	55 promil	h	12.52 m	Maximum spring values	
Δt	0.00008 s	K_{10}	56'000 N/mm	f_{cm}	35.0 N/mm ²	A	0.4902 m ²	$F_{1,max}$	3464 kN
Loading		e	0.4 m	f_s	500 N/mm ²	\varnothing_{sl}	1.007 m	$F_{2,max}$	3118 kN
V_{10}	15.67 m/s	ρ_{max}	0.2 m	E_c	30000 N/mm ²	M_2	1700 kg	$F_{3,max}$	1529 kN
M_1	800 kg	φ	33 °	E_s	210000 N/mm ²	M_{2P}	1192 kg	$(y_1-y_2)_{max}$	53.1 mm
\varnothing_b	0.7900 m	K_{1max}	500000 N/mm	γ_c	25 kN/m ²	M_3	13'781 kg	$(y_2-y_3)_{max}$	0.025 mm
g	9.81 m/s ²	c_1	7000 Ns/m	G_F	100 J/m ²	M_3^*	9'833 kg	$y_{3,max}$	27.9 mm
Slab				γ_c	1.5 -				
L_x	4.5 m			γ_y	15 %				
L_z	3.5 m			D_{max}	16 mm				
d	0.35 m								
z	0.31 m								
k_w	17 [-]								
α	0.8 [-]								
Q_u/m_u	4.0 [-]								
\bar{u}	20 mm								
\varnothing_1	22 mm								
s	155 mm								
u'	15 mm								
\varnothing_1'	10 mm								
s'	300 mm								
\varnothing_w	0 mm								
s_w	150 mm								
l_w	0.31 m								
γ_2	0.05 [-]								
γ_3	0.015 [-]								



Values for test B5

Analytical model (System of multiple degrees of freedom)

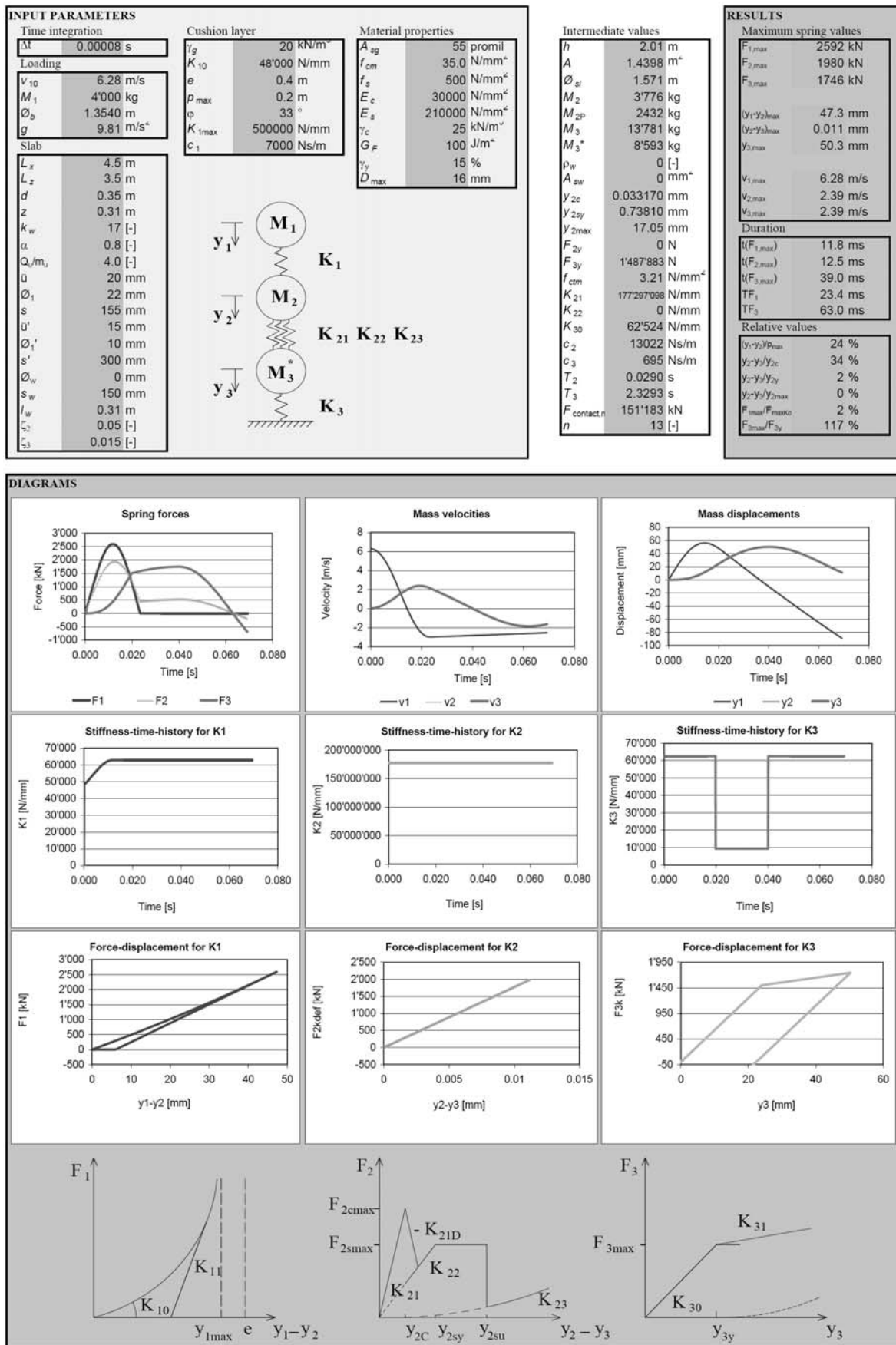
INPUT PARAMETERS		RESULTS	
Time integration		Intermediate values	Maximum spring values
Δt	0.00008 s	h	$F_{1,max}$
Loading		A	3776 kN
V_{10}	17.17 m/s	\varnothing_{sl}	3393 kN
M_1	800 kg	M_2	1553 kN
\varnothing_b	0.7900 m	M_{2P}	
g	9.81 m/s ²	M_3	1700 kg
Slab		M_3^*	13781 kg
L_x	4.5 m	G_F	9'833 kg
L_z	3.5 m	ρ_w	100 J/m ²
d	0.35 m	A_{sw}	0 [-]
z	0.31 m	y_{2c}	0 mm
k_w	17 [-]	y_{2y}	0.033170 mm
a	0.8 [-]	y_{2max}	0.73810 mm
Q_u/m_u	4.0 [-]	F_{2y}	17.05 mm
u	20 mm	F_{3y}	0 N
\varnothing_1	22 mm	f_{cm}	1'487'883 N
s	155 mm	K_{21}	3.21 N/mm ²
u'	15 mm	K_{22}	0 N/mm
\varnothing_1'	10 mm	K_{30}	124'141'395 N/mm
s'	300 mm	c_2	62'524 N/mm
\varnothing_w	0 mm	c_3	7311 Ns/m
s_w	150 mm	T_2	744 Ns/m
l_w	0.31 m	T_3	0.0232 s
γ_2	0.05 [-]	$F_{contact,n}$	2.4917 s
γ_3	0.015 [-]	n	51'466 kN
			13 [-]
		RESULTS Maximum spring values $F_{1,max}$ 3776 kN $F_{2,max}$ 3393 kN $F_{3,max}$ 1553 kN $(y_1-y_2)_{max}$ 58.9 mm $(y_2-y_3)_{max}$ 0.027 mm $y_{3,max}$ 30.6 mm Duration $t(F_{1,max})$ 5.4 ms $t(F_{2,max})$ 5.0 ms $t(F_{3,max})$ 27.0 ms TF_1 10.4 ms TF_3 49.5 ms Relative values $(y_1-y_2)\rho_{max}$ 29 % y_2-y_3/y_{2c} 82 % y_2-y_3/y_{2y} 4 % y_2-y_3/y_{2max} 0 % F_{1max}/F_{max0} 7 % F_{3max}/F_{3y} 104 %	



Appendices

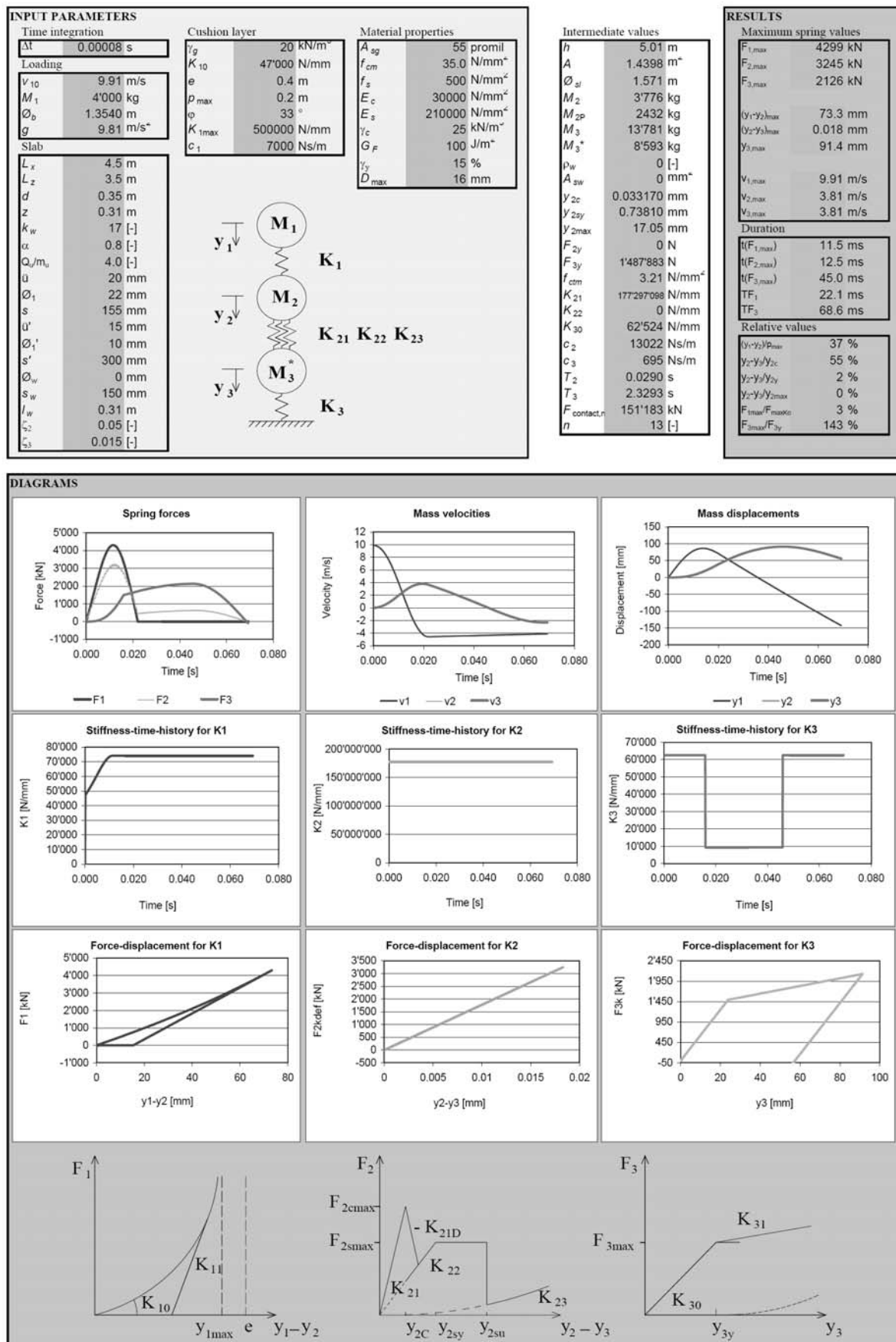
Values for test B6

Analytical model (System of multiple degrees of freedom)



Values for test B7

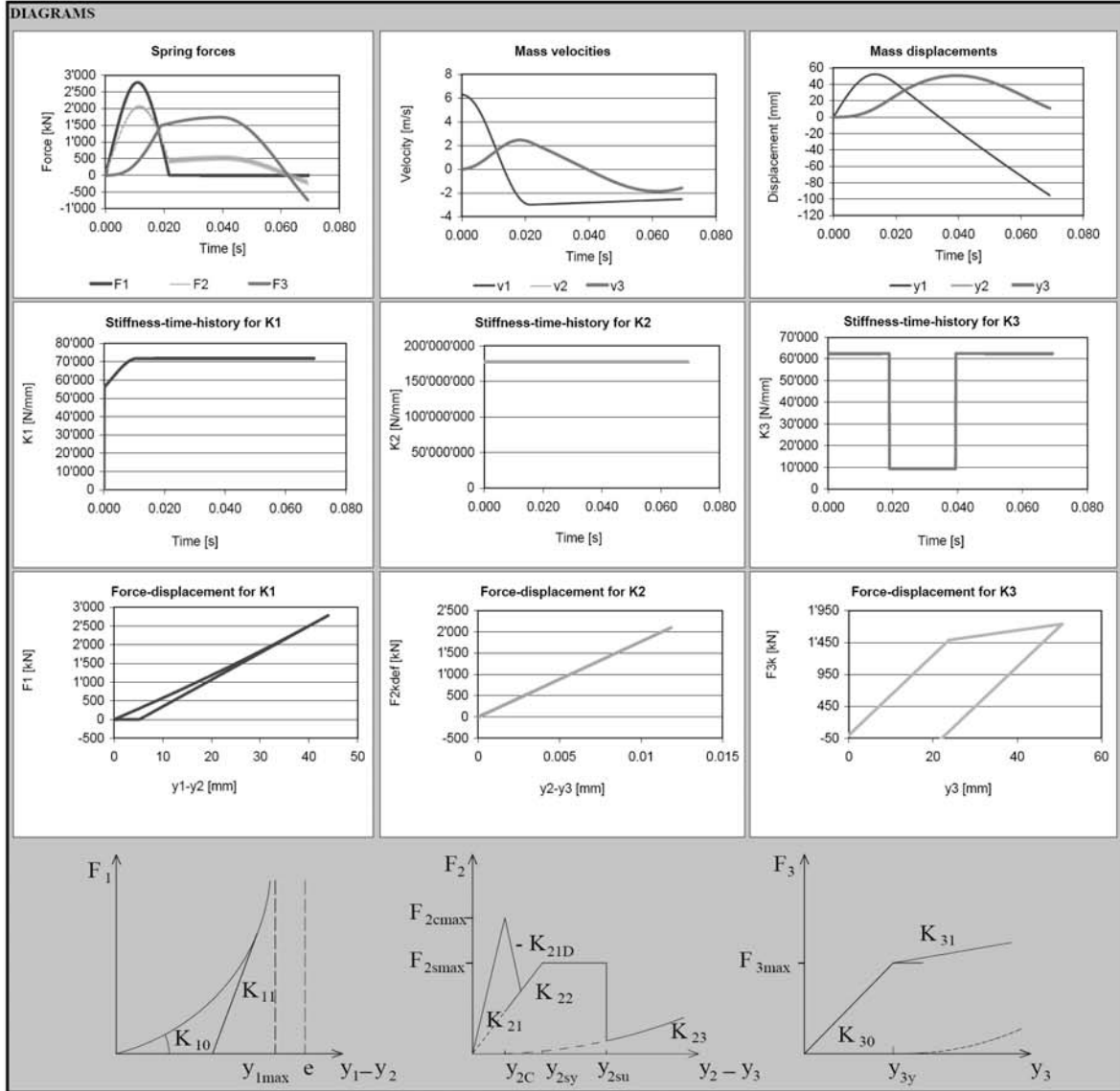
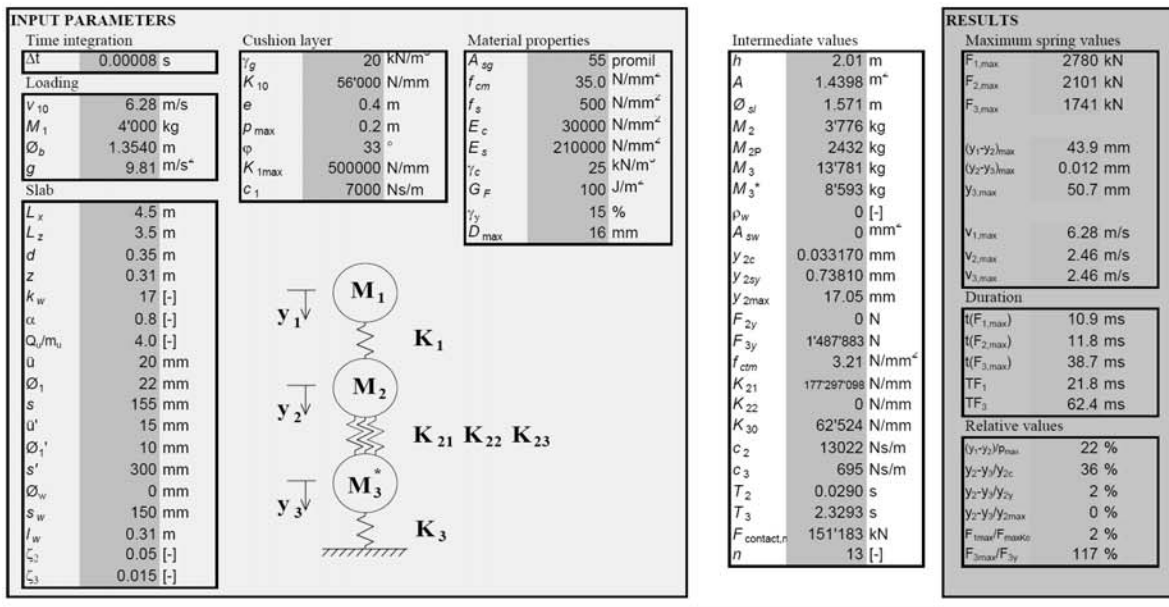
Analytical model (System of multiple degrees of freedom)



Appendices

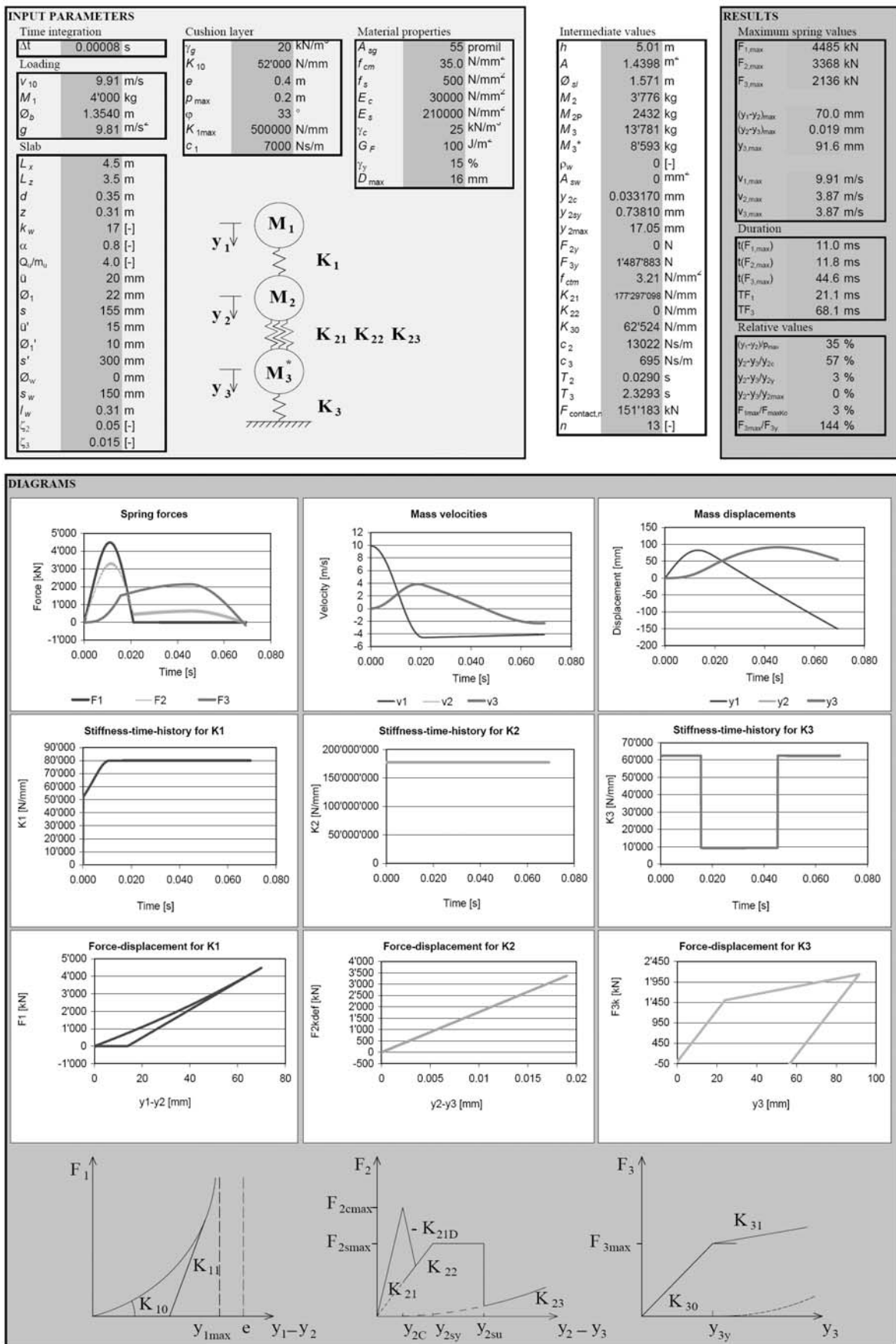
Values for test D1

Analytical model (System of multiple degrees of freedom)



Values for test D2

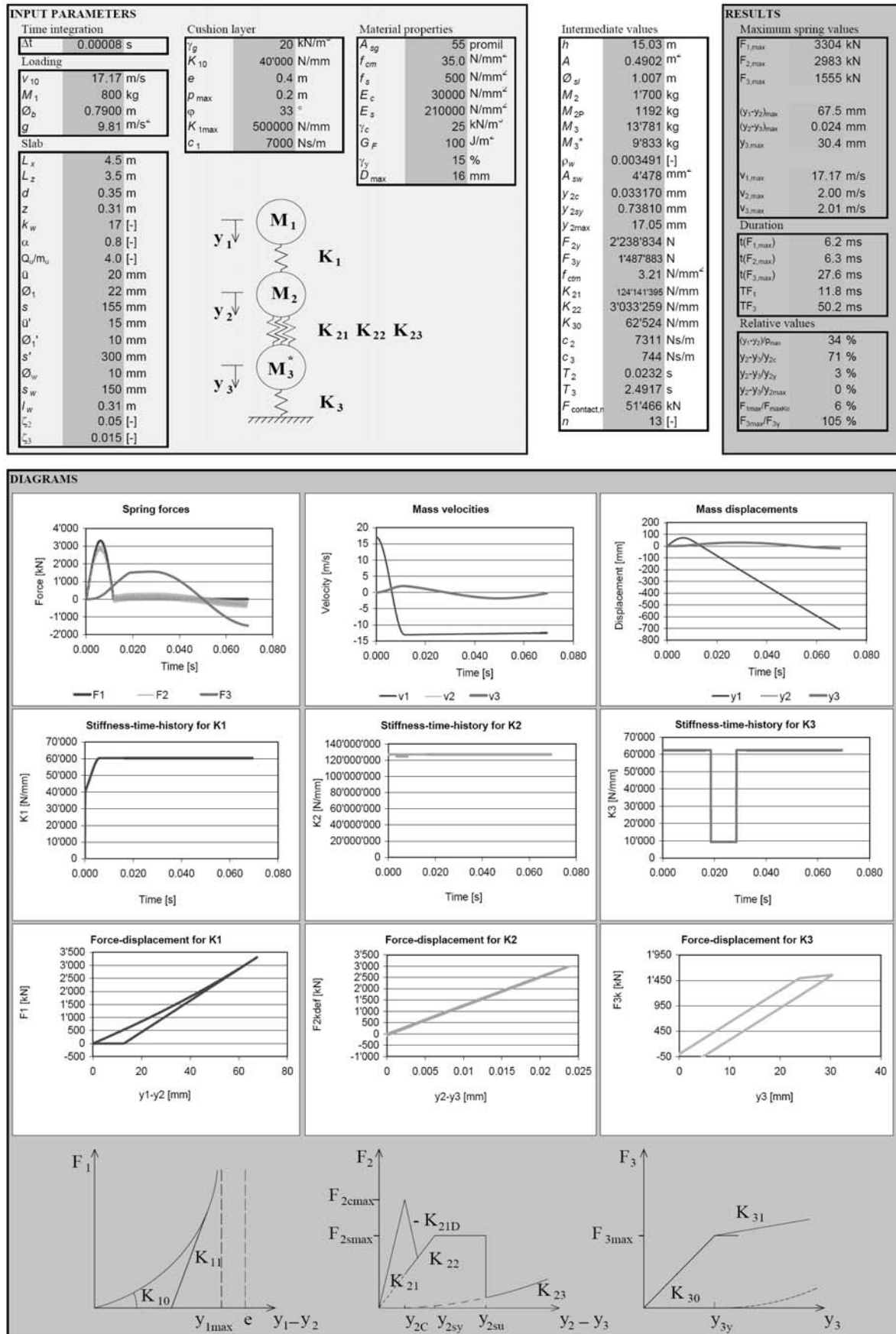
Analytical model (System of multiple degrees of freedom)



Appendices

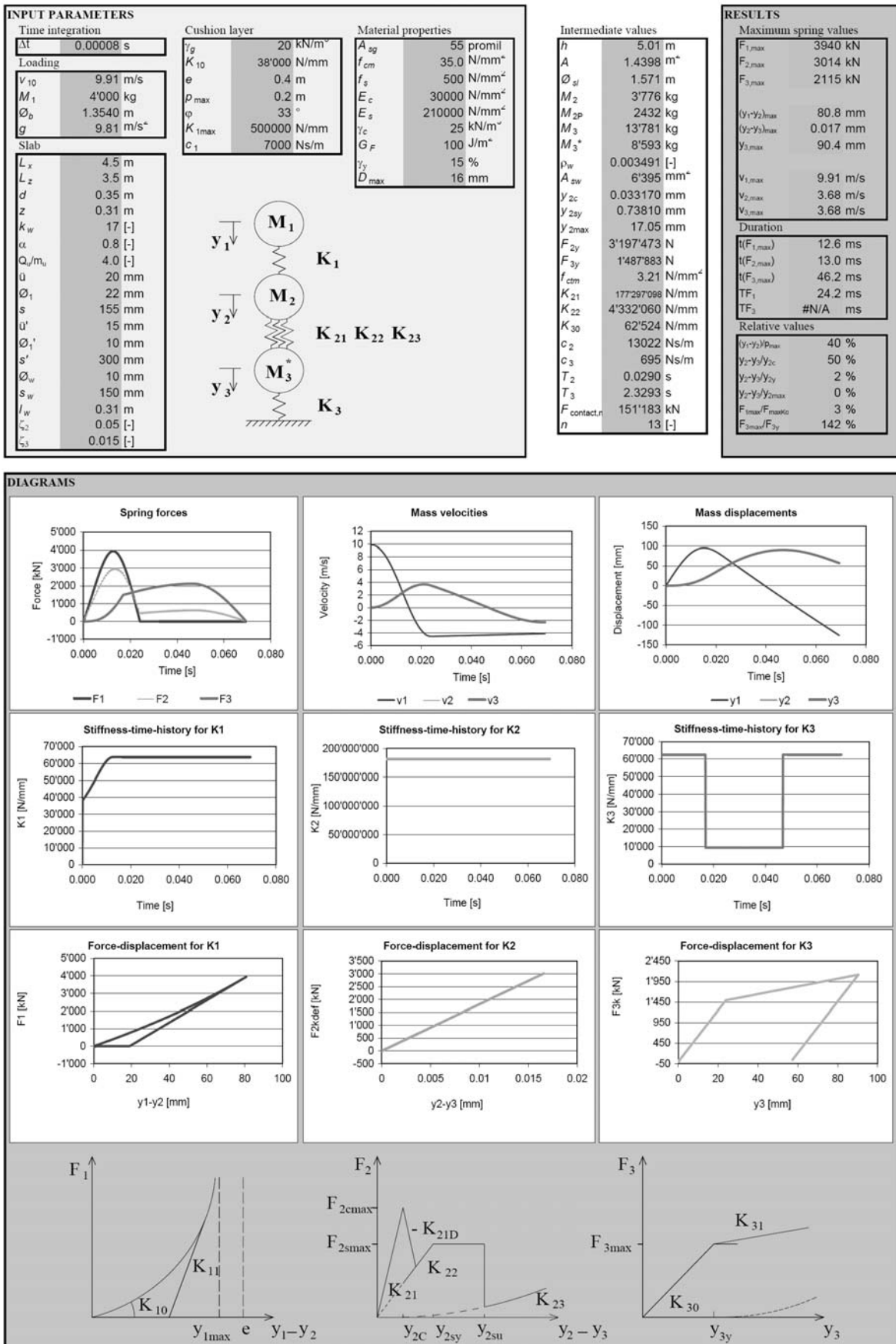
Values for tests E1 + F7

Analytical model (System of multiple degrees of freedom)



Values for test E2

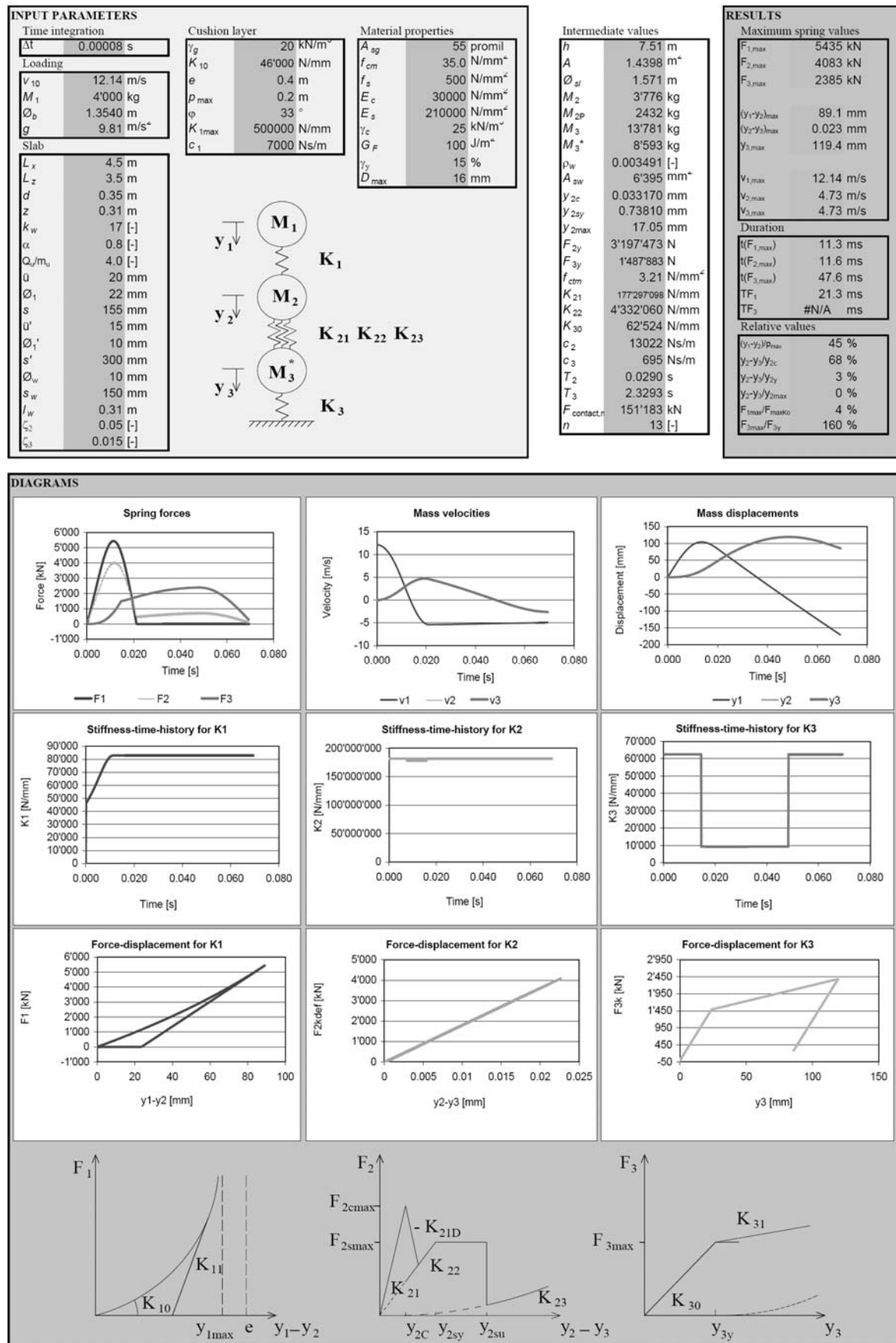
Analytical model (System of multiple degrees of freedom)



Appendices

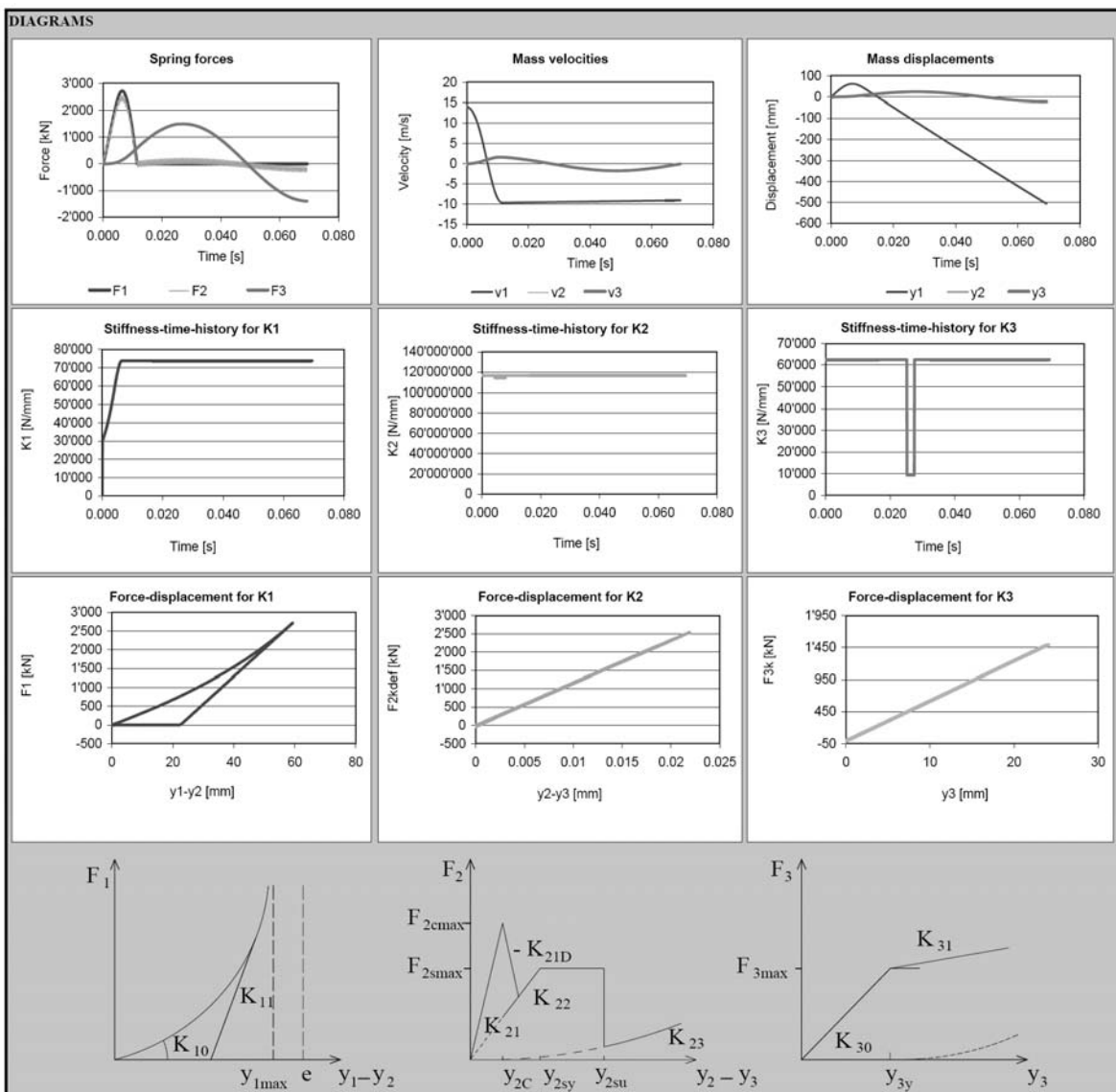
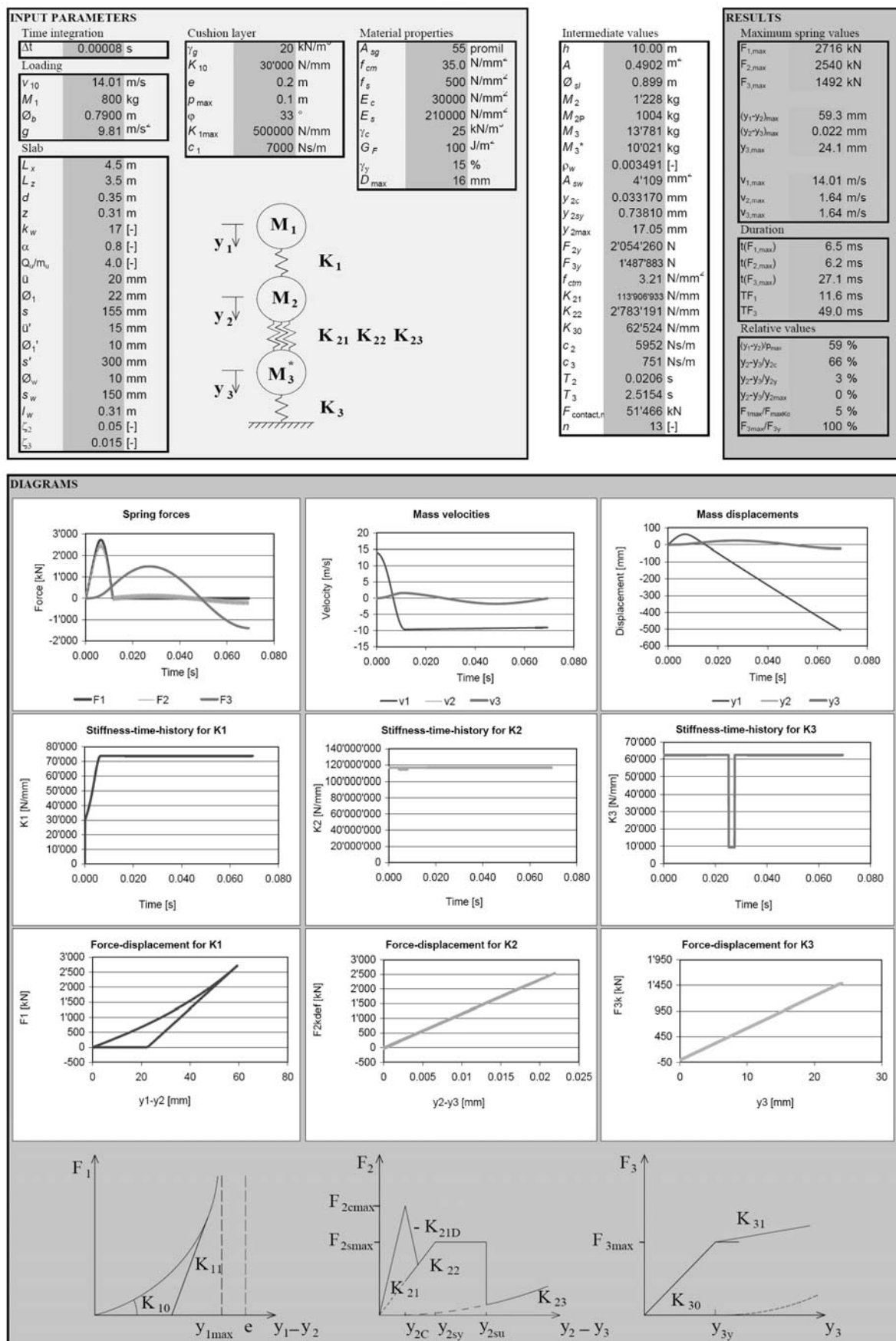
Values for test E3

Analytical model (System of multiple degrees of freedom)



Values for test F5

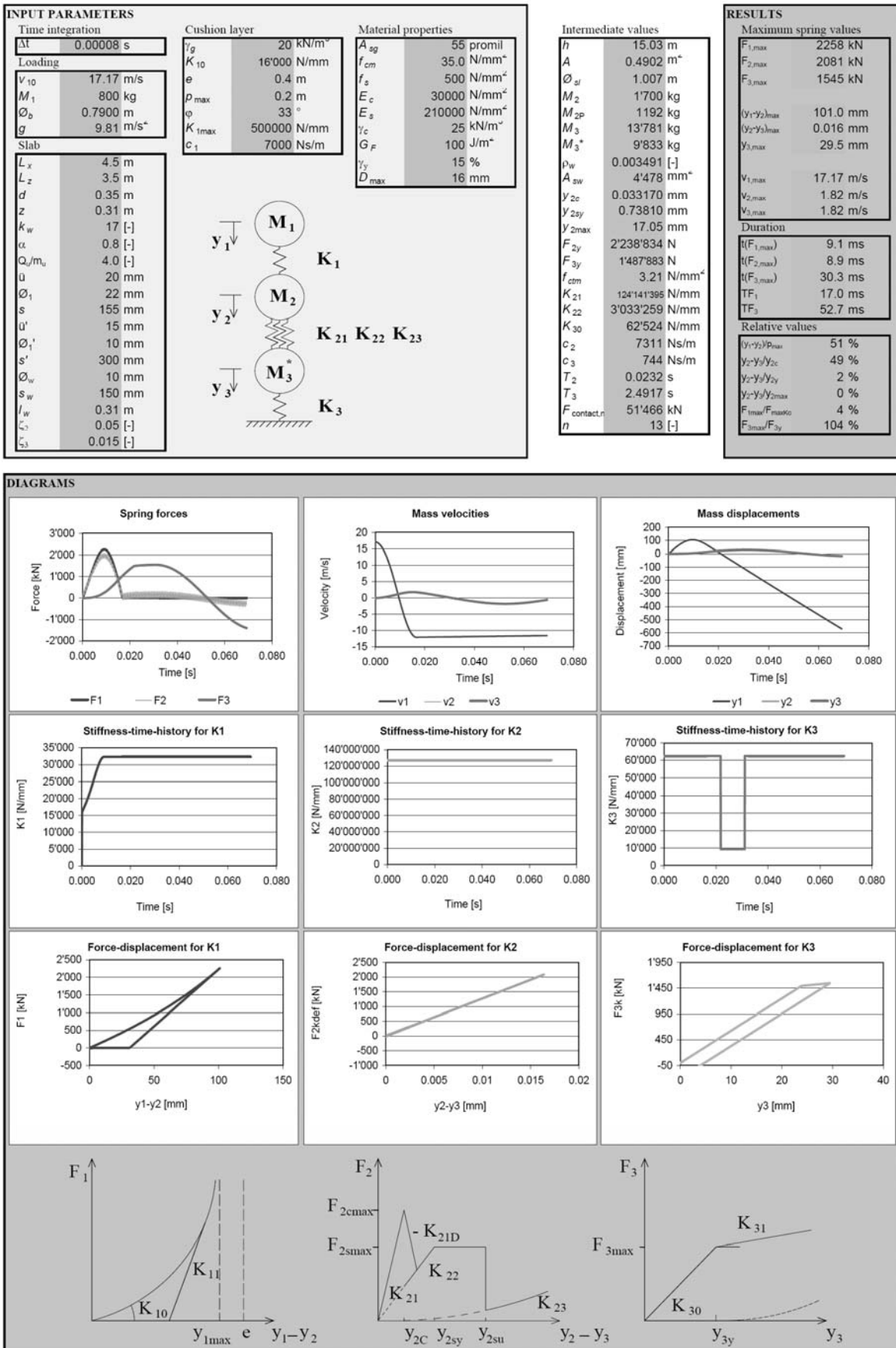
Analytical model (System of multiple degrees of freedom)



Appendices

Values for test F6

Analytical model (System of multiple degrees of freedom)



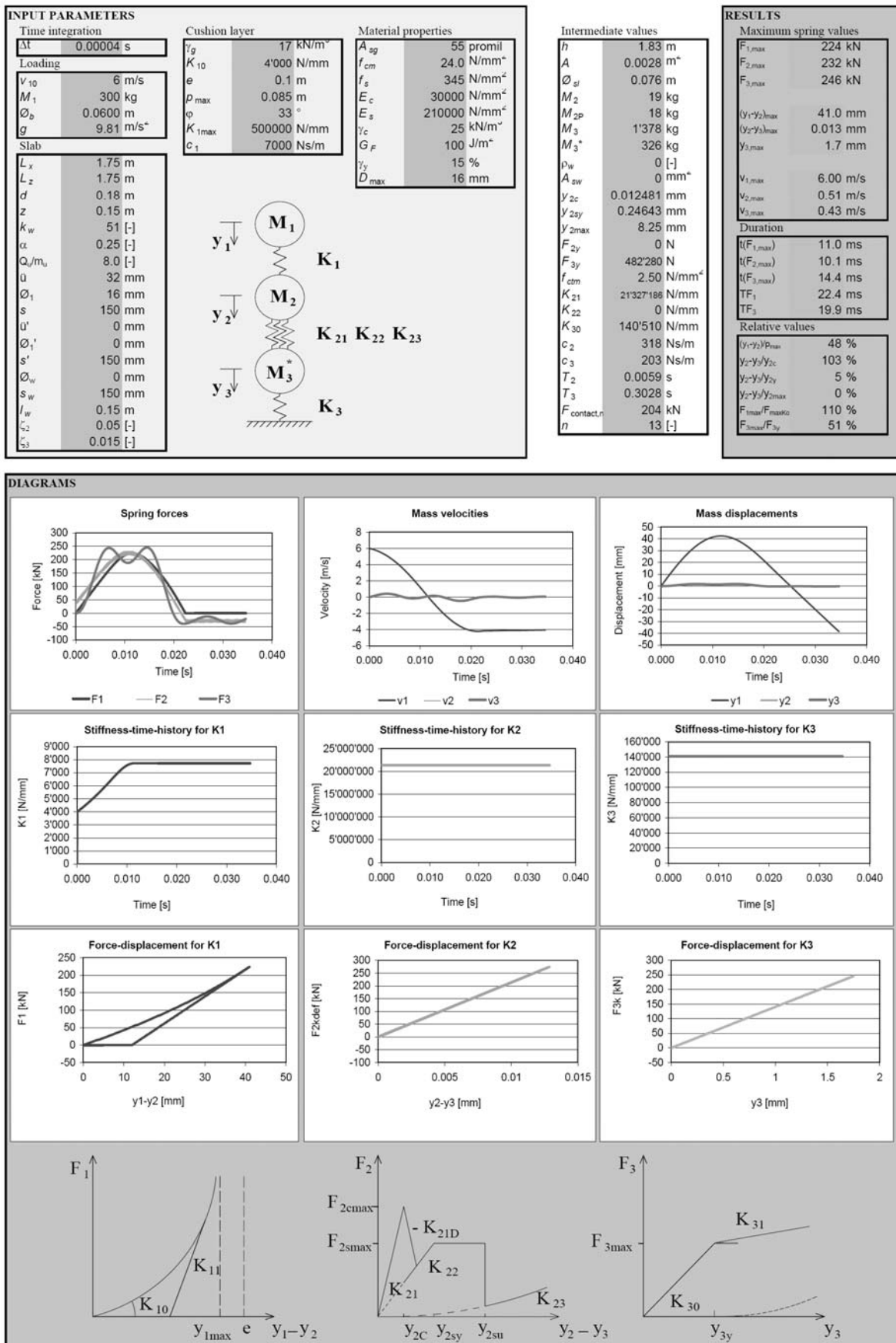
E. Input and output of SMDF for the punching tests

Test S6	156
Test S6 with $v_1 = 6.2 \text{ m/s}$	157
Test S6 with $\varphi = 90^\circ$	158
Test S15-6	159
Test S15-7	160
Test S15-8	161
Test S15-9	162
Test S15-9 with $f_{cm} = 32 \text{ N/mm}^2$	163
Test S15-10	164
Test S15-10 with $f_{cm} = 32 \text{ N/mm}^2$	165

Appendices

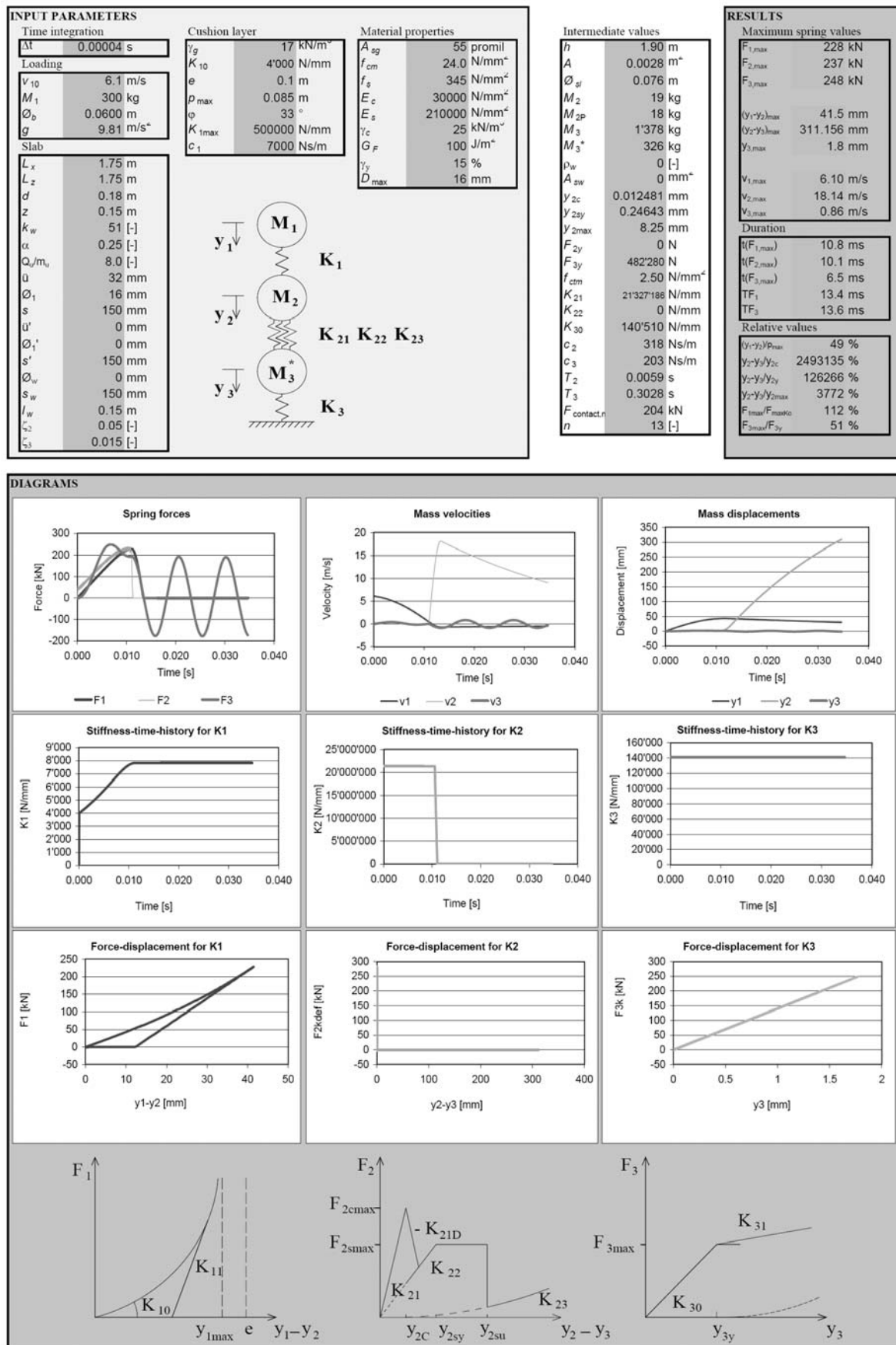
Test S6

Analytical model (System of multiple degrees of freedom)



Test S6 with $v_1 = 6.1 \text{ m/s}$

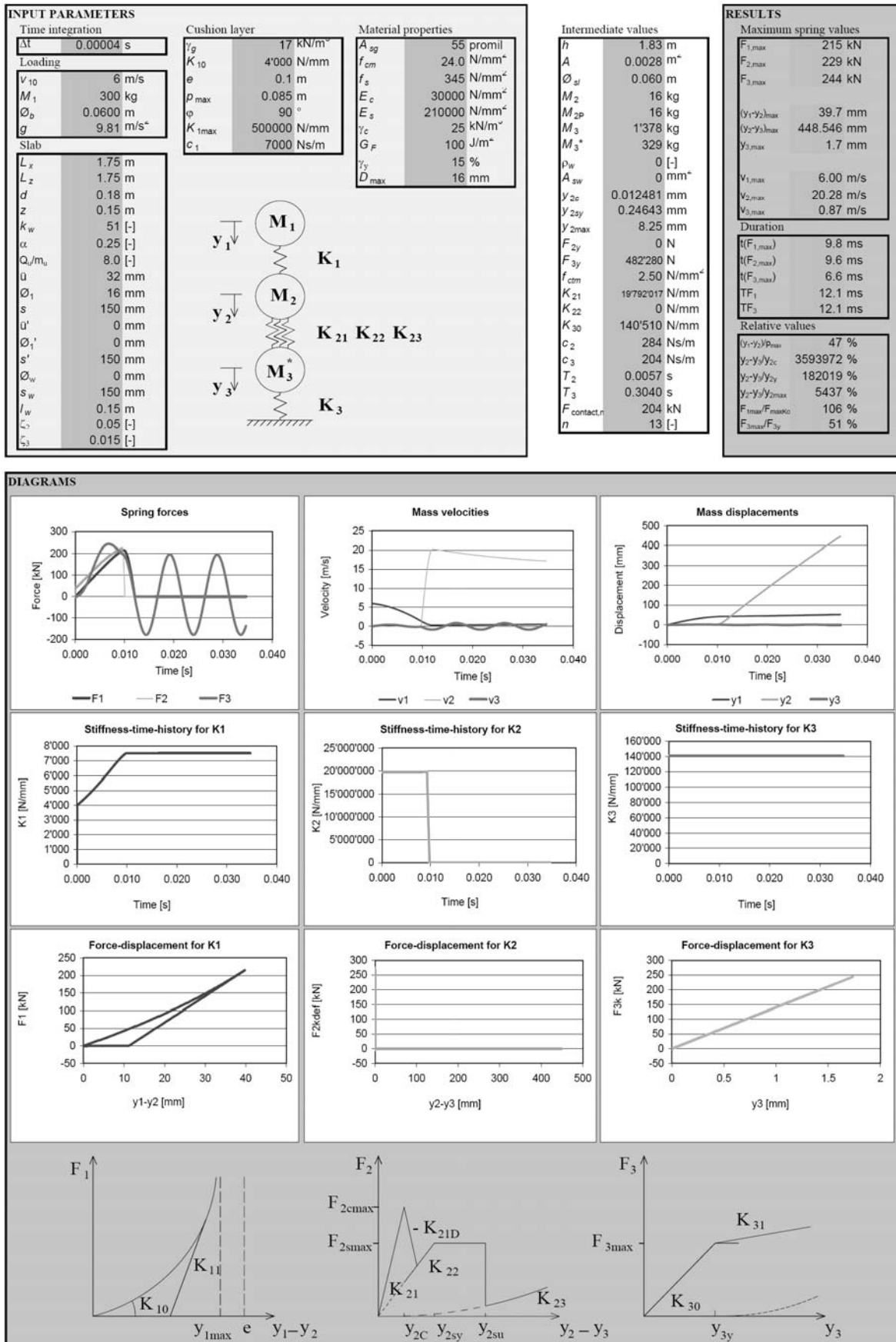
Analytical model (System of multiple degrees of freedom)



Appendices

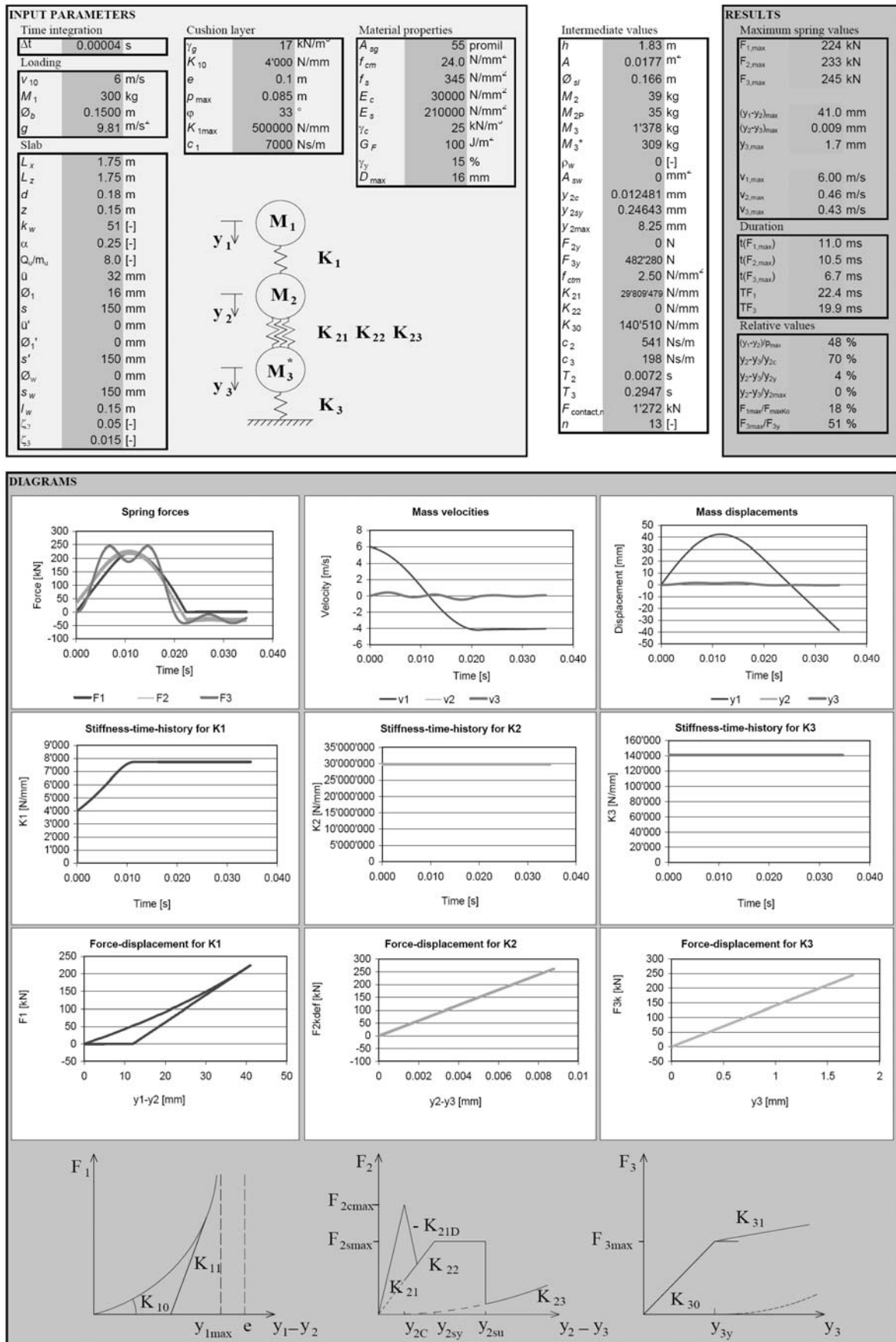
Test S6 with $\varphi = 90^\circ$

Analytical model (System of multiple degrees of freedom)



Test S15-6

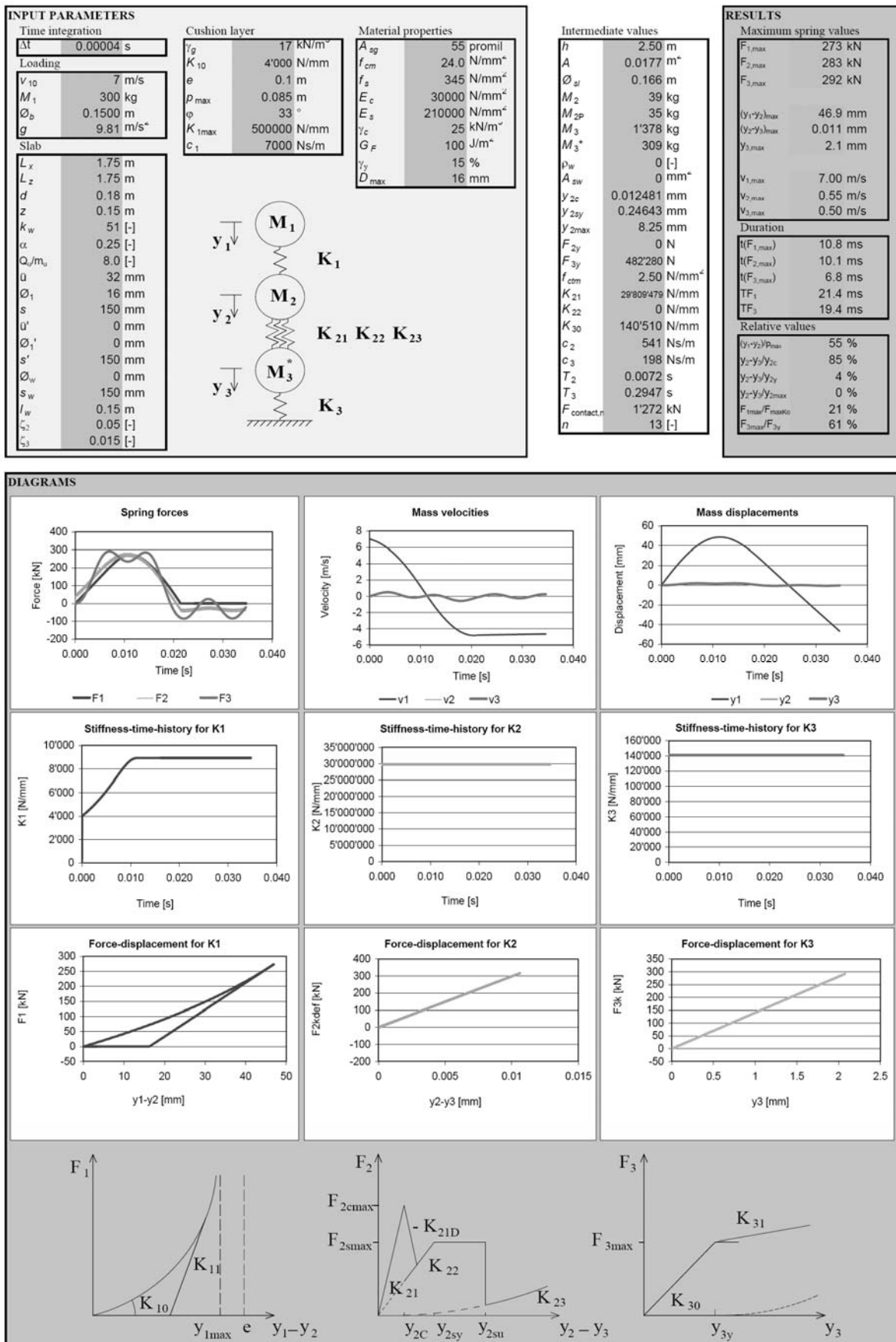
Analytical model (System of multiple degrees of freedom)



Appendices

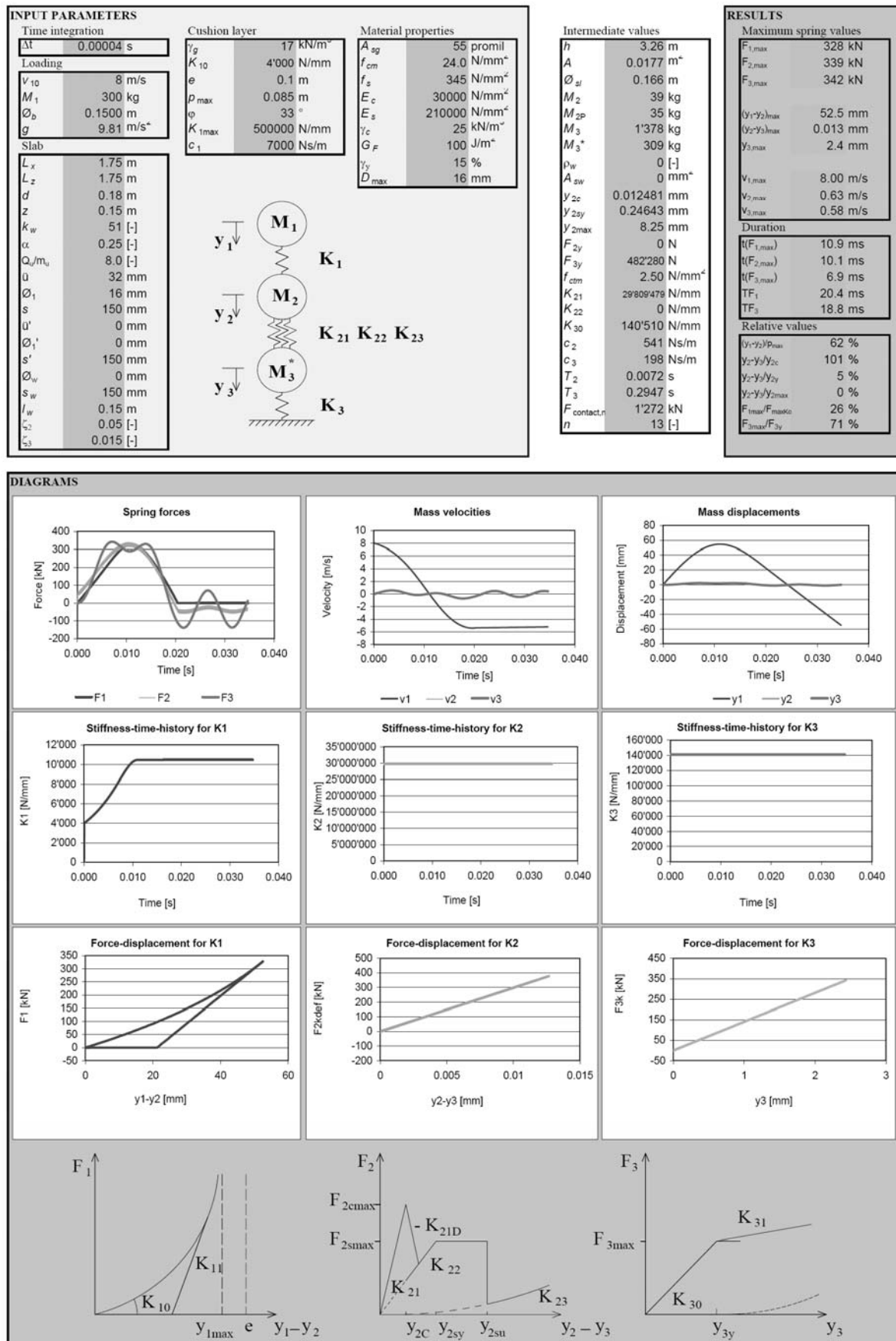
Test S15-7

Analytical model (System of multiple degrees of freedom)



Test S15-8

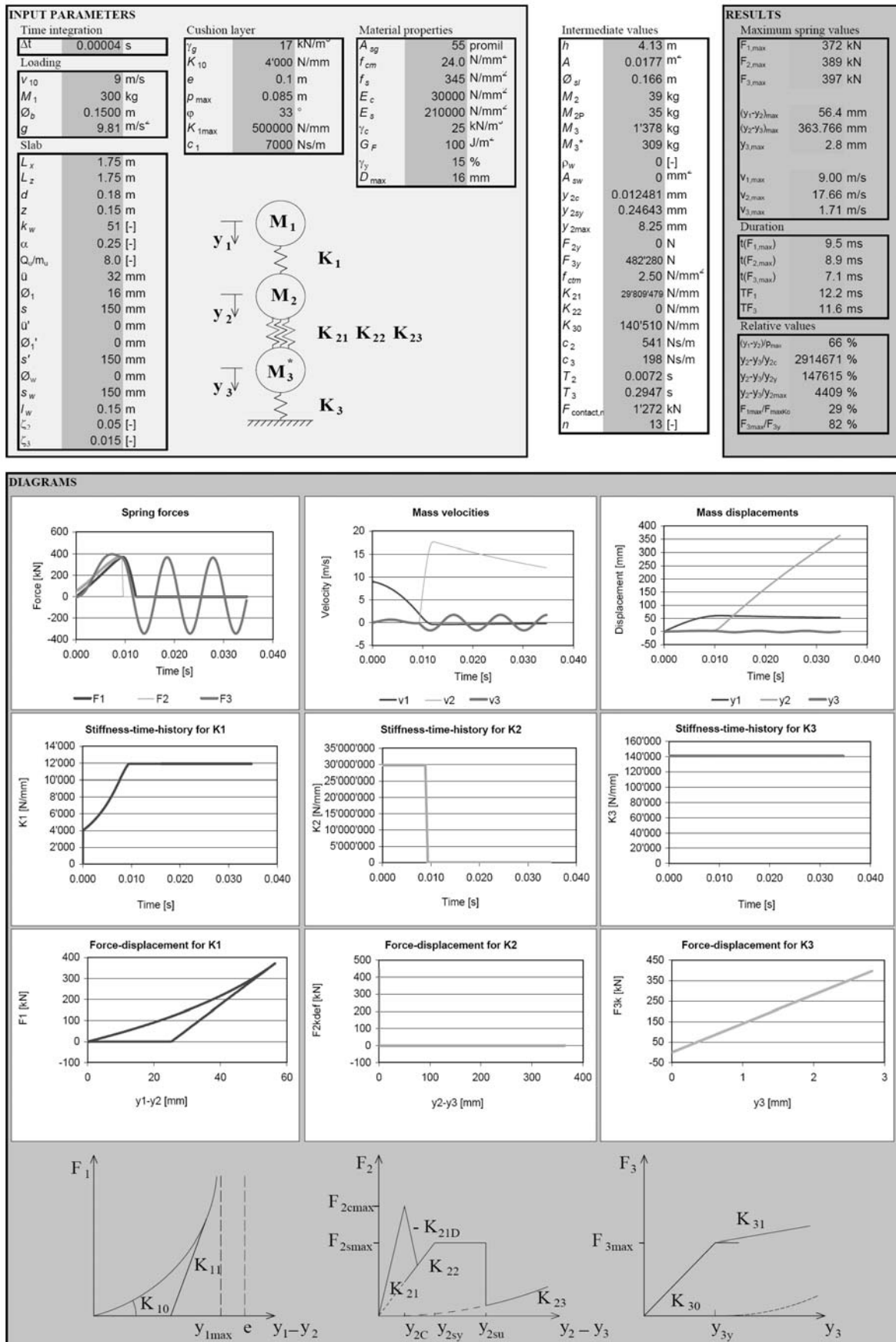
Analytical model (System of multiple degrees of freedom)



Appendices

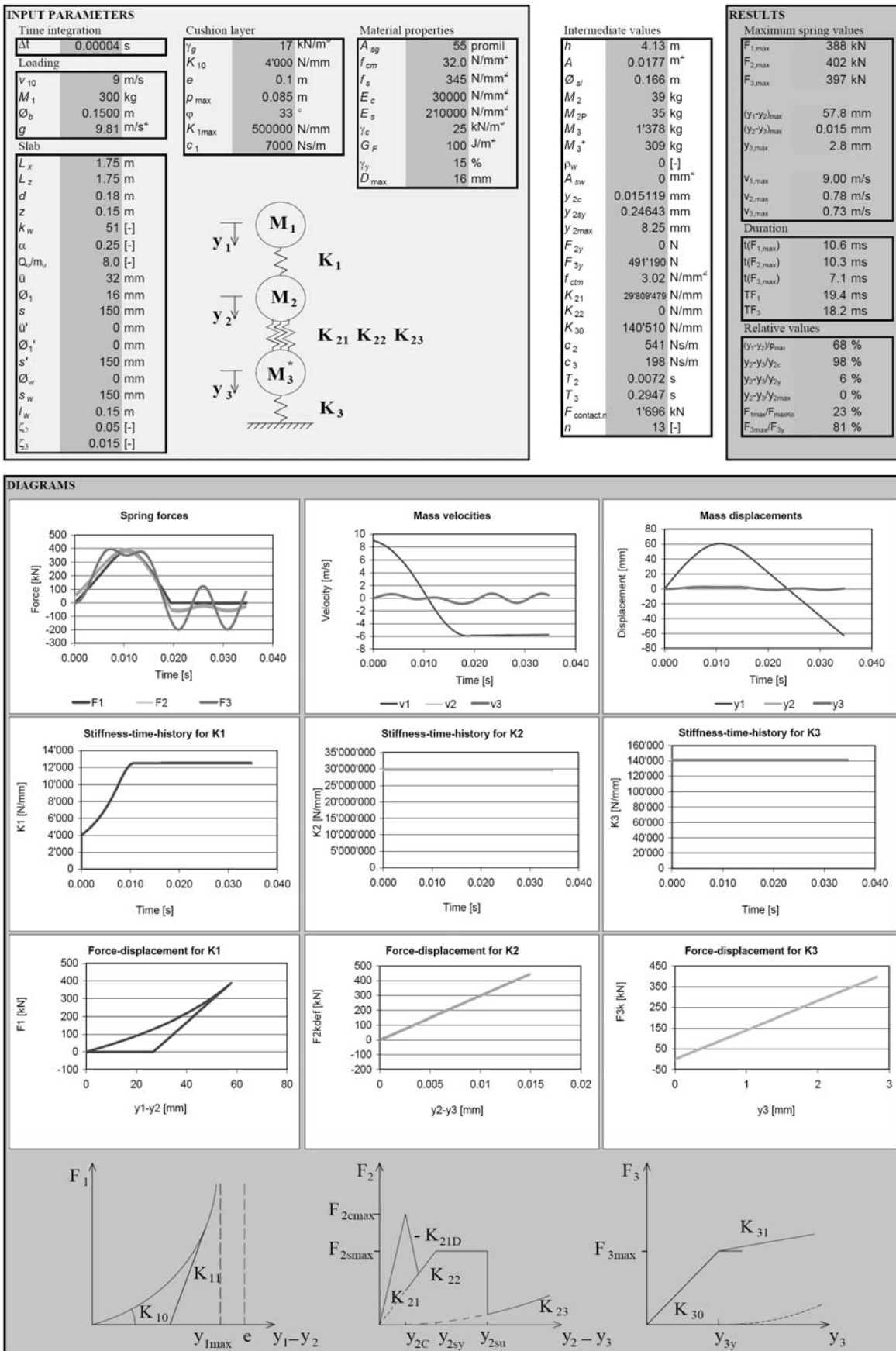
Test S15-9

Analytical model (System of multiple degrees of freedom)



Test S15-9 with $f_{cm} = 32 \text{ N/mm}^2$

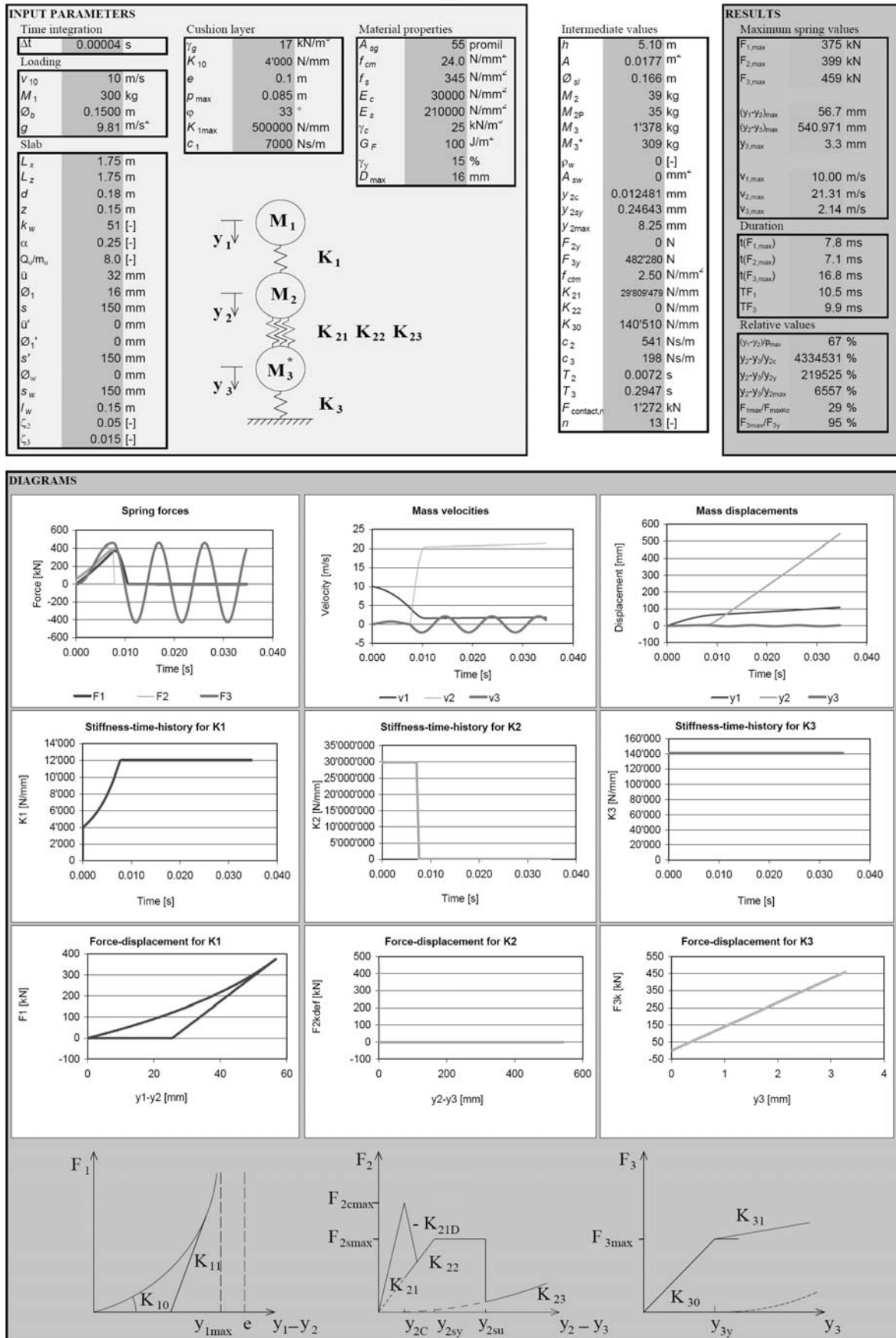
Analytical model (System of multiple degrees of freedom)



Appendices

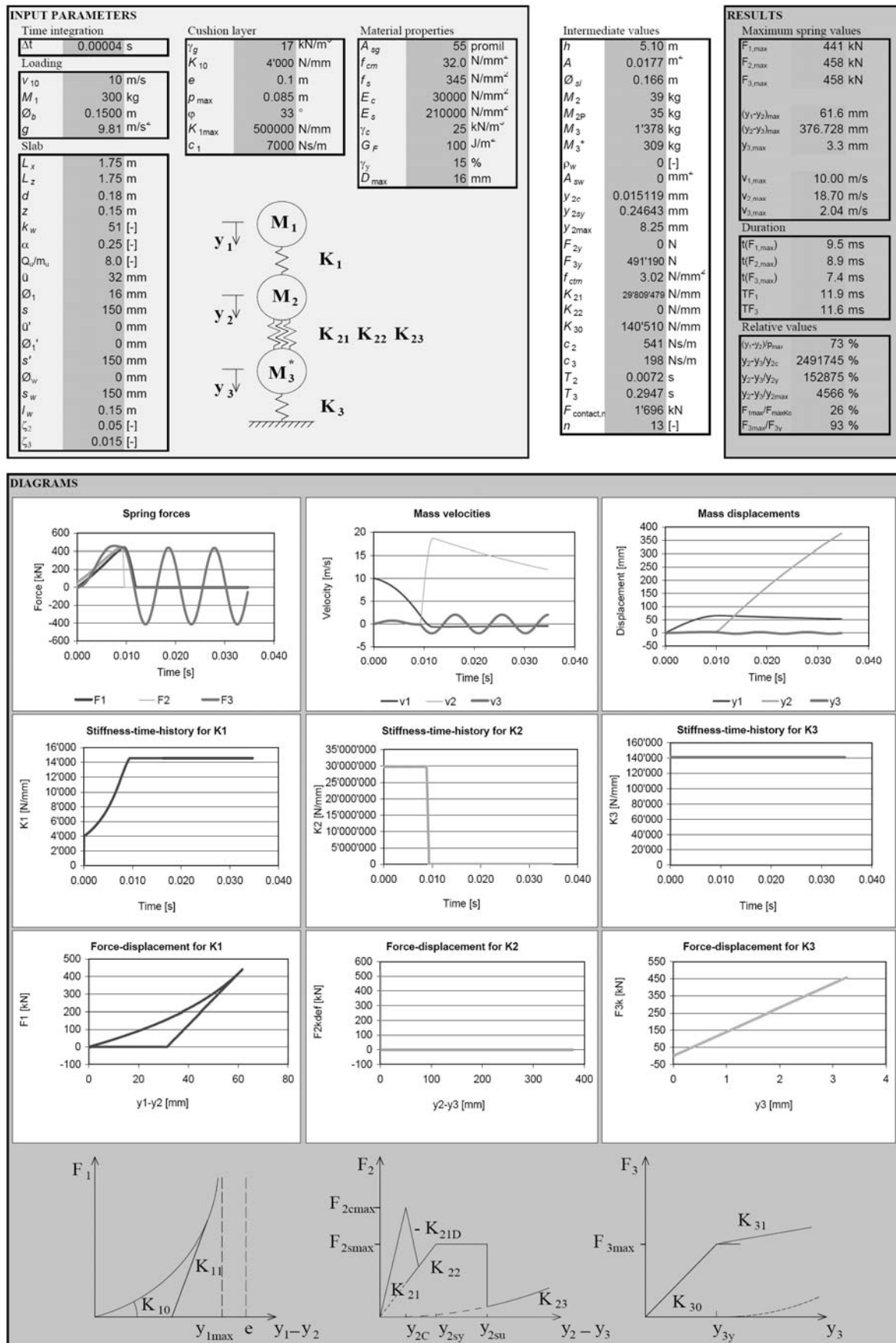
Test S15-10

Analytical model (System of multiple degrees of freedom)



Test S15-10 with $f_{cm} = 32 \text{ N/mm}^2$

Analytical model (System of multiple degrees of freedom)



F. Parameter sensitivity of SMDF

This appendix contains the results of the sensitivity analysis described in Chapter 5.3. Each of the following parameters was changed individually by 20%:

- Impact velocity v_1
- Striking mass M_1
- Static depth z and slab thickness d
- Mass factor α
- Cushion thickness e and maximum possible penetration p_{\max}
- Initial soil stiffness K_{10}
- Angle of internal friction φ
- Damping coefficient of soil c_1

From this summary, the state of each string can be observed. In particular the value $F_{3\max}/F_{3y}$ (η_3) gives additional information to judge on the increase of the spring force F_3 .

The following sheets can be found:

Case 1: large-scale test B2 (see also Appendix D)	167
Case 2: punching test S15-6 (see also Appendix E)	168
Case 3: protection gallery Axen-Süd	169
Models result for protection gallery Axen-Süd	170

Case 1: large-scale test B2

Time integration

Δt	8E-05 s
------------	---------

Loading

V_1	12.14 m/s
M_1	800 kg
\emptyset_b	0.7900 m
g	9.81 m/s ²

Slab

L_x	4.5 m
L_z	3.5 m
d	0.35 m
z	0.31 m
k_w	17 [-]
α	0.8 [-]
Q_u/m_u	4.0 [-]
\ddot{u}	20 mm
\emptyset_1	22 mm
s	155 mm
\ddot{u}'	15 mm
\emptyset_1'	10 mm
s'	300 mm
\emptyset_w	0 mm
s_w	150 mm
l_w	0.31 m
ζ_2	0.05 [-]
ζ_3	0.015 [-]

Material properties

A_{sg}	55 promil
f_{cm}	35.0 N/mm ²
f_s	500 N/mm ²
E_c	30000 N/mm ²
E_s	210000 N/mm ²
γ_c	25 kN/m ²
G_F	100 J/m ²
γ_y	15 %
D_{max}	16 mm

Cushion layer

γ_g	20 kN/m
K_{10}	56'000 N/mm
e	0.4 m
p_{max}	0.2 m
ϕ	33 °
K_{1max}	500000 N/mm
c_1	7000 Ns/m

Intermediate results

h	1.00 m
A	0.4902 m ²
\emptyset_{sl}	1.007 m
M_2	1'700 kg
M_{2P}	1192 kg
M_3	13'781 kg
M_3^*	9'833 kg
ρ_w	0 [-]
A_{sw}	0 mm ²
y_{2c}	0.033 mm
y_{2sy}	0.738 mm
y_{2max}	17.05 mm
F_{2y}	0 N
F_{3y}	1'487'883 N
f_{ctm}	3.21 N/mm ²
K_{21}	1.E+08 N/mm
K_{22}	0 N/mm
K_{30}	62'524 N/mm
c_2	7311 Ns/m
c_3	744 Ns/m
T_2	0.0232 s
T_3	2.4917 s
$F_{contact,ma}$	51'466 kN
n	13 [-]

Maximum spring values

$F_{1,max}$	2618 kN
$F_{2,max}$	2356 kN
$F_{3,max}$	1382 kN
$(y_1-y_2)_{max}$	41.6 mm
$(y_2-y_3)_{max}$	0.019 mm
$y_{3,max}$	22.1 mm
$V_{1,max}$	12.14 m/s
$V_{2,max}$	1.49 m/s
$V_{3,max}$	1.49 m/s

Duration

$t(F_{1,max})$	5.4 ms
$t(F_{2,max})$	5.0 ms
$t(F_{3,max})$	26.8 ms
TF_1	10.6 ms
TF_3	48.9 ms

Relative values

$(y_1-y_2)/p_{max}$	21 %
y_2-y_3/y_{2c}	57 %
y_2-y_3/y_{2y}	3 %
y_2-y_3/y_{2max}	0 %
F_{1max}/F_{maxKor}	5 %
F_{3max}/F_{3y}	93 %

V_1	M_1	$z (d)$	k_w	$\alpha \cdot e (p_{max})$		K_{10}	φ	c_1
+20%	+20%	+20%	+20%	+20%	-20%	+20%	+20%	-20%
14.6	960	0.37 (0.42)	20.4	0.96	1.32 (0.16) m	67200 N/mm	40°	560 Ns/m
3203	2877	2633	2618	2633	2673	2853	2617	2632
2883	2588	2375	2358	2'436	2'452	2'572	2375	2351
1512	1510	1679	1491	1313	1380	1383	1382	1396
50	45	42	42	42	41	38	42	42
0	0	0	0	0	0	0	0	0
26	26	16	20	21	22	22	22	22
15	12.14	12.14	12.14	12.14	12.14	12.14	12	12
1.763	1.730	1.230	1.461	1.290	1.497	1.499	1.488	1.491
1.766	1.728	1.231	1.463	1.289	1.494	1.502	1.486	1.491
5.3600	5.84	5.3600	5.3600	5.4400	5.2800	4.9600	5.3600	5.3600
5.0400	5.76	5.440	5.040	5.120	5.520	5.040	5.0400	5.1200
26.480	27.36	23.5	24.5	28.8	26.6	26.2	26.560	27.040
10.4	11.44	10.6	10.6	10.4	9.8	10.6	10.6	10.6
48.8	49.52	42	45	53	49	48	48.9	49.2
24.8	22.6	20.9	20.8	20.9	25.7	19.1	21	21
70.0	62.9	46.2	57.3	59.2	61.6	62.5	59.1	57.1
3.1	2.8	2.5	2.6	2.7	2.8	2.8	2.7	2.6
0.1	0.1	0.1	0.1	0.1	0.1	0.1	0.1	0.1
6.2	5.6	5.1	5.1	5.1	5.2	5.5	5.1	5.1
101.6	101.5	91.7	100.2	88.2	92.7	93.0	92.9	93.8

Appendices

Case 2: Punching test S15-6

Case 3: protection gallery Axen-Süd

Time integration

Δt	8E-05 s
Loading	
V_1	25 m/s
M_1	2'500 kg
\emptyset_b	1.1300 m
g	9.81 m/s ²
Slab	
L_x	8.6 m
L_z	7.5 m
d	0.55 m
z	0.51 m
k_w	33 [-]
α	0.2 [-]
Q_u/m_u	9.2 [-]
\ddot{u}	30 mm
\emptyset_1	30 mm
s	150 mm
\emptyset'	30 mm
\emptyset'	22 mm
s'	300 mm
\emptyset_w	0 mm
s_w	150 mm
I_w	0.51 m
ζ_2	0.05 [-]
ζ_3	0.015 [-]

Material properties

A_{sg}	55 promil
f_{cm}	35.0 N/mm ²
f_s	500 N/mm ²
E_c	30000 N/mm ²
E_s	210000 N/mm ²
γ_c	25 kN/m ²
G_F	100 J/m ²
γ_y	15 %
D_{max}	16 mm

Cushion layer

γ_g	20 kN/m ²
K_{10}	44'000 N/mm
e	0.8 m
p_{max}	0.6 m
φ	33 °
K_{1max}	500000 N/mm
c_1	7000 Ns/m

Intermediate results

h	31.86 m
A	1.0028 m ⁻²
\emptyset_{sl}	1.782 m
M_2	8'334 kg
M_{2P}	5671 kg
M_3	88'688 kg
M_{3*}	12'067 kg
ρ_w	0 [-]
A_{sw}	0 mm ⁻²
y_{2c}	0.055 mm
y_{2sy}	1.214 mm
y_{2max}	28.05 mm
F_{2y}	0 N
F_{3y}	1.E+07 N
f_{ctm}	3.21 N/mm ²
K_{21}	2.E+08 N/mm
K_{22}	0 N/mm
K_{30}	147'968 N/mm
c_2	21352 Ns/m
c_3	1268 Ns/m
T_2	0.0390 s
T_3	1.7943 s
$F_{contact,ma}$	105'299 kN
n	22 [-]

Maximum spring values

$F_{1,max}$	8569 kN
$F_{2,max}$	6763 kN
$F_{3,max}$	9045 kN
$(y_1-y_2)_{max}$	166.1 mm
$(y_2-y_3)_{max}$	0.039 mm
$y_{3,max}$	61.1 mm
$V_{1,max}$	25.00 m/s
$V_{2,max}$	4.05 m/s
$V_{3,max}$	4.05 m/s

Duration

$t(F_{1,max})$	10.3 ms
$t(F_{2,max})$	11.0 ms
$t(F_{3,max})$	28.3 ms
TF_1	20.2 ms
TF_3	46.6 ms

Relative values

$(y_1-y_2)/p_{max}$	28 %
y_2-y_3/y_{2c}	71 %
y_2-y_3/y_{2y}	3 %
y_2-y_3/y_{2max}	0 %
F_{1max}/F_{maxKor}	8 %
F_{3max}/F_{3y}	87 %

V_1	M_1	$z(d)$	k_w	$\alpha \ e (p_{max})$	K_{10}	φ	c_1
+20%	+20%	+20%	+20%	+20% -20%	+20%	+20%	-20%
30	3000	0.61 (0.66)	40	0.24 0.64 (0.48)	53000	40	5600
10535	9399	8663	8575	8648 8822	9318	8568	8602
8275	7479	7034	6873	7068 7'121	7'269	6'819	6'763
10465	10432	10779	9823	8586 9073	9138	9051	9074
197	180	168	166	167 164	152	166	167
0	0	0	0	0 0	0	0	0
73	71	43	55	58 61	62	61	61
30	25	25	25	25 25	25	25	25
4.88	4.57	4.37	4.16	3.64 4.15	4.22	4.06	4.06
4.88	4.57	4.37	4.16	3.64 4.15	4.22	4.06	4.06
10.2400	11.2	10.4800	10.4000	10.4000 10.2400	9.5200	10.4000	10.4000
10.9600	11.92	11.760	10.960	11.280 10.640	10.000	10.960	10.960
27.840	28.8	25.3	26.6	29.9 27.8	27.4	28.2	28.3
19.8	21.84	20.5	20.3	20.3 19.6	18.6	20.2	20.2
46.3	47.36	41	43	50 46	46	46	47
32.9	29.9	27.9	27.7	27.9 34.1	25.4	27.7	27.8
86.6	78.3	58.4	72.0	74.0 76.3	76.1	72.6	70.8
3.9	3.5	3.1	3.2	3.3 3.4	3.4	3.3	3.2
0.2	0.2	0.1	0.1	0.1 0.1	0.1	0.1	0.1
10.0	8.9	8.2	8.1	8.2 8.4	8.8	8.1	8.2
100.5	100.2	84.2	94.3	82.5 87.1	87.8	86.9	87.1

Appendices

Case study: Protection gallery Axen-Süd

Analytical model (System of multiple degrees of freedom)

